Departament de Teoria
del Senyal i Comunicacions

UNIVERSITAT POLITÈCNICA DE CATALUNYA

PhD Dissertation

On the Design of Microwave Radiometers with Digital Beamforming and Polarization Synthesis for Earth Observation

Xavier Bosch i Lluis

Advisor:

Prof. Adriano J. Camps Carmona

Barcelona, February 2011

ACKNOWLEDGEMENTS

This work has been conducted as part of the award “Passive Advanced Unit (PAU): A Hybrid L-band Radiometer, GNSS Reflectometer and IR-Radiometer for Passive Remote Sensing of the Ocean” made under the European Heads of Research Councils and European Science Foundation European Young Investigator (EURYI) Awards scheme in 2004, it was supported in part by the Participating Organizations of EURYI, and the EC Sixth Framework Program. It has also been supported by the Spanish National Research and EU FEDER Project TEC2005-06863-C02-01 (FPI grant BES-2006-11578, 2006-2010), and by the Spanish National Research and EU FEDER Project AYA2008-05906-C02-01/ESP.

I would like to specially thank my thesis advisor, Prof. Adriano Camps, for his guidance, dedication, advices and funding during these years.

I also would like to thank the whole PAU Team, and the rest of the laboratory members for their companionship, advices, and contributions.

Finally, I would like to thank Prof. S.C. Reising for hosting me during four months in the Microwave System Laboratory at the Colorado State University, Fort Collins, Colorado, USA.

A la meva familia,
A la Nereida, per fer de la meva vida un somni.

PREFACE

With the recent launch of the ESA's Soil Moisture and Ocean Salinity (SMOS) mission the scientific community is provided with the first polarimetric and multi-angular L-band radiometric measurements from the space. From the antenna temperature is possible to retrieve Sea Surface Salinity (SSS) and Soil Moisture (SM), which benefits both the oceanographic and climatologic studies. It is well known that it exists angular and polarization dependence for the radiometric measurements. Using this dependence, it is possible to use multi-angular and polarimetric measurements to retrieve geophysical parameters.

The main rationale that motivated the submission of the Passive Advanced Unit (PAU) project to the European Science Foundation (ESF) was to study the relationship between the brightness temperatures and some Global Navigation Satellite System Reflectometry (GNSS/R) observables, so as to improve the SSS retrievals. Also, the technical objectives of the PAU project included the development of new L-band radiometer concepts, such as a technological bed for providing new radiometer systems.

The present PhD dissertation extends the knowledge acquired in the recent years in the development of the SMOS radiometer, and is a contribution to the development of a new generation of passive sensors. For the first time – to author's knowledge – real-time digital beamforming and polarization synthesis have been successfully implemented in a real system. The system is able to steer multiple and simultaneous beams in different incidence angles without mechanical scan of the antenna, providing a new method to obtain multi-angular measurements combining an L-band radiometer with the concept of digital beamformer.

The PAU project has been developed by the Passive Remote Sensing Group of the Remote Sensing Lab, at the Department of Signal Theory and Communications of the *Universitat Politècnica de Catalunya*. The present PhD dissertation describes the work undertaken between 2005 and 2010 in both theoretical and hardware issues within the field of L-band radiometry with real-time digital beamforming with polarization synthesis.

This dissertation consists of a theoretical study performed on digital correlation radiometers with beamforming from the point of view of the synthetic aperture radiometers and an extended analysis of the impact of the digitization scheme. Moreover, the requirements to build a correlation radiometer with real-time digital beamforming and polarization synthesis have been stated. The new concept instrument has been built, internally equalized for the amplitude and phase of each receiver, tested and characterized in the anechoic chamber, and in a field campaign obtaining soil emissivity values for a range of incidence angles.

LIST OF ACRONYMS

ADC Analog-to-Digital Converter

AGC Automatic Gain Control

ALBATROSS Advanced L-Band EmissiviTy and Reflectivity Observations of the Sea Surface

ALU Arithmetic-Logic Unit

APU Arbitrary Power Unit

BPF Band-Pass Filter

C/A Coarse Acquisition

CNS Controlled Noise Source

CONAE *Comisión Nacional de Actividades Espaciales*

CPU Central Processing Unit

CU Control Unit

DBF Digital BeamFormer

DDM Delay-Doppler Map

DR Dicke Radiometer

DSP Digital Signal Processor

EMC Electro-Magnetic Compatibility

ENR Equivalent Noise Ratio

EPS Expanded Polystyrene Foam

ESA European Space Agency

ESF European Science Foundation

EURYI EURopean Young Investigator

FIR Finite Impulse Response

FFT Fast Fourier Transform

FOV Field Of View

FPGA Field Programmable Gate Array

FWF Fringe-Washing Function

GNSS/R Global Navigation Satellites Systems /Reflectometry

GODAE Global Ocean Data Assimilation Experiment

GPS Global Positioning System

GRAJO GPS and RAdiometric Joint Observations

griPAU Global navigation satellites systems Reflectometer Instrument for the Passive Advanced Unit

GUI Graphical User Interface

HAL Hardware Abstraction Layer

IDE Integrated Development Environment

IDFT Inverse Discrete Fourier Transform

IEEE Institute Electrical and Electronics Engineers

IF Intermediate Frequency

IIR Infinite Impulse Response

INTA *Instituto Nacional de Técnicas Aeroespaciales*

INTACK INTerruption ACKnowledged

IPT Interference Pattern Technique

IR Infrared Radiometer

IRQ Interrupt ReQuest

JTAG Joint Test Action Group

LAN Local Access Network

LAURA L-band AUtomatic Radiometer

LE Logic Element

LHCP Left Hand Circular Polarization

LNA Low Noise Amplifier

LPF Low-Pass Filter

LUT Look Up Table

MBE Main Beam Efficiency

MDDC Multiplexed Digital Down-Converter

MIPS Millions Instructions Per Second

MIRAS Microwave Imaging Radiometer by Aperture Synthesis

NCO Numerically Controlled Oscillator

NDN Noise Distribution Network

NF Noise Figure

NIR Noise Injection Radiometer

OS Operating System

PAU Passive Advanced Unit

PAU-GNSS/R Passive Advanced Unit - Global Navigation Satellites Systems/Reflectometry

PAU-SA Passive Advanced Unit - Synthetic Aperture

PAU-RAD Passive Advanced Unit - RADiometer

PAU-OR One Receiver

PAU-ORA Passive Advanced Unit - One Receiver Airborne

PDF Probability Density Function

PhD Philosophical Doctor

PIO Parallel Input/output

PLL Phase-Locked Loop

PR Polarimetric Radiometer

PRN Pseudo-Random Noise

PSS Practical Salinity Scale

PSU Practical Salinity Unit

RAM Random Access Memory

RF Radio Frequency

RFI Radio Frequency Interference

REMEDHUS *Red de Medida de la Humedad Salamanca*

RHCP Right Hand Circular Polarization

RISC Reduced Instruction Set Computer

RMS Root Mean Square

RMSE Root Mean Square Error

RSC Redundant Space Calibration

RTL Resistor Transistor Logic

RUT Receiver Under Test

SAC-D *Satélite de Aplicaciones Científicas-D*

SDK Software Development Kit

SDE Software Design Environment

SDRAM Synchronous Dynamic Random Access Memory

SLFMR Scanning Low-Frequency Microwave Radiometer

SLL Side Lobe Level

SM Soil Moisture

SMIGOL-R Soil Moisture Interference-pattern GNSS Observations at L-Band Reflectometer

SMOS Soil Moisture and Ocean Salinity

SNR Signal-to-Noise Ratio

SOPC System On Programmable Chip

SSS Sea Surface Salinity

TPR Total Power Radiometer

UART Universal Asynchronous Receiver-Transmitter

UPC *Universitat Politècnica de Catalunya*

UK-DMC United Kingdom -Disaster Monitoring Constellation

UAV Unmanned Aerial Vehicle

VHDL VHSIC Hardware Description Language

VHSIC Very High Speed Integrated Circuit

VWC Vegetation Water Content

OUTLINE

LIST OF FIGURES

LIST OF TABLES

Chapter 1

1 INTRODUCTION

This initial chapter provides an overview on the global context in which this Ph.D. thesis has been developed. This framework is the passive remote sensing, which has a relevant importance on oceanographic and climatologic studies.

1.1 Introduction

The interest of the scientific community in remotely measuring Sea Surface Salinity (SSS) and Soil Moisture (SM) has been increasing in the last years and much effort has been spent in that direction by the European Space Agency (ESA) and the National Aeronautics and Space Administration (NASA) in collaboration with the *Comisión Nacional de Actividades Espaciales* (CONAE) with the Microwave Imaging Radiometer by Aperture Synthesis/Soil Moisture and Ocean Salinity mission (MIRAS/SMOS) [1] and the Aquarius/*Satélite actividades Científicas*-D (SAC-D) [2] missions, respectively. Both of these missions carry aboard a microwave radiometer, which is an instrument that measures the spontaneous electromagnetic radiation emitted by all bodies at a physical temperature different from 0 Kelvin. Microwave radiometers where first used in radio-astronomy in the 1930's [3]. Since the 1960's a large number of microwave radiometers have been developed for remote sensing applications to measure a wide range of natural phenomena (for example [4] and [5]). Traditionally, these radiometers have a limited angular resolution due to the antenna size [6]. In the early 1980's, LeVine and Good [7] proposed the use of the interferometric aperture synthesis techniques used in radio-astronomy [8] as a way to overcome the limited angular resolution and avoid mechanical scanning especially at low microwave frequencies, e.g. L-band ([1], [9], and [10]), even though it has now been applied also at millimeter wave frequencies [11].

In principle, a number of radiometer architectures are suitable to be used for SSS retrieval applications, but the radiometric accuracy and resolution requirements are very challenging constraints ($\Delta T_B \sim 0.1$ K). So that, one of the major concerns on a radiometer design is its radiometric resolution that can be improved using low noise devices or even operating on a cool temperature environment. Furthermore, to achieve these tough requirements several auxiliary techniques can be used depending on the sensor type, not necessarily related to the radiometer design. For ground-based measurements, the radiometric resolution can be improved simply by increasing the integration time as long as needed due to the slow variations of the measurements. On the contrary, this is not possible for airborne or spaceborne sensors. In this case, an option is to acquire multi-angular measurements of the same scene taking advantage of the well-known dependence of the emissivity on the polarization and the incidence angle [12] (Figure 1.1).

Knowing this angular and polarization dependence it is possible to merge these measurements to retrieve geophysical parameters with a reduced standard deviation. This can be done using theoretical or semi-empirical models and minimizing a cost function following a non-linear least-squares estimation algorithm such as the Levenberg-Marquardt algorithm [13]. If the measurements' noise is uncorrelated, the standard deviation of the estimated observable is reduced as $\sqrt{N}$, where N is the number of independent measurements. If measurements are

not uncorrelated, the standard deviation decreases less rapidly following different trends [14].

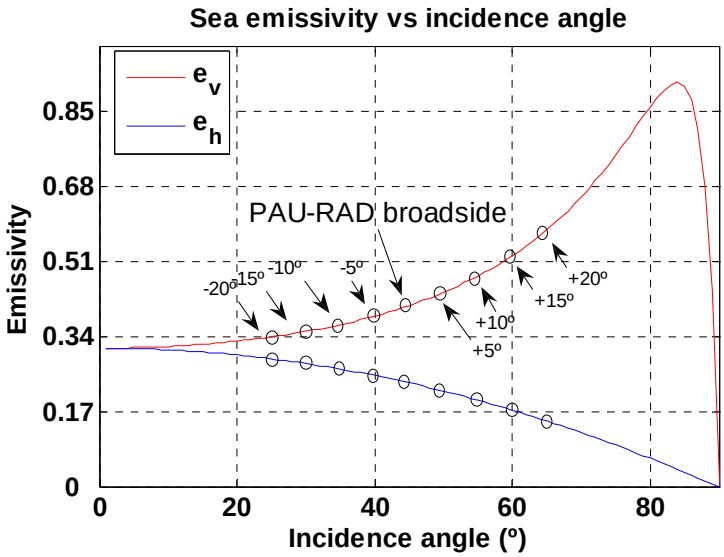

Figure 1.1. Vertical and horizontal emissivities *vs* incidence angle. PAU-RAD antenna boresight will be pointed to 45º and using the digital beamforming signal processing technique creates beams from 30º to 60º incidence angles in 5º steps. The emissivity curve corresponds to a calm sea with T_{sea}=293 K, SSS=36 psu and at $f_{GPS\text{-}L1}$=1575.42 MHz.

Typically, brightness temperature measurements at different incidence angles can be obtained simultaneously using different receivers, or with the same receiver acquiring data at different times ([15], [16]). Furthermore, multi-angular measurements are inherent in the image formation process in synthetic aperture radiometers such as SMOS/MIRAS [17] or PAU-Synthetic Aperture (PAU-SA)[18]. This PhD dissertation gives a new option to obtain multi-angular measurements combining an L-band radiometer with the concept of digital beamformer (DBF), which is able to steer multiple and simultaneous beams at different incidence angles without mechanical scan of the antenna.

While synthetic aperture radiometers generate antenna temperature maps, real aperture radiometers measure only a single pixel per antenna beam. Therefore, antenna temperatures can only be measured by mechanical scan of the antenna beam [19], in a push-broom configuration [2], or in a multiple beam array configuration [20]. However, an intermediate step between real and synthetic aperture radiometers are radiometers that use analog or digital beamforming, to electronically steer the beam. Actually, as it will be demonstrated, these instruments can be considered either as real or synthetic aperture radiometers, and they can generate not just one beam, but a number of simultaneous beams that can eventually be dynamically steered.

This PhD dissertation focuses on the design, test and performance of using digital beamforming techniques applied to an L-band radiometer.

1.2 Importance of the Sea Surface Salinity and the Soil Moisture Retrievals

Water plays a key role in all the geological and biological processes that take place in our planet. Cycling endlessly between oceans, atmosphere and land, it triggers and supports life, shapes the Earth and drives the weather and the climate (Figure 1.2). Recalling that oceans account for more than 96 % of water on Earth, it is important to study the mechanisms that govern the ocean-to-atmosphere interface.

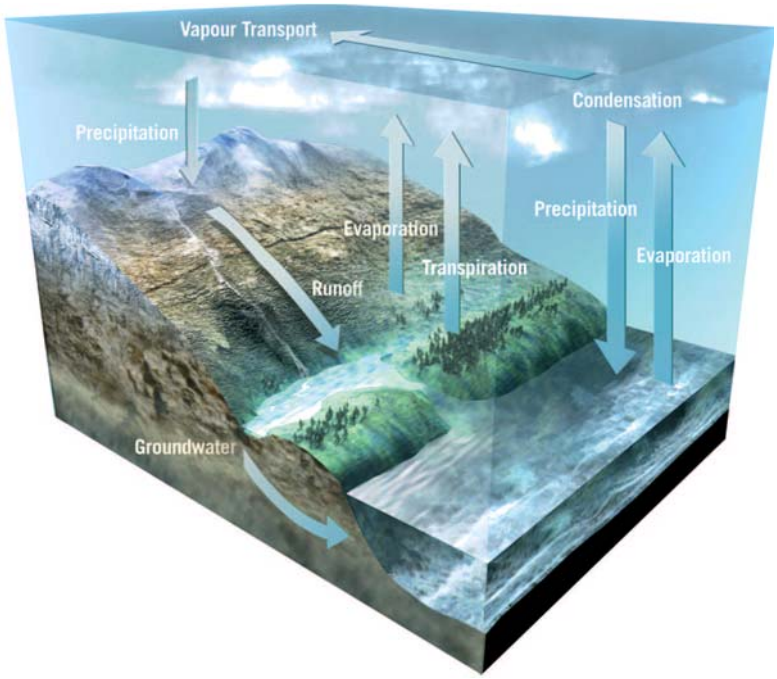

Figure 1.2. The water cycle on Earth [21].

Figure 1.2 shows the importance of the water cycle enlightening, which regulates the climate, and the Earth heat exchange. Water evaporates from the ocean, resulting as an increase of the SSS, if it rains again over the ocean, it decreases the SSS of the raining area. On the other hand, if it rains over the land, it implies an increase of the soil moisture. At the same time, the water which has precipitated over the land runs off and returns to the ocean, and the cycle starts again. Another option is that the land water evaporates, and returns to the atmosphere or it is transpired by the vegetation canopies.

1.2.1 The Sea Surface Salinity

The sea surface salinity (SSS) is an oceanographic parameter that depends on the balance between precipitation and fresh water river discharge, ice melting, atmospheric evaporation, and mixing and circulation of the ocean surface water

with deep water below. It is usually expressed using the practical salinity unit (PSU) of the practical Salinity Scale of 1978 (PSS-78). In the open ocean the SSS ranges between 32 psu and 38 psu, with an average value of 35 psu. It is maximum in sub-tropical latitudes, where evaporation is more important than precipitation. Conversely, the salinity drops below the average around the Equator, where there is more precipitation, and in Polar Regions, due to ice melting and snowfall. Salinity and temperature are the two variables that control the density of the ocean water, which increases with increasing salinity and decreasing temperature. Density itself is a very important oceanographic parameter, since ocean currents are generated by horizontal differences in density, and also its vertical profile determines the effect that surface winds, heating, and cooling have on subsurface waters. Salinity, through density, also determines the depth of convection at high latitudes. During the formation of sea ice, composed mainly of fresh water, dense cold salty water masses remain in the surface. At some point the water column losses its balance and denser water sinks. This vertical circulation is one of the engines of the global oceanic circulation known as the thermohaline circulation (Figure 1.3). This kind of oceanic conveyor belt is a key component of the Earth's heat engine, and therefore strongly influences the weather and the climate. Therefore, SSS is directly linked to the climatic cycle.

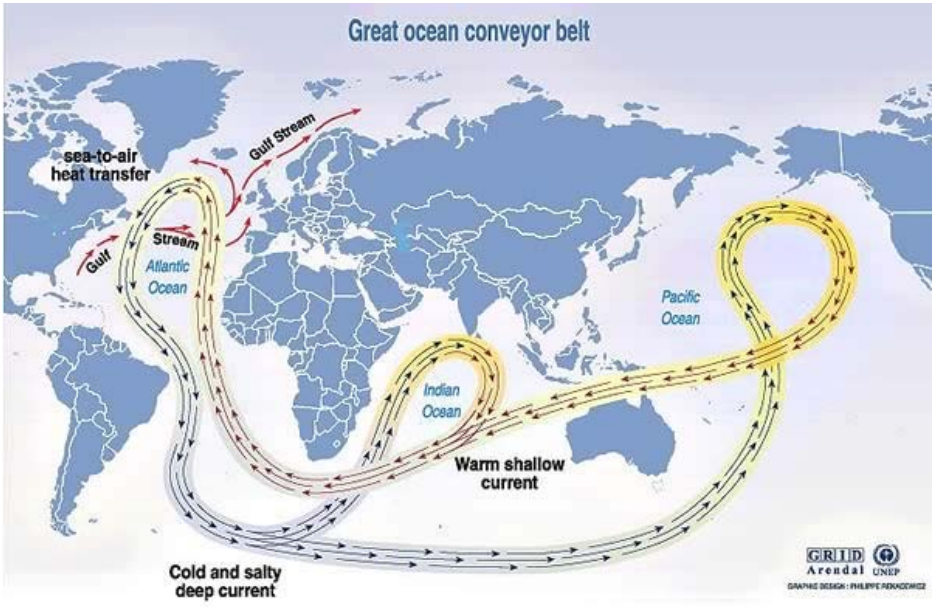

Figure 1.3. Thermohaline circulation acts as a global conveyor belt that redistributes heat throughout the whole planet [22].

Salinity also determines the behavior of the ocean-air interface where gas and heat exchange take place. The increased precipitation of tropical latitudes can locally create pockets of fresh water where the upper layer is more stable, thus reducing the gas transfer. SSS also influences the vapor pressure of sea water, thus controlling the evaporation rates.

Nowadays Sea Surface Temperature (SST) along with other oceanographic parameters such as Wind Speed (WS) or sea surface topography is monitored on a regular basis from spaceborne sensors. However, SSS retrieval from space has not

been possible so far [21]. Therefore, while ocean circulation models already incorporate satellite SST, WS and altimetry, they lack of accurate SSS data. To overcome this limitation usually temperature-salinity correlations are used, based on the density conservation principle over a certain water volume [23]. However, the validity of this principle is seriously questioned at the surface, where heat and gas exchange between sea and air takes place [24]. This results in modeling errors that hinder the modeling of surface currents. The severity of this lack of data is clearly understood considering that SSS has never measured for 42% of the ocean surface, and that has been measured less than four times over the past 125 years for 88% of the ocean surface [25].

1.2.2 The Soil Moisture

On the other hand, the soil moisture parameter is an important variable of the water cycle over the land, controls water fluxes between the atmosphere, the surface, and the subsurface. Because a large amount of heat is exchanged when water changes its phase, the water cycle is fundamental to the dynamics of the Earth's energy cycle. Also, since water is the ultimate solvent in the Earth system, biogeochemical cycles such as carbon, nitrogen and methane are embedded in the water cycle. Through these dynamics, soil moisture conditions the evolution of weather and climate over continental regions. Hence, global measurements of soil moisture are needed to improve the understanding of water cycle processes. Global soil moisture information will be transformational for the Earth's system science; it will help characterize the relationship between soil moisture, its freeze/thaw state, and the associated environmental constraints to ecosystem processes including land-atmosphere carbon, water and energy exchange, and vegetation productivity [26]. At the same time, global soil moisture information will enable societal benefit applications such as better water resource assessment, improved weather forecasts, natural hazards mitigation, predictions of agricultural productivity, and enhanced climate prediction, human health, and defense services.

1.3 Overview of Relevant Radiometric Missions

As it has been said, many microwave radiometers for Earth's remote sensing have been developed since the 1960´s, either ground-based, airborne, and space borne. For brevity, this section provides an overview of only real and synthetic aperture radiometric missions. Both missions were conceived for mapping SSS and SM, using different technologies.

1.3.1 The Aquarius Mission

The goal of the NASA/CONAE Aquarius mission [27] is to provide global mapping of SSS and soil moisture to improve the studies and modeling related to the global water cycle. Instead of a synthetic aperture radiometer, Aquarius will employ a 3-beam push-broom radiometers. It will also include a scatterometer to measure and correct for the sea surface roughness. This 1.26 GHz active sensor shall measure the power backscattered by the sea surface. This direct approach to correct for the roughness-induced bias in the retrieved SSS has the drawback of being power consuming, and the scatter plots $\sigma°$-ΔT_B still seem to exhibit a too large scatter.

1.3.2 The SMOS Mission

The spatial resolution of real-aperture radiometers depends on the antenna size. Therefore, they usually have large antennas with narrow beams to scan the field of view. However, the retrieval of some geophysical parameters, such as the soil moisture or the ocean salinity, has demanding requirements on spatial resolution (10-20 km). This implies antenna sizes on the order of 20 m of diameter from a LEO satellite, which at present are difficult to implement with the required performance. The aperture synthesis approach allows for lighter structures composed of small antennas that effectively 'synthesize' a larger one, able to meet the required spatial resolution [28]. The drawback is the increase in hardware, data processing and calibration complexity.

The ESA's SMOS mission, launched on November the 2nd 2009, is the first satellite ever attempted to globally measure the Earth's soil moisture and ocean salinity by means of L-band microwave radiometry. Despite the key role SSS plays in the water cycle, so far no global and systematic measurements are available. The SMOS mission has measured these parameters for the first time systematically from the space, globally and frequently, as previously stated in [29]. Both variables are crucial in weather, climate and extreme-event forecasting and they will be provided on spatial and temporal scales compatible with applications in the fields of climatology, meteorology and large scale hydrology [30].

The SMOS payload is MIRAS an L-band, two-dimensional, synthetic aperture radiometer with multi-angular and dual/fully-polarimetric imaging capabilities, able to measure the brightness temperature of the Earth within a wide field of view and without any mechanical antenna sweeping. It has a Y-shaped deployable structure, consisting of 3 coplanar arms, 120° apart each other. The total arm length is about 4.5 m with an angular resolution of approximately 2°. The range of incidence angles is variable (spanning from 0° to almost 65°) within the field of view (FOV) and depends on the distance between the pixel and the sub-satellite path. To achieve an even greater angular excursion and fully exploit its viewing capability the array is tilted 32° with respect to nadir.

1.4 PAU Concept

As discussed before, the collocated measurements of sea brightness temperature and reflected GNSS signal can result in a significant improvement of the retrieved SSS. The Passive Advance Unit (PAU) project aimed at demonstrating this sensor synergy. It was proposed in 2003 to the European Science Foundation (ESF) within the frame of the European Young Investigator (EURYI) Awards program, and was funded in 2004 [31]. Its scientific goals were to perform ocean monitoring by passive remote sensing, improve the knowledge of the relationship of the GNSS/R signal with the sea state, and improve the knowledge on the relationship between L-band brightness temperature and sea state. To accomplish these goals the PAU sensor consists of three instruments that operate in a synergetic way:

- PAU-RAD: an L-band radiometer with digital beam forming,
- PAU-GNSS/R: a reflectometer to measure the sea state using reflected global positioning system (GPS) opportunity signals, and
- PAU-IR: an off-the-shelf 8-14 μm thermal Infrared Radiometer (IR) to measure the sea surface temperature.

PAU is also a test bed of new technological demonstrators such as real aperture radiometers with real time digital beamforming and polarization synthesis, and fully-digital synthetic aperture radiometers, *etc*. In addition to the sea monitoring, the soil moisture (SM) monitoring using radiometric and GNSS/R signals is another target of the PAU-project.

1.5 Dissertation Organization

The present PhD dissertation is devoted to study the feasibility, build and test a real-time digital beamforming and polarization synthesis radiometer. It has been organized as it follows:

- Chapter 1 provides an overview on the global context in which this PhD thesis has been developed. This frame is the passive remote sensing, which has a relevant importance on oceanographic and climatologic studies.
- Chapter 2 provides the necessary context for this PhD dissertation by giving an overview of the whole PAU-Project. Although, the PAU-RAD instrument is the main topic of this thesis, the other PAU-project instruments are described. The main objectives and goals of the PAU-project are analyzed: PAU-RAD, PAU-SA, griPAU, MERITXELL, and SMIGOL. Finally, a brief analysis of the up to date results is presented.

- Chapter 3 provides an introduction to microwave radiometry presenting and developing the most important concepts on this field. Furthermore, the most typical types of radiometers are presented: the total power radiometer, the Dicke radiometer, the noise injection radiometer, and the polarimetric radiometer. Finally, the main applications of microwave radiometry, and its bandwidth allocations are summarized.

- Chapter 4 focuses on the relationship between real and synthetic aperture radiometers giving a general and common mathematical framework to both of them. It will be demonstrated that a real aperture radiometer array can be understood as a synthetic aperture one, with a high level of redundancy. Therefore, all the recent results from synthetic aperture radiometry can be translated to real aperture radiometers. This fact can be used to create beamforming arrays in a new way. To do this, the beamforming array equation is expressed in terms of cross-correlations between all pairs of antenna signals.

- Chapter 5 provides a general framework to analyze the effects of a generic quantization scheme and sampling process on a correlation radiometer. It reviews, unifies and expands several previous works that focused on these effects separately. In addition, it provides a general theoretical background that allows analyzing numerically any digitization scheme including any number of quantization levels, irregular quantization steps, gain compression, clipping, jitter and skew effects of the sampling period.

- Chapter 6 is devoted to the analysis of the PAU-RAD instrument. These analyses are a previous step to build the system. Hence, some preliminary studies are necessary, starting with a general overview of the instrument giving its basic requirements. Moreover, following this line, in this chapter an explanation of the PAU-RAD radiometer concept is given including not only the novelty of the digital beamforming system, but a new type of topology which is presented and analyzed using noise waves.

- Chapter 7 focuses on the practical implementation of the PAU-RAD system, covering all the topics involved on its development. In the analog part, this chapter focuses on the antenna array, the radio-frequency and intermediate frequency stages, the analog to digital converter system, and the thermal control system. On the digital part, it focuses on the digital design of the arithmetic-logic unit, and on the control unit which manages the system.

- Chapter 8 analyzes the phase and amplitude equalization procedure. This is done by presenting the voltage signals from the pair of receivers to be cross-correlated have been provided in order to analyze the impact of the different terms o the equation. Furthermore, the equations of the differential algorithm for phase and amplitude estimation have been provided, and analyzed. After the estimation of these parameters from the raw complex-cross correlation their measurement standard deviation is reduced by using a Kalman filter.

- Chapter 9 is devoted to the analysis of the PAU-RAD performance from three different aspects: the beamforming performance, the real and synthetic aperture relationship (stated in Chapter 4), and finally, the reliability of the system performing radiometric field measurements. Concluding this analysis and comparing the results with the design requirements, it can be summarized that the PAU-RAD system fulfills the design requirements and it is able to measure radiometric data depending on the measurement set up.

- Chapter 10 reaches the main conclusions of this PhD dissertation. After discussing them, the future research lines are envisaged.

Chapter 2

2 PAU PROJECT DESCRIPTION

The aim of this chapter is to provide the necessary context for this PhD dissertation by giving an overview of the PAU-Project. Although, the PAU-RAD instrument is the main topic of this thesis, a glimpse to the other Passive Remote Sensors built in the laboratory in framework of the PAU project are provided. The main objectives and goals of the PAU project are analyzed: PAU-RAD, PAU-Synthetic Aperture, griPAU, MERITXELL, and SMIGOL. Finally, an up to date results are briefly analyzed, and field campaigns information are reported.

2.1 Overview of the PAU Project

Within the frame of the European Young Investigator (EURYI) program, in 2003 the PAU (Passive Advanced Unit for ocean monitoring) project was proposed to the European Science Foundation (ESF) to test the feasibility of using Global Navigation Satellite Systems Reflectometry (GNSS/R) over the sea surface to make sea state measurements and, jointly with infra red (IR) observations to obtain the Sea Surface Temperature (SST), perform the necessary corrections of the L-band brightness temperature [32]. GNSS/R was originally devised for altimetry applications [33], and in PAU it is extended to try to obtain a direct correction for the sea state, without having to rely neither in numerical sea surface spectra models, nor in scattering and emission models. Most of the projects described on this Chapter are under development and research, with promising results. Furthermore, the up to today main results of the PAU project have been reported in [34].

The concept is simple: when the electromagnetic wave is scattered over the sea surface, the scattered signal changes its polarization from right and left hand circular polarizaniton mainly, (RHCP and LHCP, respectively) and arrives at the receiver mainly from the specular reflection point, determined by the shortest distance between the transmitting GPS satellite and the receiver, but when the sea is roughed, the scattered signals come from a wider region (known as "glistening zone") that enlarges with increasing sea state, in a similar manner as the Sun reflecting over the sea (Figure 2.1).

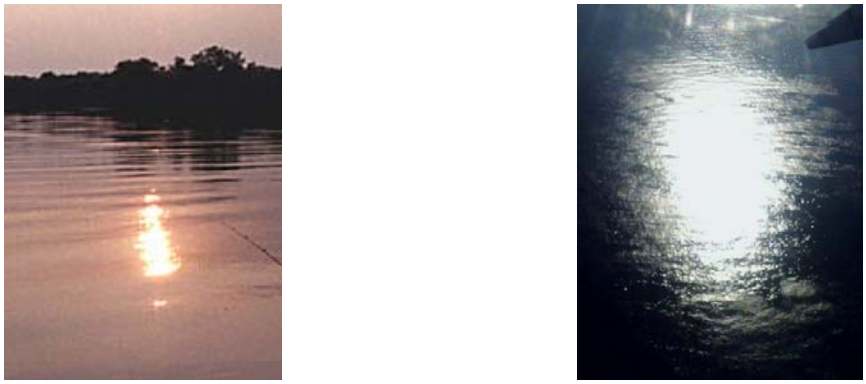

(a) (b)

Figure 2.1. Sun glint over the sea for: (a) calm, and (b) windy conditions [34].

When observing the GNSS reflected signals, two points over the sea surface correspond to the same delay and Doppler coordinates, and the point with minimum delay corresponds to the specular reflection point. In the PAU project it was proposed to measure the complete Delay-Doppler Maps (DDMs) to perform the sea state correction of the brightness temperature required for the salinity retrieval. The DDM is the square of the absolute value of the correlations of the reflected GNSS signals with local replicas of the transmitted signal, but shifted in delay and Doppler, and it is given by [35]:

$$|\mathrm{DDM}(\Delta\tau, \Delta f_d)|^2 = \mathrm{T_i^2} \iint \frac{|R|^2 \mathrm{D}^2(\vec{\rho}) \Lambda^2(\Delta\tau) |\mathrm{S}(\Delta f_d)|^2}{4\mathrm{R}_0^2(\vec{\rho})\mathrm{R}^2(\vec{\rho})} \frac{\mathrm{q}^4(\vec{\rho})}{\mathrm{q}_z^4(\vec{\rho})} \mathrm{P_v}\left(-\frac{\vec{\mathrm{q}}_\perp}{\mathrm{q_z}}\right) d^2\vec{\rho}, \quad (1)$$

where

- T_i is in the coherent integration time,
- R is the Fresnel reflection coefficient,
- D is the directivity of the receiving antenna,
- $\chi(\Delta\tau, \Delta f_d) = \Lambda(\Delta\tau)|\mathrm{S}(\Delta f_d)|$ is the Woodward ambiguity function, that can be approximated by the product of a triangle function $\Lambda(\Delta\tau) = (1 - |\Delta\tau|/\mathrm{T_c})$ if $|\Delta\tau| \leq \mathrm{T_c}$, being $\mathrm{T_c}$ the chip period, and a sinc function $\mathrm{S}(\Delta f_d) = \mathrm{e}^{-\mathrm{j}2\pi\Delta f_d \mathrm{T}i} \sin(\pi\Delta f_d \mathrm{T}_i)/\pi\Delta f_d \mathrm{T}_i$,
- $\mathrm{R}_0(\vec{\rho})$ and $\mathrm{R}(\vec{\rho})$ are the distances between the transmitter and receiver to the scattering point,
- q is the amplitude of the scattering vector $\vec{\mathrm{q}} \triangleq k(\hat{\mathrm{n}} - \hat{\mathrm{m}})$, where k is the wavenumber, $\hat{\mathrm{n}}$ and $\hat{\mathrm{m}}$ are the unit vectors of the incident and scattered waves, respectively, $\mathrm{q_z}$ is the z component of $\vec{\mathrm{q}}$, and $\vec{\mathrm{q}}_\perp$is the perpendicular component, and
- $\mathrm{P_v}$ is the sea surface slopes probability density function, and the integral is performed over the whole glistening zone.

Measuring the whole DDM, avoids the loss of information due to the asymmetry of the DDM originated by the relative orientation of the transmitter, the receiver and the wind direction, that is not captured when only the so-called waveforms (time domain correlation when the Doppler shift is compensated, waveform = $\mathrm{DDM}(\Delta\tau, \Delta f_d = 0)$) are measured.

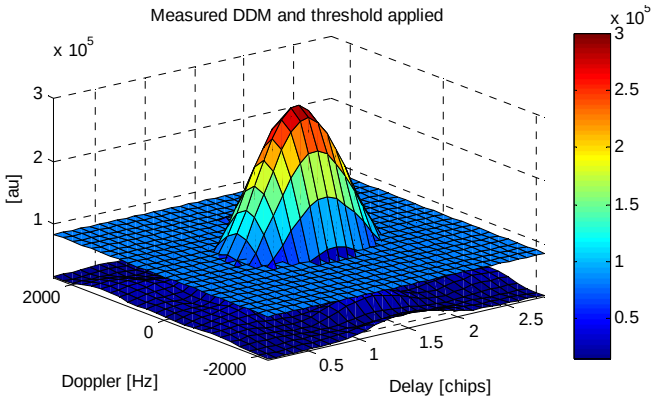

Figure 2.2. Measured (not normalized) 1 s incoherently integrated DDM with the threshold applied to compute its volume. Noise is below the threshold [34].

The volume of the normalized DDM (peak amplitude equal to 1) above a given threshold (Figure 2.2) has been found to provide a measurement of the area over which the GNSS signals are scattered, and it can be related to geophysical variables such as the sea surface roughness, without need of any intermediate model, either numerical to compute the scattering or for the sea surface spectrum ([36]-[38]).

In addition to the sea monitoring, the soil moisture (SM) monitoring using radiometric and GNSS/R signals is another target of the PAU-Project.

2.2 PAU Instrument Developments

A number of PAU system prototypes have been developed:

- PAU-RADiometer (PAU-RAD) instrument with a 4x4 element array with digital beamforming and polarization synthesis that uses of an innovative correlation radiometer topology to avoid the classical input switch in a Dicke radiometer, and
- PAU-Synthetic Aperture (PAU-SA) instrument, which is also used to test potential new technologically developments and algorithms for future SMOS missions.

In addition to these two, and in order to advance the scientific studies relating GNSS/R and radiometric observables, other PAU demonstrators have been developed:

- PAU-One Receiver (PAU-OR) with just one element for ground tests and algorithms development, and GNSS Reflectometer Instrument for PAU (griPAU), an improved PAU-OR instruments fully automated,
- PAU-One Receiver Airborne (PAU-ORA), a lighter version of PAU-OR for aircraft operations from a remote controlled aircraft,
- MERITXELL (Multi-frequency Experimental Radiometer With Interference Tracking For Experiments Over Land And Littoral) a classical Dicke radiometer, that includes not only L-band, but S-, C- X-, K-, Ka-, and W-bands, plus a multi-spectral camera, and a video camera in addition to the PAU-IR and PAU-GNSS/R units, and
- SMIGOL (Soil Moisture Interference-pattern GNSS Observations at L-band) instrument is a GNSS Reflectometer that works at GPS L1 band and which performs the Interference Pattern Technique (IPT).

In these technology demonstrators the input signals (PAU-RAD and PAU-GNSS/R) are the same: the GPS-L1 band. This should not be critical since, due to the scattering on the sea surface, the scattered GPS signal is at least 23 dB below of the thermal noise signal (to be measured by PAU-RAD). Thanks to the 30.1 dB correlation gain, PAU-GNSS/R can detect the GPS signal when the correct Coarse Acquisition (C/A) code is applied, and the error introduced in PAU-RAD observables is negligible, which only occurs when the specular reflection is coming from the antenna main beam. Taking into account that the beam can be electronically steered the chance of having a significant interference is remote. Signals' bandwidth are limited to the GPS bandwidth (2.2 MHz) and are demodulated at an Intermediate Frequency (IF) of 4.309 MHz. Signals are then digitalized at 8 bits at a sampling frequency of 5.745 MHz, to allow the use of digital demodulation, using band-pass sampling techniques.

2.2.1 PAU-RAD Real Aperture

The PAU-RAD is the main topic of this thesis. This instrument has been designed, built and tested within the frame of this PhD dissertation. Although PAU-RAD is further analyzed from various points of view, here a glimpse of it is provided in order to contextualize this PhD dissertation in the frame of the PAU project.

One of the technological goals of the project is to demonstrate the feasibility of combining in a single hardware two types of receivers: the radiometer itself (PAU-RAD) which, for stability reasons cannot be a total power radiometer, and the GNSS/Reflectometer (PAU-GNSS/R). In order to be able to use the same receivers for both the radiometer and the GPS-reflectometer, a new radiometer topology has been devised (Figure 2.3).

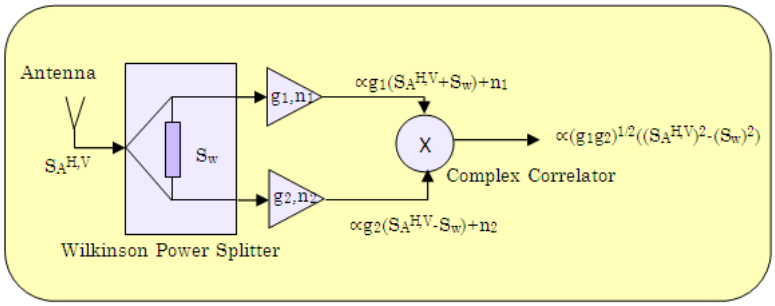

Figure 2.3. PAU-RAD concept block diagram.

Another technological goal, as challenging as the first one, is to develop an L-band radiometer with digital beamforming and polarization synthesis capabilities. This capability is a very useful novelty in microwave radiometry, since it allows obtaining simultaneously brightness temperature measurements at several incidence angles without mechanical scan of the antenna. As compared to a real aperture radiometer, instead of connecting the antenna output directly to the radiometer receiver, it is connected to the input of a Wilkinson power splitter that

divides the antenna signal (S_A) in two signals that are in phase. However, the 100 Ohm resistor of the Wilkinson power splitter that connects the two outputs also adds two noise signals that are 180º out-of-phase ($\pm S_w$).

Therefore, the signals at the input of the two channels of the radiometer are the sum and the difference of the antenna signal and the noise generated by the Wilkinson power splitter resistor, which is proportional to the physical temperature of the resistor. Once properly amplified, down-converted, and sampled they are finally cross-correlated leading to an output that is proportional to the difference between the antenna temperature and the physical temperature of the Wilkinson power splitter resistor. That is, the system output is the same as the one of the Dicke radiometer [39], but the input signal is not chopped, so that it can be used to track the GPS-reflected signal.

The extension to the *M*-element case (where *M* is the number of antennas of the PAU-RAD) is straightforward although technologically challenging. Instead of one antenna, there are *M*-dual polarization antennas, whose outputs are connected each to a Wilkinson power splitter. After amplification, down-conversion, and sampling, the *M*-outputs at each polarization are combined with the ones from other receivers with the appropriate amplitude and phases so as to digitally from the beam(s). The final output of each beam is obtained by cross-correlating the upper and lower branches, corresponding to the sum and difference signals (Figure 2.4).

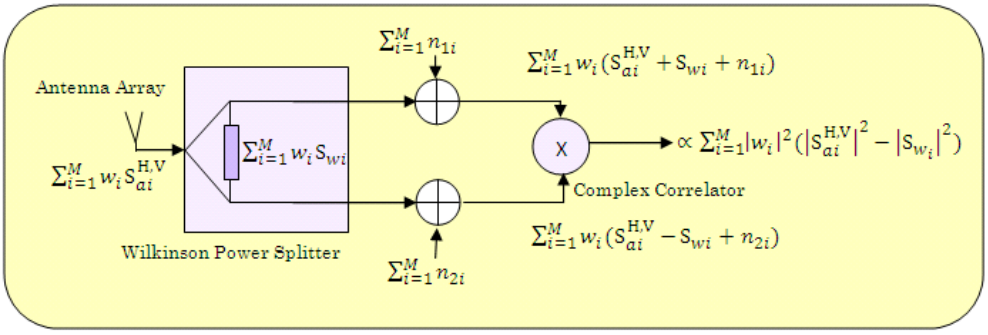

Figure 2.4. PAU-RAD equivalent sketch, where the actual signals have been substituted by the array signals.

If the vertical-polarization signals are cross-correlated, the antenna temperature at vertical polarization is measured. If the horizontal-polarization signals are cross-correlated, the antenna temperature at horizontal polarization is measured. And if the vertical-polarization signal is correlated with the horizontal-polarization one, the third and the fourth Stokes elements are measured, as twice the real and imaginary parts of the complex cross-correlation. Note that, since the vertical and horizontal channels do not share a Wilkinson power splitter, there is no "Dicke effect" (output proportional to the difference between the antenna temperature and the physical temperature of a reference) for the third and fourth Stokes parameters. Figure 2.4 shows the schematic of the whole PAU-RAD Real Aperture instrument.

In addition, two calibration signals are required for calibration purposes:

- uncorrelated noise, generated by a matched load at each input channel, to compensate for instrumental biases (cross-correlations must be zero), and
- two levels of correlated noise generated by a common noise source, to compensate for phase and amplitude mismatches among receivers.

Details on the calibration techniques and beamforming can be found in [40] and in [42].

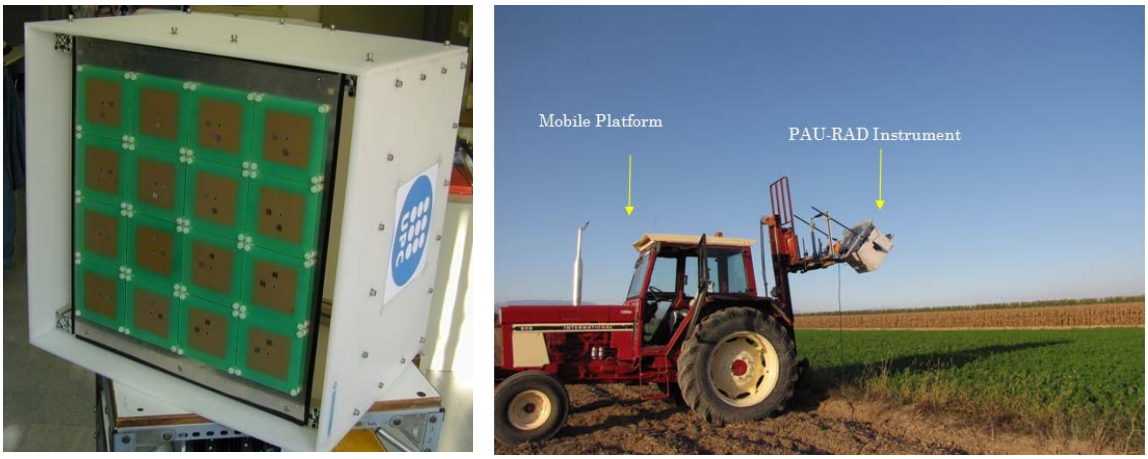

(a) (b)

Figure 2.5. PAU-RAD instrument (a) without radome, and (b) Measuring an alfalfa field, in the Palau d'Anglesola 2010 field campaign.

Figure 2.5 shows the PAU-RAD instrument without the radome, and measuring an alfalfa field during the Palau d'Anglesola 2010 campaign.

2.2.2 PAU-Synthetic Aperture

The receivers and frequency plan of PAU-SA (Figure 2.6) are the same as for PAU-RAD real aperture, but since the number of receiving elements (Y-shaped array with 8 elements per arm plus a central one) is much larger than in the PAU-RAD case (16 antenna elements), limitations in the FPGAs processing capabilities, forced to retain only one receiver chain per element and polarization, and the Wilkinson input switch was removed.

Table 2.1. MIRAS instrument and PAU-SA main parameters [43]

Parameter	MIRAS/SMOS	PAU-Synthetic Aperture	Rationale
Frequency operation	protected band: 1400-1427 MHz	GPS L1 (1575.42 MHz)	• availability of integrated circuits • limitation of integrated circuits and Field Programmable Gate Arrays (FPGAs) • minimizes spatial decorrelation.
Bandwidth	19 MHz	2.2 MHz	

Arm size	4 m	1.3 m	• operation from a truck
Altitude	755 km	ground-based experiments	-
Antenna type	dual-polarization patch antenna (non simultaneous)	dual polarization patch antenna (simultaneous)	• multiply by 2 the integration time • eliminate polarization transitions
Number of antennas per arm	23	8+1 (dummy)	• dummy antenna at edge for better pattern similarity
Total number of antennas	69	31	-
Antenna spacing	0.875 λ at 1400 MHz	0.816λ at 1575.42 MHz	• reduced antenna spacing to increase alias-free field-of-view
Receiver type	1 per element	2 per element (1 per polarization)	• double integration time • allow full-polarimetric mode without pol.-switching schemes
Topology of the LO down-converter	distributed LO (groups of 6 elements)	centralized reference clock + internal Phase Lock Loop (PLL) in each receiver for LO generator.	• avoid correlated noise from common Local Oscillator (LO) leaking to outputs through mixers and generating correlation offset
Quantization	1 bit IF sampling	8 bit IF sub-sampling using a external ADC	• use digital I/Q demodulation, low-pass filtering and power detection
I/Q conversion	analog	digital	• avoid phase quadrature errors and different receivers' noise temperature between I/Q branches
Frequency response shaped by…	analog RF filter	digital low- pass filter	• match global frequency response using narrow digital low-pass filters
Power measurement system (PMS)	analog, using detector diode	Digital (FPGA)	• avoid detector diodes thermal drifts
Digital Correlator Unit	$f_{CLK} = f_{sample}$	$f_{CLK} >> f_{sample}$	• use of band-pass sampling techniques
Imaging capabilities	dual-pol. or full-pol. (sequential)	Full-pol. (non-sequential)	• flexibility
Calibration capabilities	uncorrelated/2-level correlated noise injection	uncorrelated/2-level correlated noise injection and calibration using Pseudo-Random Noise (PRN) sequences	• test new calibration algorithms based on the injection of Pseudo-Random Noise (PRN) sequences.
Integration time	1.2 s	1 s, 0.5 s, 100 ms and 10 ms	• flexibility

Another of the objectives of PAU-SA was to test new techniques, technologies, and algorithms that could be eventually used in future SMOS missions. To better understand this, Table 2.1 summarizes the main parameters of the MIRAS instrument aboard SMOS mission [44] and the PAU-SA ones. The rightmost column lists the rationale behind each technological decision.

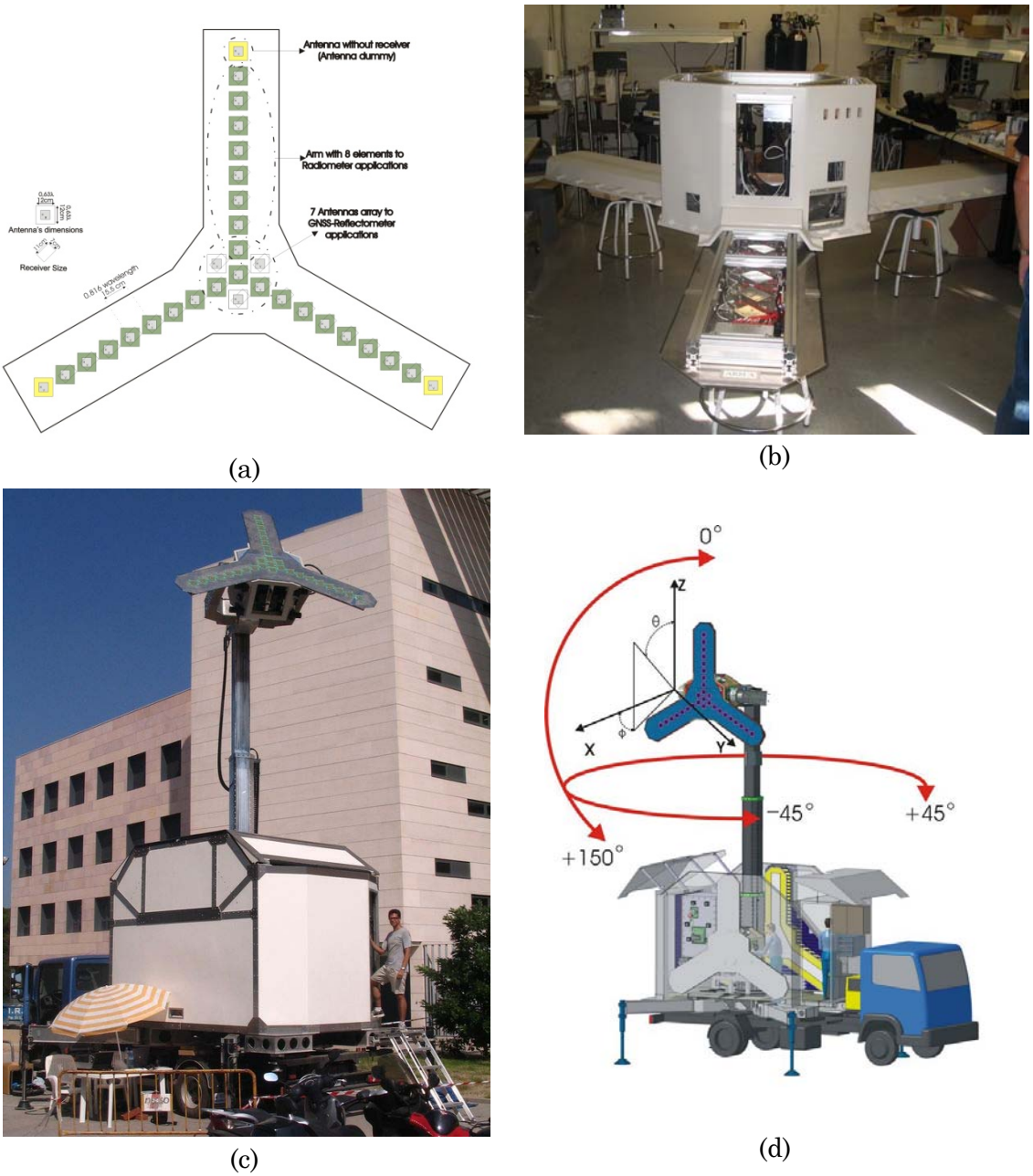

Figure 2.6 PAU-SA (a) PAU-SA's topology, (b) View of the whole instrument with one arm opened, (c) the PAU-SA mounted and deployed on its mobile unit, and (d) sketch of the functionalities of thePAU-SA's mobile unit [45].

The PAU-Synthetic Aperture is composed by a Y-shaped array of 8 antennas per arm plus the one in the center, and additional dummy antenna at the end of each arm. Moreover, the 4 central antennas plus 3 additional ones (7 in total) are used to create a steerable array for PAU-GNSS/R to point to the specular reflection points (total = 31 dual-polarization antennas). Figure 2.6 shows the PAU-Synthetic Aperture topology, and two pictures taken during the integration. Hardware, details, calibration, and simulations can be found in [18], and in [46].

2.2.3 PAU - One Receiver and griPAU

In order to develop the science behind the GNSS/R observables and their relationship with the brightness temperatures, two simplified instruments have been developed, which consist of just one LHCP down-looking antenna, a 7 LHCP path hexagonal array, and a RHCP up-looking antenna. Two of these instruments have been built, one for ground based operations (PAU-One Receiver –rev 1– [47] and griPAU –rev 2– [48]), and another one for airborne operations (PAU-One Receiver Airborne).

The griPAU instrument was deployed during the Advanced L-BAnd emissiviTy and Reflectivity Observations of the Sea Surface (ALBATROSS) 2009 field experiment in the Canary Islands. In this particular implementation of the PAU concept, two 7-patch hexagonal arrays are used: one for a dual polarization radiometer (vertical and horizontal polarizations) at 1400-1427 MHz (instead of f_0 = 1575 MHz, B = 2.2 MHz), and the second one for PAU-GNSS/R. A smaller up-looking patch antenna among the two arrays is used to track the delay of the direct signal, and fed it to the reflectometer. Figure 2.7 shows the griPAU block diagram. This instrument includes an automatic tracking of the specular reflection point of the pre-selected GPS satellite to simplify instrument's operation, while at the same time ensures observations collocated in time and space, exactly in the 1400-1427 MHz band used for passive observations.

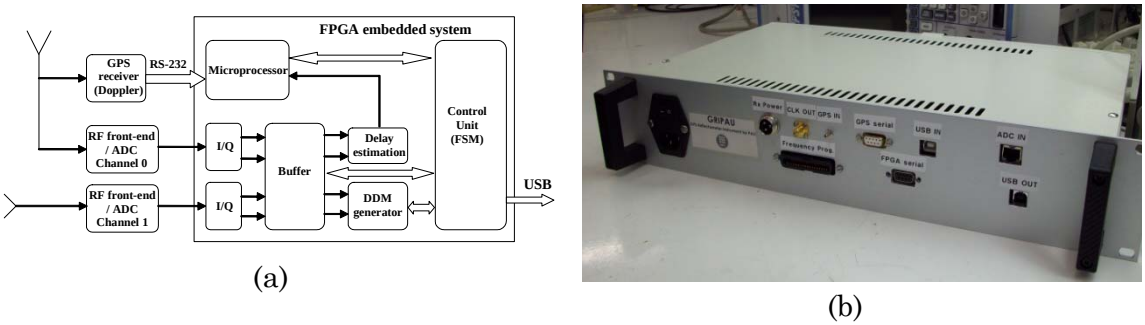

Figure 2.7 griPAU instrument (a) block diagram showing: commercial GPS receiver to provide Doppler estimates, up-looking receiving element to provide delay estimates (every 5 ms), and down-looking receiving element (with 7 LHCP hexagonal patch array) to collect the reflected signal. The whole system is embedded in a Xilinx Virtex-4 FPGA and has serial USB connectivity, and (b) a picture of the processing unit [48].

2.2.4 PAU- One Receiver Airborne

Figure 2.8a shows the PAU-One Receiver Airborne on the bay of a remote controlled aircraft. Details on the control, telemetry, data links and storage can be found in [49], and in [53]. Figure 2.8b shows the DDMs measured when the direct (RHCP) and reflected (LHCP) signals are collected simultaneously using two separated antennas connected to the inputs of a non-resistive 2-way power combiner [51].

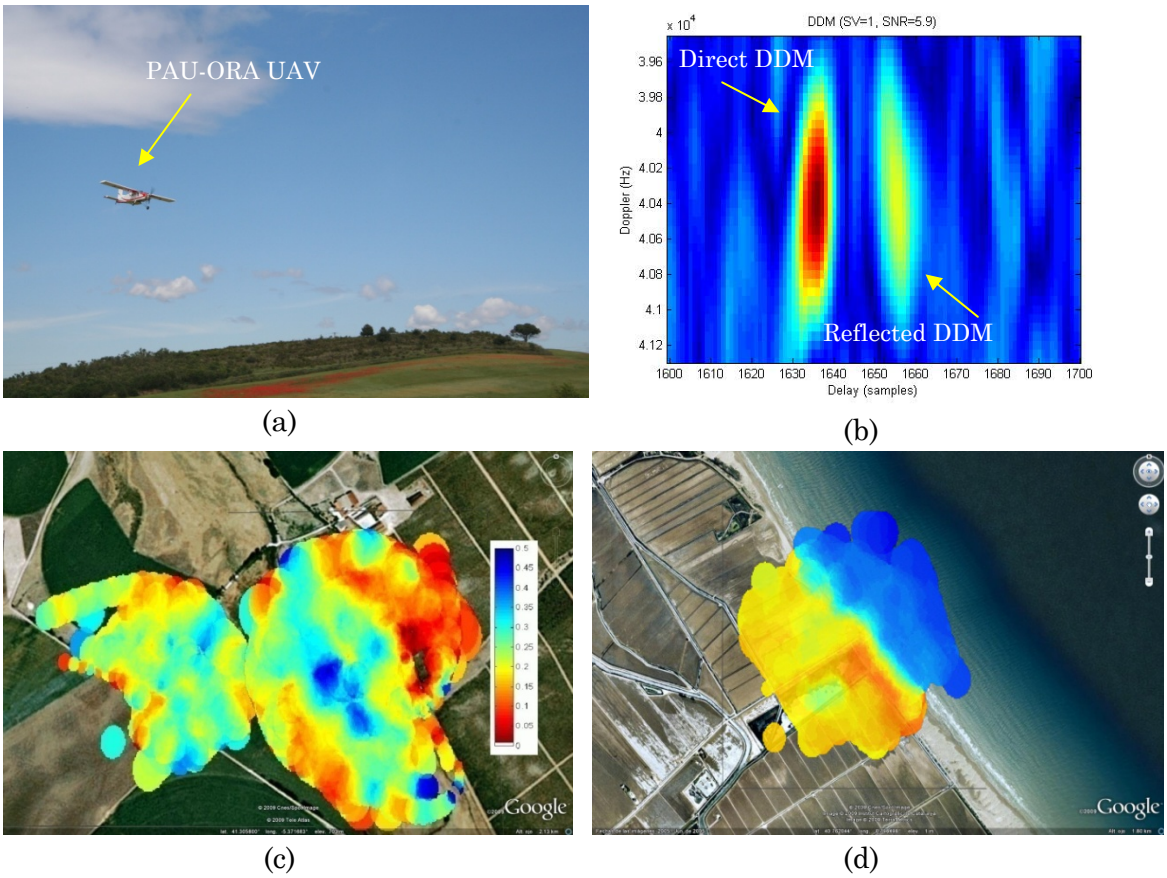

Figure 2.8. PAU-ORA overview (a) PAU – One Receiver Airborne instrument block mounted on the bay of a Remote Control aircraft, (b) DDMs obtained collecting simultaneously the direct (RHCP) and reflected (LHCP) signals [51], (c) Brightness temperature maps measured over Vadillo de la Guareña (Zamora, Spain) and (d) Marquesa Beach (Ebre river mouth, Tarragona, Catalonia)[50].

The left-hand side peak corresponds to the direct signal, which has larger amplitude, while the right-hand side one corresponds to the reflected one, which is attenuated in the scattering process and in the longer signal path. The separation between peaks is 21 samples, which correspond to ~ 770 m, since in this implementation of the instrument, the sampling frequency is 8.18 MHz [51]. Therefore, since the antenna was pointing to the nadir direction and the GPS satellite was close to the zenith, the estimated height is ~ 385 m, which is very close to the flight height (379 m). This design offers several advantages over the previous ones (just measuring the reflected signal) since it intrinsically provides absolute calibration of the scattering coefficient (ratio of peaks between direct and reflected DDM), it offers altimetry capabilities, and sea state determination using the full DDM.

2.2.5 MERITXELL

The Multi-frequency Experimental Radiometer With Interference Tracking For Experiments Over Land And Littoral (MERITXELL) radiometer is a step forward advancing our understanding of the potentials of combining data from several

sensors: microwave radiometers, multi-spectral and TIR cameras, and GNSS Reflectometers. It will also be used in testing radio frequency interference (RFI) detection and mitigation algorithms for microwave radiometry [54].

The MERITXELL microwave radiometer is a multi-band dual-polarization Dicke radiometer covering eight protected bands used for passive remote sensing: L, S, C, X, K, Ka, and W (Table 2.2). To add flexibility and simplify the design, a spectrum analyzer is used as IF stage, for filtering and power detection for all bands. This allows an easy reconfiguration of the band and/or frequency response shape, since the antennas and amplifiers response exceed those indicated in table 2. Antennas are 4 x 4 dual-polarization path arrays at L, S, and C bands, and horn antennas with a lens in the aperture to provide a quasi Gaussian beam for the other bands. In addition, MERITXELL includes a thermal camera (320 x 240 pixels) operating in the 8–14 µm range, a multi-spectral camera (640 x 480 pixels) with four spectral bands: red (λ_0 = 0.62 µm), green (λ_0 = 0.54 µm), blue (λ_0 = 0.45 µm) and Near Infra-Red (λ_0 = 0.80 µm), and a PAU-GNSS/R unit.

Table 2.2 MERITXELL microwave radiometer bands and antenna parameters [54].

Band	Central frequency	Bandwidth	Antenna beamwidth	Main beam efficiency
L	1.4135 GHz	27 MHz	~25º	98 %
S	2.695 GHz	10 MHz	~25º	98 %
C	7.185 GHz	90 MHz	~25º	98 %
X	10.69 GHz	20 MHz	~5º	95 %
K	18.7 GHz	200 MHz	~5º	95 %
K	23.8 GHz	400 MHz	~5º	95 %
Ka	36.5 GHz	1 GHz	~5º	95 %
W	89 GHz	6 GHz	~5º	95 %

Figure 2.9a shows the schematic of the MERITXELL microwave radiometer, and Figure 2.9b shows the front view with the antennas mounted (cameras and PAU-GNSS/R will be placed in the hole in the centre of the top row).

At the time of writing this manuscript the construction of a truck with a telescopic robotic mast to hold and orient both the PAU-Synthetic Aperture and MERITXELL instruments is finished (Figure 2.6c). It has been designed to hold one of these two instruments up to a 8 m height above the ground level, while the other is in the parking position (e.g. MERITXELL in Figure 2.9), and withstand up to 100 km/h wind loads.

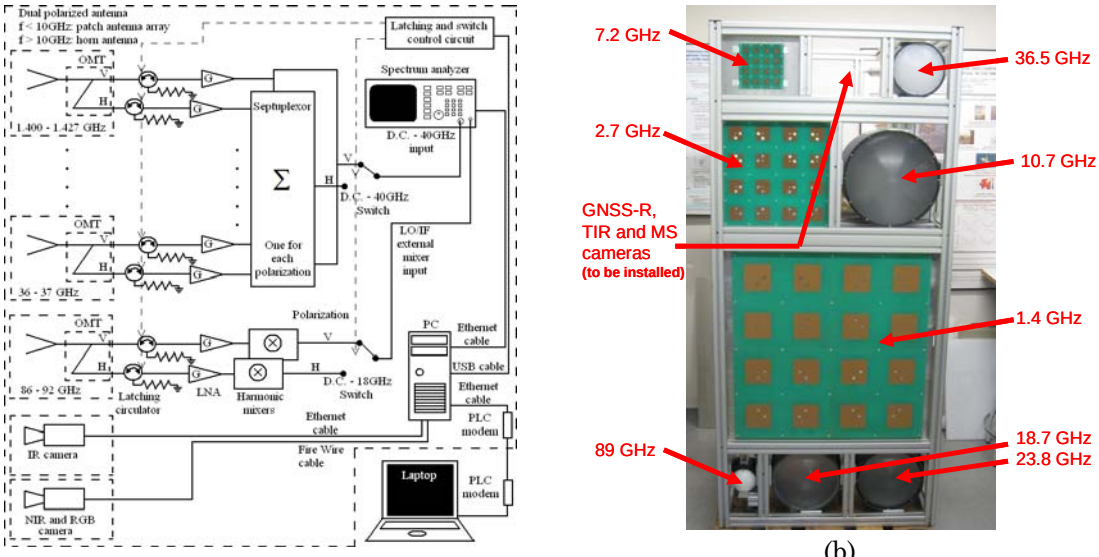

(a) (b)

Figure 2.9. (a) MERITXELL microwave radiometer schematic, and (b) front view [54].

2.2.6 SMIGOL

The Soil Moisture Interference-pattern GNSS Observations at L-band (SMIGOL) instrument is a different type of GNSS Reflectometer that works at the GPS-L1 band.

Figure 2.10. SMIGOL-Reflectometer at Palau d'Anglesola, Lleida, Catalonia [55].

The SMIGOL Reflectometer, is located pointing to the horizon, using a *v*-pol. patch antenna, and measures the interference power between the direct GPS signals and the reflected one over the surface. This technique is called Interference Pattern Technique (IPT). The IPT has been tested by measuring with the SMIGOL-Reflectometer and performing several geophysical parameters retrieval depending on the observed surface:

- Soil moisture mapping over a bare soil [55] (Figure 2.11a), vegetation growing retrieved over wheat-covered and barley-covered soils [56], and maize-covered

soils [57]. Figure 2.11b shows the vegetation growing retrieval over a wheat field, and

- topography mapping [56], Figure 2.11c shows the topography retrieval over a barley field.

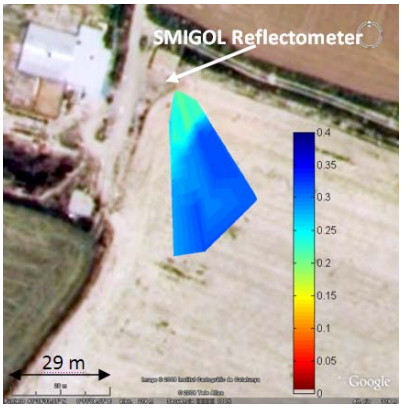

(a)

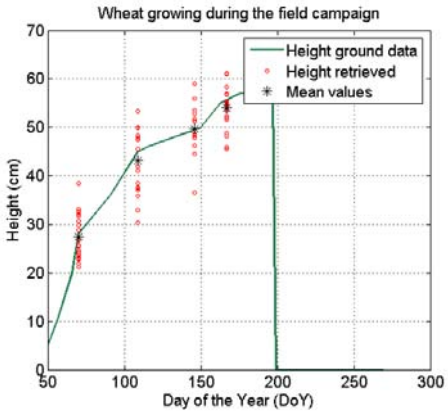

(b)

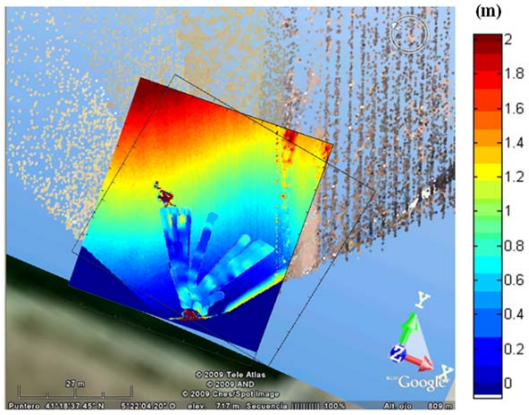

(c)

Figure 2.11. Fields observed in the various field experiments: (a) Soil moisture retrieval achieved over bare soil and (b) wheat growing retrieval achieved over wheat-covered soil, both observed at Palau d'Anglesola, Lleida (Catalonia) during 2008 and (c) topography retrieval achieved over barley-covered soil observed at Vadillo de la Guareña, Zamora (Spain) during 2009 ([55]-[57]).

2.3 Field Experiments

During May-June 2008 the first PAU-One Receiver was deployed at El Mirador del Balcón, La Aldea de San Nicolás, in the North-West coast of Gran Canaria in the Canary Islands (Spain), and gathered for the first time ever joint L-band radiometric and GNSS/R data, together with oceanographic data (sea surface temperature and sea surface directional spectrum buoys). The field experiment was repeated during the same period of time in 2009 with an improved version of the

instrument (griPAU) that collected radiometric and GNSS reflectometric data collocated both in time and space using two antennas with the same 22° beamwidth (Figure 2.12).

Figure 2.12. griPAU deployed during the ALBATROSS 2009 field experiment [38].

Figure 2.13 shows the scatter plot of the measured DDM volume (in arbitrary units) vs. the Significant Wave Height (SWH) for several threshold values despite the large scattering, this plot provides a understanding on the relationship between the sea state and the GNSS/R observables (DDMs) and the changes in the brightness temperature. It can be appreciated that increasing the threshold decreases the sensitivity to SWH, since a lower volume is being considered. However, this threshold cannot be arbitrarily small, since it has to be above the noise threshold to provide meaningful observations.

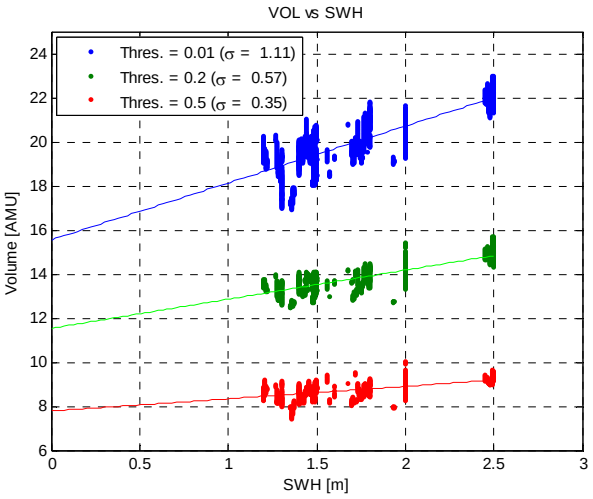

Figure 2.13. DDM-volume dependence on the SWH for three various thresholds [38]. Units are arbitrary measurement units (AMUs).

The correlation of the instantaneous brightness temperature changes and the instantaneous DDM volumes observed during ALBATROSS 2009 is shown in Figure 2.14 for incidence angles larger than 55°, since the cliff already imposed a 45° mask, and incidence angles between 45° and 50° were affected by multi-path.

Despite these encouraging results, there is still a long way to go until meaningful physical quantities can be successfully extracted from satellite data to be used by the oceanographic communities, and they can be used to perform the sea state correction in sea surface salinity retrievals. More extensive data sets need to be gathered and processed.

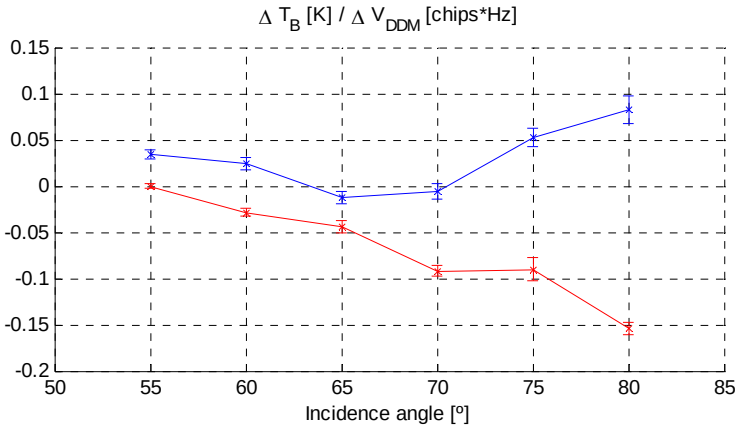

Figure 2.14. Estimated brightness temperature resolution to changes in the normalized DDM volume at vertical (red) and horizontal (blue) polarizations respectively [48].

Following this line, the GPS and RAdiometric Joint Observations (GRAJO) one year experiment was conducted from November 2008 at *Red de Medida de la Humedad Salamanca* (REMEDHUS) network [58] (Figure 2.15).

(a) (b)

Figure 2.15 GRAJO field campaign: (a) LAURA and SMIGOL deployed instruments [58], and (b) preparing the Unmanned Aerial Vehicle (UAV) of PAU-ORA for measuring [50].

At the plot scale, the goal of this experiment is to jointly use radiometry and GPS-reflectometry data to study: the potentially of the GNSS/R techniques measuring SM, the influence of the vegetation on the retrieval of geophysical parameters, and to characterize the effective roughness parameter to be used in the land emission models. The experiment site is located in a farm within the REMEDHUS network located at Vadillo de la Guareña, Zamora, Spain.

The limited GNSS/R data gathered by the United Kingdom - Disaster Monitoring Constellation (UK-DMC) satellite and publicly available [59] shows the potential of this technique, and supported the proposal of a PAU secondary payload in SeoSat/INGENIO (Spanish Earth Observation Satellite) [60]. This proposal went through phase A, but did not succeed to pass into phase B due to accommodation issues with the primary payload raised after a configuration change. A simplified, lighter and less power consuming payload is currently under development in cooperation with local aerospace industry and the *Instituto Nacional de Técnicas Aeroespaciales* (INTA) and they will be available for future launches of opportunity in micro- satellites or even in pico-satellites.

2.4 Conclusions

This chapter has presented the PAU-Project description and the main instruments developed on its frame. The suite of PAU instruments that have been (and are currently being) developed at the Remote Sensing Lab of the *Universitat Politècnica de Catalunya* has been presented. These include: PAU-RAD, PAU-Synthetic Aperture, griPAU, PAU-One Receiver Airborne, MERITXELL, and SMIGOL. These instruments have been developed for two purposes: 1) to analyze the nature of reflectometric observables and their relationship with the brightness temperature at L-band mainly over the sea and the land, and 2) to be technological demostrators of improvements to be applied in future space-borne missions (SMOS follow-on missions), or secondary payloads that can help in the sea state correction.

Furtermore, a glimpse to the basic principles of GNSS reflectometry has been given. It is important to notice that these principles are used in the PAU-project, but not in this PhD dissertation. Even though, it has been shown how these observables can be eventually used to correct the changes in the brightness temperature at L-band due to the sea state. These corrections [61] are needed to improve the quality of the sea surface salinity retrievals using L-band microwave radiometry.

Chapter 3

3 MICROWAVE RADIOMETRY BASICS

This chapter provides an introduction to microwave radiometry presenting and developing the most important concepts on this field. Furthermore, the most typical types of radiometers are presented: the total power radiometer (TPR), the Dicke radiometer (DR), the noise injection radiometer (NIR), and the polarimetric radiometer (PR). Finally, the main applications of microwave radiometry, and its bandwidth allocations are summarized.

3.1 Overview of Radiometric Techniques

This chapter provides an introduction to microwave radiometry. Radiometry is the field of science devoted to the measurement of the thermal electromagnetic energy emitted spontaneously by all bodies which at a physical temperature different from 0 K. This technique was born in the radio-astronomy field to measure the electromagnetic emissions coming from the outer space. Since the 1960's it has became a common and powerful tool for Earth remote sensing. With the study and analysis of the physical processes related with this spontaneous emission, it is possible to infer the parameters that have caused it, such as atmospheric or geophysical parameters. Hence, a radiometer is an instrument that measures this emitted energy (brightness temperature) with high resolution and accuracy.

In this chapter microwave radiometry concepts are presented and then different types of radiometers are described: the total power radiometer (TPR), the Dicke radiometer (DR), the noise injection radiometer (NIR), and the polarimetric radiometer (PR).

3.2 Main Concepts on Microwave Radiometry

In this section the main concepts on microwave radiometry are presented and analyzed, starting from the power collected by an antenna up to the concept of emissivity and brightness temperature.

3.2.1 Power Collected by an Antenna

The power emitted by an extended body per solid angle, per unit of radiating surface and per Hertz is called spectral brightness density ([Wsr^{-1} $m^{-2}Hz^{-1}$]). If the emitting surface radiates with a pattern $F_t(\theta,\phi)$, the brightness $B(\theta,\phi, f)$ is given by Eqn. (3.1) [39]:

$$B(\theta,\phi,f) = \frac{F_t(\theta,\phi)}{A_t}, \tag{3.1}$$

where A_t is the total area which is radiating, θ and ϕ are the azimuth and zenith angles, respectively, and f is the frequency dependency of the spectral brightness density. Thence, the power collected by a lossless antenna surrounded by a distribution of incident power $B(\theta,\phi,f)$ can be computed as (Eqn. (3.2)):

$$P = F_t \frac{A_{eff}}{R^2} = B(\theta, \phi, f) A_t \frac{A_{eff}}{R^2} \tag{3.2}$$

where A_{eff} is the effective area of the antenna and R is the distance to the radiating surface (the effective area is given by $A_{eff} = \mathrm{D}\lambda^2/4\pi$, where D is the antenna directivity, and λ^2 the squared wavelength). Taking into account that the solid angle Ω_t subtended by the transmitting antenna is defined by (Eqn.(3.3)):

$$\Omega_t = \frac{A_t}{R^2}, \tag{3.3}$$

then, the power collected by the antenna can be computed as (Eqn. (3.4)):

$$P = B(\theta, \phi, f) A_{eff} \Omega_t, \tag{3.4}$$

replacing the solid angle by a differential solid angle *($d\Omega$),* the corresponding power received by the antenna from an extended source of incidence brightness $B(\theta, \phi, f)$ can be expressed as:

$$d\mathrm{P} = A_{eff} B(\theta, \phi, f) |F_n(\theta, \phi)|^2 d\Omega, \tag{3.5}$$

where $|F_n(\theta, \phi)|^2$ is the normalized antenna radiation pattern. The total power collected by the antenna is then obtained by integrating Eqn. (3.5) over the system's bandwidth and over the space:

$$\mathrm{P} = \frac{1}{2} A_{eff} \int_{f-\mathrm{B}/2}^{f+\mathrm{B}/2} \iint_{4\pi} B(\theta, \phi, f) |F_n(\theta, \phi)|^2 d\Omega df, \tag{3.6}$$

where B is the bandwidth of the receiving system, and the $1/2$ factor accounts for the fact that the observing antenna can only measure the noise in one polarization, so only half of the incident power (random polarization of $B(\theta, \phi, f)$, equally distributed in two orthogonal polarizations) can be measured.

3.2.2 Thermal Radiation

This section gives an overview over the quantum theory radiation, and the Plank's law.

3.2.2.1 Quantum Theory of Radiation

All bodies receive electromagnetic energy from its surroundings. Part of this incident energy is reflected on the body's surface. The rest is absorbed and, if in thermodynamic equilibrium, re-radiated. According to Bohr's equation, the frequency *f* of an emitted radiation is given by:

$$f = \frac{\varepsilon_1 - \varepsilon_2}{h}, \tag{3.7}$$

where ε_1 and ε_2 are different energy levels in Joules ([J]), and h is the Planck's constant (h = 6.63·10^{-34} J). The emission of radiation is caused by electrons changing its energy. The emission probability is a function of the density of the particles and the kinetic energy of their random motion. The increase of the intensity of the energy radiated by a body is proportional to the increase of its absolute temperature.

3.2.2.2 Planck's Radiation Law

In general, part of the electromagnetic energy incident on a surface is absorbed, and part is reflected. The amount of energy that is absorbed is re-radiated, if in thermodynamic equilibrium.

A black-body is defined as an ideal body that absorbs all of the incident electromagnetic energy (at all wavelengths, directions and polarizations) and, in thermodynamic equilibrium, radiates it back. According to Planck's law, a black-body radiates uniformly towards all directions with a spectral brightness density given by Eqn. (3.8):

$$B_{bb}(f) = \frac{2hf^3}{c^2} \frac{1}{e^{\frac{hf}{kT_{ph}}} - 1}, \tag{3.8}$$

where:

- $B_{bb}(f)$ is the black-body spectral brightness density,
- f is the frequency in Hertz [Hz],
- k is the Boltzmann's constant (k = 1.38·10^{-23} J K^{-1}),
- T_{ph} is the absolute physical temperature in Kelvin, and
- c is the speed of light (c =299.792.458 m/s).

According to Eqn. (3.8), the brightness of a black-body depends on the frequency of observation and on its physical temperature. Different plots of the black-body's brightness at different physical temperatures are shown in Figure 3.1.

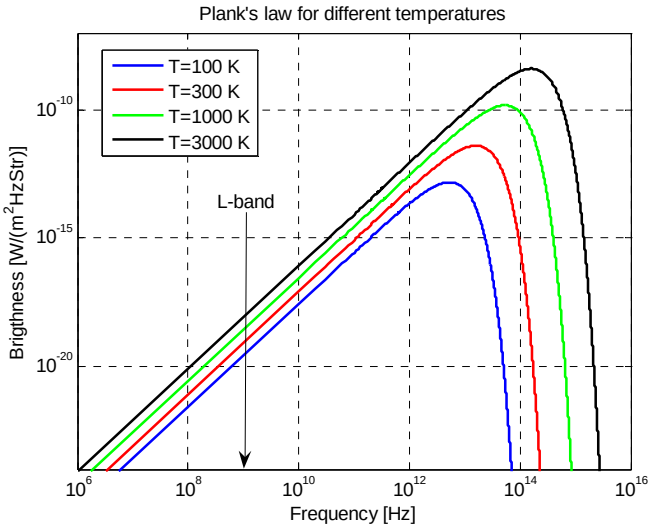

Figure 3.1 Black body's brightness for different temperatures. Both axes are logarithmic units.

In Figure 3.1, it can be seen that the brightness of a black-body for a given physical temperature has a rising region and a falling region, separated by a peak. These regions can be approximated by Rayleigh-Jeans' law (rise) and Wien's law (fall), respectively. The Rayleigh-Jeans' law can be derived from the first order Taylor polynomial expansion of the Planck's law (Eqn.(3.9)) for low frequencies. Hence, at low microwave frequencies the Rayleigh-Jeans law can be used as good approximation of the Planck's law and can be written as:

$$B_{bb}(f) \sim \frac{2f^2 k \mathrm{T}_{ph}}{c^2} = \frac{2k\mathrm{T}_{ph}}{\lambda^2}, \tag{3.9}$$

The error committed by the Rayleigh-Jeans' approximation, which covers a large part of the microwave spectrum, is smaller than 0.12 %, if the physical temperature is 300 K and the frequency is 1.57542 GHz (GPS-L1 band). Therefore, Eqn. (3.9) will be used from now on. Note that there is a linear relationship between the spectral brightness density and the physical temperature.

3.2.2.3 Antenna Surrounded by a Black Body

The power received by a lossless antenna with normalized radiation pattern $|F_n(\theta,\phi)|^2$, over a B bandwidth around a working frequency *f*, placed inside of a black-body at a constant physical temperature T_{ph} is already obtained using the Eqns. (3.6) and (3.9), and it is described by:

$$\mathrm{P_{bb}} = \frac{1}{2} A_{eff} \int_{f-\mathrm{B}/2}^{f+\mathrm{B}/2} \iint_{4\pi} \frac{2k\mathrm{T}_{ph}}{\lambda^2} |F_n(\theta,\phi)|^2 d\Omega df. \tag{3.10}$$

The detected power is limited by the receiver's bandwidth B. If this bandwidth is small enough to assume that the spectral brightness density does not change over the frequency range, Eqn. (3.10) reduces to:

$$\mathrm{P_{bb}} = \frac{k\mathrm{T}_{ph}}{\lambda^2} A_{eff} \mathrm{B} \iint_{4\pi} |F_n(\theta,\phi)|^2 d\Omega, \tag{3.11}$$

which leads to:

$$\mathrm{P_{bb}} = \frac{k\mathrm{T}_{ph}}{\lambda^2} A_{eff} \mathrm{B}\Omega_{eff} = k\mathrm{B}\mathrm{T}_{ph}, \tag{3.12}$$

when integrating the normalized antenna radiation pattern over the entire space and using $\Omega_{eff} = \lambda^2/A_{eff}$. The result in Eqn. (3.12) was also found by Johnson and Nyquist in 1928 when calculating the available thermal noise power from an electrical resistor at a physical temperature T_{ph}.

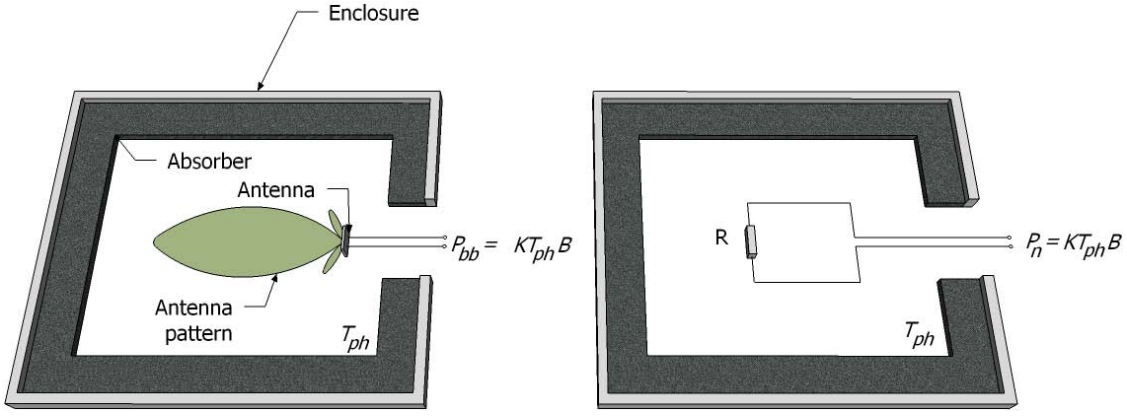

Figure 3.2 The power delivered by: (a) an antenna surrounded by a black-body enclosure with a temperature T_{ph}, and (b) a resistor maintained at the same physical T_{ph} (assuming each one is connected to a matched receiver of bandwidth B).

Equation (3.12) shows that the power in a bandwidth B received by a lossless antenna surrounded by a black-body is linearly dependent on the physical temperature of the body. Using Johnson's and Nyquist's results, an ideal receiver with a bandwidth B collects as much power from a matched resistor at a physical temperature T_{ph} than from a lossless antenna connected to it. This means that, for an ideal receiver of bandwidth B, the antenna delivers to the load the same power as a resistor at a temperature T_A, which is called the antenna temperature (Figure 3.2).

3.2.2.4 Gray Body Radiation

A black-body is an idealized body and it is a perfect absorber and emitter. These bodies absorb all the incident energy, and when the thermodynamic equilibrium is reached at a physical temperature T_{ph}, the energy is radiated back without any preferred direction. However, actual materials (usually called gray-bodies) emit less energy than a black-body, since they do not capable to absorb all the incident energy on them.

3.2.2.4.1 Brightness Temperature and Emissivity Concepts

Since the actual materials are usually gray-bodies two new concepts are introduced, the brightness temperature $T_B(\theta,\phi,f)$ and the emissivity $e(\theta,\phi,f)$. Eqn. (3.13) shows the relationship between these two concepts:

$$e(\theta,\phi,f) \triangleq \frac{B(\theta,\phi,f)}{B_{bb}} = \frac{T_B(\theta,\phi,f)}{T_{ph}}, \tag{3.13}$$

where B_{bb} is the brightness of the black-body at a temperature T_{ph}. The brightness temperature emitted by a black-body coincides with its physical temperature, hence its emissivity is 1 ($e(\theta,\phi,f)=1$). Consequently the brightness temperature emitted by real bodies is less than the physical temperature ($0 \le T_B(\theta,\phi,f) \le T_{ph}$), and then their range of emissivity values is between 0 and 1 ($0 \le e(\theta,\phi,f) \le 1$). In conclusion, the emissivity of a perfect reflecting material is equal to zero ($e(\theta,\phi,f)=0, T_B(\theta,\phi,f)=0$) and the emissivity of a perfect absorber is one ($e(\theta,\phi,f)=1, T_B(\theta,\phi,f)=T_{ph}$).

3.2.2.4.2 Apparent Temperature

In a real measuring environment, it is not possible to isolate the brightness temperature of the target from other sources that radiated energy. In this situation, it is convenient to define another term, the apparent brightness temperature $T_{AP}(\theta,\phi,f)$, which accounts for all sources of thermal noise, as seen from an antenna's point of view (Figure 3.3). In this case, the apparent temperature T_{AP} is the key parameter that depends on:

- the brightness temperature of the surface under observation (T_B),
- the atmospheric upward radiation (T_{UP}),
- the atmospheric downward radiation scattered reflected by the surface (T_{SC}), and
- the atmospheric attenuation (L_A),

and it can be written as:

$$T_{AP} = T_{UP} + \frac{1}{L_A}(T_{SC} + T_B). \tag{3.14}$$

Following Eqn. (3.14), when the atmospheric losses are high, the apparent temperature is almost equal to the atmospheric temperature. This happens at high frequencies or at the absorption windows of some gases. If the brightness temperature of the Earth's surface is being measured, it will be necessary to work at frequencies that exhibit low atmospheric attenuation. In the frequency range from 1 GHz to 10 GHz losses for a cloud-free atmosphere are very small and can be mostly neglected. Consequently the apparent brightness temperature (T_{AP}) can be approximated by the brightness temperature (T_B).

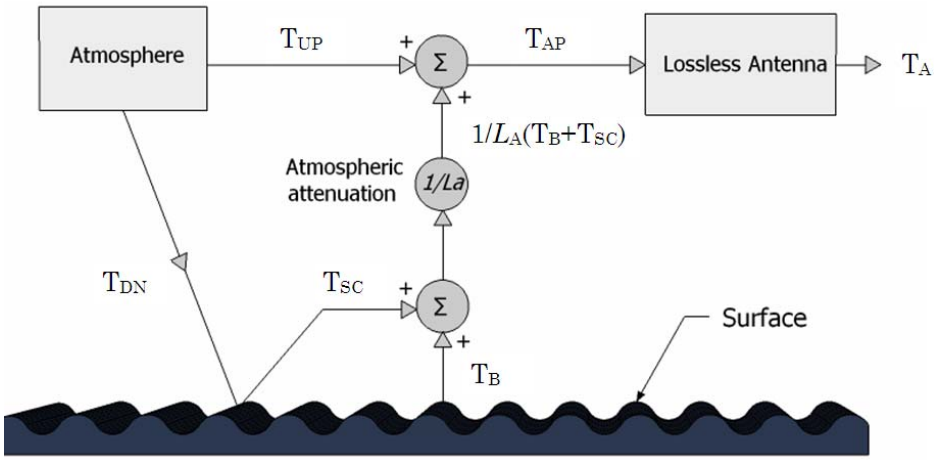

Figure 3.3 Relationship between the antenna temperature T_A, the apparent temperature and the brightness temperature T_B.

According to Figure 3.3 and taking into account the normalized antenna pattern ($|F_n(\theta,\phi)|^2$) and normalized by the antenna pattern solid angle Ω_p, the antenna temperature is given by:

$$T_A = \frac{1}{\Omega_p}\iint_{4\pi} T_{AP}(\theta,\phi)\,|F_n(\theta,\phi)|^2 d\Omega. \tag{3.15}$$

From a receiver point of view (assuming a lossless antenna), T_A can be considered as the physical temperature of a matched resistor at its input.

3.2.2.5 Polarized Emission: Stokes' Parameters

In the most general case, the electromagnetic emission from a body is partially polarized. This means that it cannot be expressed as a single vertical, horizontal, circular left-hand or right-hand polarized electromagnetic field. Instead, it must be decomposed as a pair of orthogonally polarized signals having, in principle, a non-zero cross-correlation. Since electromagnetic waves are transverse waves, the

polarization of the electric field can be represented in a coordinate system by means of two orthogonal unit vectors ($\hat{p}$ and $\hat{q}$) in a plane orthogonal to the propagation direction ([62]- [63]).

$$\vec{E}(t) = E^v(t)\hat{p} + E^h(t)\hat{q}. \tag{3.16}$$

A partially polarized thermal radiation is related to different parameters such as the incidence angle, the dielectric constant, the surface temperature, the surface roughness and many others. Furthermore, there are several other phenomena may be responsible for partial polarization of electromagnetic waves. For example, it is known that the radiation from the Sun can be observed at different wavelengths, in the visible and infrared spectrum (optics) and at radio wavelengths (HF, VHF and microwave). It is generally observed that the waves are depolarized or partially polarized (owing to the action of the solar magnetic field on charged particles). The same observations can be carried out on galactic or extra galactic radio sources. In order to study the properties of partially polarized waves, two analysis tools have been developed:

- the Coherence matrix (Eqn. (3.17)), and
- the Stokes parameters, in the microwave remote sensing frame, the polarimetric measurements are usually given as Stokes parameters.

The Coherence matrix is defined in equation Eqn. (3.17), where the electrical field has been expressed according Eqn. (3.16) and in vector format. Note that it is a hermitic matrix whose principal diagonal terms are the average power of the polarization components. The other diagonal terms represent the correlation coefficients between the components:

$$\bar{\bar{J}} = < \vec{E}\vec{E}^H > = < \begin{bmatrix} E^v \\ E^h \end{bmatrix} [E^{v*} E^{h*}] > = \begin{bmatrix} |E^v|^2 & < E^v E^{h*} > \\ < E^{v*} E^h > & |E^h|^2 \end{bmatrix}, \tag{3.17}$$

where

- ^{H} is the hermitian operator,
- <> is the expectation operator, and
- $(\,)^*$ is the conjugate operator.

On the other hand, a polarized emission can be completed described by four measurable quantities known as the Stokes' polarization parameters [64]. The first parameter expresses the total intensity of the field, while the remaining three parameters describe the polarization state. Furthermore, the four Stokes' parameters can be directly derived from Maxwell laws. The Stokes vector composed of four elements is defined as:

$$\bar{S} = \begin{bmatrix} S_0 \\ S_1 \\ S_2 \\ S_3 \end{bmatrix} = \begin{bmatrix} \mathrm{I} \\ \mathrm{Q} \\ \mathrm{U} \\ \mathrm{V} \end{bmatrix} = \begin{bmatrix} |E^v|^2 + |E^h|^2 \\ |E^v|^2 - |E^h|^2 \\ 2Re\langle E^v \cdot E^{h^*} \rangle \\ 2Im\langle E^v \cdot E^{h^*} \rangle \end{bmatrix}, \tag{3.18}$$

where S_0 is the total available power, and *Re* and *Im* are the real and imaginary parts respectively. I is the modulus of the mean Poynting vector per unit frequency of the emission, Q is the difference between the powers related to the vertical and horizontal polarizations; U and V measure the common part between the vertical and the horizontal-polarized signals, computed as the real and the imaginary part of the complex cross-correlation between the electrical fields, respectively. Moreover, as they are described in Eqn. (3.18), the Stokes' parameters are power flux spectral density, so their units are Watts per surface unit and per Hertz ($\left[\frac{W}{m^2 \cdot Hz}\right]$). However, in radiometric applications, the first and second Stokes parameters are sometimes expressed in a different, but equivalent, way:

$$\bar{S} = \begin{bmatrix} |E^h|^2 \\ |E^v|^2 \\ 2Re\langle E^v \cdot E^{h^*} \rangle \\ 2Im\langle E^v \cdot E^{h^*} \rangle \end{bmatrix}. \tag{3.19}$$

Since in radiometry it is more usual to use brightness temperatures than power fluxes, a thermal emission vector ($\overline{\mathrm{T}}_B$, with units of Kelvin) can be defined as a four element Stokes vector [65]. From now on, the Stokes vector defined in Eqn. (3.20) will be used.

$$\overline{\mathrm{T}}_B = \begin{bmatrix} \mathrm{T}_h \\ \mathrm{T}_v \\ \mathrm{T}_3 \\ \mathrm{T}_4 \end{bmatrix} = \mathrm{T}_{ph} \begin{bmatrix} e_h \\ e_v \\ e_U \\ e_V \end{bmatrix} = \frac{\lambda^2}{k \cdot \eta} \cdot \begin{bmatrix} |E^h|^2 \\ |E^v|^2 \\ 2Re\langle E^v \cdot E^{h^*} \rangle \\ 2Im\langle E^v \cdot E^{h^*} \rangle \end{bmatrix}, \tag{3.20}$$

where:

- T_h and T_v are the horizontal and vertical brightness temperatures, respectively,
- T_3 and T_4 are the third and fourth Stokes' parameters that account for the correlation between polarizations,
- T_{ph} is the temperature of the surface,
- $e_h, e_v, e_U,$ and e_V are the emissivities corresponding to the thermal emission vector, and

- η is the intrinsic impedance of the medium.

The measurements of the four elements of the Stokes vector are currently planned in several remote sensing applications. The brightness temperature of a surface has a polarized component if the target has a directional roughness or its inner scatterers are not randomly oriented. Several studies have been performed so as to model the behavior of T_3. For the sea surface roughed by the wind it is found as a sinusoidal variation of the form ([65]-[66]).

3.3 Types of Microwave Radiometers

As it has been seen, if an antenna is pointing to a body, the power that is collected at its output (expressed in term of antenna temperature T_A) is related to the brightness temperature T_B of this body. A microwave radiometer is an instrument that measures the antenna temperature (T_A) with highly resolution and accuracy. In fact, a microwave radiometer is a well calibrated and high sensitive microwave receiver. The performance of a radiometer is characterized by two main factors: resolution and accuracy [67]. The first one determines the smallest change in T_A that can be detected by the radiometer output. The second one indicates the correspondence of the measurement of the true value.

In order to illustrate these two aspects, the following example is analyzed; a radiometer is connected to an antenna which is exposed to a temperature T_A = 200 K, and the resolution requirement of the measure is of 1 K. The noise temperature introduced by the radiometer, like any receiver, has to be taken in account; a typical value will be T_{REC} = 500 K. Then the aim of the radiometer is to perform a measurement which matches with a variation of 1 K over 700 K (200 K + 500 K). In order to achieve this resolution, a radiometer uses an integration technique. Therefore, if the radiometer's gain G and the noise temperature T_{REC} are added in Eqn.(3.21), the resulting output power is:

$$P = kBG(T_A + T_{REC}). \tag{3.21}$$

As it is shown, the stability of the power measurement depends on the stability of the factors in Eqn.(3.21): B, G and $T_{REC.}$ As B is a parameter of the filter (passive device), it is assumed to be rather constant. Back to the previous example, if the required resolution is 1 K, it means that G and T_{REC} have to be stable in an interval of ≤0.5 %, which corresponds to about 0.004 dB. Therefore the following problem appears that it will be difficult to get these requirements from an amplifier. After having seen the two mains problems linked to the design of a radiometer, the main radiometer types and their behavior are presented in term of resolution and accuracy. A radiometer block diagram consists basically of an antenna, a super-

heterodyne receiver which translates the radio frequency signal to an intermediate frequency, a detector and a low-pass filter.

3.3.1 Total Power Radiometer

The TPR is the most common radiometer used. It is easy to understand and it can illustrate the most important notions of the performance of such instrument. Figure 3.4 is used to explain it with more details.

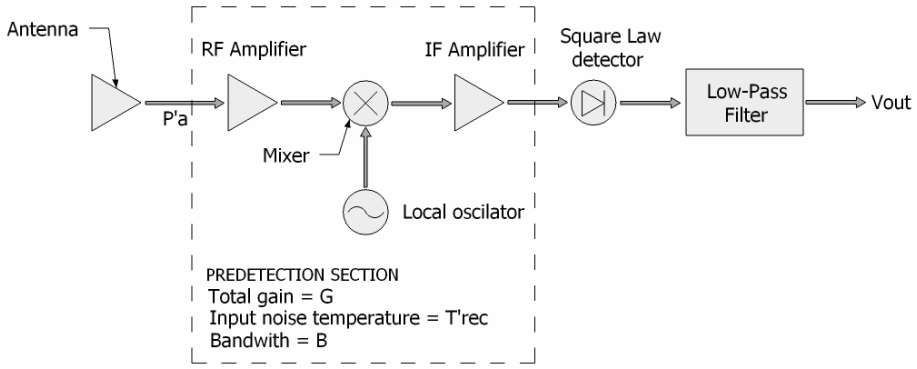

Figure 3.4 Total power radiometer block diagram.

In the radiometer of the Figure 3.4, the gain (G) is represented by an amplifier and B is the system noise equivalent bandwidth. To measure the noisy input signal, a square low detector is used. Its output is directly proportional related to the input signal and so to the temperature T_A. An integrator is used to reduce the fluctuations in the detected signal and therefore to increase the stability of the measurement. Taking into account that the input signal is thermal noise, the voltage output of the IF frequency is a random variable which follows a Gaussian pdf, having 0 mean and an standard deviation which follows a Rayleigh law (Eqn. (3.22)):

$$p(V_e) = \begin{cases} \frac{V_e}{\sigma^2} e^{-\frac{{V_e}^2}{2\sigma^2}}, & V_e \geq 0 \\ 0, & V_e < 0 \end{cases}. \tag{3.22}$$

So, the mean value of V_e is the available power at the output of the IF amplifies over a unitary resistor:

$$P_{FI} = \overline{{V_e}^2} = 2\sigma^2 \quad [W]. \tag{3.23}$$

Then, the relationship between the output and the input of the quadratic law diode can be described as:

$$V_d = C_d {V_e}^2 \quad [V], \tag{3.24}$$

where C_d stands for the power sensibility constant of the power detector, with the units volts over Watts ($[V/W]$). Thence, the mean value of V_d can be expressed as:

$$\bar{V}_d = C_d \bar{V}_e^{\,2} = 2C_d\sigma^2 = C_d \mathrm{P_{FI}} = C_d GkBT_{SYS} \quad [V]. \tag{3.25}$$

On the other hand, the low pass filter (LPF) output voltage ($\bar{V}_{out}$) depends on two factors, a constant value ($\bar{V}_d$) and a random component ($V_{ac}(t)$). The parameter $V_{ac}(t)$ accounts for the standard deviation of $\bar{V}_d$and is related with the uncertainly created by the intrinsic noise of the system ($\mathrm{P_{sys}}$). The constant value is related with the input power ($\mathrm{P_A}$), thus the radiometric temperature $\mathrm{T_A}$ using the following equation:

$$\bar{V}_{out} = G_{LPF}\bar{V}_d \quad [V], \tag{3.26}$$

where G_{LPF} is the gain of the LPF. So that, the output of a TPR is proportional to the radiometric temperature and its value is given by the following equation:

$$V_{out}(t) = \bar{V}_{out} + V_{ac}(t) = G_{LPF}C_d GkBT_{SYS} + V_{ac}(t) = G_s T_{SYS} + V_{ac}(t) \ [V]. \tag{3.27}$$

For a Rayleigh distribution, the squared mean value is equal to its variance, which means that the standard deviation and the mean value at the output of the quadratic law diode are the same:

$$\frac{\sigma_d}{\bar{V}_d} = 1 \rightarrow \sigma_d = \bar{V}_d \quad [V]. \tag{3.28}$$

Following Eqn. (3.28), it implies that the measurement uncertainly has the same value of its mean, which corrupts the measurements. The main function of the LPF is to avoid this effect, by integrating V_d V_d over a period of time τ (which, in fact is the time constant of the filter, $\tau = 1/\mathrm{B_{LPF}}$). In that way the variance of the measurement is reduced by a factor $N = B\tau$, where N is the number of independent samples used for the integration. Therefore, the relationship between the standard deviation and the mean value at the LPF filter is:

$$\frac{\sigma_{out}}{\bar{V}_{out}} = \frac{1}{\sqrt{B\tau}} \rightarrow \sigma_{out} = \frac{\bar{V}_{out}}{\sqrt{B\tau}}. \tag{3.29}$$

Hence, assuming that the parameters of Eqn. (3.29) remain constant, this relationship can be re-written as a function of the standard deviation associated to the mean value $\mathrm{T_{SYS}}$ ($\Delta\mathrm{T_{SYS}}$, where $\mathrm{T_{SYS}}=\mathrm{T_A}+\mathrm{T_{REC}}$):

$$\frac{\Delta \mathrm{T}_{SYS}}{\mathrm{T}_{SYS}} = \frac{1}{\sqrt{B\tau}}. \tag{3.30}$$

From Eqn. (3.30) it is possible to infer the radiometric resolution (ΔT), which is defined as the minimum input temperature which the radiometer is able to infer a change at its voltage output. The radiometric resolution of a TPR is described as [39]:

$$\Delta T_N \triangleq \Delta T_{SYS} = \frac{T_{SYS}}{\sqrt{B\tau}} = \frac{T_A + T_{REC}}{\sqrt{B\tau}} \quad [K]. \tag{3.31}$$

However, Eqn. (3.31) does not take into account the system gain fluctuations, so all the real fluctuations that occur in a receiver are missing from Eqn. (3.31). The gain uncertainly can be defined as:

$$\Delta T_G = T_{SYS}\left(\frac{\Delta G_S}{G_S}\right) \quad [K], \tag{3.32}$$

where G_S is the total receiver gain and ΔG_S is the root mean square (rms) variation of the detected power for a constant power input signal. Taking into account that the noise and the gain fluctuations are statistically independent, the final system resolution can be written as:

$$\Delta T = [(\Delta T_N)^2 + (\Delta T_G)^2]^{\frac{1}{2}} = T_{SYS}\left[\frac{1}{B\tau} + \left(\frac{\Delta G_S}{G_S}\right)^2\right]^{\frac{1}{2}} \quad [K]. \tag{3.33}$$

From Eqn. (3.33) it can be inferred that the radiometric sensibility of a TPR has a strong dependence on the gain fluctuations. It is important to notice that the best theoretical radiometric resolution can be achieved with an ideal TPR. However due to the gain fluctuations problems, a calibration process is required frequently.

3.3.2 Dicke Radiometer

With the aim to correct the stability problems associated to gain fluctuations existing in the TPR, Dicke published in 1946 a radiometer design which is named after him (Figure 3.5) [3]. The Dicke radiometer (DR), instead of measuring directly the antenna temperature, performs the measurement of the difference between T_A and a known reference temperature T_{REF}. With this method, the noise temperature instability T_R is filtered out and the impact of the gain is largely reduced.

As it is shown in Figure 3.5, a DR is a modified TPR with an input switch that changes of position at a given frequency (f_s) between the antenna and the reference temperature T_{REF} and a synchronous demodulator (±1 multiplier). Therefore, two different outputs in distinct time slots are obtained. The output depends on the half period of f_S, the detector output gives:

$$\bar{V}_{dANT} = C_d GkB(\mathrm{T}_A + \mathrm{T}_{REC}) \quad \text{for } 0 \le t \le \frac{\tau_s}{2}, \quad [V] \tag{3.34}$$

$$\bar{V}_{dREF} = C_d GkB(\mathrm{T}_{REF} + \mathrm{T}_{REC}) \quad \text{for } \frac{\tau_s}{2} \le t \le \tau_s, \quad [V] \tag{3.35}$$

where T_{REF} is the reference noise temperature, τ_s is the switching period, and T_{REC} is the receivers noise temperature, including the noise of the input switch. On the other hand, the synchronous demodulator has another synchronous switch. This switch, gives the input signal to two unitary gain amplifiers, which have opposed signs, one amplifier has the $\bar{V}_{dANT}$ and the other has $\bar{V}_{dREF}$.

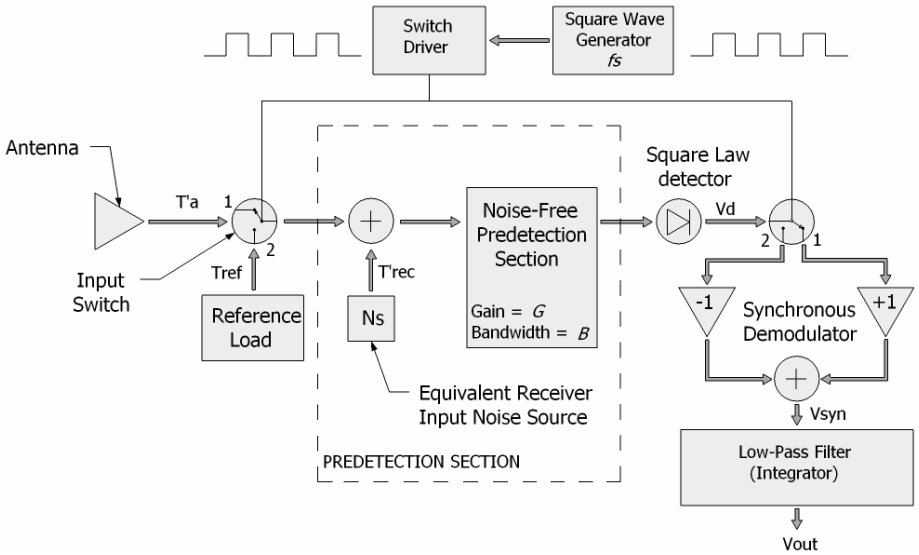

Figure 3.5 Dicke radiometer sketch.

The outputs of these amplifiers are added, and finally low-pass filtered. If the switching frequency f_s is sufficiently fast to consider the parameters T_A, T_{REF} and G constants during an entire period, and also that the period is smaller than the integration time ($f_s >> \tau^{-1}$), then the radiometer output can be expressed as:

$$V_{SYN} = \frac{1}{2}(\bar{V}_{dANT} - \bar{V}_{dREF}) = \frac{1}{2} C_d GkB(\mathrm{T}_A - \mathrm{T}_{REF}) \quad [V]. \tag{3.36}$$

As it can be observed in Eqn. (3.36), the output of the Dike radiometer is proportional to the $(\mathrm{T}_A - \mathrm{T}_{REF})$ term. So that, the uncertainly of this new term (T_{REF}) has to be taken into account in the radiometric resolution calculation. The resolution of a Dike radiometer can be expressed as it follows:

$$\Delta\mathrm{T} = \left[\frac{(\mathrm{T}_A + \mathrm{T}_{REC})^2}{\frac{B\tau}{2}} + \frac{(\mathrm{T}_{REF} + \mathrm{T}_{REC})^2}{\frac{B\tau}{2}} + \left(\frac{\Delta G_S}{G_S}\right)(\mathrm{T}_A - \mathrm{T}_{REF})^2 \right]^{\frac{1}{2}} [K]. \tag{3.37}$$

It is said that a Dicke radiometer is balanced in the ideal case in which the antenna the reference temperatures are identical ($T_A = T_{REF}$), and then the resolution reduces to:

$$\Delta T = \frac{2(T_A + T_{REC})}{\sqrt{B\tau}} = 2\Delta T_{TPR}, \quad [K] \tag{3.38}$$

where ΔT_{TPR} is the radiometric resolution of a TPR in the total absence of fluctuations. As it can be observed, in this ideal case Eqn. (3.38), there are not gain fluctuations on the radiometric resolution, but the resolution is twice worse than in a TPR, due to the integration time has been split by 2, half the period it is looking to the antenna and the other half the period it is looking to a reference load.

In a real case, when the temperature T_{REF} is chosen close to the antenna temperature T_A, the impact of G fluctuations is small. Then if (T_A - T_{REF}) << (T_A + T_R) is fulfilled, the DR decreases the resolution respect to the TPR. Although the stability of the system is improved, by measuring the antenna temperature just half of the time, there is a loss of resolution as compared to a TPR. Indeed, on each half period, the radiometer can be assimilated to a TPR pointing to the antenna or to the reference load, using an integration time of $\tau/2$.

3.3.3 Noise Injection Radiometer (NIR)

The noise injection radiometer is a particular case of a Dicke radiometer. It has been optimized to ensure that its output is always independent on the gain fluctuations and on the receiver noise. To achieve that purpose a NIR has a feedback loop which is shown in Figure 3.6.

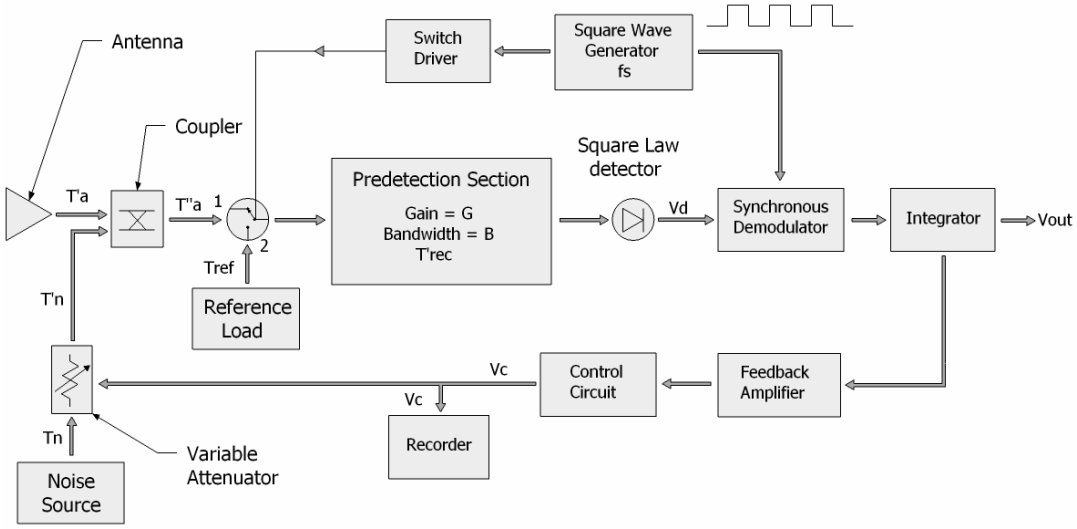

Figure 3.6 Block diagram of a noise injection radiometer.

The aim of the feedback loop is to balance the radiometer (obtaining the same result as in the ideal case of a balanced Dicke radiometer) by injecting noise in the system input through a directional coupler ensuring that always is fulfilling:

$$T_a'' = T_{REF} = 0 \quad [K]. \tag{3.39}$$

The amount of injected power is controlled by a variable attenuator, which is controlled by the feedback loop. Thence, the amount of power entering to the system can be calculated as:

$$T_a'' = \left(1 - \frac{1}{F_c}\right) T'_a + \frac{T'_N}{F_c} \quad [K], \tag{3.40}$$

where F_c is the coupling factor of the directional coupler, and T_N' is the amount of injected noise, attenuated by the variable attenuator. The voltage V_c, which controls the attenuation is proportional to the antenna and the system physical (T_{ph}~290 K) temperature difference, and is given in the following expression:

$$V_C = \frac{F_C - 1}{T_N - T_{ph}} \left(T_{ph} - T'_a\right) \quad [V]. \tag{3.41}$$

Using this technology, the output of the NIR is independent on the gain fluctuations and on the receiver's noise. The radiometric resolution of a NIR in the case of $T_{ph} = T_A'$ can be described as it follows:

$$\Delta T = \frac{2(T_{ph} + T'_{REF})}{\sqrt{B\tau}} = 2\Delta T_{TPR} \ [K]. \tag{3.42}$$

As it can be seen in Eqn. (3.42), the NIR radiometric resolution is the same as that of balanced Dicke, but with the advantage that this does not depend on receiver's noise.

3.3.4 Polarimetric Radiometers

A Polarimetric Radiometer (PR) is an instrument devoted to the measurement of the four Stokes parameters. A block diagram of a sample PR is shown in Figure 3.7. The radiometer is a Dicke type, super-heterodyne receiver and the antenna has separate outputs for vertical and horizontal polarizations. The third and fourth Stokes parameters can be obtained in several ways such as with a linear combination of the collected powers at ±45º polarizations or using a complex correlator between the *h* and the *v*-pol. signals. In the example shown in Figure 3.7, a complex correlator provides the third (obtained by in-phase correlation) and the fourth (obtained after a 90º phase shift) Stokes parameters. The error caused

by differences in signal propagation times is minimized using a delay line in one of the correlator channels. The phase differences in different channels are equalized using a phase shifter in the RF-block or some other advanced techniques. The correlator block that multiplies the vertical and horizontal signals is the heart of the PR. The obtained DC-component at the correlator output is proportional to the phase difference between the signals.

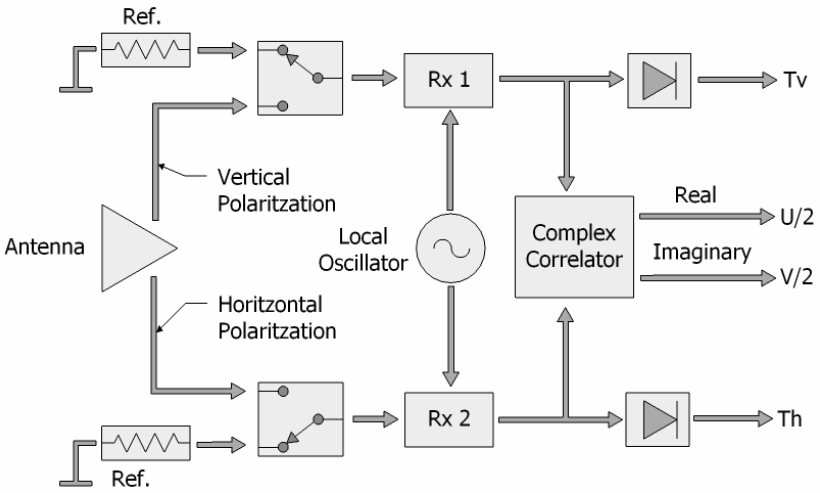

Figure 3.7. Block diagram of a sample polarimetric radiometer.

In this case, the radiometric resolution of a PR is the same than the DR.

3.4 Microwave Radiometry Applications

There are many microwave radiometry applications. Mainly, they can be included in two groups: atmospheric applications and Earth's surface applications. The main applications and their suitable frequencies are listed below (Table 3.1).

Table 3.1 Relationship between the radiometry application and its suitable frequency [28].

Application	Frequency (GHz)
Clouds water content	21, 37, 90
Ice Classification	10, 18, 37
Sea Oil spills tracking	6.6, 37
Rain over soil	18, 37, 55, 90, 180
Rain over the ocean	10, 18, 21, 37
Sea Ice concentration	18, 37, 90
Sea Surface Salinity	**1.4**, 6.6
Sea Surface Temperature	6.6, 10, 18, 21, 37
Sea Surface Wind Speed	10, 18
Snow Coating	6.6, 10, 18, 37, 90
Soil Moisture	**1.4**, 6.6
Atmospheric Temperature Profiles	21, 37, 55, 90, 180
Atmospheric Water Vapor	21, 37, 90, 180

As shown, the frequency at L band (1.4 GHz) is the most suitable for applications related with the sea surface salinity or the soil moisture.

3.5 Conclusions

This chapter has provided a brief introduction to microwave radiometry. Radiometry is the field of science devoted to the measurement of the thermal electromagnetic energy spontaneously emitted by all bodies at a physical temperature different from 0 K. Furthermore, the fundamentals of radiometry theory have been presented such as the brightness temperature and the apparent temperature concepts, as well as the black and gray body relationships through the emissivity.

The main types of radiometers have been presented and their radiometric resolution computed included their dependence on the gain fluctuations. It has been shown that the one that presents the best radiometric resolution performance (TPR) is the most prone to gain fluctuations, and on the other side, the most robust versus the gain fluctuations (NIR) has the worst performance in terms of radiometric resolution.

Finally, the main applications of microwave radiometry have been provided with their suitable frequency bands.

Chapter 4

4 RELATIONSHIP BETWEEN SYNTHETIC AND REAL APERTURE RADIOMETERS

This chapter focuses on the relationship between real and synthetic aperture radiometers giving a general and common mathematical framework to both of them. It will be demonstrated that a real aperture radiometer array can be understood as a synthetic aperture one, with a high level of redundancy. Therefore, all the recent results from synthetic aperture radiometry can be translated to real aperture radiometers. This fact can be used to create beamforming arrays in a new way. To do this, the beamforming array equation will be expressed in terms of cross-correlations between all pairs of antenna signals (visibility samples). By properly combining the visibility samples, a new type of digital beamforming radiometer can be implemented, which will benefit from the high calibration accuracy achieved in synthetic aperture radiometers, and the flexibility to electronically steer the beam.

4.1 Radiometric Techniques Overview

The electric field arriving at an antenna element m at time t is usually polarized and it can be expressed as $\vec{E}_m(t) = E_m^v(t)\hat{v} + E_m^h(t)\hat{h}$, where $\hat{v}$ and $\hat{h}$ are two orthonormal vectors parallel and perpendicular to the incidence plane, respectively, and both perpendicular to the direction of propagation. A partially polarized thermal radiation is related to different parameters such as the incidence angle, the dielectric constant, the surface temperature, the surface roughness and many others. The polarization state can be fully characterized by the full Stokes vector [67[69]. In a general case, the voltage signals ($S_m^{p,q}(t)$) collected by antenna m in two orthogonal polarizations $\hat{p}_m$ and $\hat{q}_m$, can be described as:

$$S_m^p(t) = \vec{E}_m(t)\vec{l}_{eff_m}^p = \left(E_m^v(t)a_m^p + E_m^h(t)b_m^p\right)\left|l_{eff_m}^p\right|, \text{ and} \tag{4.1}$$

$$S_m^p(t) = \vec{E}_m(t)\vec{l}_{eff_m}^q = \left(E_m^v(t)a_m^q + E_m^h(t)b_m^q\right)\left|l_{eff_m}^q\right|, \tag{4.2}$$

where:

- $\hat{p}_m = a_m^p\hat{v} + b_m^p\hat{h}$, $\hat{q}_m = a_m^q\hat{v} + b_m^q\hat{h}$, with $\left|a_m^{p,q}\right|^2 + \left|b_m^{p,q}\right|^2 = 1$, and $a_m^p a_m^{q*} + b_m^p b_m^{q*} = 0$,
- $\vec{l}_{eff_m}^p = \left|l_{eff_m}^p\right|\hat{p}_m$ and $\vec{l}_{eff_m}^q = \left|l_{eff_m}^q\right|\hat{q}_m$ are the effective length vectors [70] of antenna m at $\hat{p}_m$ and $\hat{q}_m$ polarizations, and
- $\vec{E}_m(t)$ is the electric field received by the antenna m.

Then, the cross-correlation of the signals collected by two antennas m and n at time t can be computed as [44]:

$$\begin{aligned}\langle S_m^p(t)S_n^{q*}(t)\rangle = \left|l_{eff_m}^p\right|\left|l_{eff_n}^q\right|\{&a_m^p a_n^{q*}\langle E_m^v(t)E_n^{v*}(t)\rangle + a_m^p b_n^{q*}\langle E_m^v(t)E_n^{h*}(t)\rangle \\ &+ b_m^p a_n^{q*}\langle E_m^h(t)E_n^{v*}(t)\rangle + b_m^p b_n^{q*}\langle E_m^h(t)E_n^{h*}(t)\rangle\}\end{aligned} \tag{4.3}$$

From Eqn. (4.3), the modified Stokes vector can be readily obtained if the two antennas, m and n, are the same (m=n):

$$\frac{1}{2}\langle S_m^p(t)S_n^{q*}(t)\rangle \propto \mathrm{T}_v\left(a_m^p a_m^{q*}\right) + \mathrm{T}_h\left(b_m^p b_m^{q*}\right) + \frac{\mathrm{T}_3+\mathrm{jT}_4}{2}(a_m^p b_m^{q*}) + \frac{\mathrm{T}_3-\mathrm{jT}_4}{2}(b_m^p a_m^{q*}), \tag{4.4}$$

where j is the imaginary constant ($j = \sqrt{-1}$).

From Eqn. (4.4):

- the signals' correlation is proportional to the modified first Stokes parameter in brightness temperature [67] (T_v) when $a_m^p = a_m^q = 1$ and $b_m^p = b_m^q = 0$,
- the second modified Stokes parameter (T_h) is obtained when $a_m^p = a_m^q = 0$ and $b_m^p = b_m^q = 1$,
- the third modified Stokes parameter (T_3) is obtained as twice the real part when $a_m^p b_m^{q*} = 1$, $b_m^p a_m^{q*} = 0$ and $a_m^p a_m^{q*} = 0$, $b_m^p b_m^{q*} = 0$, and finally
- the fourth modified Stokes parameter (T_4) is obtained as twice the imaginary part when $a_m^p b_m^{q*} = 0$, $b_m^p a_m^{q*} = 1$ and $a_m^p a_m^{q*} = 0$, $b_m^p b_m^{q*} = 0$.

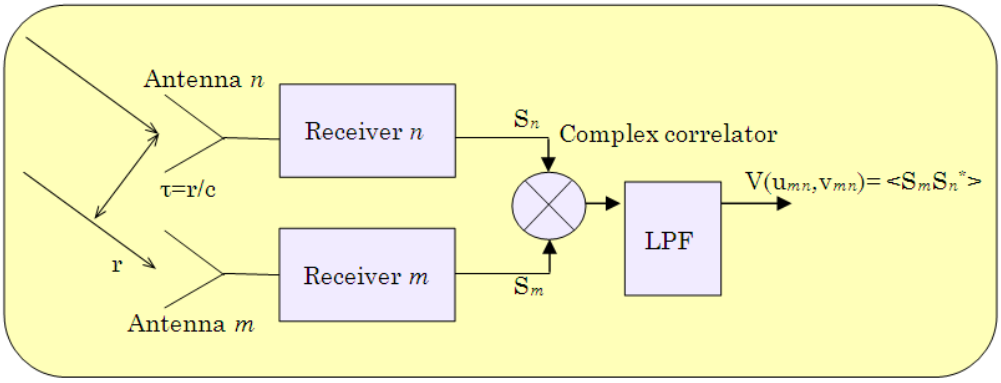

Figure 4.1 Sketch of a baseline in an interferometer: Signals are collected by antennas m and n and the complex cross-correlation is computed. Note that, after the complex multiplier, the low pass filter (LPF) output is the estimation of the visibility sample.

If the two antennas are physically spaced, the complex cross-correlation is a sample of the polarimetric visibility function (Eqn.(4.5)) [71] with units of Kelvin (Figure 4.1).

$$V^{pq}(u_{mn}, v_{mn}) = \frac{1}{k_B\sqrt{B_m B_n}\sqrt{G_m G_n}} \frac{1}{2} \langle S_m^p(t) S_n^{q*}(t) \rangle, \tag{4.5}$$

where:

- $(u_{mn}, v_{mn}) \equiv (x_n - x_m, y_n - y_m)/\lambda_0$ is the spatial frequency (baseline),
- $x_{m,n}$ and $y_{m,n}$ are the coordinates of the m and n antennas on the plane xy, and
- $G_{m,n}$ is the gain for the m and n receiver channels.

Assuming that the signals' statistics are wide sense stationary random processes (thermal noise radiation) that fulfill the ergodicity property, then Eqn. (1), can be computed in practice using the cross-correlation (time average) of the in-phase and quadrature components ($S_m^p(t) = I_m^p(t) + jQ_m^p(t)$ and $S_m^q(t) = I_m^q(t) + jQ_m^q(t)$). From

the Van–Cittert Zernicke theorem, the visibility function can be related to the brightness temperature distribution [72]:

$$\begin{aligned} V^{pq}(u_{mn}, v_{mn}) &= R_{I_m^p I_n^q}(0) + jR_{Q_m^p I_n^q}(0) \\ &= \frac{1}{\sqrt{\Omega_m^p \Omega_n^q}} \iint_{\xi^2+\eta^2 \le 1} \frac{T_B^{pq}(\xi,\eta) - T_r \delta_{pq}}{\sqrt{1-\xi^2-\eta^2}} F_m^p(\xi,\eta) F_n^{q*}(\xi,\eta) \tilde{r}_{mn}\left(-\frac{u_{mn}\xi + v_{mn}\eta}{f_0}\right) e^{-j2\pi(u_{mn}\xi + v_{mn}\eta)} d\xi d\eta \end{aligned} \tag{4.6}$$

where:

- $(\xi, \eta) = (\sin\theta\cos\varphi, \sin\theta\sin\varphi)$ are the director cosines with respect the x and y axes,
- $T_B^{pq}(\xi, \eta)$ is the brightness temperature distribution at pq polarization coming from the (ξ, η) direction [71],
- T_r is the receiver's physical temperature,
- δ_{pq} is the Kronecker's delta: $\delta_{pq} = 1$ if $p = q$ and $\delta_{pq} = 0$ if $p \neq q$,
- f_0 is the central working frequency,
- Ω_m^p, Ω_n^q and $F_m^p(\xi, \eta)$, $F_n^q(\xi, \eta)$ are the equivalent solid angles and the normalized radiation voltage patterns of the antennas, and
- $\tilde{r}_{mn}(t) \triangleq \frac{e^{-j2\pi f_0 t}}{\sqrt{B_m B_n}} \int_0^\infty H_m(f)\, H_n^*(f) e^{j2\pi f t} df$ is the so-called fringe-washing function (FWF) [73,[74], where $H_{m,n}(f)$ is the normalized frequency response for each channel.

In addition, Eqn. (4.6) is normalized by the terms k_B, $\sqrt{B_m B_n}$, $\sqrt{G_m G_n}$, and $\sqrt{\Omega_m^p \Omega_n^q}$ to ensure that the visibility function has units of Kelvin.

Actually, all different types of radiometers can be derived from the general version stated in Eqn. (4.6) using the proper considerations and particularizations [75]. The simplest one is the total-power radiometer (described in detail on Chapter 3), that is inferred from Eqn. (4.6) in the particular case of having only one visibility sample from one antenna $m=n$, (u, v) = (0, 0) with the same linear polarization ($\hat{p} = \hat{q}$), as discussed above.

$$V^{pq}(0,0) = T_A^p = \frac{1}{\Omega_m^p} \iint_{\xi^2+\eta^2 \le 1} \frac{T_B^{pp}(\xi,\eta) - T_r}{\sqrt{1-\xi^2-\eta^2}} \left|F_m^p(\xi,\eta)\right|^2 d\xi d\eta. \tag{4.7}$$

The polarimetric radiometer is similar to the previous equation, but using a single antenna m=n, (u, v) = (0, 0) with two linear orthogonal polarizations ($\hat{p}\hat{q}$=0) (Eqn. (4.8)). Then, the visibility function is:

$$\mathrm{V}^{pq}(0,0) = \frac{1}{2}(\mathrm{T}_3 + \mathrm{jT}_4) = \frac{1}{\sqrt{\Omega_m^p \Omega_n^q}} \iint_{\xi^2+\eta^2\leq 1} \frac{\mathrm{T}_\mathrm{B}^{pq}(\xi,\eta)}{\sqrt{1-\xi^2-\eta^2}} \mathrm{F}_m^p(\xi,\eta)\mathrm{F}_n^{q*}(\xi,\eta) d\xi d\eta, \tag{4.8}$$

where T_3 and T_4 are the third and fourth Stokes parameters. A particular type of correlation radiometer [76] can be inferred from two antennas, m and n, located at different physical positions (u, v) = (u_{mn}, v_{mn}) (Eqn.(4.6) repeated here for convenience):

$$\begin{aligned} &\mathrm{V}^{pq}(\mathrm{u}_{mn},\mathrm{v}_{mn}) = \mathrm{R}_{\mathrm{I}_m^p \mathrm{I}_n^q}(0) + \mathrm{jR}_{\mathrm{Q}_m^p \mathrm{P}_n^q}(0) \\ &= \frac{1}{\sqrt{\Omega_m^p \Omega_n^q}} \iint_{\xi^2+\eta^2\leq 1} \frac{\mathrm{T}_\mathrm{B}^{pq}(\xi,\eta) - \mathrm{T}_\mathrm{r}\delta_{pq}}{\sqrt{1-\xi^2-\eta^2}} \mathrm{F}_m^p(\xi,\eta)\mathrm{F}_n^{q*}(\xi,\eta)\tilde{\mathrm{r}}_{mn}\left(-\frac{\mathrm{u}_{mn}\xi + \mathrm{v}_{mn}\eta}{f_0}\right) \mathrm{e}^{-\mathrm{j}2\pi(\mathrm{u}_{mn}\xi+\mathrm{v}_{mn}\eta)} d\xi d\eta. \end{aligned} \tag{4.9}$$

Finally, a polarimetric aperture synthesis radiometer ([1], [9], [10], and [43]) generates a brightness temperature map from a set of visibility samples ($\overline{\mathrm{V}}^{pq}$) (Eqn.(4.4)) [17, [77]:

$$\overline{\mathrm{T}}_\mathrm{A}^{pq} = \overline{\overline{\mathrm{G}}}\overline{\mathrm{V}}^{pq}, \tag{4.10}$$

where $\overline{\overline{\mathrm{G}}}$ is a linear operator matrix that accounts for instrument non-idealities [17]. In an ideal system ($\tilde{\mathrm{r}}_{mn}(\mathrm{t}) = 1$ and $\mathrm{F}_m^p(\xi,\eta) = \mathrm{F}_n^q(\xi,\eta)$), the modified brightness temperature can be defined as in Eqn. (4.11) [78]:

$$\tilde{\mathrm{T}}_\mathrm{A}^{pq}(\xi,\eta) = \mathrm{T}_\mathrm{A}^{pq}(\xi,\eta) \frac{\left|\mathrm{F}_m^{pq}(\xi,\eta)\right|^2}{\Omega_m^p \sqrt{1-\xi^2-\eta^2}}, \tag{4.11}$$

and the imaging process reduces to an inverse discrete Fourier transform (IDFT) [78].

$$\tilde{\mathrm{T}}_\mathrm{A}^{pq}(\xi,\eta) = \mathrm{IDFT}\{\overline{\mathrm{V}}^{pq}(\mathrm{u},\mathrm{v})\}. \tag{4.12}$$

4.2 Radiometers with Beamforming

A beamformer can be understood as a spatial filter that properly weights and adds together the signals ($S_m^p(t)$) collected by a set of M antennas to get the system's

output. The complex weight $w_m(\xi_0, \eta_0)$ applied to each signal attenuates some directions and reinforces others, creating an interference pattern of the impinging wavefront that steers the beam in a particular direction (ξ_0, η_0). The beamformer implementation (Eqn. (4.13)) is straightforward:

$$S^p_{\mathrm{DBF}}(t, \xi_0, \eta_0) = \sum_{\mathrm{m}=1}^{M} w_m(\xi_0, \eta_0)\, S^p_m(t), \tag{4.13}$$

where:

- $S^p_{\mathrm{DBF}}(t, \xi_0, \eta_0)$ is the resulting signal at the beamformer's output at time t, polarization p, and steered in the (ξ_0, η_0) direction, and
- $S^p_m(t)$ is the signal collected by the m^{th} antenna at time t and p polarization (Eqn.(4.2)).

From Eqn. (4.13), it is possible to obtain signals from different directions by applying different w_m coefficients (beam steering). Moreover, this procedure can be applied simultaneously to different beams, obtaining the modified antenna temperatures (Eqn. (4.11)) from several directions ([42], [79], and [80]). Using array notation from Eqn. (4.13) it is possible to express the antenna temperature as a function of the visibility samples (Eqn. (4.14)) except for the normalization constants used in Eqn. (4.5), which have been omitted for the sake of simplicity

$$\begin{aligned} \widetilde{\mathrm{T}}^{pq}_{\mathrm{a}}(\xi_0, \eta_0) &= \frac{1}{2}\langle S^p_{\mathrm{DBF}} S^{q*}_{\mathrm{DBF}}\rangle = \frac{1}{2}\overline{w}^T(\xi_0, \eta_0)\langle \bar{\mathrm{S}}^p \bar{\mathrm{S}}^{q\mathrm{H}}\rangle \overline{w}^*(\xi_0, \eta_0) \\ &= \overline{w}^T(\xi_0, \eta_0)\overline{\overline{\mathrm{V}}}^{pq}\overline{w}^*(\xi_0, \eta_0), \end{aligned} \tag{4.14}$$

where $\overline{\overline{\mathrm{V}}}^{pq}$ is a matrix that contains all the visibility samples that can be measured by all antenna pairs (m and n) in the array (Eqn. (4.15)) and $\mathrm{V}^{pq}(\mathrm{u}_{mn}, \mathrm{v}_{mn}) = \mathrm{V}^{pq*}(\mathrm{u}_{nm}, \mathrm{v}_{nm})$.

$$\overline{\overline{\mathrm{V}}}^{pq} \triangleq \frac{1}{2}\begin{bmatrix} \langle S^p_1(t) S^{q*}_1(t)\rangle & \cdots & \langle S^p_M(t) S^{q*}_1(t)\rangle \\ \vdots & \ddots & \vdots \\ \langle S^p_1(t) S^{q*}_M(t)\rangle & \cdots & \langle S^p_M(t) S^{q*}_M(t)\rangle \end{bmatrix} = \begin{bmatrix} \mathrm{V}^{pq}(\mathrm{u}_{11}, \mathrm{v}_{11}) & \cdots & \mathrm{V}^{pq}(\mathrm{u}_{1M}, \mathrm{v}_{1M}) \\ \vdots & \ddots & \vdots \\ \mathrm{V}^{pq}(\mathrm{u}_{M1}, \mathrm{v}_{M1}) & \cdots & \mathrm{V}^{pq}(\mathrm{u}_{MM}, \mathrm{v}_{MM}) \end{bmatrix} \tag{4.15}$$

and $\overline{w}(\xi_0, \eta_0)$ is the normalized vector of complex weights (Eqn. (4.16)):

$$\begin{aligned} \overline{w}(\xi_0, \eta_0) &= (w_1, w_2, \ldots, w_M)^T = \\ &= \left(A_1 e^{j2\pi(\mathrm{u}_{11}\xi_0 + \mathrm{v}_{11}\eta_0)}, A_1 e^{j2\pi(\mathrm{u}_{12}\xi_0 + \mathrm{v}_{12}\eta_0)}, \ldots, A_1 e^{j2\pi(\mathrm{u}_{1M}\xi_0 + \mathrm{v}_{1M}\eta_0)}\right)^T. \end{aligned} \tag{4.16}$$

After some straightforward algebraic manipulations, it is possible to re-write Eqn. (4.14) in a more convenient form for subsequent analyses:

$$\widetilde{\mathrm{T}}_{\mathrm{A}}^{pq}(\xi_0,\eta_0) = \overline{\mathrm{W}}^{\mathrm{T}}(\xi_0,\eta_0)\overline{\mathrm{V}}^{pq}, \tag{4.17}$$

where:

- $\overline{\mathrm{V}}^{pq} \triangleq \left(\bar{\mathrm{n}}_1\,\overline{\overline{\mathrm{V}}}^{pq}, \bar{\mathrm{n}}_2\,\overline{\overline{\mathrm{V}}}^{pq}, \ldots, \bar{\mathrm{n}}_M\,\overline{\overline{\mathrm{V}}}^{pq}\right)^T$ and $\bar{\mathrm{n}}_m \triangleq (0,\ldots,1,\ldots 0)^T$ is a zero vector except for the m^{th} position that is equal to 1,

- $\overline{\mathrm{W}}^{\mathrm{T}}(\xi_0,\eta_0) \triangleq \left(\bar{\mathrm{n}}_1\overline{\overline{\mathrm{W}}},\ \bar{\mathrm{n}}_2\overline{\overline{\mathrm{W}}}, \ldots, \bar{\mathrm{n}}_M\overline{\overline{\mathrm{W}}}\right)^T$ and $\overline{\overline{\mathrm{W}}} \triangleq \overline{w}^*(\xi_0,\eta_0)\overline{w}^T(\xi_0,\eta_0)$, where $\overline{w}$ is given in Eqn. (4.16) and all the terms depend on the beam steering direction (ξ_0,η_0).

Equation (4.17) expresses the beamformer equation in terms of the visibility samples. Therefore, all the experience of synthetic aperture radiometers (for example: antenna effects, calibration, *etc.* [81] and [82]) can be used to study the parameters that can degrade the beamformer performance. These parameters are the differences in the phase and amplitude errors (value of $\tilde{\mathrm{r}}_{mn}(0)$ at the origin), the elementary complex antenna voltage patterns, the fringe-washing function (Eqn. (4.6)) that accounts for the spatial decorrelation effects when the array size (L) is large as compared to the correlation length $L > c/\mathrm{B}$, where c is the speed of the light. If spatial decorrelation effects are not negligible, the angular resolution degrades out-of-boresight. These effects can only be mitigated using true time delays as in [83] or by sub-banding [71].

From Eqns. (4.15) and (4.17), it is shown that $\overline{\mathrm{V}}^{pq}$ depends on the antenna array distribution and contains a high level of redundancy, for example, there are M zero baselines. Since the spatial cross-correlation is only a function of the antenna separation, all the antennas spaced the same distance in the same direction measure the same baseline. After instrument equalization (correction of relative phase and amplitude errors between receivers) all the baselines with the same distance can be properly averaged [71], and the result is only one visibility per baseline weighted by the number of times that particular baseline is repeated:

$$\widetilde{\mathrm{T}}_{\mathrm{A}}^{pq}(\xi_0,\eta_0) = \overline{\mathrm{W}}_2^T(\xi_0,\eta_0)\overline{\overline{\mathrm{U}}}\overline{\mathrm{V}}_2^{pq}, \tag{4.18}$$

where:

- $\overline{\mathrm{V}}_2^{pq}$ is the visibility vector without redundancy, *i.e.* redundant baselines have been properly averaged to reduce noise,

- $\overline{\overline{\mathrm{U}}}$ is a diagonal matrix whose diagonal is a windowing vector that takes into account the number of times each baseline is repeated. For example, if all visibility samples have the same noise level, for a linear and equally-spaced array: $\mathrm{diag}\left(\overline{\overline{\mathrm{U}}}(n)\right) = (M+1-|n|)$ which corresponds to a triangular

illumination. On the other hand, when the array is randomly spaced and there is no redundancy: $\mathrm{diag}(\overline{\overline{\mathrm{U}}}(n)) = 1$, except for the zero baseline that is weighted by M, and

- $\overline{\mathrm{W}}_2^T(\xi_0, \eta_0)$ is a non-repeated baselines complex weight vector (one for each different) to steer the beam in the (ξ_0, η_0) direction.

Antenna temperatures from several directions can be obtained simultaneously by replacing the vector $\overline{\mathrm{W}}_2^T(\xi_0, \eta_0)$ in Eqn. (4.18) by a matrix $\overline{\overline{\mathrm{W}}}_2$ where each column focuses a beam in a given direction (Eqn. (4.19)). From the columns point of view the matrix consists of normalized vectors, but without the requirement to be orthogonal. Theoretically, it is possible to obtain a continuous scan over the (ξ, η) space, although the number of antennas limits the number of independent beams:

$$\overline{\overline{\mathrm{W}}}_2 = \left(\overline{\mathrm{W}}_2(\xi_0, \eta_0), \overline{\mathrm{W}}_2(\xi_1, \eta_1), \ldots, \overline{\mathrm{W}}_2(\xi_{M-1}, \eta_{M-1})\right)^T. \tag{4.19}$$

Finally, the modified brightness temperature vector (or image) can be obtained by replacing the vector $\overline{\mathrm{W}}_2$ (Eqn. (4.18)) by the matrix $\overline{\overline{\mathrm{W}}}_2$ (Eqn. (4.19)):

$$\overline{\widetilde{\mathrm{T}}_{\mathrm{A}}^{pq}} = \overline{\overline{\mathrm{W}}}_2^T(\xi_0, \eta_0)\overline{\overline{\mathrm{U}}}\overline{\mathrm{V}}_2^{pq}, \tag{4.20}$$

where:

- $\overline{\widetilde{\mathrm{T}}_{\mathrm{A}}^{pq}} = \left(\widetilde{\mathrm{T}}_{\mathrm{A}}^{pq}(\xi_0, \eta_0), \widetilde{\mathrm{T}}_{\mathrm{A}}^{pq}(\xi_1, \eta_1), \ldots, \widetilde{\mathrm{T}}_{\mathrm{A}}^{pq}(\xi_{M-1}, \eta_{M-1})\right)^T$, is the modified brightness temperature vector in directions $(\xi_{\mathrm{m}}, \eta_{\mathrm{m}})$.

Equation (4.20) can be easily identified as a version of Eqn. (4.10), so a real aperture radiometer with a beamformer can be understood in the frame of synthetic aperture radiometers. To synthesize all the non-overlapped beams a C^M basis (a complex basis of M elements) can be used: a set of M normalized and orthogonal (orthonormal) complex vectors. For example, the inverse discrete Fourier transform fulfills this requirement and can be applied to the visibility samples to get all the uncorrelated antenna temperature measurements from a scene:

$$\widetilde{\mathrm{T}}_{\mathrm{A}}^{pq}(\xi, \eta) = \mathrm{IDFT}\left\{\overline{\overline{\mathrm{U}}}\overline{\mathrm{V}}_2^{pq}(\mathrm{u}, \mathrm{v})\right\}. \tag{4.21}$$

A subtle, but important difference between Eqns. (4.10), (4.12) and (4.21) lies in the $\overline{\overline{\mathrm{U}}}$ matrix that is actually a window function that weights the visibility samples due to the array baselines redundancy. In the case of equally-spaced linear array, this function is a triangular window that corresponds to the well known fact that the angular resolution of a uniform illumination real aperture array is half that of the synthetic aperture array. Moreover, other windows can be applied to reduce even

further the amplitude of the side lobes, and improve the image quality at the expense of poorer angular resolution [77].

4.3 Beamformer Analysis From a Synthetic Aperture Point of View

Once the relationship between a synthetic aperture radiometer and the real aperture radiometer with beamforming has been shown, its performance can be analyzed from the synthetic aperture radiometer point of view. Some basic and well-known concepts from general array antenna theory can be directly applied to radiometers with beamforming:

- the dependence of the field of view on the antenna spacing, and the appearance of diffraction lobes (aliasing) when the Nyquist criterion is not fulfilled, and

- the angular resolution of a synthetic aperture radiometer dependence on the number of elementary antennas and their spacing. For a Y-array as MIRAS in SMOS [1], when no windowing is applied, the spatial resolution is approximately given by $\Delta\xi_{-3\text{dB Synthetic}} \sim \pi/(2\Delta u_{\max})$ [28]. As shown in Section 4.2, that beamwidth of a uniformly illuminated *M*-elements array as a synthetic aperture radiometer is half of the beamwidth of the same array when as a real aperture radiometer with beamforming ($\Delta\xi_{-3\text{dB Real}} \sim \pi/(\Delta u_{\max})$). Furthermore, at the same time the side lobes are twice larger (~-7 dB instead of ~ -14 dB). This conclusion apparently stands in contradiction to the equivalence shown in Eqns. (4.21) and (4.12). However, it must be recalled that the real aperture array with beamforming exhibits an intrinsic windowing ($\overline{\overline{U}}$), when it is understood as a synthetic aperture array.

4.3.1 Radiometric Resolution

A fundamental parameter in microwave radiometers is the signal to noise ratio (SNR) defined as the ratio between the expected value (μ) of the collected power and its standard deviation (σ). Considering the beamformer signal (Eqn. (4.14)), and taking into account that long series of the radiometer output can be considered to be Gaussian stochastic processes (inferred by the central limit theorem, Section 3.3.1), its SNR is shown in Eqn. (4.22):

$$\text{SNR}(\tau_i) = \frac{\mu}{\sigma(\tau_i)} = \frac{\langle S_{DBF}^{p} S_{DBF}^{q*} \rangle}{\sqrt{\langle S_{DBF}^{p} S_{DBF}^{p*} S_{DBF}^{q*} S_{DBF}^{q} \rangle - \langle S_{DBF}^{p} S_{DBF}^{q*} \rangle \langle S_{DBF}^{p*} S_{DBF}^{q} \rangle}/\sqrt{B\tau_i}}, \tag{4.22}$$

where the standard deviation depends on the product of the pre-detection noise bandwidth and the integration time (τ_i). From the complex Gaussian moment theorem [72], the fourth order moment in Eqn. (4.22) can be decomposed into second order moments:

$$\langle S_{DBF}^{p} S_{DBF}^{p*} S_{DBF}^{q*} S_{DBF}^{q} \rangle = \langle S_{DBF}^{q} S_{DBF}^{p*} \rangle \langle S_{DBF}^{p} S_{DBF}^{q*} \rangle + \langle S_{DBF}^{p} S_{DBF}^{p*} \rangle \langle S_{DBF}^{q} S_{DBF}^{q*} \rangle, \tag{4.23}$$

and then the standard deviation can be computed as follows:

$$\begin{aligned} \sigma(\tau_i) &= \sqrt{\langle S_{DBF}^{p} S_{DBF}^{p*} S_{DBF}^{q*} S_{DBF}^{q} \rangle - \langle S_{DBF}^{p} S_{DBF}^{q*} \rangle \langle S_{DBF}^{p*} S_{DBF}^{q} \rangle} / \sqrt{B\tau_i} \\ &= \sqrt{\langle S_{DBF}^{p} S_{DBF}^{p*} \rangle \langle S_{DBF}^{q*} S_{DBF}^{q} \rangle} / \sqrt{B\tau_i}. \end{aligned} \tag{4.24}$$

From Eqns. (4.22) and (4.24), it can be inferred that the SNR depends on a cross-polarization term $SNR(\tau_i) = \rho_{nm}^{pq} \sqrt{B\tau_i}$ where the cross-polarization term is defined as $\rho_{nm}^{pq} = \langle S_{DBF_n}^{p} S_{DBF_m}^{q*} \rangle / \sqrt{\langle S_{DBF_n}^{p} S_{DBF_m}^{p*} \rangle \langle S_{DBF_n}^{q*} S_{DBF_m}^{q} \rangle}$ and m=n is the beam number being considered. Recall that when the system is a TPR then $SNR(\tau_i) = \sqrt{B\tau_i}$ as expected. Following [85] it is possible to relate the SNR to the radiometric resolution (ΔT^{pq}). Hence, the ΔT^{pq} term can be calculated for each beam as follows:

$$\Delta T^{pq}(\xi_0, \eta_0, \tau_i) = \frac{T_{SYS}^{pq}(\xi_0, \eta_0)}{SNR(\xi_0, \eta_0, \tau_i)}. \tag{4.25}$$

The system temperature in Eqn. (4.25) ($T_{SYS}^{pq}(\xi_0, \eta_0)$), can be computed from Eqn. (4.14), as:

$$\begin{aligned} T_{SYS}^{pq}(\xi_0, \eta_0) &= \frac{1}{2} \langle S_{DBF}^{p} S_{DBF}^{q*} \rangle = \frac{1}{2} \overline{w}^{T} \langle (\bar{S}^{p} + \bar{n}^{p})(\bar{S}^{q} + \bar{n}^{q})^{H} \rangle \overline{w}^{*} \\ &= \overline{w}^{T} \overline{\overline{V}}^{pq} \overline{w}^{*} + \overline{w}^{T} \overline{\overline{N}}^{pq} \overline{w}^{*}, \end{aligned} \tag{4.26}$$

where the first term is related to the expected value, the ideal visibility samples, and the second one is related the noise covariance matrix whose elements are defined as follows [86]:

$$N_{ij} = \frac{1}{B\tau_i} \begin{cases} V_{km} V_{ln}^{*} & k \neq m, l \neq n \\ V_{km} V_{ln}^{*} + T_{Rl} V_{km} & k \neq m, l = n \\ V_{km} V_{ln}^{*} + T_{Rk} V_{ln}^{*} & k = m, l \neq n \\ V_{km} V_{ln}^{*} + T_{Rl} V_{km} + T_{Rk} V_{ln}^{*} + T_{Rk} T_{Rl} & k = m, l = n. \end{cases} \tag{4.27}$$

The matrix $\overline{\overline{N}}$ can be separated as the contribution of four different matrixes:

$$\overline{\overline{\mathrm{N}}}^{pq}(\mathrm{u},\mathrm{v}) = \overline{\overline{\mathrm{C}}}_{pq}(\mathrm{u},\mathrm{v}) + \overline{\overline{\mathrm{C}}}_{pr}(\mathrm{u},\mathrm{v}) + \overline{\overline{\mathrm{C}}}_{rq}(\mathrm{u},\mathrm{v}) + \overline{\overline{\mathrm{C}}}_{rr}(\mathrm{u},\mathrm{v}), \tag{4.28}$$

where $\overline{\overline{\mathrm{C}}}_{pq}$ depends only on the target, $\overline{\overline{\mathrm{C}}}_{rr}$ only on the receiver's noise (it is a diagonal matrix), and $\overline{\overline{\mathrm{C}}}_{pr}$ and $\overline{\overline{\mathrm{C}}}_{rq}$ depend on both of them, and are affected by the configuration of the array. Finally, the general expression for $\Delta\mathrm{T}$ is summarized in Eqn. (4.29):

$$\Delta\mathrm{T}^{pq}(\xi_0,\eta_0,\tau_\mathrm{i}) = \frac{\overline{w}^T\overline{\overline{\mathrm{V}}}^{pq}\overline{w}^* + \overline{w}^T\overline{\overline{\mathrm{N}}}^{pq}\overline{w}^*}{\rho_{nm}^{pq}\sqrt{\mathrm{B}\tau_\mathrm{i}}} = \frac{\sqrt{\overline{w}^H(\overline{\overline{\mathrm{V}}}^{pp} + \overline{\overline{\mathrm{N}}}^{pp})\overline{w}\overline{w}^H(\overline{\overline{\mathrm{V}}}^{qq} + \overline{\overline{\mathrm{N}}}^{qq})\overline{w}}}{\sqrt{\mathrm{B}\tau_\mathrm{i}}}. \tag{4.29}$$

Some particular cases can be deduced from Eqn. (4.29) assuming that all antenna patterns are the same ($\mathrm{T}_{\mathrm{A}_\mathrm{m}} = \mathrm{T}_{\mathrm{A}_\mathrm{n}} = \mathrm{T}_\mathrm{A}$), that all receivers have the same noise temperature ($\mathrm{T}_{\mathrm{R}_\mathrm{m}} = \mathrm{T}_{\mathrm{R}_\mathrm{n}} = \mathrm{T}_\mathrm{R}$), that errors between visibility samples are uncorrelated ($\overline{\overline{\mathrm{C}}}_{pq}(\mathrm{u},\mathrm{v}) = \overline{\overline{0}}$, indeed $\overline{\overline{\mathrm{N}}}^{pq}(\mathrm{u},\mathrm{v}) = \overline{\overline{\mathrm{C}}}_{rr}(\mathrm{u},\mathrm{v})$), and that the steering vector is normalized ($\sum_{\mathrm{m}=1}^{M} w_m^2(\xi_0,\eta_0) = 1$):

- if $p = q$ then:

$$\Delta\mathrm{T}^{pp}(\xi_0,\eta_0,\tau_\mathrm{i}) = \frac{\mathrm{V}^{pp} + \mathrm{C}_{rr}}{\sqrt{\mathrm{B}\tau_\mathrm{i}}}\sum_{\mathrm{m}=1}^{M} w_m^2(\xi_0,\eta_0) = \frac{\mathrm{T}_\mathrm{A}^{pp} + \mathrm{T}_\mathrm{R}}{\sqrt{\mathrm{B}\tau_\mathrm{i}}}, \tag{4.30}$$

- if $p \neq q$ then:

$$\begin{aligned}\Delta\mathrm{T}^{pq}(\xi_0,\eta_0,\tau_\mathrm{i}) &= \frac{1}{\sqrt{\mathrm{B}\tau_\mathrm{i}}}\overline{w}^H\sqrt{(\mathrm{V}^{pp} + \mathrm{C}_{rr})(\mathrm{V}^{qq} + \mathrm{C}_{rr})}\,\overline{\overline{\mathrm{I}}}\,\overline{w} \\ &= \frac{\sqrt{\left(\mathrm{T}_\mathrm{A}^{pp} + \mathrm{T}_\mathrm{R}\right)\left(\mathrm{T}_\mathrm{A}^{qq} + \mathrm{T}_\mathrm{R}\right)}}{\sqrt{\mathrm{B}\tau_\mathrm{i}}}.\end{aligned} \tag{4.31}$$

Results from Eqn. (4.30) and Eqn. (4.31) agree with a previous work [32] where the same relationships where found following a completely different derivation. Moreover, it also agrees with the radiometric resolution reached in [85] when the number of antenna elements is limited to one: $\Delta\mathrm{T}^{pq}(\xi_0,\eta_0,\tau_\mathrm{i}) = \mathrm{T}_{\mathrm{SYS}}^{pq}(\xi_0,\eta_0)/\sqrt{\mathrm{B}\tau_\mathrm{i}}$.

4.3.2 Scanning Angular Resolution

Equation (4.21) has a significant impact from a theoretical point of view because it relates synthetic and real aperture radiometers. Nevertheless, the selection of the number of beams and their associated steering angles depends on the purpose of

the system, then the use of the Fourier transform can be limiting from an operational point of view especially when considering an array with few elements. As stated in Section 4.2, for an *M*-element array the inverse Fourier transformation creates *M* fixed, orthogonal and equally spaced beams within the domain $\xi^2 + \eta^2 \leq 1$. Orthogonal beams imply that the central peak of any beam lies in a null of all other beams, so that, the system provides uncorrelated measurements. It is possible to increase the number of synthesized beams at the expense of increasing the correlation between two consecutive beams (Eqn.(4.32)). A simple and straightforward way to synthesize more beams is by zero padding techniques coupled with the inverse Fourier transform (Eqn. (4.21)) or directly using the $\overline{\overline{W}}_2$ linear transformation matrix with a column rank higher than *M* (Eqn. (4.21)). Although any beam configuration different than that, implicitly assumes a loss of information per beam, the angular scanning resolution is usually increased considering the array beamwidth, defined as the angular distance from the peak up to a fall of -3 dB in power of the array pattern (θ_{-3dB}). Then, instead of having the peaks on the nulls, two consecutive beams overlap up to θ_{-3dB}. It is possible to overlap even more the beams, in this case, the information of each beam becomes highly correlated to the adjacent ones, but it is still contributing with relevant information. The limit of the situation is when two consecutive beams totally overlap, then $\rho_{n(n+1)}^{pq} = 1$. From Eqn. (4.17) and taking advantage of the correlation coefficient definition given in Section 4.3.1 ($\rho_{nm}^{pq} = \langle S_{DBF_n}^{p} S_{DBF_m}^{q*} \rangle / \sqrt{\langle S_{DBF_n}^{p} S_{DBF_m}^{p*} \rangle \langle S_{DBF_n}^{q*} S_{DBF_m}^{q} \rangle}$) it is easy to compute the correlation between two beams, using two different beams instead of the same (*n* and *n*+1), for a given array (Eqn. (4.32)):

$$\rho_{n(n+1)}^{pq} = \frac{\overline{W}^{T}(\xi_{n,n+1}, \eta_{n,n+1})\overline{V}^{pq}}{\sqrt{\tilde{T}_{A}^{pq}(\xi_{n}, \eta_{n})\tilde{T}_{A}^{pq}(\xi_{n+1}, \eta_{n+1})}} = \frac{1}{\tilde{T}_{n,n+1}^{pq}} \overline{W}^{T}(\xi_{n,n+1}, \eta_{n,n+1})\overline{V}^{pq}, \tag{4.32}$$

where:

- $\overline{W}^{T}(\xi_{n,n+1}, \eta_{n,n+1})$ is defined as in Eqn. (4.17), but with $\overline{W}^{T}(\xi_{n,n+1}, \eta_{n,n+1}) = \overline{w}^{*}(\xi_{n}, \eta_{n})\overline{w}^{T}(\xi_{n+1}, \eta_{n+1})$,
- *n* and *n*+1 are two consecutive synthesized beams, and
- $\tilde{T}_{n,n+1}^{pq}$ is the geometric mean of $\tilde{T}_{A}^{pq}(\xi_{n}, \eta_{n}) = \overline{W}^{T}(\xi_{n}, \eta_{n})\overline{V}^{pq}$ and $\tilde{T}_{A}^{pq}(\xi_{n+1}, \eta_{n+1}) = \overline{W}^{T}(\xi_{n+1}, \eta_{n+1})\overline{V}^{pq}$.

As it is shown in Eqn. (4.32), $\rho_{n(n+1)}^{pq}$ depends on the angular distance as the square root of its array factor. Moreover, the correlation of two consecutive beams for any given array depends on two terms. The first one is the visibility matrix ($\overline{V}^{pq}$) which depends on the observation angle due to the antenna pattern and $\tilde{T}_{a}^{pq}(\xi_{n}, \eta_{n})$ (Eqn.(4.11)), while second one ($\overline{W}^{T}(\xi_{n,n+1}, \eta_{n,n+1})$) only depends on the antenna

array configuration. Another important conclusion from Eqn. (4.32) is that the $\rho_{n(n+1)}^{pq}$ coefficient matches the array factor in voltage terms. Figure 4.2 shows the correlation coefficient versus the angular distance of two beams and the array factor of two linear arrays $M = 4$ and $M = 10$.

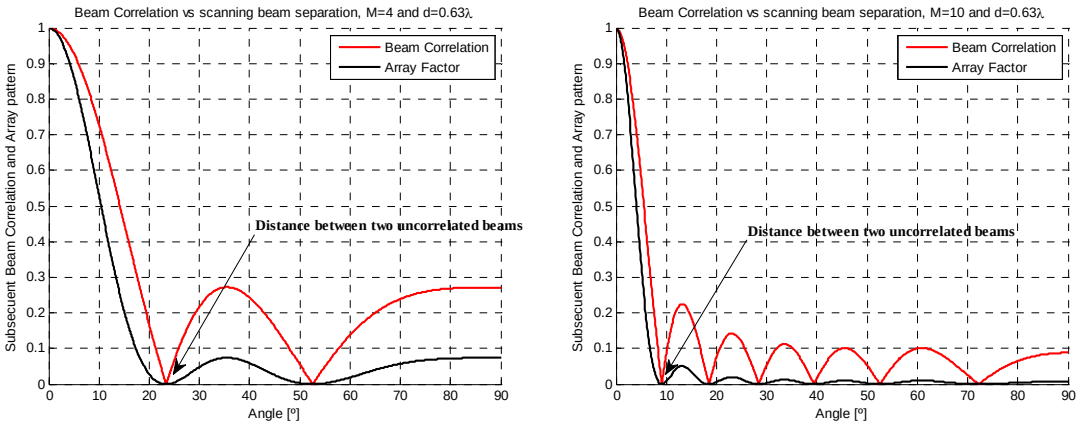

(a) (b)

Figure 4.2 Correlation coefficient versus the angular distance of two beams and array factor with d = 0.63 wavelengths linear array, (a) $M = 4$ and (b) $M = 10$ elements.

This section has shown the equivalence between real and synthetic aperture techniques. In this section the main parameter that defines the radiometric performance has been translated from the synthetic aperture to real aperture radiometers with beamforming systems, having found a complete agreement between them.

4.4 Possible Beamforming Implementations

One of the most critical issues to properly steer a beam is the phase and amplitude equalization between receivers. Inter-element equalization and relative weighting to steer the beam in the desired direction are performed before the signals are added to get the beamformer output, which is a challenging issue for real time systems. In [40] was found that in order to have the main beam efficiency (MBE) degradation smaller than 2% residual calibration errors have to be smaller than ±0.1 dB in amplitude and ±2º in phase. This calibration has two strong requirements:

- to spend time to calibrate the system, reducing the available observation time, and
- to dedicate hardware resources to estimate and calibrate the phase and amplitude differences between receivers, increasing the total hardware complexity.

Another important design issue is to improve the radiometric resolution (ΔT^{pq}). According to the Friis formula [87], the system's noise temperature is driven by the noise figure of the elements before the first amplifier. Usually, in a radiometer chain the first element is a switch that allows switching between the antenna and one or several internal references: to measure cross-correlation offsets, or a common signal distributed to each receiver to compute phase and amplitude differences [40]. Depending on the technology a beamformer can be implemented at different stages, e.g.:

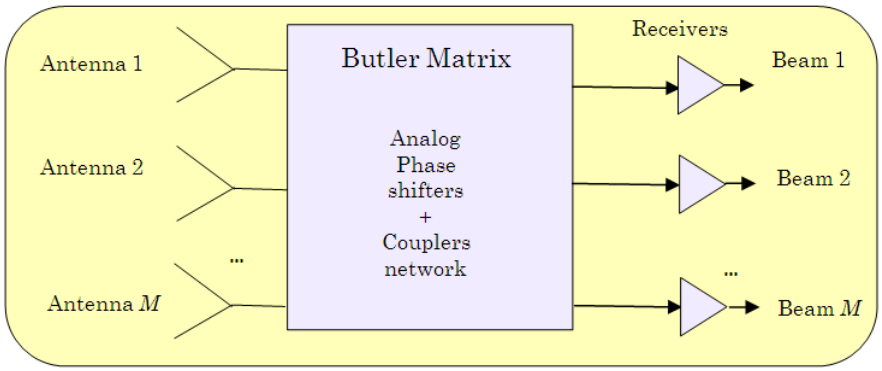

Figure 4.3 Sketch of Butler matrix beamformer. The matrix is fed with M antenna signals. The output is a set of *M* equally spaced beams at RF.

- It can be implemented at radiofrequency stage by directly adding the signals from the antennas using phase shifters or transmission lines (true time delay). This implementation has the advantage that only one receiving chain per beam is needed, but has a limited dynamic configurability. A clever implementation of the beamformer network was conceived by Butler and Lowe [79] creating all independent beams simultaneously with a passive circuit. Despite its beams are static, this technique has the advantage that does not require any previous phase or amplitude calibration because it uses an independent receiver for each beam (Figure 4.3). An example of a successfully developed and deployed instrument capable of these features is the Scanning Low-Frequency Microwave Radiometer (SLFMR) [20] used for sea surface salinity applications.

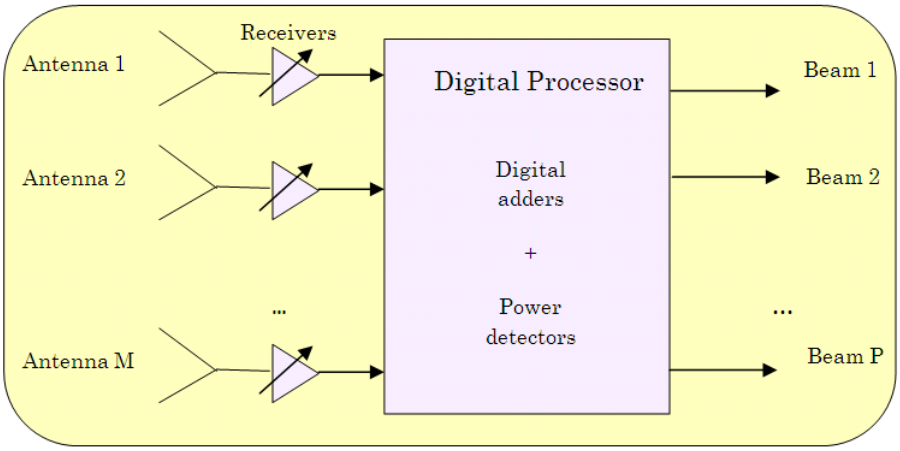

Figure 4.4 Sketch of a digital beamformer consisting of a digital processor and *M* receivers. Phase and amplitude calibrations and steering can be applied at the receiver or

at a digital level. The number of output beams can be higher than *M*, (redundant beams), or lower (losing antenna information).

- On the other hand, the beamformer can be implemented once the signals have been down-converted at an intermediate frequency stage or at base band (in-phase and quadrature components), using the local oscillator of each receiver as a phase shifter. This choice has the advantage of working at lower frequencies where it is easier to design precisely, and digital technologies can be applied in Digital Signal Processors (DSP) or Field Array Gate Arrays (FPGA), but it needs as many receiving chains as antennas the system has. Nowadays, digital technology allows dealing with enough bandwidth and bits resolution to ensure results with the same resolution as analog systems, providing a high level of configurability in real time (Figure 4.4).

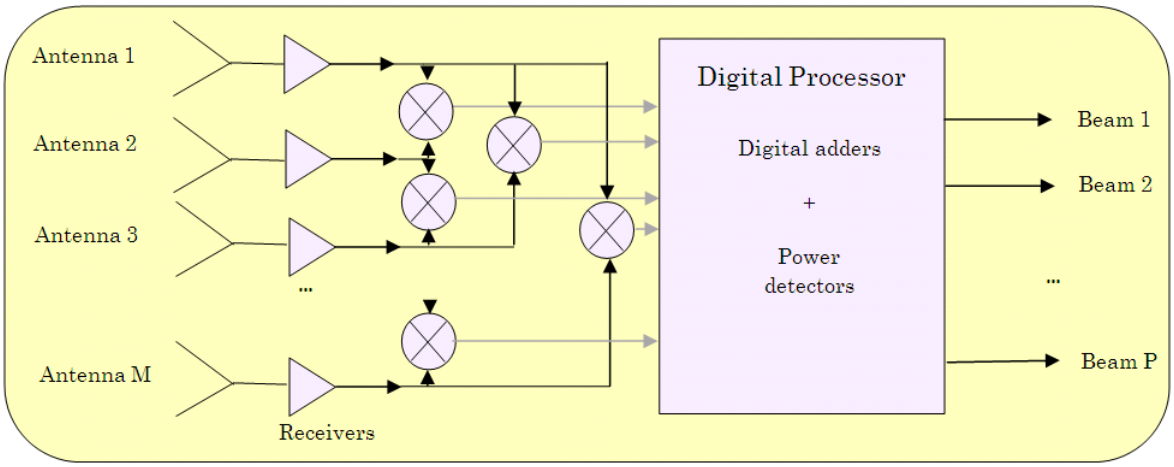

Figure 4.5 Sketch of a digital beamformer using complex correlators. It consists of a digital processor, *M* receivers and a set of correlators. The number of output beams can be higher (redundant beams), or lower (lost of antenna information) than *M*.

- From results of Section 4.3 a new way to implement a digital beamformer for remote sensing applications using complex correlators and software routines (Figure 4.5) can be envisaged, providing an optimum scheme for real time digital beamforming and calibration of the receivers' phase and amplitude differences using Redundant Space Calibration (RSC) [88]. This way, the noise injection network and inputs switches can be eliminated.

4.5 Beamforming Implementation Using Visibility Samples Formulation

Figure 4.6 shows a flow chart for implementing a DBF using the matrix of visibility samples as shown in Section 4.3.

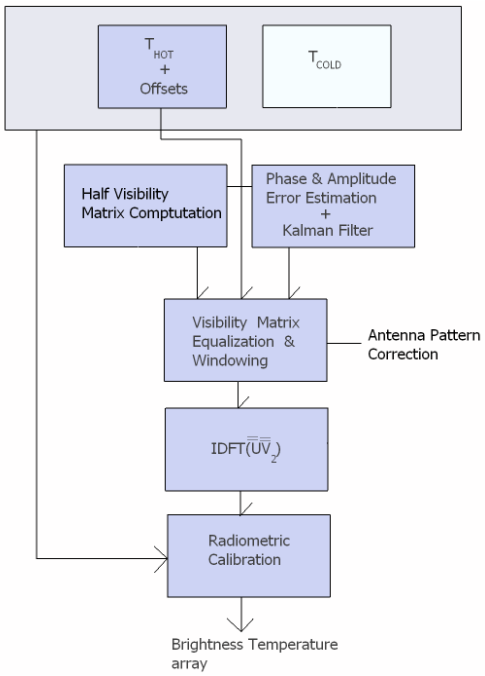

Figure 4.6 Synthesis of simultaneous multiple beams data flow including hardware calibration errors with the antenna visibility samples e.g.: the RSC algorithm. The hardware equalization and the phase center correction are done using rotation matrices. The beams are synthesized using the inverse Fourier transformation (IDFT) when the antenna pattern compensation is performed. Finally, all data is radiometric calibrated to get a brightness temperature vector.

The flow chart includes the necessary procedures to achieve this implementation:

- Matrix of visibility samples has to be measured ( ). This matrix includes information regarding the scene, including phase and amplitude differences. Therefore, it is possible to estimate these differences using the RSC algorithm of phase and amplitude closures [88]. As it has been stated in Eqn. (4.21), if all the receivers have the same phase and the same amplitude, then it is possible to create several and simultaneous beams from the visibility matrix. Actually, only the diagonal and the upper half of the visibility matrix have to be measured since reducing the amount of digital resources required. Hence, the visibility matrix computation requires as many complex correlators (2 multi-bit multipliers and 2 adders [89]) as the number of non-redundant baselines.

- The visibility matrix has to be calibrated, windowed and the antenna pattern has to be compensated. If receivers have different phases or amplitudes, these have to be compensated before creating the beamforming by previous estimation of the error. These errors can be further reduced using a Kalman filter [96] to achieve the residual errors specifications [40]. This external phase and amplitude calibration strategy can replace the input switch and the correlated noise distribution network, because it computes the calibration coefficients during the measurements.

- Using only the non-redundant information ($\bar{V}_2^{pq}$) and the Inverse Discrete Fourier Transform (IDFT) algorithm the synthetic image is obtained.

- Collected power measurements from synthetic images have then to undergo a radiometric absolute calibration using, for example, the T_{hot} (*i.e.* a thermally controlled microwave absorber) - T_{cold} (*i.e.* the sky) calibration line strategy in order to get brightness temperatures. Correlation offsets between visibilities can be computed, for example, when measuring $T_{hot.}$

This proposed implementation of the digital beamformer simplifies the digital hardware architecture taking advantage of the visibility matrix concept (Eqn. (4.15)). It is capable to synthesize multiple beams simultaneously reducing the hardware complexity and removing the internal switch between the antenna and the low noise amplifier for hardware calibration. As an important part of the digital beamforming radiometer, the system avoids errors present in analog systems such as quadrature errors, non-linearity, *etc*. However, at the same time other problems from digitalization and quantification may appear such as information losses, clipping, reduction of the available integration time, that can be avoided using a high enough sampling rate and a multi-bit scheme (> 6 bits), or with appropriate post-processing techniques to get the true cross-correlation value [89]. These effects will be studied and further detailed in Chapter 5.

4.6 Non-Radiometric Applications

Although this technique has been conceived in the frame of microwave radiometry, it can be easily extended to other remote sensing applications, such as Synthetic Aperture Radar (SAR) or GNSS/Reflectometry ([90], [91]) in which the received signal is correlated with some reference signal. In this case Eqn. (4.13) becomes Eqn. (4.33) and all the above description applies:

$$\begin{aligned} Y^p(\xi_0,\eta_0,t+\tau) &= \langle S^p_{DBF}(\xi_0,\eta_0,t) S^*_{REF}(\tau)\rangle = \bar{w}^T(\xi_0,\eta_0)\langle \bar{S}^p(t)\bar{S}^H_{REF}(\tau)\rangle, \\ &= \bar{w}^T \bar{C}^p(t+\tau) \end{aligned} \tag{4.33}$$

$$\bar{C}^p(\tau) = \begin{pmatrix} C^p(u_1,v_1,\tau) \\ \dots \\ C^p(u_M,v_M,\tau) \end{pmatrix}, \tag{4.34}$$

$$C^p(u_m,v_m,\tau) = \iint\limits_{\xi^2+\eta^2\le 1} \frac{P^p(\xi,\eta,\tau)}{\sqrt{1-\xi^2-\eta^2}} F^p_m F^*_{ref} \tilde{r}_m\left(\tau - \frac{u_m\xi + v_m\eta}{f_0}\right) e^{-j2\pi(u_m\xi+v_m\eta)} d\xi d\eta, \tag{4.35}$$

where:

- $Y^p(\xi_0, \eta_0, t+\tau)$ is the cross-correlation value between the received signal coming from the (ξ_0, η_0) direction at p polarization, with a reference signal locally generated or obtained from another source. In GNSS/R applications this is known as the "waveform". Similarly to Eqn. (4.12) where units are Kelvin ([K]), this equation has units of power ([W]),

- τ is a delay with respect to a time origin,

- $P^p(\xi, \eta)$ is the ideal cross-correlation in the (ξ, η) domain,

- $\tilde{r}_m$ is the fringe-washing function obtained from the frequency response of the m^{th} channel and the Fourier transform of the reference signal,

- $C^p(u_m, v_m, \tau)$ is the measured cross-correlation between the signal collected by the m^{th} antenna and the reference signal,

- $(u_{mn}, v_{mn}) \equiv (x_{ref} - x_m,\ y_{ref} - y_m)/\lambda_0$, is the spatial frequency, and

- x_{ref} and y_{ref} are arbitrary coordinates of the reference system, for example the phase center of the array.

Finally, for this case it is possible to get an expression similar to Eqn. (4.21) (Eqn. (4.36)). The most significant differences are that there is no redundancy, so the cross-correlation is not windowed in natural way and that the angular resolution is halved, the inverse Fourier transform is only on the positive domain and the resolution is being affected in this case by the weights.

$$Y^p(\xi, \eta, t+\tau) = \mathrm{IDFT}\{C^p(u, v, \tau)\}. \tag{4.36}$$

4.7 Conclusions

The relationship between synthetic aperture and real aperture radiometers has been demonstrated theoretically. Experimental validation results will be shown in Chapter 9. Some advanced analysis performed for synthetic aperture radiometers have now been extrapolated to beamforming radiometers. A performance analysis of the radiometric resolution and the scanning angular resolution has been performed. For imaging radiometers, it has been found that the use of orthonormal vectors such as IDFT provide uncorrelated measurements. However, it is possible to increase the sampling resolution using non-orthogonal vectors, but then the correlation increases rapidly as the square root of the array pattern. Finally, a new implementation of a digital beamforming using the concept of visibility samples has been envisaged. Real measurements will be provided in Chapter 9. This concept can be extrapolated to other receivers used for remote sensing such as SAR and GNSS/Reflectometers.

Chapter 5

5 IMPACT OF THE DIGITIZATION ON A CORRELATION RADIOMETER

This chapter provides a general framework to analyze the effects of a generic quantization scheme and sampling process on a correlation radiometer. It reviews, unifies and expands several previous works that focused on these effects separately. In addition, it provides a general theoretical background that allows analyzing numerically any digitization scheme including any number of quantization levels, irregular quantization steps, gain compression, clipping, jitter and skew effects of the sampling period.

5.1 Overview of Digitization Effects in Microwave Radiometry

One of the most relevant novelties in the radiometry field on the 60´s ([92]-[93]) was the digitization of the signals and the capabilities that emerge from specialized platforms such as today's powerful an omnipresent DSP and FPGA. Although digitization provides versatility, re-configurability and other advantages for microwave radiometry, it also has side effects that must be carefully analyzed. Digitization effects can be separated into quantization and sampling effects. Mainly, the effects related with the quantization of the input signal, thermal noise, imply the lost of its statistical properties due to the non-linear quantization process. Then, it is not possible to apply the well-known Gaussian statistical relationships to the quantified signal. This effect has a large impact when limited quantization levels are considered, and it can be mitigated by increasing the number of quantization levels. Non-linear effects studies over Gaussian signals started with the early analysis of the spectrum of clipped noise by Van Vleck and Middleton [94]. In the late 1950's, R. Price published a work focusing on the relationship between the ideal correlation between two random signals with Gaussian probability density function (pdf), and the correlation measured after a non-linear manipulation of these random signals [95]. This relationship is now used to study the effect of arbitrary quantization schemes on the correlation of two signals.

Sampling affects the correlation of the two input signal by creating spectrum replicas. Additional noise can be added to the mean correlation value due to spectra replication depending on the ratio between the sampling frequency and the signal's bandwidth. Moreover, the sampling period and its inaccuracies (skew and jitter in the sampling times) of the Analog to Digital Converter (ADC) can affect and distort the sampled signal and so the cross-correlation value.

To compare different sampling and quantization schemes an equivalent integration time is defined as the one required getting the same accuracy than in the ideal (analog) correlation. Hagen and Farley [89] conducted an important work on this topic, were the effective time was defined and some easy-to-calculate digitization configurations were analyzed in depth. More recent works have extended the initial digital radiometer proposed by Weinreb in 1961 [92] for autocorrelation spectrometers for radio-astronomy to include total power radiometers, polarimeters [97], and the digitization impact on interferometric radiometers ([98]-[101]). This chapter provides a general framework to analyze the digitization effects over the cross-correlation of two Gaussian random signals in the most general case including any number of quantization levels, irregular quantization steps, gain compression, clipping, bandwidth, sampling frequency, and the skew and jitter inaccuracies of the sampling times.

5.2 Non-Linearity Impact on the Correlation of Two Gaussian Random Signals

The input signal of a microwave radiometer comes from natural thermal emission. Let us consider here two independent Gaussian random processes with a certain cross-correlation coefficient characterized by their probability density functions (pdf). The previous assumptions hold if there are not radiofrequency interferences (RFI). Furthermore, both input signals are assumed to be statistically identical and stationary, so the properties of the signals at a given time (T_0) are independent of T_0. Furthermore, both signals fulfill that their statistical properties can be deduced from a single, sufficiently long sample (realization) of the process, *i.e.* there are ergodic processes [102]. Thus, the variance of each series is constant and the covariance between elements depends only on their time separation. Finally, let x and y be two radiometer input signals fulfilling the previous requisites. Usually, these random variables have zero mean ($\mu_{x,y}$=0), except for offsets, and are considered to have normalized standard deviation ($\sigma_{x,y}$=1). In this case, the joint probability of density is defined as in Eqn. (5.1):

$$f(x,y) = \frac{1}{2\pi\sigma_x\sigma_y\sqrt{1-\rho_{xy}^2}} e^{-\frac{1}{2}\frac{(x^2+y^2-2\rho_{xy}^2 xy)}{\sigma_x\sigma_y(1-\rho_{xy}^2)}}, \tag{5.1}$$

where:

- $\sigma_{x,y}$ are the standard deviation of x and y signals, and
- ρ_{xy} is the Pearson correlation coefficient and it is defined as the ratio between the covariance of x and y and the geometric mean of the product of their variances (Eqn. (5.2)):

$$\rho_{xy} = \frac{\langle xy^* \rangle}{\sqrt{\langle xx^* \rangle \langle yy^* \rangle}}, \tag{5.2}$$

where the brackets $\langle \cdot \rangle$ indicate a statistical average, over a time sequence with identical statistics (ergodic properties).

Price's theorem [95] relates the correlation coefficient of x and y after (R_{xy}) and before (ρ_{xy}) the application of non-linear functions ($g_1(\cdot)$ and $g_2(\cdot)$) to the random variables (Eqn. (5.3)).

$$\frac{\partial^k R_{xy}}{\partial \rho_{xy}} = \sigma_x^k \sigma_y^k \langle g_1^k(x) g_2^k(y) \rangle, \tag{5.3}$$

where:

- R_{xy} is the correlation coefficient of x and y after the non-linear functions $g_1(\cdot)$ and $g_2(\cdot)$ are applied to x and y, respectively,
- P is the ideal correlation coefficient of x and y (before the non-linear functions $g_1(\cdot)$ and $g_2(\cdot)$),
- $\sigma_{x,y}^k$ are the standard deviation of x and y signals and usually are normalized, (for the sake of clarity, from now on $\sigma_{x,y}^k = 1$), and
- k denotes the k^{th} derivative of each function.

From Eqn. (5.3), it is possible to recover ρ, the ideal correlation between x and y, by k-derivate and further correlating the $g_1(x)$ and $g_2(y)$ signals and then k-integrating with respect to the ρ variable from -1 to +1. These operations can be defined as a relationship between both magnitudes, the ideal and the non-linear correlations, and it is defined here as the function q [·]:

$$\rho_{xy} = q^{-1}[R_{xy}], \tag{5.4}$$

Considering the correlation for two delay-dependent signals ($x \rightarrow x$(t=0) and $y \rightarrow y$(t= τ)) the effect of the hardware response can be included as a function of τ, then Eqn. (5.2) becomes:

$$\rho_{xy}(\tau) = \langle xy^* \rangle = \rho_{xy}(0)\tilde{r}_{xy}(\tau), \tag{5.5}$$

where:

- $\rho_{xy}(0)$ is the Pearson correlation coefficient (Eqn. (5.2)) at τ=0, and
- $\tilde{\mathrm{r}}_{xy}(\mathrm{t}) \triangleq \frac{\mathrm{e}^{-\mathrm{j}2\pi f_0 \mathrm{t}}}{\sqrt{\mathrm{B}_x \mathrm{B}_y}} \int_0^\infty \mathrm{H}_x(f)\, \mathrm{H}_y^*(f) \mathrm{e}^{\mathrm{j}2\pi f \mathrm{t}} df$ is the so-called fringe-washing function (FWF), as defined in [103], where B_x and B_y are the equivalent noise bandwidths, f_0 is the central frequency, and $\mathrm{H}_x(f)$ and $\mathrm{H}_y(f)$ are the normalized frequency responses of the x and y channels, respectively. Note that, if the channels' frequency response are equal, with rectangular shape of bandwidth B, and centered frequency f_0, the fringe-washing function reduces to the well-known formula $\tilde{\mathrm{r}}_{xy}(\tau) = \mathrm{sinc}(\mathrm{B}_{xy}\tau)$.

Equation (5.5) depends on the correlation coefficient and the hardware characteristics. Usually, to avoid an underestimation of the correlation coefficient, Eqn. (5.4) has to be compensated by the existing delay between x and y as it follows:

$$\rho_{xy}(0) = \frac{q^{-1}\left[R_{xy}(\tau)\right]}{r_{xy}(\tau)}, \tag{5.6}$$

Assuming that the x and y statistics are stationary random processes (thermal noise radiation) that fulfill the ergodic property, then Eqns. (5.2) and (5.5) can be calculated in practice using the cross-correlation technique (time averaging).

5.3 Quantization Impact

This section particularizes the previous analysis to a generic ADC function. The degree of non-linearity of an ADC function depends on the number of quantization levels and its span window (V_{ADC}), going from 2 levels (1 bit) the most non-linear scheme, up to an infinite number of levels with an infinite V_{ADC}, which can be considered linear. As explained before, quantization does not take into account the sampling, so that this analysis considers an infinite frequency sampling ($F_s \to \infty$).

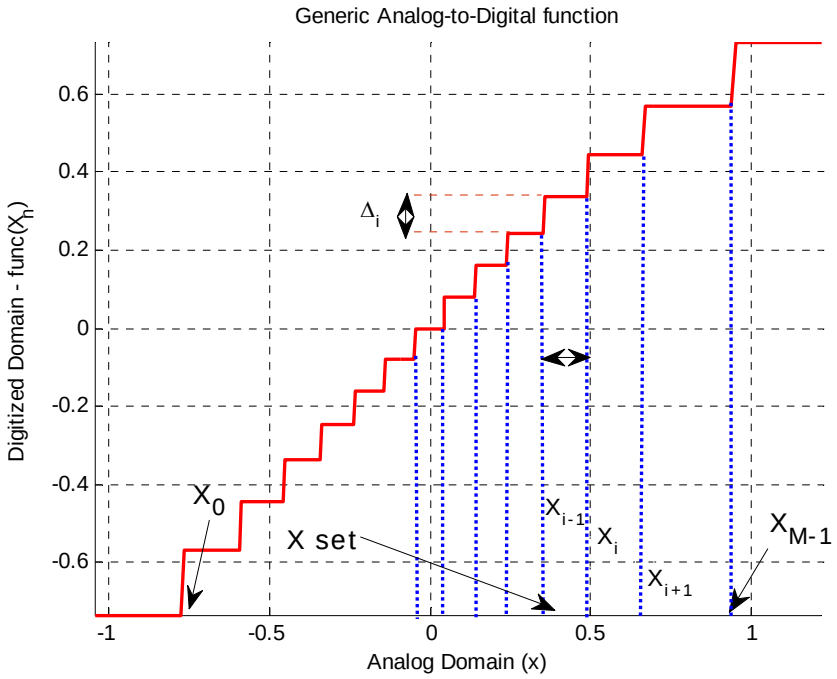

Figure 5.1 Generic analog-to-digital transfer function. The function plotted has a compression gain and different steps in both domains.

Equation (5.7) shows a general quantization function (Figure 5.1):

$$g_i(x) = \sum_{m=0}^{M-1} \Delta_m^i \, u(x - X_m), \tag{5.7}$$

where:

- x is the value of the signal in the analog domain (continuous in time and values),
- X_m and X_{m+1} are two consecutive threshold values of the input signal in the $\bar{X}$ space (see Figure 5.1), where $\bar{X}$ is the set of all the input threshold values in the digital domain ($\bar{X} = \{X_m\}$, m=0… $M-1$). Note that, in the most general case the distance between two consecutive steps does not have to be necessarily constant ($X_m - X_{m-1} \neq X_{m+1} - X_m$),
- $u(x - X_m)$, is the Heaviside function (step function) centered at X_m,
- Δ_m^i is the quantization step value between the $[X_{m-1}, X_m)$ interval. Note that, in the most general case the distance between two consecutive steps does not have to be necessarily constant either ($\Delta_m^i \neq \Delta_{m+1}^i$), and
- the values X_0 and X_{M-1} defines the lower and upper bounds of the quantization window. Again, in a general case, the lower bound can be different from the upper bound ($X_m \neq -X_{M-1}$).

The derivative function of Eqn. (5.7) is given by:

$$\frac{\partial g_i(x)}{\partial x} = \sum_{m=0}^{M-1} \Delta_m^i \, \delta(x - X_m), \tag{5.8}$$

where δ is the Kronecker's delta: δ=1 if $x = X_m$ and δ=0 if $x \neq X_m$.

Substituting the results obtained in Eqn. (5.8) in Eqn. (5.3), with different $g(\cdot)$ functions for x and y, and considering the first derivative function (k=1), the relationship between the correlation of two signals before and after the quantization process is obtained in Eqn. (5.9):

$$\frac{\partial R_{xy}}{\partial \rho_{xy}} = \frac{1}{2\pi\sqrt{1-\rho_{xy}^2}} \iint_{-\infty}^{\infty} \sum_{p=0}^{P-1} \Delta_p^x \delta(x - X_p) \sum_{q=0}^{Q-1} \Delta_q^y \delta(y - Y_q) \, \mathrm{e}^{-\frac{1(x^2+y^2+2xy\rho_{xy})}{2\ (1-\rho_{xy}^2)}} dxdy, \tag{5.9}$$

Then, it is easy to compute the integrals over the x and y directions by evaluating them at the points where Kronecker's delta does not vanish. Therefore, Eqn. (5.9) becomes Eqn. (5.10):

$$\frac{\partial R_{xy}}{\partial \rho_{xy}} = \frac{1}{2\pi\sqrt{1-\rho_{xy}^2}} \sum_{p=0}^{P-1} \sum_{q=0}^{Q-1} \Delta_p^x \, \Delta_q^y \, \mathrm{e}^{-\frac{1(X_p^2+Y_q^2+2X_pY_q\rho_{xy})}{2\ (1-\rho_{xy}^2)}}, \tag{5.10}$$

and finally, the integration over the ρ_{xy} domain is performed from -1 to 1.

$$R_{xy} = \int_{-1}^{1} \frac{1}{2\pi\sqrt{1-\rho_{xy}^2}} \sum_{p=0}^{P-1}\sum_{q=0}^{Q-1} \Delta_p^x \Delta_q^y \, \mathrm{e}^{-\frac{1}{2}\frac{(X_p^2+Y_q^2+2X_pY_q\rho_{xy})}{(1-\rho_{xy}^2)}} d\rho_{xy}. \tag{5.11}$$

From Eqn. (5.11) it is straightforward to include the impulse response of the system by considering different values of ρ_{xy} for different delays (τ):

$$R_{xy}(\tau) = \int_{0}^{\rho_{xy}(\tau)} \frac{1}{2\pi\sqrt{1-\rho_{xy}^2(\tau)}} \sum_{p=0}^{P-1}\sum_{q=0}^{Q-1} \Delta_p^x \Delta_q^y \, \mathrm{e}^{-\frac{1}{2}\frac{\left(X_p^2+Y_q^2+2X_pY_q\rho_{xy}(\tau)\right)}{\left(1-\rho_{xy}^2(\tau)\right)}} d\rho_{xy}(\tau). \tag{5.12}$$

In some particular and simplified cases, Eqn. (5.12) can be obtained analytically, as for example in the case of quantifying at two levels (one bit, $Q = \mathrm{P} = 1$ and $\Delta_0^x = \Delta_0^y = 2$). In this case, Eqn. (5.12) becomes the well-known solution stated in Eqn. (5.13) [94]:

$$R_{xy}\left(\rho_{xy}(\tau)\right) = \frac{2}{\pi}\arcsin\left(\rho_{xy}(\tau)\right). \tag{5.13}$$

Otherwise, when the quantization scheme is more complex Eqn. (5.13) can only be analyzed numerically, such as having different number of bits, when signals are clipped, when the quantization steps are irregular, when the ADC has a non-linear circuit before that exhibits gain compression, when there is no symmetry between the positive and negative parts or many other possibilities.

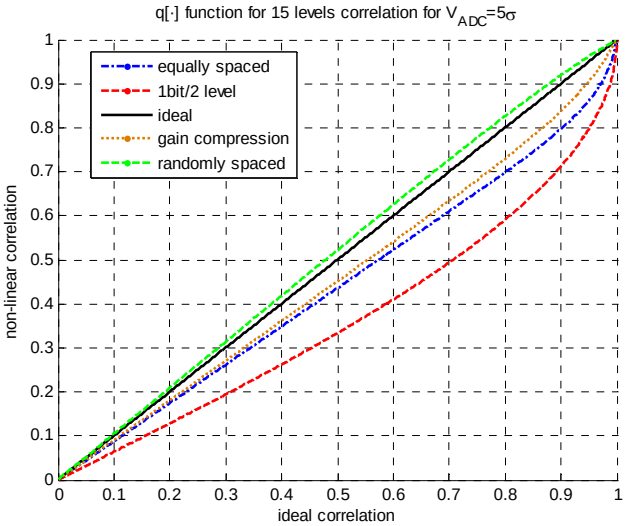

Figure 5.2 Relationship between the non-linear and the ideal correlation for different digitization schemes.

Figure 5.2 has been obtained from Eqn. (5.12) for different quantization schemes. Two $q[\cdot]$ functions are plotted for reference, the coarsest quantization scheme (*i.e.* 2 levels/1 bit, Eqn. (5.13)), and the ideal one (*i.e.* infinite levels, $R_{xy}(\tau) = \rho_{xy}(\tau)$). Three more functions are shown considering an ADC span window of $5\sigma_{x,y}$ (V_{ADC}= $5\sigma_{x,y}$), 15 quantization levels or 3.9 bits ($\log_2 15 = 3.9$, note that is not necessary to have an integer number of bits), but changing the non-linear function. Different $g(x)$ functions have been considered such as equally spaced levels, using a gain compression modeled by a hyperbolic tangent ($g(x) = \tanh(x)$) or having randomly spaced levels. All, results are different from the others, showing the need of a deeper analysis.

The root mean square error (RMSE) coefficient between $R_{xy}(\tau)$ and $\rho_{xy}(\tau)$ has been chosen to measure the linearity degree of $q[\cdot]$. So, the RMSE has been selected to be the figure of merit of different quantization schemes comparisons. Obviously, the linearity of any $q[\cdot]$ function is better as the RMSE is closer to zero. For a given application, there is a maximum distortion of the RMSE that can be afforded by the $q[\cdot]$, and that is called Max_{RMSE}. If the relationship between the quantized and the ideal correlations is linear enough (RMSE < Max_{RMSE}), then the value of the quantized correlation matches with the ideal correlation and there is no need of using the $q^{-1}[\cdot]$ function. Otherwise, if it is not linear enough (RMSE ≥ Max_{RMSE}) then, the obtained correlation has to be modified by the $q^{-1}[\cdot]$ function in order to retrieve the real correlation with an error lower than the maximum acceptable one.

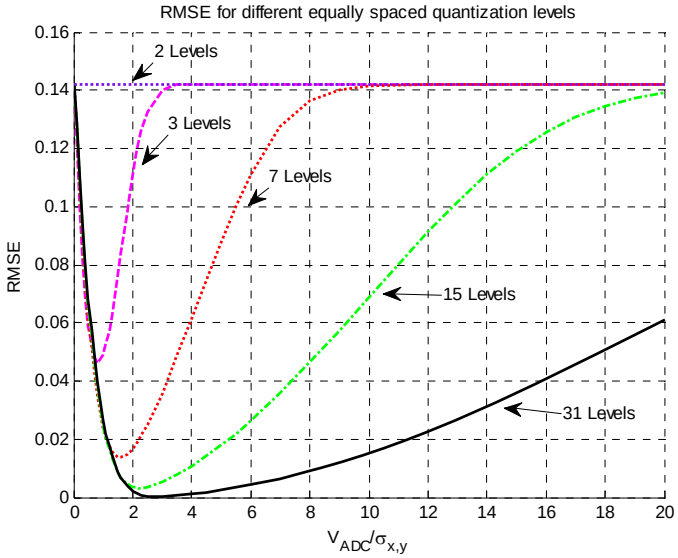

Figure 5.3 Root mean square error and ADC span window relationship for different equally spaced quantification levels.

Figure 5.3 presents the RMSE computed numerically using Eqn. (5.12), with different quantization levels and V_{ADC}. Each curve has a minimum that corresponds to the optimum configuration of V_{ADC} with respect $\sigma_{x,y}$. As the number of quantization levels increases, the minimum value of RMSE gets closer to 0, and the $V_{ADC}/\sigma_{x,y}$ range where the curves remain close to 0 also increases, since the function $q[\cdot]$ is linear over a wider range of input powers. By inspecting Figure 5.3

it is clear that for $V_{ADC} < 2\sigma_{x,y}$, clipping has a dominant impact over the non-linear correlation. This effect has the maximum impact when the clipping reduces the whole ADC to a 2 level decision (1 bit). As the clipping effect increases, the RMSE value converges to the RMSE of the 1bit/2 levels quantization (RMSE =14.2 %), which is the most non-linear quantization scheme possible.

On the other hand, plots also have a common trend in the region above the minimum, where the ratio $V_{ADC}/\sigma_{x,y}$ increases. As the number of quantization levels increases, the correlation becomes more a linear function over a wider range of input power (the region around the minimum widens). But when $V_{ADC}/\sigma_{x,y} \rightarrow \infty$, the RMSE asymptotically increases again up 14.2 %, the value of the 1 bit/2 levels quantization scheme. This effect can be understood as fewer bits are being used as the $V_{ADC}/\sigma_{x,y}$ ratio increases, and it can be understood as a decreasing of the effective number of bits. The maximum effect occurs when the V_{ADC} is so spread over $\sigma_{x,y}$ that only two levels are effectively used for quantization.

Another conclusion that can be drawn from Figure 5.3, it is that each quantization level has its own optimum ADC span window (V_{ADC}) with relation of the standard deviation of the input signal. This is a critical design parameter and it has been summarized on Table 5.1 for some quantization schemes.

Table 5.1 Summary of the critical design parameter $V_{ADC}/\sigma_{x,y}$. Relationship between its optimal configuration and the minimum root mean square error obtained for some quantization schemes.

Levels	$V_{ADC}/\sigma_{x,y}$ optimum	RMSE minimum [%]
2 (1 bit)	no optimum	14.2
3 (1.6 bits)	0.7	4.7
7 (2.8 bits)	1.8	1.4
15 (3.90 bits)	2.2	0.3
31 (4.95 bits)	3.0	0.02
63 (5.97 bits)	3.5	0.0066

Table 5.1 shows that the 2 levels quantization scheme is not sensitive to the $V_{ADC}/\sigma_{x,y}$ relationship and the RSME is always 14.2 % and for 31 levels the relationship between quantized and ideal correlation is almost linear. Furthermore, as the number of levels increases the minimum RMSE decreases exponentially (Figure 5.4) and occurs at a higher $V_{ADC}/\sigma_{x,y}$ ratio.

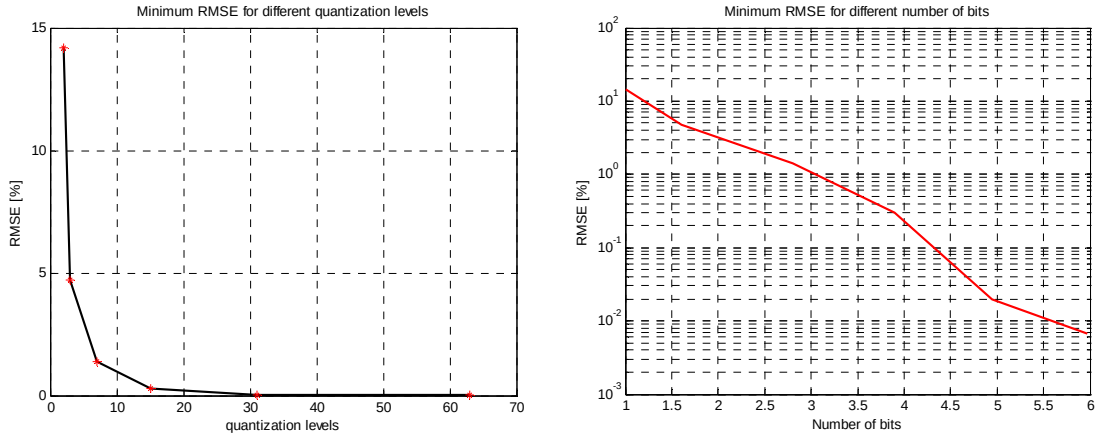

(a) (b)

Figure 5.4 Minimum root mean square errors for different quantization levels, it decreases following an exponential trend, (a) RMSE decreasing in front of the quantization levels, and (b) RMSE in a semi-log axis decreasing in front of the number of bits

Figure 5.5 shows the effect of using different $g(x)$ functions. It compares an equally spaced quantification with a hyperbolic tangent spacing, used to compress the gain.

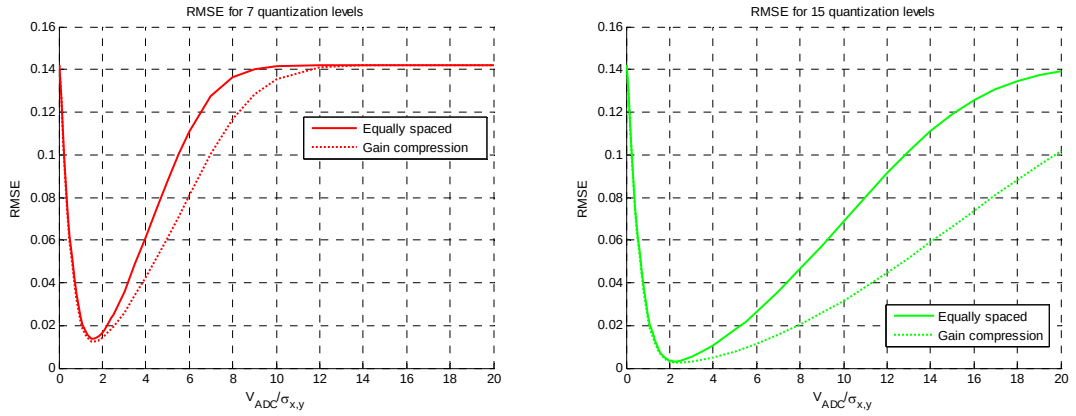

(a) (b)

Figure 5.5 Root mean square error for different levels and different spaced quantification levels, (a) 7 quantification levels, and (b) 15 quantification levels.

In both cases, Figure 5.5a (7 levels) and Figure 5.5b (15 levels), there are no changes in the clipping area, but there are as the $V_{ADC}/\sigma_{x,y}$ ratio increases. The effect is that an ADC with gain compression has lower RMSE than the equally spaced level scheme for a wider area. This is equivalent to increasing the number of quantization levels. An ADC with gain compression can be useful to ensure linearity over a wide range of input signal power, reducing the necessary number of bits. A common radiometric application where a high range of input power is measured is during the T_{hot}- T_{cold} calibration.

5.4 Quantization Impact on the Correlation Spectrum

In [94] some analytically easy-to-solve quantization schemes were analyzed using Taylor series approximations for $\rho<<1$, which applies in the most radio-astronomical measurements, but not necessarily in Earth remote sensing or during the calibration. The correlation spectrum, the frequency power density is spread and distorted due to quantization and clipping. In this work, the spectrum is computed numerically following Eqn. (5.12). So, the analysis can be exhaustive and can include different quantization levels for two input signals for any complexity, gain compression, different bandwidths, and different channel frequency responses. The frequency power density is the Fourier transformation of the cross-correlation function, which is the Wiener-Khinchin theorem (Eqn.(5.14)):

$$S_{xy}(f) \int_{-\infty}^{\infty} R_{xy}(\tau)\, \mathrm{e}^{-\mathrm{j}2\pi\tau f} d\tau = F\{g_1(x(t))\}F\{g_2(x(t))\}^{*}. \tag{5.14}$$

Furthermore, in Eqn. (5.14) there is also shown the relationship of the correlation spectrum with the individual signals spectrum, which is the multiplication of the Fourier transforms of the output signals passed through the quantize functions. By replacing Eqn. (5.4) in Eqn. (5.14) the spectral power density of the non-linear correlation can be readily obtained (Eqn. (5.15)):

$$S_{xy}(f) \int_{-\infty}^{\infty} q[\rho_{xy}(\tau)]\, \mathrm{e}^{-\mathrm{j}2\pi\tau f} d\tau, \tag{5.15}$$

where the function $q[\rho_{xy}(\tau)]$ can be analytically obtained as in Eqn. (5.13) or numerically following Eqn. (5.12).

The effect of the quantization in the cross-correlation spectrum is to decrease and distort it in the pass-band and spread it over the rejected band. Figure 5.6 presents an example of the impact of the quantization on the spectrum computed following Eqn. (5.15). The input signals, x and y, that have been considered for this analysis have a rectangular frequency channel's response with a pass-band bandwidth of 2B and a $V_{ADC}=5\sigma_{x,y}$ relationship for all the quantization schemes.

Figure 5.6a presents the x and y linear cross-correlation on the delay domain and for several quantization levels. The lower the number of levels, the higher the correlation distortion. Figure 5.6b is the corresponding spectrum of Figure 5.6a computed following Eqn. (5.15). As expected, the 2 levels scheme has the highest spectrum distortion, the spectrum spread increases on the rejected band and the pass-band decreases.

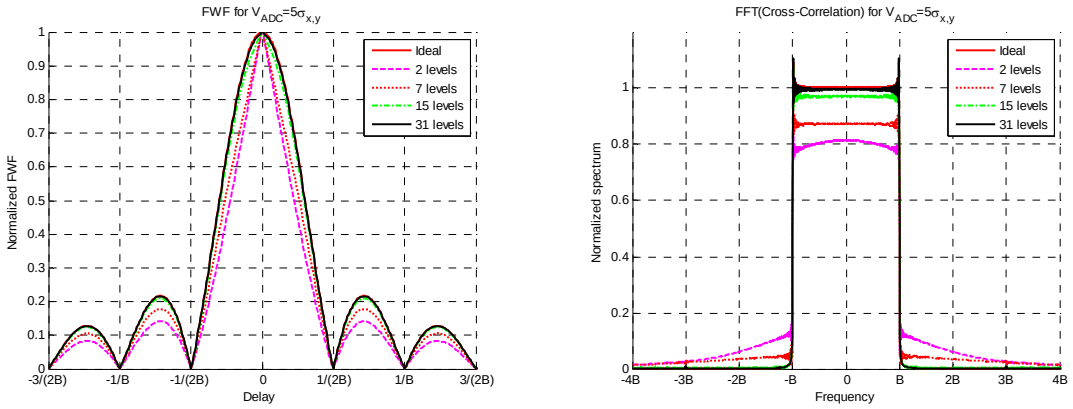

(a) (b)

Figure 5.6 Effect of the quantization on the cross-correlation spectra, (a) ideal cross-correlation ($\rho_{xy}(\tau)$) and cross-correlation for different quantization levels, and (b) their corresponding spectra.

Table 5.2 summarizes these results, the main conclusion is that using $V_{ADC}=5\sigma_{x,y}$ and at least 15 quantization levels it can be assumed that it neither spreads nor distorts the spectrum.

Table 5.2 Summary of the spectrum distortion and spread for $V_{ADC}=5\sigma_{x,y}$ and different quantization schemes.

Levels	Pass-band	Rejected band increase
2 (1 bit)	80 %	13 %
7 (2.8 bits)	87 %	5 %
15 (3.90 bits)	97 %	1.3 %
31 (4.95 bits)	99 %	1 %
Ideal	100 %	0 %

Figure 5.7 analyzes the effect for two different g functions, for 7 quantization levels. It can be appreciated that the compression gain reduces the distortion and the spectrum spread.

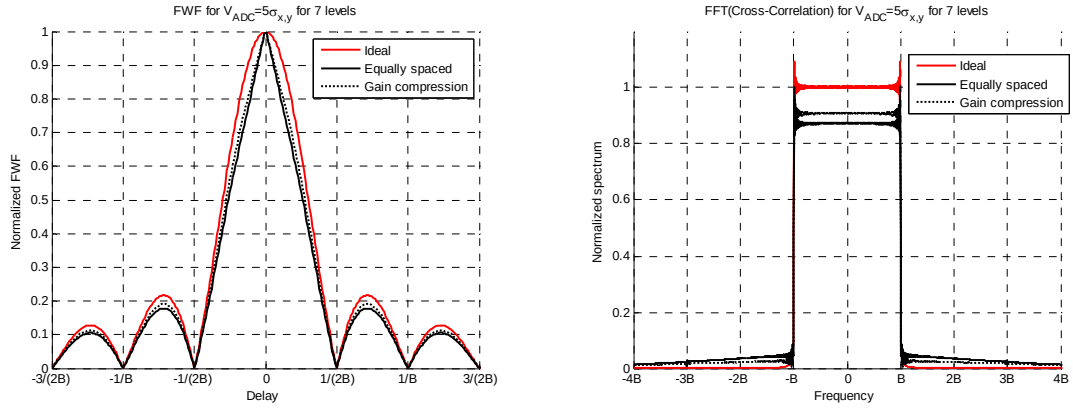

(a) (b)

Figure 5.7 Effect of the quantization on the cross-correlation spectrum, (a) ideal cross-correlation ($\rho_{xy}(\tau)$) and cross-correlation for two different quantization schemes using 7 levels, and (b) presents their corresponding spectra.

In this section, it has been shown that the quantization can be successfully expressed and analyzed as a non-linear transformation. Despite the quantization can affect significantly the value of the correlation of two signals x and y, it is possible to recover the ideal correlation using the non-linear inverse function $q^{-1}[\cdot]$, which can be numerically obtained. Furthermore, for each quantization scheme there is an optimum configuration, in terms of linearity, of the $V_{ADC}/\sigma_{x,y}$ relationship. Furthermore, quantization distorts and spreads the cross-correlation spectrum. Finally, the quantization not only has an impact on the value of the cross-correlation and on the spread of the spectrum, but it increases de variance of the correlation, as it will be shown in the next section.

5.5 Sampling Impact

The main effect of sampling is that it creates replicas of the spectrum. Usually, in a standard digital radiometer topology there is an anti-aliasing filter before the digitization process. Even in this case, the digitization can introduce some alias due to the quantization spectrum spread depending on the sampling frequency (F_s) and baseband bandwidth (B). To understand how this effect impacts on the sampling it is necessary to define the Signal to Noise Ratio (SNR) as (Eqn. (5.16)):

$$\mathrm{SNR} = \frac{\bar{R}_{xy}}{\sigma_{R_{xy}}}, \tag{5.16}$$

where $\bar{R}_{xy}$ is the expected non-linear cross-correlation value, and $\sigma_{R_{xy}}$ is its standard deviation. Moreover, the SNR term is related with the radiometric resolution [85], which is one of the figures of merit of a radiometer. The SNR can decrease due to an increase of the standard deviation of the correlation or due to a decrease of the $\bar{R}_{xy}$, *i.e.* a noise increment on the pass-band (Eqn. (5.2)).

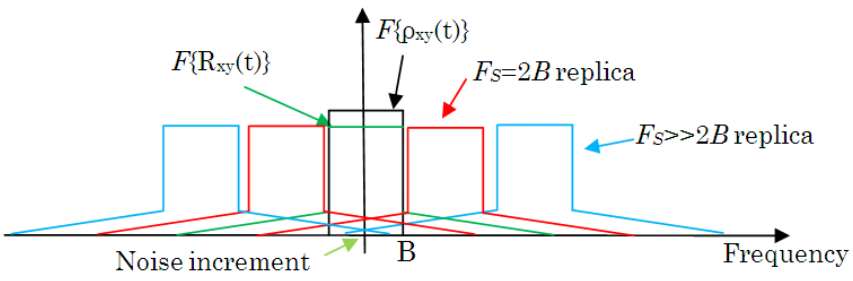

Figure 5.8 Effect of the sampling on the correlation spectrum, ($F\{\}$ stands of Fourier transform). Spectrum of the ideal and the quantized correlation at base band, black and green, respectively. In red, it is the first spectrum replica for the minimum sampling frequency which fulfills the Nyquist criterion (Fs=2B). In blue, it is the first spectrum replica for Fs >>2B.

Figure 5.8 shows an ideal base-band spectrum with an infinite sampling frequency ($F\{\rho_{xy}(\tau)\}$, in black) and a cross-correlation spectrum spread due to quantization ($F\{R_{xy}(\tau)\}$, in green) for different F_s and its replicas. After quantization and sampling, and further cross-correlation of the signals, the quantization tail of the Nyquist's replica (F_s=2B, in red) overlaps the pass-band of the base-band replica, so an extra amount of noise is included in the measurement of $\bar{R}_{xy}$, and the effect is a decrease on the calculated mean value (Eqn. (5.2)). On the other hand, the standard deviation remains constant, but the SNR decreases, which has a large impact when considering sub-Nyquist sampling.

If the sampling frequency increases, then the first replicas (F_s >> 2B, in blue) appear further away from the band-pass replica and the tail effect has less impact than before. This is why when only few quantization levels are used, an increase of the sampling frequency has a significant impact. Even though, it has less impact, when more quantization levels are used.

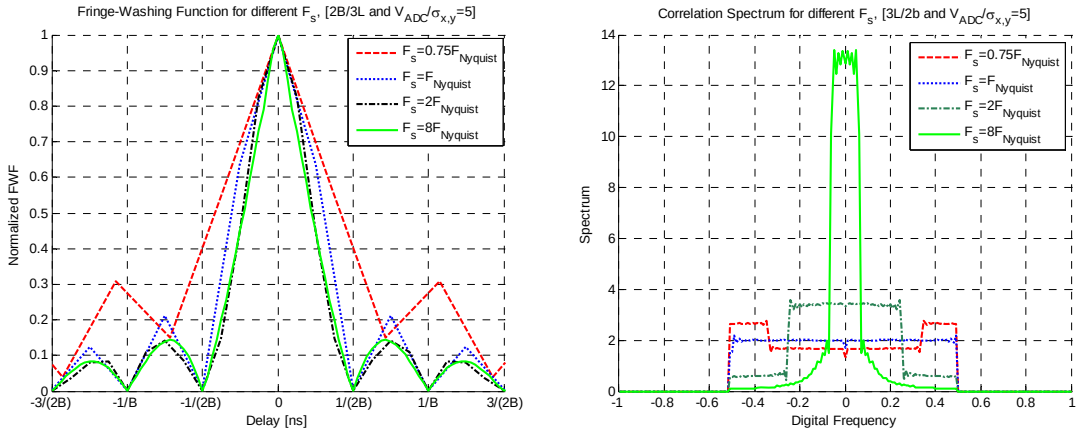

(a) (b)

Figure 5.9 Impact on the quantized correlation of different sampling frequencies. For 2 quantization levels, a bandwidth 2B, and $V_{ADC}=5\sigma_{x,y}$. (a) shows the deformation for the fringe-washing function, and (b) shows the effect on their spectrum.

Figure 5.9 shows the impact on the quantized correlation of different sampling frequencies. The considerations for these plots are a 2 quantization levels scheme, a noise equivalent band-pass bandwidth of 2B, and $V_{ADC}=5\sigma_{x,y}$, taking into account the previous considerations about the spectrum replicas. Figure 5.9a shows the deformation of the fringe washing function considering different sampling rates. The sub-Nyquist sampling (F_s = 0.75 $F_{Nyquist}$) is the one with the deformation more accentuated: it is wider, sharper than the rest of them, and the side lobes are higher. For the exactly Nyquist sampling rate the fringe-washing function is still sharp and wide. For a higher sampling rate (F_s > 2 $F_{Nyquist}$) the function seems to not be affected by the sampling rate. On the other hand, the spectrum in Figure 5.9b is totally distorted in the sub Nyquist sampling rate case, and recovers its original shape as the sampling rate increases.

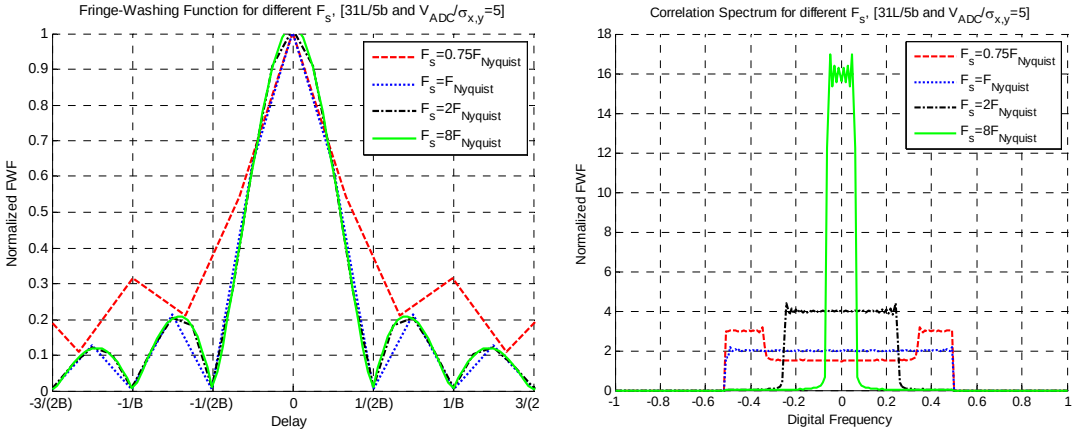

(a) (b)

Figure 5.10 Impact on the quantized correlation of different sampling frequencies. For 31 quantization levels, a bandwidth 2B, and $V_{ADC}=5\sigma_{x,y}$. (a) shows the deformation for the fringe-washing function, and (b) shows the effect on their spectrum.

Figure 5.10 shows the impact on the quantized correlation of different sampling frequencies. The different considerations from the previous analysis are that for these plots there are 31 quantization levels. As this quantization scheme spread less the spectrum than the previous one, it is expected to have better performance for lower sampling rates. Figure 5.10a shows the distortion of the fringe-washing function considering different sampling rates. The sub-Nyquist sampling ($F_s = 0.75\ F_{Nyquist}$) is the one with the more accentuated deformation: it is wider, sharper than the rest of them, and the side lobes are higher. For a larger sampling rate ($F_s \geq F_{Nyquist}$) the function seems to not be affected by the sampling rate. On the other hand, the spectrum in Figure 5.10b is completely distorted in the sub Nyquist sampling rate case, and recovers its original shape as the sampling rate increases. As expected, it has better performance for higher sampling rates.

5.6 Sampling Rate Inaccuracies

In the conversion between digital and analog signals, the sampling frequency is normally assumed to be constant; samples should be converted at regular intervals. Nevertheless, the sampling, clock is prone to interferences, thermal drifts and other effects that can change the oscillating frequency and introduce sampling inaccuracies.

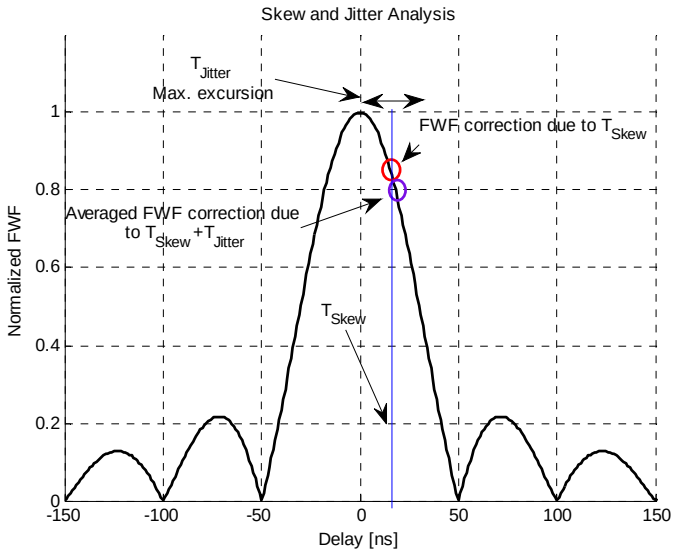

Figure 5.11 Impact of the clock inaccuracies on the correlation value. T_{skew} is the sampling rate offset between x and y, and T_{Jitter} is its fluctuations due to clock inaccuracies.

Figure 5.11 shows the effect of these inaccuracies, that can be summarized into skew (T_{Skew}), which is the delay offset between the sampling time of x and y, and jitter, which is the time fluctuation above the mean value (T_{Jitter}). The impact of the skew is changing the point where the FWF is evaluated and a phase rotation of the correlation coefficient if the working frequency is not exactly zero. Meanwhile, jitter creates a perturbation for each correlation sample around the mean point with zero mean.

A clock skew error not only has an effect on the modulus of the correlation coefficient, but it affects its phase by rotating the real and imaginary parts [104] as it is shown in Eqn. (5.17):

$$\begin{aligned}\langle x(n\mathrm{T}_1)y^*(n\mathrm{T}_2)\rangle &= r_{xy}(\mathrm{T}_1-\mathrm{T}_2)\{[\rho_R\cos\omega_\mathrm{r}(\mathrm{T}_1-\mathrm{T}_2)-\rho_I\sin\omega_\mathrm{r}(\mathrm{T}_1-\mathrm{T}_2)]\\ &+ j[\rho_I\cos\omega_\mathrm{r}(\mathrm{T}_1-\mathrm{T}_2)+\rho_R\sin\omega_\mathrm{r}(\mathrm{T}_1-\mathrm{T}_2)]\},\end{aligned} \tag{5.17}$$

where:

- $\langle x(n\mathrm{T}_1)y^*(n\mathrm{T}_2)\rangle = \rho = \rho_R + j\rho_I$, the correlation coefficient is a complex value with modulus and phase ($\mathrm{j} = \sqrt{-1}$),
- $\omega_\mathrm{r} = 2\pi\frac{f_r}{F_s}$ is the ratio between the residual frequency (f_r) and the sampling frequency, residual digital frequency of the signals, and $F_s = 1/\mathrm{T}_s$,
- $r_{xy}(\mathrm{T}_1-\mathrm{T}_2)$ is the fringe-washing function evaluated at $\mathrm{T}_1-\mathrm{T}_2$, and

- T_1 and T_2 are the sampling periods for the x and y inputs, respectively. Both sampling times are identical except for the skew and jitter effects ($n(T_1 - T_2) = T_{Skew} + T_{Jitter}(t)$).

On the other hand, the jitter is a random variable effect that can be statistically modeled as a polynomial of standard deviation depending on the time ($\sigma_{Jitter} = \sigma_{app} + \sqrt{c_{clk}(n-m)T_s}$), where n and m are two different samples. So that, it can be associated to two different and independent processes ([105]-[106]):

- the aperture jitter, which is related to the random sampling time variations in the ADC caused by thermal noise in the sample&hold circuit. The aperture jitter is commonly modeled as an independent Gaussian variable with zero mean and a standard deviation of $\sigma_{Jitter} = \sigma_{app}$, and

- the clock jitter, which is a feature of the clock generator that feeds the ADC with the clock signal. The clock jitter is modeled as a Wiener process, *i.e.* a continuous-time non-stationary random process with independent Gaussian increments with a standard deviation of $\sigma_{Jitter} = \sqrt{c_{clk}(n-m)T_s}$.

Taking into account a wideband signal in jitter terms (fulfill the inequality $2\pi B\sigma_{Jitter} > 1$). From here, x can be defined using its discrete-time Fourier transformation Eqn. (5.18):

$$x(nT_s + T_{J_n}) = T_s \int_{-F_s/2}^{F_s/2} X(f)\, e^{-j2\pi f(nT_s + T_{Jn})} df, \tag{5.18}$$

where T_{J_n} is the value of the instantaneous jitter. Thence, following Eqn. (5.18) the correlation can be defined again using Eqn. (5.14) and (5.18):

$$R_{xy}(\tau) = \langle x(mT_s) y^*(nT_s + T_{J_{|m-n|}}) \rangle = \tag{5.19}$$
$$= \langle \int_{-F_s/2}^{F_s/2} \left(X(f) Y^*(f) e^{j2\pi f T_{J_{|m-n|}}} \right) e^{-j2\pi f(m-n)T_s} df \rangle,$$

$$R_{xy}(\tau) = \int_{-F_s/2}^{F_s/2} S_{xy}(f) \langle e^{j2\pi f T_{J_{|m-n|}}} \rangle e^{-j2\pi f(m-n)T_s} df, \tag{5.20}$$

where

- $\langle e^{j2\pi f T_{J_{|m-n|}}} \rangle$ is the expected value of the jitter and it depends on the jitter type [105],

- $T_{J_{|m-n|}}$ is the existing jitter between the m^{th} sample of x and the n^{th} sample y, and
- τ is the digital delay between the cross-correlation samples ($\tau = (m-n)T_s$).

Equation (5.21) applies for an aperture jitter and Eqn. (5.22) applies for the clock jitter:

$$\langle e^{j2\pi f T_{Japp_n}} \rangle = e^{2\pi^2 f^2 \sigma_{app}^2}, \text{ and } \langle e^{j2\pi f T_{Japp_{|m-n|}}} \rangle = e^{-2\pi^2 f^2 2\sigma_{app}^2}, \text{ if n}\neq\text{m else 1,} \quad (5.21)$$

$$\langle e^{j2\pi f T_{Jclk_n}} \rangle = e^{2\pi^2 f^2 c_{clk} n T_s}, \text{and } \langle e^{j2\pi f T_{Jclk_{|m-n|}}} \rangle = e^{-2\pi^2 f^2 c_{clk} T_s |m-n|}, \quad (5.22)$$

where c_{clk} is the phase noise constant of the oscillator. Thence, the impact of the aperture jitter to the cross-correlation coefficient is shown in Eqn. 24

$$\begin{aligned} \check{R}_{xy}(\tau) &= \int_{-\infty}^{\infty} S_{xy}(f) e^{-2\pi^2 f^2 \sigma_{\text{jitter}}^2} e^{-j2\pi f\tau} df \\ &= \int_{-\infty}^{\infty} S_{xy}(f) e^{-2\pi^2 f^2 ((2-\delta_x)\sigma_{app}^2 + c_{clk} T_s |m-n|)} e^{-j2\pi f\tau} df \end{aligned} \quad (5.23)$$

$$\check{R}_{xy}(\tau) = R_{xy}(\tau) * \frac{e^{-\frac{\tau^2}{2\sigma_{app}^2}}}{\sqrt{2\pi\sigma_{app}}} * \frac{e^{-\frac{\tau}{2c_{clk}}}}{\sqrt{2\pi c_{clk}\tau}} \quad (5.24)$$

where

- $\check{R}_{xy}(\tau)$ is the cross-correlation coefficient modified by the jitter,
- $R_{xy}(\tau)$ is the cross-correlation coefficient, and
- * denotes the convolution operator,

From Eqn. (5.22) it can be inferred that the aperture jitter does not depend on the sampling rate and it has a low pass filter effect on the correlation spectrum with its cut frequency depends on σ_{app}. Particularizing Eqn. (5.24) in the case of having a rectangular spectrum, then Eqn. (5.24) becomes Eqn. (5.25), and the cross-correlation function is multiplied by an erf(x) function ($\text{erf}(x) = \frac{2}{\sqrt{\pi}} \int_0^x e^{-t^2} dt$).

$$\check{R}_{xy}(\tau) = \int_{-B/2}^{B/2} \sigma_x \sigma_y \rho(\tau) e^{-2\pi^2 f^2 (2-\delta_x)\sigma_{app}^2} e^{-j2\pi f\tau} df = R_{xy}(\tau) \frac{\text{erf}\left(\frac{\pi}{\sqrt{2}} B\sigma_{app}\right)}{\sqrt{2\pi\sigma_{app}}}, \quad (5.25)$$

As it can be seen, in the case of aperture jitter the coherence loss ratio (Eqn.(5.20)) is independent of the number of sampling points N (therefore of the integration block length T_sN), while in the case of clock jitter it strongly depends on it (Eqn.(5.21)).

5.7 Analysis of the Cross-Correlation Variance due to the Digitization

In the previous sections, the quantization and the sampling have been analyzed as the impact on the retrieved value of the correlation. In this section, the variances are analyzed taking into account both effects, quantization and sampling. In a general case, the output of a correlator of two quantized and sampled signals after averaging N_q samples is defined as:

$$R_{xy}(\tau) = \frac{1}{N_q}\sum_{n=1}^{N_q} g_1\left(x(n\mathrm{T_s})\right)g_2^*(y(m\mathrm{T_s})), \tag{5.26}$$

where:

- T_s is the sampling period for the x and y inputs, respectively. In most of the applications both sampling times are identical except for skew and jitter effects ($\mathrm{n}(\mathrm{T}_1 - \mathrm{T}_2) = \mathrm{T}_{\mathrm{Skew}} + \mathrm{T}_{\mathrm{Jitter}}(t)$), for simplicity but without loss of generality, skew and jitter can be simulated as well), and
- $g_{1,2}$ are defined in Eqn. (5.3).

Obviously, the product of a pair of samples of $p_{|m-n|} = g_1(x(n\mathrm{T}_s))g_2^*(y(m\mathrm{T}_s)$ in Eqn. (5.26) does not follow a Gaussian pdf. Rather, the distribution of $p_{|m-n|}$ follows a Rayleigh pdf when the g functions are linear (no quantization). In a more general case, having non-linear $g_{1,2}$ functions, the distribution of $p_{|m-n|}$ follows different trends depending on the quantization scheme. However, the average of many of these products, over a large number of pairs of samples, approaches a Gaussian pdf, as implied by the central limit theorem. The variance of the correlator output is calculated as in Eqn. (5.27):

$$\sigma_{R_{xy}}^2 = \langle R_{xy}R_{xy}^*\rangle - \langle R_{xy}\rangle^2 \tag{5.27}$$

where the first term of this summation is expanded as (Eqn.(5.28)):

$$\langle R_{xy}R_{xy}^{*}\rangle = \frac{1}{N_q^2}\sum_{n=1}^{N_q}\sum_{m=1}^{N_q}\langle g_1(x(nT_s))g_2^{*}(y(mT_s))g_1^{*}(x(nT_s))g_2(y(mT_s))\rangle. \tag{5.28}$$

Thence, Eqn. (5.28) is split in two parts, the first one takes only into account the elements which have the same n and m time indexes, and a second part, the rest of the Eqn. (5.28):

$$\langle R_{xy}R_{xy}^{*}\rangle = \frac{1}{N_q^2}\left\{\begin{array}{l}\displaystyle\sum_{n=1}^{N_q}\langle g_1(x(nT_s))g_2^{*}(y(nT_s))g_1^{*}(x(nT_s))g_2(y(nT_s))\rangle + \\ \displaystyle\sum_{n=1}^{N_q}\sum_{\substack{m=1\\ m\neq n}}^{N_q}\langle g_1(x(nT_s))g_2^{*}(y(nT_s))g_1^{*}(x(mT_s))g_2(y(mT_s))\rangle\end{array}\right\}, \tag{5.29}$$

the first term of Eqn. (5.29) can be computed using the properties of the fourth and second statistical moments relationship for zero mean Gaussian random variables [72], as follows:

$$\begin{aligned}\langle g_1(x(nT_s))g_2^{*}(y(nT_s))g_1^{*}(x(nT_s))g_2(y(nT_s))\rangle &= \\ &= \left\{\begin{array}{l}\langle g_1(x(nT_s))g_1^{*}(x(nT_s))\rangle\langle g_2^{*}(y(nT_s))g_2(y(nT_s))\rangle \\ +\langle g_1(x(nT_s))g_2^{*}(y(nT_s))\rangle\langle g_1^{*}(x(nT_s))g_2(y(nT_s))\rangle\end{array}\right\} = \\ &= \sigma_{g_1(x)}^2\sigma_{g_2(y)}^2 + \left|q\left[\rho_{xy}(0)\right]\right|^2\sigma_{g_1(x)}^2\sigma_{g_2(y)}^2 \\ &= \sigma_{g_1(x)}^2\sigma_{g_2(y)}^2\left(1 + \left|q\left[\rho_{xy}(0)\right]\right|^2\right),\end{aligned} \tag{5.30}$$

where:

- $\sigma_{g_1(x)}^2$and $\sigma_{g_2(y)}^2$are the variances of $g_1(x)$ and $g_2(y)$, respectively, and
- $\left|q\left[\rho_{xy}(0)\right]\right|$ is the modulus of the correlation coefficient of the input signals after the non-linear manipulation.

The second term in Eqn. (5.30) can be expanded using the same statistical moments' relationship:

$$\frac{1}{N_q^2}\sum_{n=1}^{N_q}\sum_{\substack{m=1\\m\neq n}}^{N_q}\langle g_1(x(nT_s))g_2^*(y(nT_s))g_1^*(x(mT_s))g_2(y(mT_s))\rangle = \tag{5.31}$$

$$= \left\{\begin{array}{l} \dfrac{N_q-1}{N_q^2}\displaystyle\sum_{n=1}^{N_q}\langle g_1(x(nT_s))g_1^*(x(mT_s))\rangle\langle g_2^*(y(nT_s))g_2(y(mT_s))\rangle \\ +\dfrac{1}{N_q^2}\displaystyle\sum_{n=1}^{N_q}\sum_{\substack{m=1\\m\neq n}}^{N_q}\langle g_1(x(nT_s))g_2^*(y(nT_s))\rangle\langle g_1^*(x(mT_s))g_2(y(mT_s))\rangle \end{array}\right\}$$

$$= \frac{N_q-1}{N_q}\left|q[\rho_{xy}(0)]\right|^2\sigma_{g_1(x)}^2\sigma_{g_2(y)}^2 + \frac{2}{N_q^2}\sum_{n=1}^{N_q}(N_q-n)\,R_{xx}(nT_s)R_{yy}(nT_s),$$

where:

- $R_{xx}(nT_s)$ and $R_{yy}(nT_s)$ are the auto-correlation of the $g_1(x)$ and $g_2(y)$, respectively taking into account all the samples between sample 1 and the N_q, as in Eqn. (5.12).

The first part of the variance of the correlation is obtained by combining the results obtained in Eqns. (5.30) and (5.31):

$$\langle R_{xy}R_{xy}^*\rangle = \tag{5.32}$$

$$= \left\{\begin{array}{c} \dfrac{\sigma_{g_1(x)}^2\sigma_{g_2(y)}^2}{N_q}\left(1+\left|q[\rho_{xy}(0)]\right|^2\right)+ \\ \dfrac{N_q-1}{N_q}\left|q[\rho_{xy}(0)]\right|^2\sigma_{g_1(x)}^2\sigma_{g_2(y)}^2 + \dfrac{2}{N_q^2}\displaystyle\sum_{n=1}^{N_q}(N_q-n)\,R_{xx}(nT_s)R_{yy}(nT_s) \end{array}\right\}$$

$$= \frac{\sigma_{g_1(x)}^2\sigma_{g_2(y)}^2}{N_q} + \frac{2}{N_q^2}\sum_{n=1}^{N_q}(N_q-n)\,R_{xx}(nT_s)R_{yy}(nT_s) + \left|q[\rho_{xy}(0)]\right|^2\sigma_{g_1(x)}^2\sigma_{g_2(y)}^2$$

Finally, the value of the variance of the N_q samples averaged correlation is given by:

$$\sigma_{\hat{R}_{xy}}^2 = \frac{\sigma_{g_1(x)}^2\sigma_{g_2(y)}^2}{N_q} + \frac{2}{N_q^2}\sum_{n=1}^{N_q}(N_q-n)\,R_{xx}(nT_s)R_{yy}(nT_s), \tag{5.33}$$

and arranging Eqn. 23, the variance appears in its usual form, as it is known in the literature [101]:

$$\sigma_{\hat{R}_{xy}}^2 = \frac{\sigma_p^2}{N_q} + \frac{2}{N_q^2}\sum_{n=1}^{N_q}\left(N_q - n\right) R_{xx}(n\mathrm{T}_s)R_{yy}(n\mathrm{T}_s) \tag{5.34}$$

where, $\sigma_p^2 = \sigma_{g_1(x)}^2\sigma_{g_2(y)}^2$ and it is the variance for each sample of the correlation ($N_q = 1$).

Following Eqn. 25, Figure 5.12 shows the evolution of $\sigma_{\hat{R}_{xy}}^2$ with the integration time. The signals considered on these plots have a noise equivalent squared bandwidth of pass-band of $2B$, $\rho_{xy}(0) = 1$, and $V_{ADC}=5\sigma_{x,y}$. Figure 5.12a shows the results for the 3 quantization levels, all the curves converge to zero asymptotically. The F_s=0.75 $F_{Nyquist}$ curve is the one which converges faster, because its samples are uncorrelated among them. For a given number of averaged samples, the variance of the quantized correlation increases with the sampling rate, because successive samples are more and more correlated. Recall that, these plots are in number of averaged samples, not in integration time units. Obviously, for a given integration time, the plot with the highest sample rate has the lowest $\sigma_{\hat{R}_{xy}}^2$, it has had time to average more samples despite that for a given number of samples gives the worst performance.

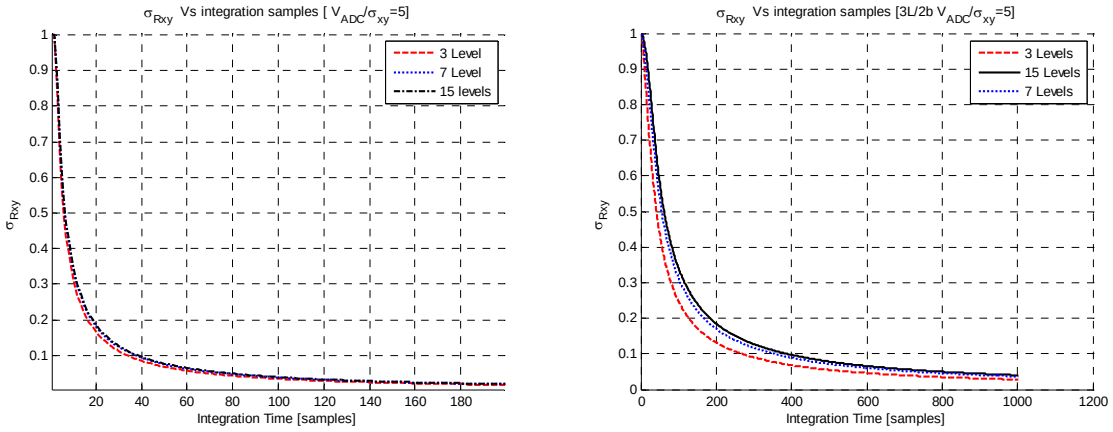

(a) (b)

Figure 5.12 Impact of the number of averaged samples on the $\sigma_{\hat{R}_{xy}}^2$, (a) shows impact for a 3 level quantization scheme and different sampling rate, and (b) shows a constant sampling rate changing the number of quantization levels.

In Figure 5.12b the sampling rate has been frozen to F_s=$F_{Nyquist}$ and two quantization schemes has been analyzed (3 and 15 levels). The 3 levels curve converges more quickly to zero than the 15 levels curve. This is because the fringe washing function is shaper due to the higher non-linear distortion in 3 levels than in the 15 levels quantization. This effect of sharpness is equivalent to have more uncorrelated samples. Despite the mean of the correlation is lower for the 3 level that the 15 level quantizations, the variance of the correlation is also lower in this case.

5.8 Conclusions

The impact of a general quantization scheme has been expressed and analyzed as a non-linear transformation. Despite the quantization can significantly affect the value of the ideal cross-correlation (ρ_{xy}), it is possible to recover the ideal correlation (ρ_{xy}) from the measured one (R_{xy}) using the inverse function $\rho_{xy} = q^{-1}[R_{xy}]$, which can be always numerically obtained. It has been found that for each quantization scheme there is an optimum configuration of the $V_{ADC}/\sigma_{x,y}$ relationship for which the linearity with respect the ideal correlation is minimized. Furthermore, quantization distorts and spreads the cross-correlation spectrum, decreasing the resolution.

Sampling also affects the spectrum of the cross-correlation function, and depending on the sampling rate, replicas of the spectrum can overlap the main spectrum. This can be due to a sampling rate below the Nyquist rate or, even above the Nyquist rate, due to the non-linear quantization process which spreads the spectrum. In both cases, there is an impact on the SNR, and so on the radiometric resolution. Other sampling effects have been analyzes such as the clock inaccuracies: skew and jitter.

Finally, the impact of both effects, quantization and sampling, on the variance of the measurements is studied. It has been found that it strongly depends on the relationship between the bandwidth of the cross-correlation and the sampling rate. As the sampling rate increases, the successive samples are more correlated, so they add less new information to the measurement and the variance decreases slowly.

Chapter 6

6 ANALYSIS OF THE PAU-RAD INSTRUMENT

After analyzing the digital beamformer insights in Chapter 4 and the quantization and sampling impacts, in Chapter 5, this chapter is devoted to the analysis of the PAU-RAD instrument. These analyses are a previous step to build the system. Hence, some preliminary studies are necessary, starting with a general overview of the instrument giving its basic requirements.

Moreover, following this line, in this chapter an explanation of the PAU-RAD radiometer concept is given including not only the novelty of the digital beamforming system, but a new type of topology which is presented and analyzed using noise waves.

Then, some basic concepts of the DBF are included in this part for convenience and to clarify the main concepts which are used in the next section, where the Stokes parameters and the radiometric systems resolution are theoretically derived. This part is analyzed from a theoretical point of view, and also taking into account the impact of the hardware constrictions.

6.1 PAU-RAD Instrument Overview

PAU-RAD is a full-polarimetric 4x4 element array with real-time digital beamforming (DBF) radiometer. The main design requirements related with the antenna are to have a 20º half-power beamwidth, to have a main beam efficiency (MBE) larger than 90%, and the system has to be able to vertically steer angles up to ±20º from the boresight direction, which will be pointed 45º off nadir to cover the range of incidence angles from 25º to 65º. As the system requirement specifies that the beam has to be steerable along the vertical axis direction, the antennas are analog combined by rows (horizontal axis) and the DBF is created following columns (vertical axis) (Figure 6.1).

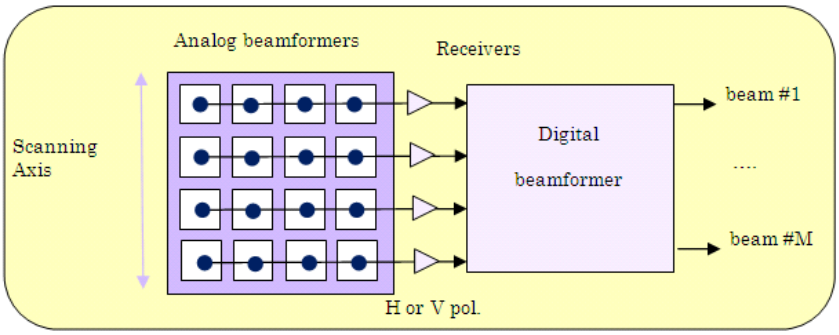

Figure 6.1 Sketch of the PAU-RAD array antenna configuration. The system has digital beamforming capabilities in the vertical direction, and signals are analog combined by rows.

Each combiner has its own receiver that down-converts the Radio Frequency (RF) signal to an Intermediate Frequency (IF) signal. Once all signals are at IF, they are digitalized and processed in a Field Programmable Gate Array (FPGA). In the FPGA, signals are amplitude and phase equalized and then processed in order to calculate the four Stokes parameters.

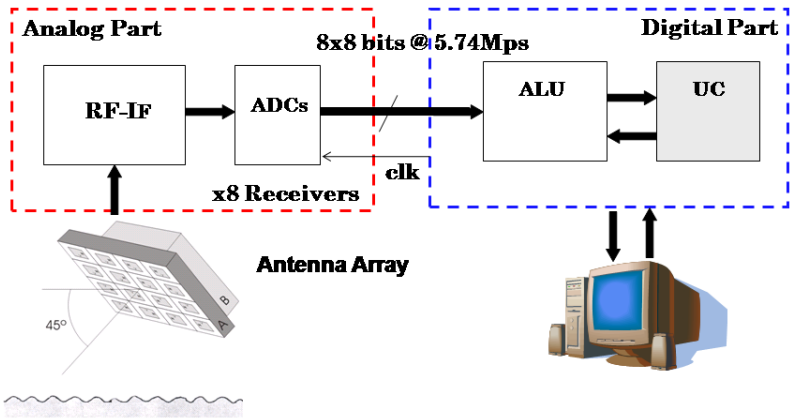

Figure 6.2 PAU-RAD instrument block diagram.

As stated, PAU-RAD (Figure 6.2) has an analog part, where the signal is received, amplified and partially down-converted, and a digital part (FPGA) where the

digital radiometer is embedded. The analog part consists of 8 (4 receivers x 2 polarizations times) commercial GPS L1 frequency (1.57542 GHz) down-converters with a bandwidth of 2.2 MHz (Zarlink GP2015 [107]). Each receiver has its own local oscillator driven by a master clock at 10 MHz. Hence, it can be assumed that each receiver's Phase-Locked Loop (PLL) has a fixed, but possibly slowly varying, random phase variable uniformly distributed within $[0-2\pi)$. In addition, each receiver has a nominal gain that has been characterized by a Gaussian random variable with a standard deviation of 1 dB. Furthermore, component tolerances, aging and thermal drifts can affect the nominal gain. These phase and gain disagreements between receivers have to be equalized in the digital part, before the synthesis of the beams.

The digital part has been coded using the Very High Speed Integrated Circuit (VHSIC) Hardware Description Language 93 (VHDL-93) [108] and embedded into an FPGA. The digital design has been split in two parts for an easier implementation. One of the digital blocks is the so-called Control Unit (CU) that manages the system. The other block is the so-called Arithmetic-Logic Unit (ALU) where the four Stokes parameters are obtained with the highest achievable accuracy. In general, the main tasks to be accomplished in real time for the digital part can be summarized as follows:

- I/Q demodulation of 16 input signals from IF to base-band,
- automatic gain equalization (within ±1 dB), and also ,
- automatic phase equalization between receivers (within the range 0 to 2π),
- implementation of a digital beamformer with the 4x4 element array in order to be able to steer the beam up to ±20º from boresight in 5º steps,
- computation of the four Stokes parameters using correlation techniques,
- estimation and cancellation of signal offsets by a dedicated circuit, and
- the system re-configurability to optimize the integration and calibration times, and the inter-calibration period depending on the scene and application.

6.2 PAU-RAD Radiometer Concept

PAU-RAD radiometer differs from other radiometers in the fact that it has been conceived to share its front-end with a GPS reflectometer [32]. So that, a new radiometer topology was developed to fulfill the reflectometric specifications, not to chop the signal and be able to track the GPS signal, without diminishing the radiometric resolution. The PAU-RAD concept is somehow inspired on the Plank

radiometer architecture, shown in Figure 6.3 [5]. It consists of two 180º hybrids in cascade with two amplifiers and receiving chains. The first hybrid it is connected to an antenna and to a reference load.

Both signals, antenna and load reference, are added in an analog way at the output of the first hybrid, the upper branch the signals are added in phase and the lower branch signals are added 180º out of phase. The second hybrid inputs are the first hybrid outputs and its outputs are one signal proportional to the antenna signal and the other proportional to the reference load. Signals are continuously acquired as in a total power radiometer. Moreover, the reference load signal gives immunity to receiver's thermal noise and gain compensation, as in a Dicke radiometer.

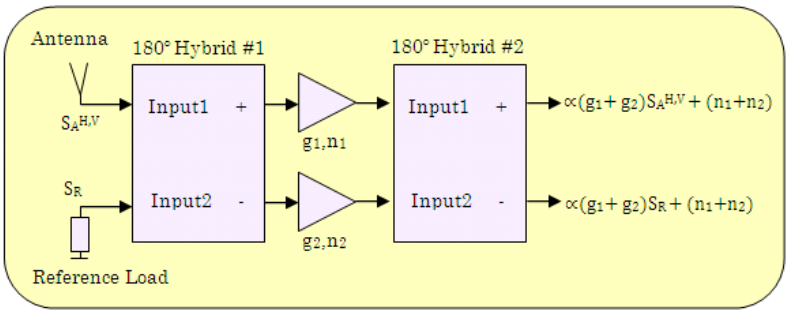

Figure 6.3 First approximation to PAU radiometer theoretical diagram.

The block diagram of PAU-RAD is shown in Figure 6.4. Instead of using a hybrid, it uses a Wilkinson power splitter which divides the antenna signal in two (S_A) and the Wilkinson's load replaces the reference load ($\pm S_w$). The internal load generates 180º out of phase noise at the power splitter outputs having the same result as at the first hybrid output in Figure 6.3, and then these signals are correlated. An advantage from this architecture is that it does not requires a perfect matching of the amplifiers output since PAU-RAD system allows gain and phase equalization.

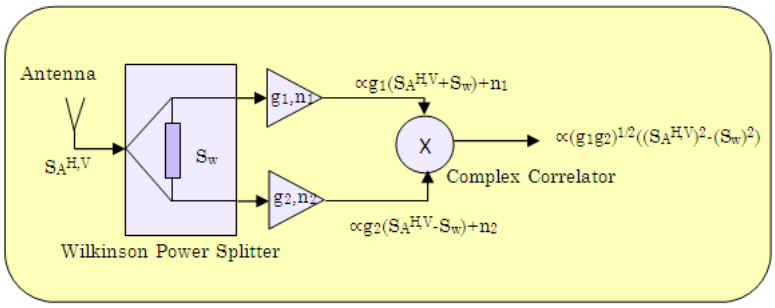

Figure 6.4 PAU-RAD conceptual diagram.

In the followings sections, this diagram is extended to an array with digital beamforming with full polarimetric capabilities in order to compute the four Stokes parameters. Therefore, the antenna must be a dual-polarization one with two receiving chains connected at its outputs, one for the horizontal polarization and the other for the vertical.

6.3 Noise Wave Analysis for a Single Element

In order to understand the operation of the PAU-RAD concept, the analysis of a single receiver element is performed using noise waves. Then, results are extended for the general case of an array of M receiver elements and performing digital beamforming [32].

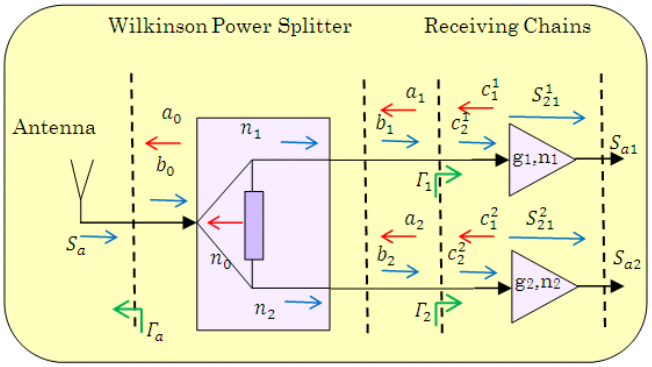

Figure 6.5 Noise wave analysis of the PAU-RAD.

A linear N-port can be represented by its N×N scattering matrix ($\bar{\bar{S}}$) and by an N×1 noise vector ($\bar{n}$) that accounts for the noise waves generated internally [109]:

$$\bar{b} = \bar{\bar{S}}\bar{a} + \bar{n}, \tag{6.1}$$

where $\bar{a}$ and $\bar{b}$ are the usual incident and outgoing N×1 wave vectors defined over a 1 Hz bandwidth. The incident wave vector can also be written as [110]:

$$\bar{a} = \bar{\bar{\Gamma}}\bar{b} + \bar{a}_s, \tag{6.2}$$

where $\bar{a}_s$ is the vector of source waves connected to each of the N ports. In our case (Figure 6.5):

$$\bar{a}_s = \begin{bmatrix} S_{\mathrm{A}} \\ c_1^1 \\ c_1^2 \end{bmatrix}, \tag{6.3}$$

whose elements are S_{A}, which is the noise collected by the antenna from the outside plus the one internally generated because of its Ohmic losses, and c_1^{i} which the noise wave generated by the i^{th} receiving chain towards the input.

On the other hand $\bar{\bar{\Gamma}}$ is an N×N diagonal matrix whose elements are the reflection coefficients of each of the ports as seen from the network (Figure 6.5, the antenna and the two receiving chains):

$$\bar{\bar{\Gamma}} = \begin{bmatrix} \Gamma_A & 0 & 0 \\ 0 & \Gamma_1 & 0 \\ 0 & 0 & \Gamma_2 \end{bmatrix}. \tag{6.4}$$

Substituting Eqn. (6.1) in (6.2) and isolating $\bar{b}$, the following expression is readily obtained:

$$\bar{b} = \bar{\bar{\Lambda}}\bar{\bar{S}}\bar{a}_s + \bar{\bar{\Lambda}}\bar{n}, \tag{6.5}$$

and defining:

$$\bar{\bar{\Lambda}} \triangleq (\bar{\bar{I}} - \bar{\bar{S}}\bar{\bar{\Gamma}})^{-1}. \tag{6.6}$$

Finally, to take into account the equivalent noise waves $\bar{c}$ (Figure 6.5) at the amplifiers' input, the $\bar{b}'$ vector is defined:

$$\bar{b}' = \bar{b} + \bar{c}, \tag{6.7}$$

in which $\bar{c}$ is defined as:

$$\bar{c} = \begin{bmatrix} 0 \\ c_2^1 \\ c_2^1 \end{bmatrix}. \tag{6.8}$$

The radiometer's output is the correlation of the noise waves at the receivers' output:

$$\langle S_{A1} S_{A2} \rangle = S_{21}^1 S_{21}^{2*} \langle \bar{b}_1' \bar{b}_2'^* \rangle, \tag{6.9}$$

where S_{21}^i is the S_{21} parameter of the i^{th} receiving chain and can be identified as the amplitude and phase of the chains. In order to compute Eqn. (6.9) the correlation matrix $\bar{\bar{N}}$ of vector $\bar{b}'$ must be first computed:

$$\begin{aligned} \bar{\bar{N}} = \langle \bar{b}' \bar{b}'^H \rangle = \langle (\bar{\bar{\Lambda}}\bar{\bar{S}}\bar{a}_s + \bar{\bar{\Lambda}}\bar{n} + \bar{c})(\bar{\bar{\Lambda}}\bar{\bar{S}}\bar{a}_s + \bar{\bar{\Lambda}}\bar{n} + \bar{c})^H \rangle = \bar{\bar{\Lambda}}\bar{\bar{S}} \langle \bar{a}_s \bar{a}_s^H \rangle \bar{\bar{S}}^H \bar{\bar{\Lambda}}^H + \\ + \bar{\bar{\Lambda}}\bar{\bar{S}} \langle \bar{a}_s \bar{c}^H \rangle + \bar{\bar{\Lambda}} \langle \bar{n}\bar{n}^H \rangle \bar{\bar{\Lambda}}^H + \langle \bar{c}\bar{a}_s^H \rangle \bar{\bar{S}}^H \bar{\bar{\Lambda}}^H + \langle \bar{c}\bar{c}^H \rangle. \end{aligned} \tag{6.10}$$

In evaluating Eqn. (6.10), the correlation matrices of the different signals involved must first computed. The noise matrix of the incoming noise waves is a diagonal one, since the noise coming from the antenna, and the noise waves generated by the receivers towards the input are uncorrelated:

$$\langle \bar{a}_s \bar{a}_s^H \rangle = k_B \begin{bmatrix} \mathrm{T_A} & 0 & 0 \\ 0 & \mathrm{T_{r1}} & 0 \\ 0 & 0 & \mathrm{T_{r2}} \end{bmatrix}. \tag{6.11}$$

And in a similar way:

$$\langle \bar{a}_s \bar{c}^H \rangle = \begin{bmatrix} S_\mathrm{A} \\ c_1^1 \\ c_1^2 \end{bmatrix} [0 \quad c_2^{1*} \quad c_2^{1*}] = k_B \begin{bmatrix} 0 & 0 & 0 \\ 0 & \mathrm{T_{c1}} & 0 \\ 0 & 0 & \mathrm{T_{c1}} \end{bmatrix}, \tag{6.12}$$

$$\langle \bar{c} \bar{a}_s^H \rangle = \begin{bmatrix} 0 \\ c_2^1 \\ c_2^2 \end{bmatrix} [S_a^* \quad c_1^{1*} \quad c_1^{1*}] = k_B \begin{bmatrix} 0 & 0 & 0 \\ 0 & \mathrm{T_{c1}^*} & 0 \\ 0 & 0 & \mathrm{T_{c2}^*} \end{bmatrix}, \tag{6.13}$$

$$\langle \bar{c} \bar{c}^H \rangle = \begin{bmatrix} 0 \\ c_2^1 \\ c_2^2 \end{bmatrix} [0 \quad c_2^{1*} \quad c_2^{1*}] = k_B \begin{bmatrix} 0 & 0 & 0 \\ 0 & \mathrm{T_{R1}} & 0 \\ 0 & 0 & \mathrm{T_{R2}} \end{bmatrix}, \tag{6.14}$$

and [109]:

$$\langle \bar{n} \bar{n}^H \rangle = k_B \mathrm{T_w} \left(\bar{\bar{I}} - \bar{\bar{S}} \bar{\bar{S}}^H \right). \tag{6.15}$$

In the previous equations: k_B is the Boltmann's constant, $\mathrm{T_A}$ is the antenna temperature at a given polarization, $\mathrm{T_w}$ is the temperature of the Wilkinson power splitter, $\mathrm{T_{ri}}$, $\mathrm{T_{ci}}$, and $\mathrm{T_{Ri}}$ are the three receiver equivalent noise temperatures defined in [103], and $\mathrm{T_{Ri}}$ are the receivers' noise temperatures with the standard definition for zero reflection coefficient [109]. Substituting Eqns. (6.11)-(6.15) in Eqn. (6.10):

$$\begin{aligned} \bar{\bar{N}} = k_B \Bigg\{ & \bar{\bar{\Lambda}} \bar{\bar{S}} \begin{bmatrix} \mathrm{T_A} & 0 & 0 \\ 0 & \mathrm{T_{r1}} & 0 \\ 0 & 0 & \mathrm{T_{r2}} \end{bmatrix} \bar{\bar{S}}^{\mathrm{H}} \bar{\bar{\Lambda}}^{\mathrm{H}} + \begin{bmatrix} 0 & 0 & 0 \\ 0 & \mathrm{T_{R1}} & 0 \\ 0 & 0 & \mathrm{T_{R2}} \end{bmatrix} + \bar{\bar{\Lambda}} \mathrm{T_w} (\bar{\bar{I}} - \bar{\bar{S}} \bar{\bar{S}}^H) \bar{\bar{\Lambda}}^{\mathrm{H}} \\ & + \bar{\bar{\Lambda}} \bar{\bar{S}} \begin{bmatrix} 0 & 0 & 0 \\ 0 & \mathrm{T_{c1}} & 0 \\ 0 & 0 & \mathrm{T_{c1}} \end{bmatrix} + \begin{bmatrix} 0 & 0 & 0 \\ 0 & \mathrm{T_{c1}^*} & 0 \\ 0 & 0 & \mathrm{T_{c2}^*} \end{bmatrix} \bar{\bar{S}}^{\mathrm{H}} \bar{\bar{\Lambda}}^{\mathrm{H}} \Bigg\}. \end{aligned} \tag{6.16}$$

The first term in Eqn. (6.16) contains the radiometer's output correlation from the input noise (the one collected by the antenna and generated by the antenna losses). The second term contains the noise generated by each receiver that appears at their outputs. Since these noise waves are uncorrelated among the different amplifiers, the second matrix is diagonal. The third term contains the noise generated by the power divider network. Note that this term will vanish if this network unitary ($\bar{\bar{I}} = \bar{\bar{S}} \bar{\bar{S}}^H$), which is not the case for a Wilkinson power divider since ideally $S_{12} = S_{21} = 0$. Finally, the fourth and fifth terms contain the

radiometers' output generated by the outgoing noise that enters in the power divider and leaks into the other output port due to the finite isolation. The radiometer's output can be computed as:

$$\langle S_{A1} S_{A2} \rangle = S_{21}^{1} S_{21}^{2*} \overline{\overline{N}}_{2,3}. \tag{6.17}$$

In the general case, the expansion of Eqns. (6.16) and (6.17) is quite cumbersome, and even though Eqn. (6.17) can be developed analytically, the physical meaning is lost. In order to gain insight in the process, several particular cases of interest are studied below:

- Perfect matching of the antenna and receivers' input ports $\Gamma_A = \Gamma_1 = \Gamma_2 = 0$:

$$\begin{aligned}\langle S_{A1} S_{A2} \rangle = S_{21}^{1} S_{21}^{2*} \overline{\overline{N}}_{2,3} == S_{21}^{1} S_{21}^{2*} k_B \{ S_{10} S_{20}^{*} \mathrm{T_A} + S_{11} S_{21}^{*} \mathrm{T_{r1}} + S_{12} S_{22}^{*} \mathrm{T_{r2}} + S_{12} \mathrm{T_{c2}} + \\ S_{21}^{*} \mathrm{T_{c1}} - \mathrm{T_w} (S_{10} S_{20}^{*} + S_{11} S_{21}^{*} + S_{12} S_{22}^{*}) \},\end{aligned} \tag{6.18}$$

where the second and third terms correspond to outputs originated by reflections of the outgoing noise waves from the receiving chains in the Wilkinson power divider output ports. The fourth and fifth terms correspond to correlations between the outgoing noise waves from the receiving chains that leak through the power divider and enter into the other chain,

- perfect matching of the antenna and receivers' input ports $\Gamma_A = \Gamma_1 = \Gamma_2 = 0$, and of the Wilkinson power divider $S_{00} = S_{11} = S_{22} = 0$. Equation (6.18) now simplifies to:

$$\langle S_{A1} S_{A2} \rangle = S_{21}^{1} S_{21}^{2*} \overline{\overline{N}}_{2,3} = S_{21}^{1} S_{21}^{2*} k_B \{ S_{10} S_{20}^{*} (\mathrm{T_A} - \mathrm{T_w}) + S_{12} \mathrm{T_{c2}} + S_{21}^{*} \mathrm{T_{c1}} \}, \tag{6.19}$$

and

- perfect matching of the antenna and receivers' input ports $\Gamma_A = \Gamma_1 = \Gamma_2 = 0$, and of the Wilkinson power divider $S_{00} = S_{11} = S_{22} = 0$, and perfect isolation of its outputs $S_{12} = S_{21} = 0$. Equation (6.19) reduces to the quasi-ideal case:

$$\langle S_{A1} S_{A2} \rangle = S_{21}^{1} S_{21}^{2*} \overline{\overline{N}}_{2,3} = S_{21}^{1} S_{21}^{2*} S_{10} S_{20}^{*} k_B (\mathrm{T_A} - \mathrm{T_w}) \tag{6.20}$$

Note that:

- The radiometer's output is proportional to the difference between the antenna temperature, and the physical temperature of the antenna and Wilkinson power divider, as in a Dicke radiometer, but without the input switch.

- If not calibrated (Eqn. (6.19)), the former equations contain a term which is proportional to $\mathrm{T_A} - \mathrm{T_w}$ and an offset term that depends on the receiving chains

noise temperatures. This offset can be cancelled by injection of correlated noise and by subtracting the two measured cross-correlations.

- If channels are not equalized ($S_{21}^{1}S_{10} \neq S_{21}^{2}S_{20}$), Eqn.(6.20) can be a complex number due to imperfect mismatch of the two receiving chains and of the Wilkinson power divider. This error is corrected by the injection of correlated noise and compensation of the phase and amplitude of the raw cross-correlation Eqn. (6.20).

- As compared to the Plank radiometer [5], both receiving chains do not have to be perfectly matched in amplitude and phase, which significantly relaxes the instrument specifications.

6.4 DBF General Considerations

Despite the DBF technique has been deeply analyzed in Chapter 4, some of the basic concepts are repeated here for the sake of clarity. DBF is a signal processing technique used in sensor arrays to steer the transmitted or received signal. The technique is well known and widely used in communications systems and the remote sensing framework albeit this is the first time – to the authors' knowledge – it is used in real-time microwave radiometry. Both concepts, digital beamforming and phased array, are similar, but some substantial differences exist. The phased array is based on the variation of the phase for each individual antenna in such a way that the effective radiation pattern of the array is steered to the desired angle. In addition, the phase shifters typically used in phased arrays, introduce losses that degrade the noise figure, and therefore the radiometric resolution. On the other hand, DBF is the result of digital signal processing, which implies absolute re-configurability. Furthermore, since each antenna signal is digitized, it is possible to obtain more than one beam simultaneously. In theory, a continuous scan can be performed obtaining an infinite number of beams simultaneously, only limited by the hardware requirements. These differences make the DBF more suitable for passive remote sensing applications.

A DBF is a spatial filter. All the collected antenna signals are properly weighted and added to get the system output. The system digitally controls the complex weight (phase and amplitude) of each antenna in order to attenuate some directions and reinforce others, so it creates an interference pattern in the wavefront to steer the beam. The DBF implementation (Eqn. (6.21)) is straightforward: each antenna's signal is amplified, down-converted, digitally acquired, weighted with a complex coefficient and, finally, added with the other antenna signals to get the signal at the out-port of the DBF:

$$S_{DBF,i}^{p}(t_i, \varphi_0, \theta_0) = \sum_{n=1}^{M} w_m S_{A_n}^{p}(t_i) \tag{6.21}$$

where:

- $S_{DBF,i}^{p}(t_i, \varphi_0, \theta_0)$ is the resulting signal of the digital beamforming steered to the (φ_0, θ_0) direction at the t_i instant for the p polarization,
- (φ, θ) are the azimuth and zenith angles of the system,
- M is the total number of antennas distributed over a line in a one dimension or over a plane in a two dimension distribution,
- w_n is the complex weight applied to the n^{th} antenna to steer the beam to (φ_0, θ_0), and
- $S_{A_n}^{p}(t_i)$ is the collected signal of the n^{th} antenna at the t_i instant and at p-polarization.

6.5 Theoretical Stokes Parameters and Radiometric Resolution

In this section the parameterized Stokes parameters and their radiometric resolution results are presented taking into account the already presented PAU-RAD topology, its noise wave analysis and the DBF general considerations [32]. In the following derivations it is implicitly assumed that all the ports of the system are properly matched, the different signal groups (*i.e.* antenna signal, Wilkinson's noise, and receiver's thermal noise) are statistically independent among them and, finally, the signals are calibrated so that the output has units of Kelvin, and not Watts.

PAU-RAD can have M generic elements, each of it has its own antenna signal, Wilkinson noise, and thermal noise from the receiver. These signals have to be combined to obtain a unique signal that will correspond to the steered beam. The result is as follows:

$$S_{p+} = \sum_{n=1}^{M} w_n \left\{ \frac{1}{\sqrt{2}} \left(S_{A_n}^{p} + S_{w_n}^{p} \right) + S_{R_n}^{p,1} \right\}, \tag{6.22}$$

$$S_{p-} = \sum_{n=1}^{M} w_n \left\{ \frac{1}{\sqrt{2}} \left(S_{A_n}^{p} - S_{w_n}^{p} \right) + S_{R_n}^{p,2} \right\}, \tag{6.23}$$

where:

- S_{p+} and S_{p-} are the complex digital beamformer outputs at p-polarization ($p = v$, h: vertical or horizontal), and the time and angular steering terms (t_i,φ_0,θ_0) have been eliminated for clarity. The + subscript corresponds to the receiving chain where the antenna signal and the noise signal generated by the Wilkinson power splitter load are added in phase (by definition, the upper receiving chain, see Figure 6.2), and the – subscript corresponds to the branch where they are added 180º out of phase (by definition, the lower receiving chain).

- w_n is the complex weight for each array element, note that $\sum_{n=1}^{M} |w_n|^2 = 1$,

- $S_{A_n}^{p}$ is the signal at the output of the p-polarization antenna of the n^{th} element. In this case, as the DBF is performed at base band, $S_{A_n}^{p}$

- $S_{w_n}^{p}$ is the noise signals generated by the Wilkinson power splitter of the n^{th} element at p-polarization, and

- $S_{R_n}^{p,i}$ is the thermal noise signal from each receiver of the n^{th} element at p-polarization.

The first and second Stokes parameters are obtained from the cross-correlation of the signals in Eqns.(6.22) and (6.23) at v- and h-polarizations:

$$\begin{aligned} < S_{p+} S_{p-}^{*} > = & \frac{1}{2} \sum_{n=1}^{M} \sum_{m=1}^{M} w_n w_m^{*} < S_{A_n}^{p} S_{A_m}^{p*} > - \frac{1}{2} \sum_{n=1}^{M} \sum_{m=1}^{M} w_n w_m^{*} < S_{w_n}^{p} S_{w_m}^{p*} > \\ & + \sum_{n=1}^{M} \sum_{m=1}^{M} w_n w_m^{*} < S_{R_n}^{p1} S_{R_m}^{p2*} >, \end{aligned} \tag{6.24}$$

where:

- $<\cdot>$ is the expectation operator in the statistical sense which is replaced by time average operator when the signals fulfills the ergodic properties, ($< AB >= \lim_{T\to\infty} \frac{1}{T} \int_0^T AB dt$, where A and B are two ergodic random processes, and T is the integration time),

- $T_{A_p} \triangleq \sum_{n=1}^{N} \sum_{m=1}^{N} w_n w_m^{*} < S_{A_n}^{p} S_{A_m}^{p*} >$,

- $T_{w_p} \triangleq \sum_{m=1}^{N} |w_m|^2 \left|S_{w_m}^{p}\right|^2$, note that the rest of the terms of this second term are uncorrelated among them due to its thermal noise nature, and
- the third term is zero, since all the terms are uncorrelated among the other ones of the same group.

Then Eqns. (6.22) and (6.23) simplify to:

$$T_v = < S_{v+} S_{v-}^* > = \frac{1}{2}(T_{A_v} - T_{w_v}), \tag{6.25}$$

$$T_h = < S_{h+} S_{h-}^* > = \frac{1}{2}(T_{A_h} - T_{w_h}). \tag{6.26}$$

The third and fourth Stokes parameters are computed by cross-correlating the signals of different polarizations, such as S_{v+} and S_{h-}:

$$\begin{aligned} < S_{v+} S_{h-}^* > = & \frac{1}{2}\sum_{n=1}^{N}\sum_{m=1}^{N} w_n w_m^* < S_{A_n}^{v} S_{A_m}^{h*} > - \frac{1}{2}\sum_{n=1}^{N}\sum_{m=1}^{N} w_n w_m^* < S_{w_n}^{v} S_{w_m}^{h*} > \\ & + \sum_{n=1}^{N}\sum_{m=1}^{N} w_n w_m^* < S_{R_n}^{v1} S_{R_m}^{h2*} >, \end{aligned} \tag{6.27}$$

where:

- $T_{A_{vh}} \triangleq \sum_{n=1}^{N}\sum_{m=1}^{N} w_n w_m^* < S_{A_n}^{v} S_{A_m}^{h*} >$, and
- the second and the third terms are zero since all the terms are uncorrelated among the other ones.

$$T_3 = 2Re < S_{v+} S_{h-}^* > = Re(T_{A_{vh}}) \text{ , and} \tag{6.28}$$

$$T_4 = 2Im < S_{v+} S_{h-}^* > = Im(T_{A_{vh}}) \text{ .} \tag{6.29}$$

At this point it is important to analyze the impact of calibration errors in the radiometric results. From Eqns. (6.24) and (6.25) it can be inferred that hardware calibration errors can be expressed as an error on the w_n complex coefficient, which creates, a steering misalignment and an antenna pattern degradation with the consequent lost of the main beam efficiency, increasing the error of the measurement. On the other hand, amplitude or phase errors have no effect on the T_{w_p} term as it is uncorrelated with all the other terms. Furthermore, equalization errors change the value of the weighted mean temperature of the Wilkinson power splitters, which do not have a big impact since all the receiving elements are assumed to be at the same physical temperature. So that, an error on the hardware

calibration leads to an increase in the measurements error due to the MBE degradation.

6.5.1 Radiometric Resolution for the Stokes Parameters

Assuming that all receiving elements are at the same physical temperature (T_w) and that all the receivers' noise temperature (T_R) are the same, the radiometric resolution of the first and second Stokes parameters can be computed from the standard deviation of the radiometer's output:

$$\sigma^2 = < (S_{p+}S_{p-}^*)(S_{p+}S_{p-}^*)^* > - < S_{p+}S_{p-}^* >^2. \tag{6.30}$$

From the complex Gaussian random variables moment theorem [72], (Eqn. (6.31))

$$< u_1^* u_2^* u_3 u_4 > = < u_1^* u_3 >< u_2^* u_4 > + < u_1^* u_4 >< u_2^* u_3 >, \tag{6.31}$$

the fourth order moment in Eqn. (6.30) can be decomposed into second order moments:

$$\langle S_{p+}S_{p-}^* S_{p+}^* S_{p-} \rangle = \langle S_{p+}S_{p+}^* \rangle \langle S_{p-}S_{p-}^* \rangle + \langle S_{p+}S_{p-}^* \rangle \langle S_{p-}S_{p+}^* \rangle. \tag{6.32}$$

All the individual terms of the Eqn. (6.32) can be calculated as in Eqn. (6.31) by properly substituting the subscripts. Then, the variance can be computed as follows:

$$\sigma^2 = < (S_{p+}S_{p-}^*)(S_{p+}S_{p-}^*)^* > - < S_{p+}S_{p-}^* >^2 = \frac{1}{2}(T_{A_p} + T_{w_p}) + T_R, \tag{6.33}$$

from which the radiometric resolution can be readily derived for an integration time τ as:

$$\Delta T_1 = \frac{1}{2}\frac{T_{A_v} + T_{w_v} + 2T_R}{\sqrt{B\tau}}, \tag{6.34}$$

$$\Delta T_2 = \frac{1}{2}\frac{T_{A_h} + T_{w_h} + 2T_R}{\sqrt{B\tau}}, \tag{6.35}$$

where B is the pre-detection bandwidth (the bandwidth of the input signals, which corresponds to a correlation time $\tau_c = 1/B$) and $n \equiv \tau/\tau_c = B\tau$ is the number of independent samples that are averaged [85], and therefore – assuming random Gaussian variables (Section 3.3.1) – the standard deviation reduces by a factor $\sqrt{B\tau}$.

In a similar way, the radiometric resolution can be derived for T_3 and T_4 using Eqn. (6.32) and the final result is:

$$\Delta T_{3,4} = \frac{\sqrt{(T_{A_v} + T_{w_v} + 2T_R)(T_{A_h} + T_{R_h} + 2T_R)}}{\sqrt{B\tau}}. \tag{6.36}$$

The radiometric resolution of the first two Stokes parameters corresponds to that a total power radiometer with an equivalent antenna temperature which is the mean between the real antenna temperature and the temperature of the Wilkinson's resistor. The result for the radiometric resolution of the third and fourth Stokes parameters is also intuitive, with the replacement of the system temperatures in both channels by new ones and taking into account, the standard deviation of the third and fourth Stokes parameters is twice the standard deviation of the real and imaginary parts of $T_{A_{vh}}$ [65].

6.5.2 Impact of the Receiver's Frequency Response in the Stokes Parameters

As in [112], this section analyzes the differences between the receivers' frequency responses, including the complex weights that are assigned to each receiver to steer the beam in a given direction, the impact of the overall frequency response, and how it may distort the Stokes parameters, that will be measured by a radiometer with just two elementary identical antennas.

$$\tilde{S}_{p\pm}(t) = \sum_{n=1}^{N} w_n \left\{ \frac{1}{\sqrt{2}} \left(\tilde{S}_{A_n}^{p} \left(t - \frac{r_n}{c} \right) e^{-jkr_n} \pm \tilde{S}_{w_n}^{p} \right) + \tilde{S}_{R_n}^{p,1,2} \right\} * h_n(t), \tag{6.37}$$

where:

- $\tilde{S}_{p\pm}(t)$ is the complex digital beam former output at *p*-polarization taking into account the receivers' frequency response, and ± accounts for the two branches of the system,
- $w_n = a_n e^{j\theta_n}$ is the complex weight for each array element. Note that $\sum_{n=1}^{N} |w_n|^2 = 1$,
- $\tilde{S}_{A_n}^{p} \left(t - \frac{r_n}{c} \right) e^{-jkr_n}$ is the signal at the *p*-polarization output of the antenna n^{th} of the element, before being affected by the receiver's response, c is the speed of light (c=299.792.458 m/s), r_n is the path length from the surface under observation and the radiometer, when there is enough distance with respect the maximum distance between antennas then r_n=r for all *n* for the envelope, but not for the phase of the received signals,

- $\tilde{S}_{w_n}^{p}$ is the noise signal generated by the Wilkinson power splitter of the n^{th} element at *p*-polarization, before being affected by the receiver's response,

- $S_{R_n}^{p,1,2}$ is the thermal noise signal from each receiver of the n^{th} element at p-polarization, before being affected by the receiver's response, and

- h_n(t) is the impulse response of the n^{th} receiver

Then, as in the previous section, the first and second Stokes parameters are obtained from the cross-correlation of the signal (Eqn. (6.24)) at *v*- and *h*-polarizations, respectively:

$$< \tilde{S}_{p+}\tilde{S}_{p-}^{*} >= \frac{1}{2}\sum_{n=1}^{N}\sum_{m=1}^{N} a_n a_m^{*} V_{A_{nm}}^{p}(\tau_1) e^{-j(kr_n-\theta_n)} e^{-j(kr_m-\theta_m)} \tilde{r}_{mn}(\tau_1) - \frac{1}{2}\sum_{n=1}^{N}\sum_{m=1}^{N} w_n w_m^{*} V_{w_{nm}}^{p}(\tau_2)\, \tilde{r}_{mn}(\tau_2), \tag{6.38}$$

where:

- $V_{A_{nm}}^{p}(\tau_1) =< \tilde{S}_{A_n}^{p}(t)\tilde{S}_{A_m}^{p*}(t-\tau_1) >$ is the correlation between the antenna signals at τ_1,where $\tau_1 = \frac{1}{c}(r_n - r_m)$ is the delay between the antenna *n* and,

- $V_{w_{nm}}^{p}(\tau_2) =< \tilde{S}_{w_n}^{p}(t)\tilde{S}_{w_m}^{p*}(t-\tau_2) >$ is the correlation between the reference signals at τ_2, where τ_2 is the delay of the reference signals between the receiver *n* and *m*, note that this term is 0 except for *m*=*n*,

- $\tilde{r}_{mn}(t) = \frac{e^{-j2\pi f_0 t}}{\sqrt{B_m B_n}} \int_0^{\infty} H_m(f) H_n^{*}(f) e^{j2\pi f_0 t} df$ is the so called fringe-washing function, which takes into account the hardware response [103], and

- the receivers' thermal noise term has not been considered, since as it is uncorrelated among all the terms of the equations as in Eqn. (6.27).

From Eqn. (6.38) is easy to infer that the digital beamformer results have a strong dependence on the hardware ($\tilde{r}_{mn}(t)$), for instance a maximum antenna separation exists due to spatial decorrelation effects (the fringe-washing function), which decreases dramatically its value with the delay, depending on the system's bandwidth. The first noticeable effect is an intrinsic smoothing of the correlation values, making impossible to create a larger beamformer array, unless signals are affected by true time delays.

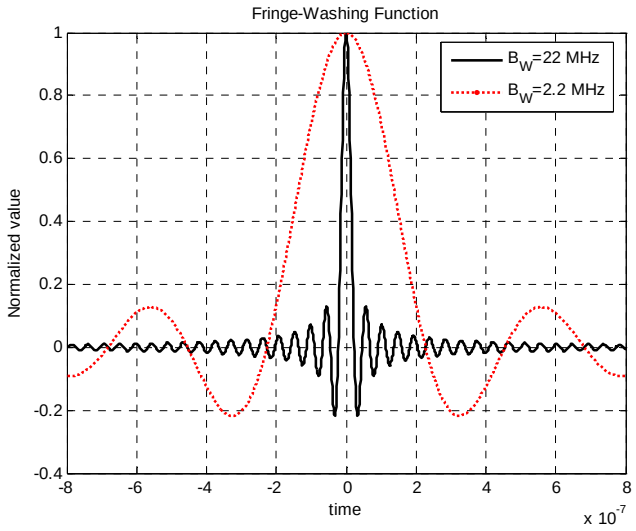

Figure 6.6 Fringe-washing function plots for two ideal squared frequency receiver responses and different system bandwidths

As it can be observed in Figure 6.6 the larger the system bandwidth, the faster the correlation lost due to the hardware limitations. For instance, having a $B_W = 2.2$ MHz the value of the correlation halves its value at t ~ 137 ns (a separation between antennas of 41 m) and $B_W = 22$ MHz the correlation halves at t ~ 13 ns (a separation between antennas of only 4.1 m).

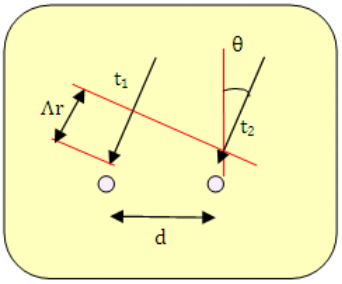

Figure 6.7 Sketch of a two antenna array with a separation among them of d, receiving a planar wave with an incidence angle of θ.

Following Figure 6.7 it is possible to calculate the maximum length for a system $\Delta r = d\sin\theta$, where d is the antenna's separation and θ is the impinging angle. Then, the time delay for the signal of the first antenna with respect the arrival time of the signal at the second antenna can be defined in terms of the distance between antennas, the impinging angle and the speed of the light (c) ($t_1 - t_2 = \Delta r/c = d/c\,\sin\theta$). To ensure negligible FWF effects $d/c\,\sin\theta \ll 1/B$, where B is the system bandwidth. Thence, the worse case is for considering a signal with θ=90º (sinθ=1). In this worse situation two cases can be considered, one forcing to the FWF to be negligible above all the Field of View (FOV) in this case this relationship has to be fulfilled is $d \ll c/B$, and the other case consists of relaxing this requirement at the half of the FOV, in this case this relationship has to be fulfilled is $d \ll c/(B\sin(FOV/2))$.

The most common solution to build larger arrays is to use the well-known technique called channelization or sub-banding [9]. It consists of splitting the signal's spectrum creating different signals with reduced bandwidth (B*)*. This technique makes the FWF wider as it can be seen in Figure 6.6. Finally, the different calibrated visibilities are added to create the global visibility [9].

6.6 Maximum Residual Error Equalization

Once the Stokes parameters have been analyzed and the impact of the DBF errors has been raised, in this section the residual equalization errors that PAU-RAD can afford are discussed. Although the DBF presents several and clear advantages, it has drawbacks to be solved as well. The main one is the requirement that the signals to be combined by the DBF have to be previously equalized in phase and amplitude. Thereby, since it is not possible to ensure this by system design, the whole receiver set has to be equalized in phase and amplitude. This point is a key issue to compose the digital array.

As explained in Section 6.1, analog receivers are driven from an ovenized 10 MHz master clock that is distributed to all receivers to generate their own local oscillator. Hence, it can be assumed that each receiver's PLL has a fixed, but possibly slowly varying, random phase variable uniformly distributed within $[0 - 2\pi)$. Furthermore, each receiver has a nominal 110 dB gain chain. For this reason, each receiver has a potentiometer that controls the last amplifier stage at IF to manually equalize all receivers' gain within 110 dB ± 1 dB. Even with this functionality, the gain has to be considered, as a first approximation, a random variable with a normal probability density function with a standard deviation of ~1 dB. The residual calibration errors will ultimately determine the quality of the synthesized array factor and hence the quality of the radiometric data.

The impact of the residual equalization errors on a 4x4 antenna array factor is analyzed in Figure 6.8. The impact of the residual phase error (Figure 6.8a), assuming that has zero mean along the steering axis, consists of a reduction of the notch level with respect of a theoretical array pattern, an increase of the side lobe levels (SLL) and a slight increase of the array factor beamwidth. When the phase standard deviation error is too high (> 5^{o}) the beam is totally distorted. All these effects have a significant impact on the beam quality but not on the steering angle, that can be steered precisely due to previously assumed zero degrees mean error. On the other hand, the impact of the residual phase error (Figure 6.8b), is similar to the phase, it does not changes the pointing angle, but it distorts the beam by increasing the SLL and the beamwidth. For high residual errors (> 4 dB) the beam is totally distorted. Notice that results obtained on Figure 6.8 are only valid for a 4x4 antenna array, since they depend on the number of antennas and their spatial distribution.

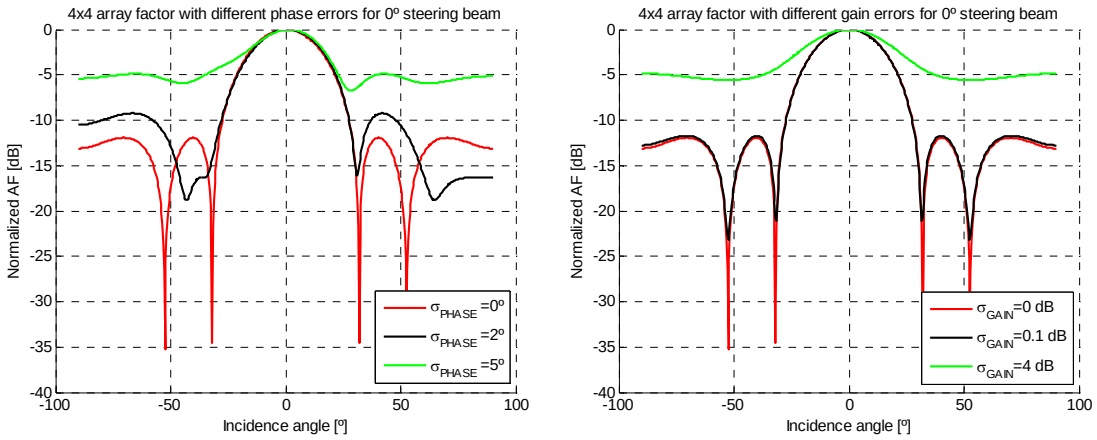

(a) (b)

Figure 6.8 Impact on a 4x4 array factor for residual calibration errors, (a) considering the phase, and (b) considering the gain.

There are some figures of merit to measure the quality of an array. In this study the main beam efficiency (MBE) has been selected among all them because it unifies different parameters (main beamwidth, SLL, back lobe …) in a single one. In general, the MBE is defined as the ratio between the power collected by the main beam of the array and the total power collected by the same array. Theoretically, the main beam ends in the nulls between the main beam and the first side lobes, but in practice, these nulls are difficult to determine due to noise phase errors and the angular resolution of the measurement system. In practice, to compute the edge of the main beam, it is considered that the main beam ends when it reaches the maximum side lobe amplitude level. In any case, this approximation gives a slightly lower MBE value than the real one.

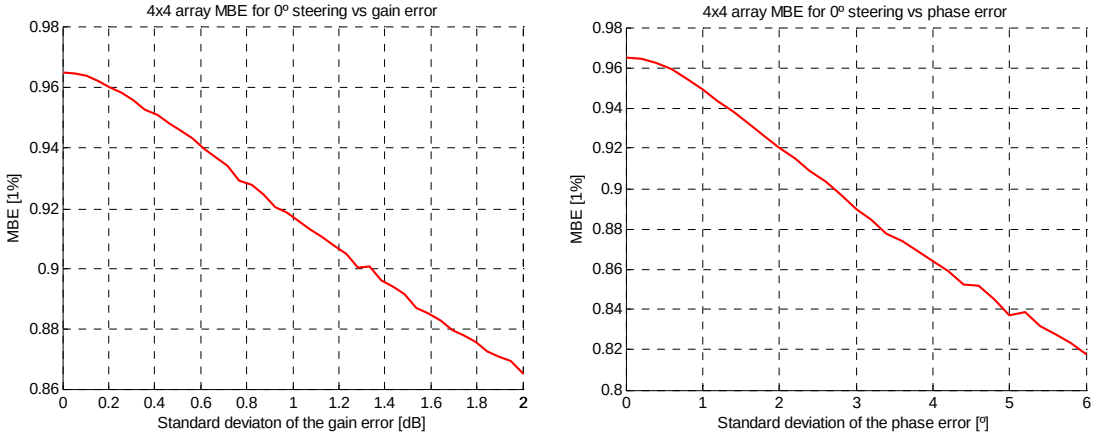

(a) (b)

Figure 6.9 Degradation of the MBE vs (a) the amplitude, and phase (b) residual calibration error, obtained using a theoretical approximation and simulations pointing to the boresight. The considered array has 4x4 elements spaced 0.63 wavelength with triangular illumination in both directions.

Figure 6.9 shows the MBE degradation dependence with the residual amplitude and phase equalization error, respectively. The most limiting parameter is the residual phase error, which rapidly degrades the MBE. To fulfill the radiometric

requirements, a MBE equal to 0.94 is obtained with residual standard deviation error of 2º for the phase and 0.1 dB for the amplitude. These values have been obtained from these analyses and become specifications for the hardware equalization performance. It is important to note that the phase and amplitude errors drift with temperature and time. So that, the hardware equalization has to be periodically performed, each time the residual errors cross over these specified thresholds.

6.7 Number of Bits Required to Equalize the Phase and Amplitude Simultaneously

The impact of the digitization in a correlation radiometer has been analyzed in Chapter 5. Nevertheless, there is still another quantization effect that has to be taken into account before starting the system's design. Let us assume that there is a digital trigonometric function that not only down-converts the input signal to base-band, but it changes the phase and amplitude of the signal following an equalization criteria. In this case, the digital frequency of the trigonometric function is not relevant because it is a question of the number of samples per period. Using such signal to equalize the input signal involves the problem that there are a finite number of values that the trigonometric quantized signal can have (depending on the number of bits).

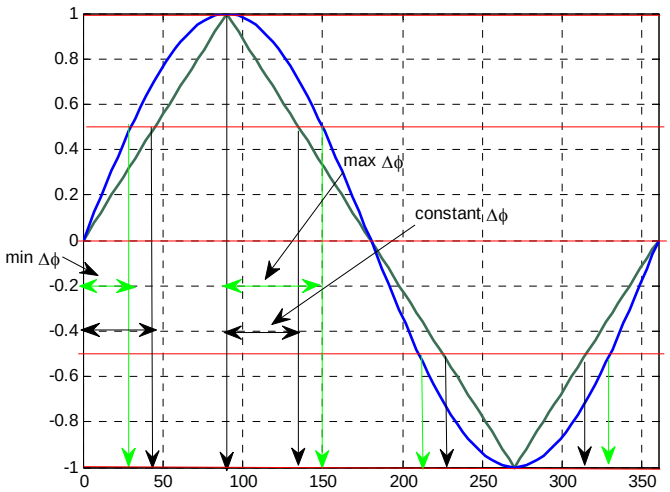

Figure 6.10 Quantization (5 levels) of a cosine and triangular signals.

Using this finite set of possible values, the signal has to modulate its phase and its amplitude to be able to equalize the input signal with respect a reference signal. There is a relationship between the amplitude step and the phase step that depends on the number of bits (Figure 6.10). Even though, when few levels are considered a phase change can infer an undesired amplitude change, creating a high degree of correlation between the phase and amplitude residual errors. Figure 6.10 illustrates this relationship without taking into account the amplitude (A=1),

and considering only 5 quantization levels. The cosine function shows that the phase resolution is not constant (min(Δφ) or max(Δφ)), this is related with the non-linearity of the cosine function. On the other hand, when the triangular function is analyzed, the phase resolution is always constant Δφ. Figure 6.11 shows the evolution of the phase resolution (max(Δφ)) for a cosine signal depending on the number of bits. The resolution is better than 1º when the signal is quantized using at least 14 bits.

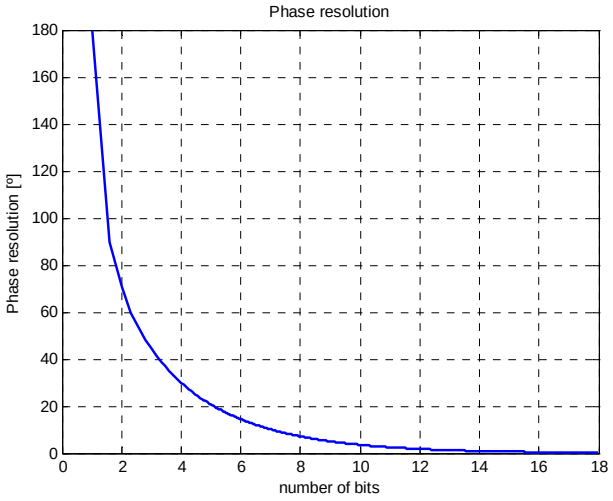

Figure 6.11 Phase resolution taking into account the number of bits to quantize the cosine signal .

The relationship between the phase and the amplitude is shown (6.39):

$$\Delta\varphi = \cos^{-1}\left(1 - \frac{\Delta A}{A_{max}}\right), \tag{6.39}$$

where:

- $\Delta\varphi$ is the phase resolution of the trigonometric function
- ΔA is the amplitude resolution $\Delta A = 2\,A_{max}/M$, where M is the number of quantization levels, and
- A_{max} is the maximum possible value of the cosine, it determines the minimum input power that can be calibrated.

Figure 6.12 shows Eqn. (6.39) graphically for two different maximum possible value of the cosine (A_{max}= 10, green curve, and A_{max}=1, red curve)

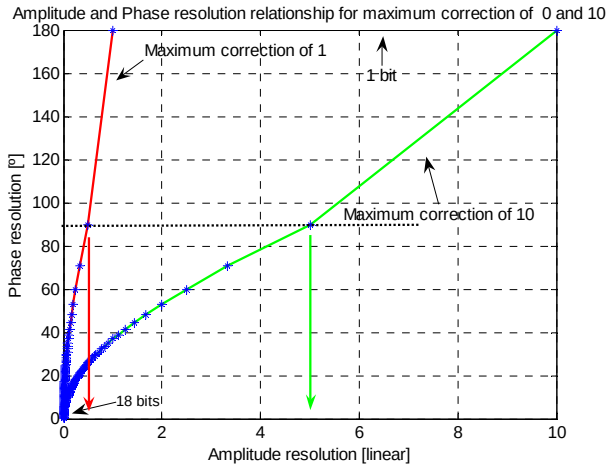

Figure 6.12 Phase resolution and amplitude resolution for two different amplitude correction ranges (A_{max}= 10 (green), and A_{max}=1 (red)).

Figure 6.12 shows that for the performance of the calibration increases as it increases the number of bits used for quantize the cosine function. When only 1 bit is used the phase resolution is 180º, and as the number of bits increases the phase resolution goes asymptotically to 0º. The phase resolution does not depend on the maximum amplitude, as the black dotted line suggests, the phase is the same for the same number of bits, but the amplitude resolution changes (red and green arrows). Furthermore, the phase and amplitude resolution are the phase and amplitude dependence, the impact on amplitude when only changing the phase and the impact on the phase when only changing the amplitude.

Using 9 bits to quantize the cosine function the equalization performance is 5.07º for the worst phase (max(Δφ)) and 0.02 for the amplitude when A_{max}=10 (~ 0.1 dB) and 0.002 when A_{max}=1 (~ 0.01 dB). On the other hand when using 18 bit to quantize the cosine function the equalization performance is 0.224º (max(Δφ)) and $4 \cdot 10^{-5}$ for the amplitude when A_{max}=10 (~ 0.001 dB) and $4 \cdot 10^{-6}$ when A_{max}=1 (~ 0.0001 dB). The 18 bits fulfills the PAU-RAD equalization requirements and has been settled as design parameter.

6.8 PAU-RAD Array Specifications

The PAU-RAD antenna array requirements were defined taking into account previous radiometer designs [113]. Furthermore, the main concern was that the resulting beams would be suitable for radiometric applications [114]. The main specifications of the antenna array are:

- beamwidth, $\Delta\theta_{-3dB} < 25^{o}$ and main beam efficiency, MBE > 0.94,
- minimum mutual coupling between the array elements, and cross-pol. coupling < -23 dB, and

- steering angle up to ±20º from the array boresight in 5º steps to achieve an angular scan range from 25º to 65º when the antenna is tilted 45º.

The above specifications have been settled taking into account that PAU-RAD is a ground-based instrument. In this case, the array beamwidth and the beam overlapping rate do not compromise the retrieval process of the geophysical parameters. Otherwise, in case the system was an airborne or spaceborne instrument, some of these parameters are not suitable for those applications, and they should be re-settled taking into account the new measurement environment. For example, the beamwidth should be reduced to have and acceptable spatial resolution and non-overlapped beams, which can only be achieved with an array larger than 4x4. The antenna spacing (d) and the elementary antenna patterns are the design parameters to optimize in order to fulfill the antenna array specifications. The most difficult parameters to adjust, within the specifications, are the pair beamwidth, and MBE, because they are not independent one from the other. It is not possible to simultaneously optimize both parameters, so that a tradeoff between them is required to find the solution which fulfills the specifications. The beamwidth decreases when the antenna spacing increases. On the other hand, when the antenna spacing increases the scanning angle interval is dramatically reduced due to the quick degradation of the MBE ratio with the incidence angle. The MBE degradation is related with the low spatial sampling rate (d, antenna spacing) which does not fulfill the Nyquist sampling criterion (d=0.5λ, where $\lambda \triangleq c/f$, and f is the working frequency). Not fulfilling the Nyquist criterion leads an array with diffraction lobes at high incidence angle. The larger the antenna spacing, the lower the steering angle affected by the main lobe aliases. Fortunately, this effect is partially compensated by the elementary antenna pattern (a cardioid for an ideal antenna patch) which for high incidence angles attenuates enough the incoming signal.

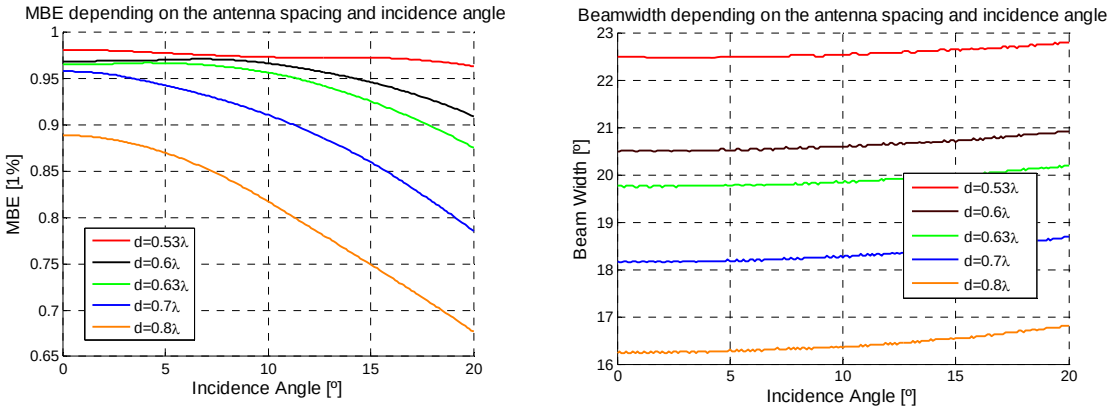

Figure 6.13 Simulation taking into account the elementary antenna pattern, of a 4x4 array with different antenna spacing (d) (a) evolution of the MBE vs. incidence angle, and (b) half-power beamwidth vs incidence angle.

Figure 6.13 illustrates the tradeoff between the antenna beamwidth (at -3 dB) and the MBE depending on the antenna spacing. For these simulations a patch antenna pattern (a cardioid) has been considered. For small antenna spacing, those closer to the Nyquist criterion (d = 0.5 λ), the MBE is higher and less depending on the steering angle, because diffraction lobes appear only for large steering angles. The MBE rapidly decreases when the antenna spacing increases, even at 0º steering angle due to the increase of the number of side lobes. On the other hand, the beamwidth decreases with the antenna spacing and remains quite constant (~ 0.5º in the whole range) for the entire incidence angle and for all the antenna spacing. After this analysis, the chosen antenna spacing was d = 0.63 λ because it has the best tradeoff between the beamwidth and the MBE.

Once the antenna spacing has been selected, the impact of the unitary antenna has to be analyzed from the point of view of the full pattern array. Figure 6.14 shows the two array factors for an antenna spacing of 0.63 λ (d = 0.63 λ) and incidence angle of 20º (θ_i = 20º) one assuming an isotropic and ideal elemental antenna pattern (red curve), and another one taking into account the patch element antenna pattern (blue curve).

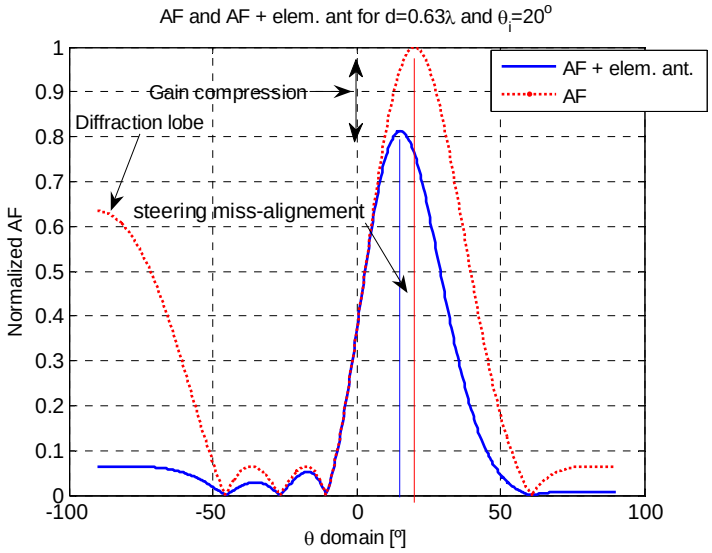

Figure 6.14 Array factor with an ideal and a patch element antenna patterns, respectively. Three main effects show up: the AF alias mitigation, the gain compression, and the steering miss alignment.

Including the elementary antenna pattern has four effects: the main lobe diffraction is mitigated, the main lobe shape is distorted, there is a steering miss-alignment and, finally, there is a gain compression. The alias mitigation and the beam distortion effects are somehow taken into account in the MBE study. The gain compression and the steering miss-alignment have to be quantified, for further beam correction.

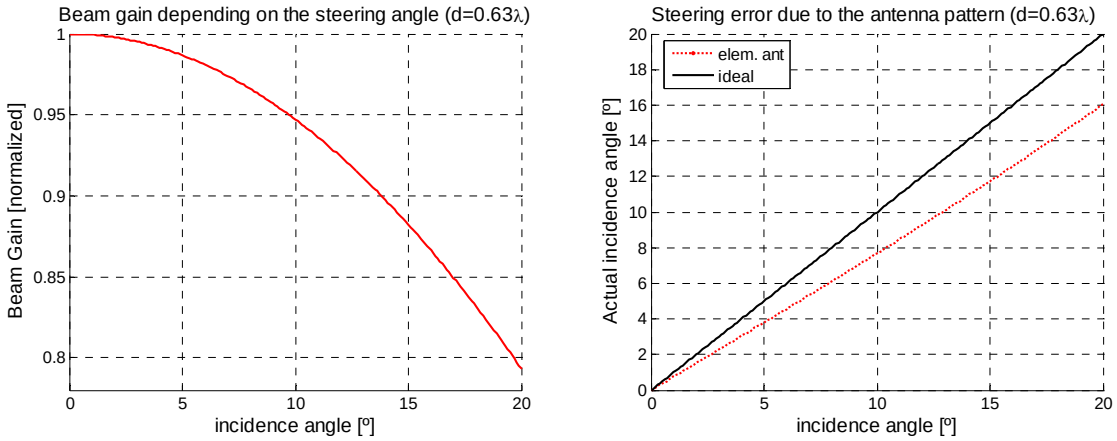

Figure 6.15 Elementary antenna pattern effects for d = 0.63 λ, (a) beam gain compression, and (b) steering miss-alignment.

Figure 6.15 shows the gain compression and steering miss alignment effects due to the elemental antenna pattern. The gain decreases as the incidence angle increases, this value has to be taken into account to be able to compare results obtained with different beams. For d = 0.63 λ, the gain decreases from 1, when the steering angle is 0º, down to 0.8 when the steering angle is 20º. The incidence angle miss alignment error increases as the steering angle increases, and it is always lower than the expected value. There is no error for the 0º steering, and it increases up 4º for a steering angle of 20º. To overcome this miss-alignment the angle to be steered has to be the one which takes into account the antenna pattern instead of the ideal array factor one, *i.e.* to steer a beam to 10º, the progressive phase has to such that for a pencil-beam array the steering angle be 12.5º instead of 10º.

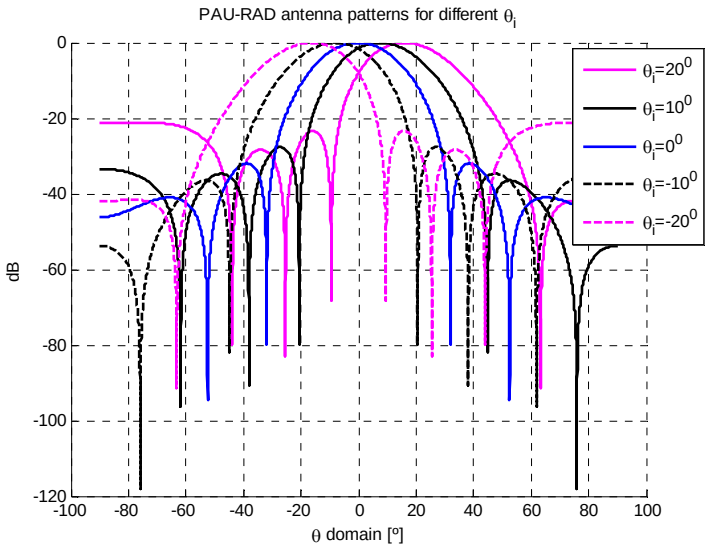

Figure 6.16 Normalized theoretical array beams for a 4x4 patch antenna array with d = 0.63 λ and 0º, ±10º, and ±20º.

Figure 6.16 shows five synthesized beams for a 4x4 patch antenna array with d = 0.63 λ and 0º, ±10º, and ±20º. As it can be seen, the beams are more distorted, and have larger side lobes for larger steering angles.

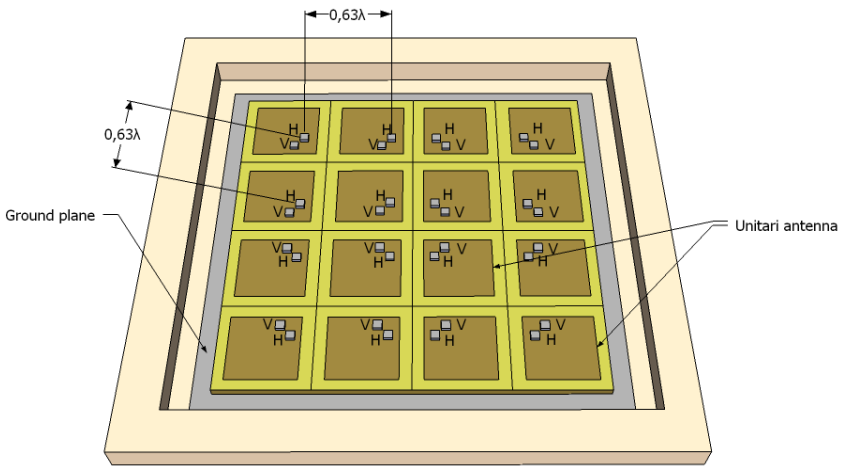

Figure 6.17 Polarimetric antenna array for the DBF. Using patch 90º rotated antennas and a distance between elements of 0.63 λ.

Figure 6.17 shows the PAU-RAD 4x4 rectangular antenna array with triangular illumination in both directions. The orientation of these elementary antennas over the ground plane takes into account the antennas feeders. For that reason the elementary antennas have been rotated within adjacent elements to reduce the mutual coupling and the cross-polar component (Figure 6.17)[113].

6.9 Impact of the GNSS Signal on the Radiometer

To achieve the best performance, the L-band radiometer should operate in the 1400-1427 MHz "protected" band and the GPS reflectometer at 1575.42 MHz (GPS-L1 band), where open C/A codes can be used to generate the local replicas of the GPS signal. However, in the PAU instrument demonstrator, the GPS reflectometer and the L-band radiometer share the same front-end and band: a commercial GPS down-converter (Zarlink GP2015 [107]). As a result, both operate at 1575.42 MHz. This architecture reduces the required hardware resources, using only one RF-IF front end instead of two, one for the radiometer and another for the GPS reflectometer (Figure 6.4). Although sharing the same RF-IF front-end provides a significant hardware reduction, the system has to deal with some inferred handicaps. The first one concerns to the bandwidth, the radiometer uses only the 2.2 MHz GPS-L1 band, instead of the nearly 27 MHz available in the protected passive L-band (1400-1427 MHz). Obviously, it has an impact on the radiometric resolution, which can only be compensated by increasing the integration time. The second handicap concerns to the interference that GPS signals can introduce in the radiometric measurements (Figure 6.18), including the P, M and C/A code. Although the spread-spectrum modulation GPS signal is lower than the noise level (~ -27 dB below the noise level), the impact of the GPS interference on the radiometer measurements has to be quantified [40].

Figure 6.18 shows the auto-correlation for a GPS-L1 signal from a Block II-F satellite. The L1 signal has the P code, with a large repetition period (~ 75 dB of compression gain spread over 22 MHz, and a density of power ~ -173 dBW/m^2 using a linear polarization antenna), the M code and the C/A code (~ 30 dB of compression gain spread over 2.2 MHz, and a density of power ~ -163 dBW/m^2 using a linear polarization antenna) [115].

Despite the P code has a higher auto-correlation peak, the C/A code has a higher impact on the radiometer. When computing the power of the GPS signal from a radiometric point of view, the compression of the CDMA modulation does not take any effect (it only has when correlating the incoming signal with a local replica of it). So that, it only has impact the density of power associated to each codes. The C/A code has a density power higher in 10 dB with respect the P code, so that, the highest impact comes from the C/A code instead of the P. The M code is still experimental and not all the satellites are transmitting it. Anyway its modulation distributes its power at the edges of the band, having less effect even than the P code.

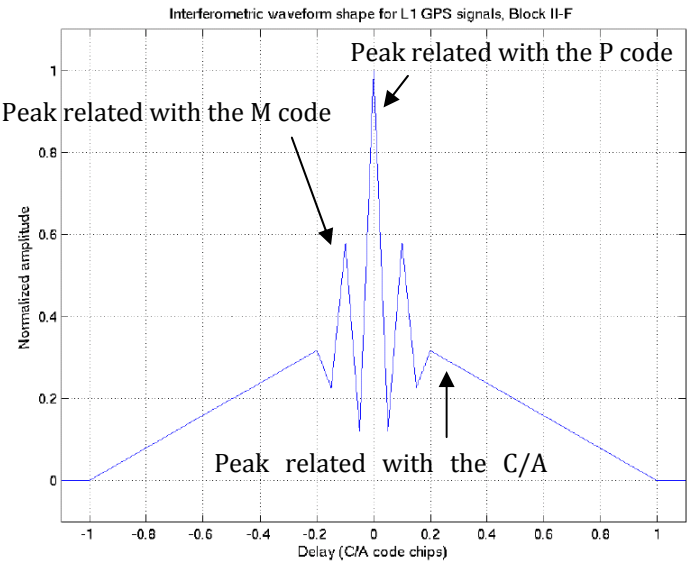

Figure 6.18 Auto-correlation for GPS L1 from a Block II-F [117].

To measure the impact of the C/A code in the radiometric measurements, two extreme scenarios are distinguished considering a sea surface reflection coefficient of Γ=0.7, a height of h=110 m (which can be achieved with a ground based instrument from the top of a cliff as in [36]), and an antenna's effective area of A_{eff} = 0.16 m^2 (D = 17.5 dB, antenna directivity) for both cases:

- the worst situation occurs when the specular reflection point is at the antenna's boresight. In this case the antenna temperature increase due to the GPS interference is T_{GPS} = 65 K,

- the best situation occurs when the reflection point comes 90^o out of boresight (and the attenuation due to the antenna pattern is at least -25 dB), the radiometric measurement contribution is then T_{GPS} ~ 0.35 K (~0.6 psu salinity

error in warm water), above the 0.1 psu requirement of GODAE for open ocean [116], but this value can be reduced even further by using radio frequency interferences (RFI) removing techniques.

Taking into account that the radiometer beam can be electronically steered, the system can point to the North to perform radiometric measurements (where there are no GPS satellites due to their orbital plane distribution), and that the specular reflection points are know and can be tracked, the chances of having a significant interference level are low.

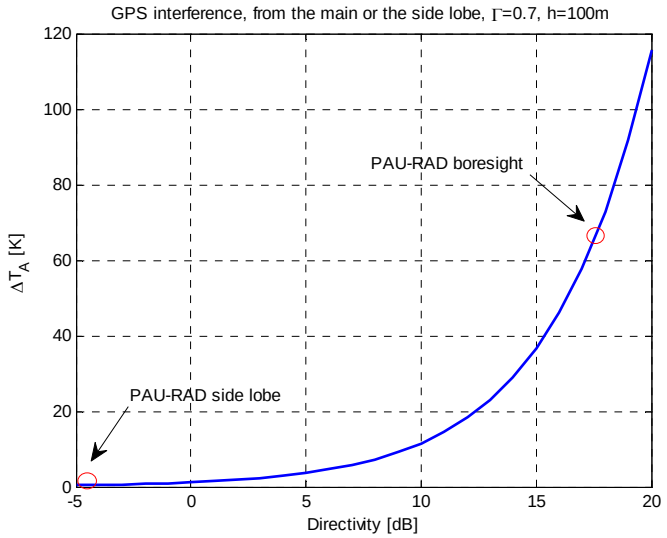

Figure 6.19 Contribution to the antenna temperature (ΔT_A [K]) of a GPS signal from one satellite when performing radiometry in the GPS-L1 band, taking into account the direction of arrival of the GPS signal.

Figure 6.19 illustrates the GPS-L1 interference on a radiometric measurement, depending on the signal's entering point. When entering from the main lobe (D=17.5 dB) the GPS signal contribution is 65 K. On the other hand, when entering from a side lobe, with 25 dB of attenuation with respect the boresight, the contribution is 0.35 K.

6.10 Conclusions

This chapter has focused on the analysis of the PAU-RAD instrument from theoretical and design points of view. These analyses have been the previous and necessary step to be able build the system.

The chapter has started with a general overview of the instrument giving its basic requirements. Each antenna of the antenna array is combined in an analog way with the other three that compose a row. Each combiner has its own receiver that down-converts the RF signal to an IF signal. Once the signals are at IF, they are digitalized and processed in a FPGA. In the FPGA, signals are amplitude and

phase equalized and then processed in order to calculate the four Stokes parameters.

The PAU-RAD radiometer architecture has been analyzed. It is somehow inspired on the Plank radiometer architecture. But differs from other radiometers in the fact that has been conceived to share the front-end with a GPS reflectometer. Furthermore, a noise wave analysis for one received has been performed to understand the basic interactions of the system. The main result of this analysis is that the radiometer output is proportional to the antenna temperature minus the Wilkinson power splitter physical temperature ($T_A - T_w$), and if channels are not equalized ($S_{21}^1 S_{10} \neq S_{21}^2 S_{20}$), the output can be a complex number due to imperfect mismatch of the two receiving chains and of the Wilkinson power divider. This error can be corrected by the injection of correlated noise and compensation of the phase and amplitude of the raw cross-correlations.

The theoretical Stokes parameters has been obtained from a DBF point of view, with the same result, (proportional to $T_A - T_w$), and the radiometric sensibility has been computed for the first and the second Stokes' parameters ($\Delta T = \frac{1}{2}(T_{A_p} + T_{w_p} + 2T_R)/\sqrt{B\tau}$) and for the third and fourth parameter ($\Delta T_{3,4} = \sqrt{(T_{A_v} + T_{w_v} + 2T_R)(T_{A_h} + T_{w_h} + 2T_R)}/\sqrt{B\tau}$) . Furthermore, the receiver response impact over the Stokes parameters has been analyzed using the well-know fringe-washing function.

From the point of view of the maximum residual equalization errors, the most limiting parameter is the residual phase error, which rapidly degrades the MBE. To fulfill the radiometric requirements, a MBE equal to 0.94 can be achieved with a residual standard deviation phase error of 2º and amplitude error of 0.1 dB. Furthermore, the trigonometric signal that has to equalize these errors has to be quantized with a minimum number of bits to overcome the problem of the phase-amplitude dependence. It has been found that the phase resolution only depends on the number of bits, but not on the maximum range of amplitude to equalize. When using 18 bits, the best equalization performance is 0.224^o and $4 \cdot 10^{-5}$ for the amplitude when A_{max}=10 (~ 0.001 dB) and $4 \cdot 10^{-6}$ when A_{max}=1 (~ 0.0001 dB). The 18 bits fulfill the PAU-RAD equalization requirements.

PAU-RAD antenna is a 4x4 rectangular antenna array with a antenna spacing of 0.63 λ (d = 0.63 λ) and triangular illumination in both directions. It is capable to steer the beam up to ±20º from the array boresight in 5º steps. A comprehensive analysis has been performed taking into account the impact of the array factor and the patch antenna pattern (cardioid) on the MBE, the beamwidth, the gain compression, and the steering miss alignment. The orientation of the elementary antennas over the ground plane has been 90º rotated taking into account the antennas feeders.

Finally, the GPS-L1 signal impact on the radiometric measurement has been assessed. It can be separated in two different situations:

- the worst situation occurs when the specular reflection point is at the antenna's boresight. In this case the antenna temperature increases due to the GPS interference is T_{GPS} ~ 65 K, and

- the best situation occurs when the reflection point comes 90º out of boresight the radiometric measurement contribution is then T_{GPS} ~ 0.35 K. This scenario allows performing radiometric measurements with enough radiometric resolution.

Chapter 7

7 PAU-RAD IMPLEMENTATION

After analyzing the impact of the digitization on a correlation radiometer, analyzing the DBF from real and synthetic aperture points of view, and performing an analysis on the PAU-RAD instrument concepts, this chapter focuses on the practical implementation of the PAU-RAD system, covering all the topics involved on its development. In the analog part, this chapter focuses on the antenna array, the radio-frequency (RF) and intermediate frequency (IF) stages, the analog to digital converter (ADC) system, and the thermal control system. On the digital part, it focuses on the digital design of the arithmetic-logic unit (ALU), and on the control unit (CU) which manages the system.

7.1 PAU-RAD Implementation Overview

As it has been discussed in Chapter 4, there is not only one way to perform a beamformer. In fact, there are several of options to implement the phase shifting, digital or analog. The digital implementation chosen for PAU-RAD beamformer is one among the possible ones, which gives the system the required versatility. This allows the possibility to try different data processing algorithms for the beamforming, and analyze it from different point of views, as a real or a synthetic aperture.

In this section the PAU-RAD implementation is defined for a better understanding of the next sections. Mainly, the radiometer's core (Figure 7.1) consists of an analog part that collects the input signals thought the antennas, and then it performs the RF-IF down-conversion from 1.57542 GHz to 4.039 MHz. Once the signals are at IF, they are digitized using 8 bits and input into the FPGA. Inside the FPGA, each channel is equalized, in phase and amplitude, and down-converted to baseband using its own Numerically Controlled Oscillator (NCO). Then the DBF is performed and finally signals are properly correlated in order to obtain the Stokes parameters. Furthermore, there are two other sub-systems, one to estimate the amplitude and phase error of each channel using a Controlled Noise source and another to use internal loads for radiometric calibration applications.

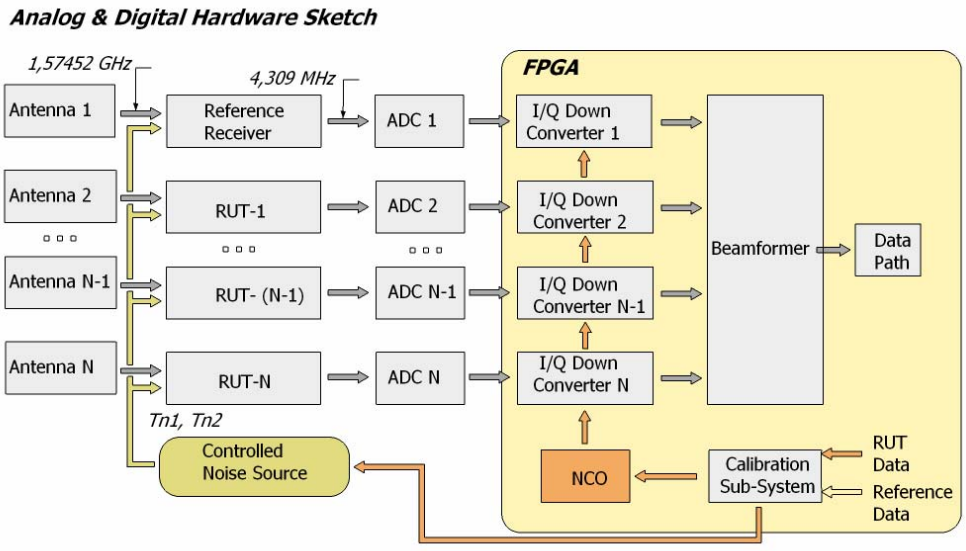

Figure 7.1 Analog and digital hardware block diagram. Each I/Q down-converter has its own Numerical Controlled Oscillator (NCO).

In addition, PAU-RAD requires two more systems not displayed in the Figure 7.1, a finite state machine to manage autonomously the hardware part, and an external interface, which collects the processed raw data sent by the PAU-RAD and allows the user to control and supervise the system.

The implementation of PAU-RAD has been done in several affordable work packages (Figure 7.2). This *a priori* subsystems identification allows a better identification of the implementation problems and has been a very convenient way to proceed. These subsystems can be classified in two groups:

- a hardware group (in blue in Figure 7.2): consisting of the mechanical structure, the antennas, the Controlled Noise Source (CNS), the RF-IF analog receivers, the thermal stabilized 10 MHz clock, ADCs, the power supplies, the thermal control, the auxiliary data such as the clinometer, the thermometers, and the digital design of the ALU, where the digital radiometer is embedded, and

- a software group (in grey in Figure 7.2): involving the receiver equalization algorithms placed in the Control Unit (CU), the machine state control to manage the digital system and placed in the CU as well, and the PC control interface which collects the data generated by the PAU-RAD and allows the user to control and real-time supervision the instrument.

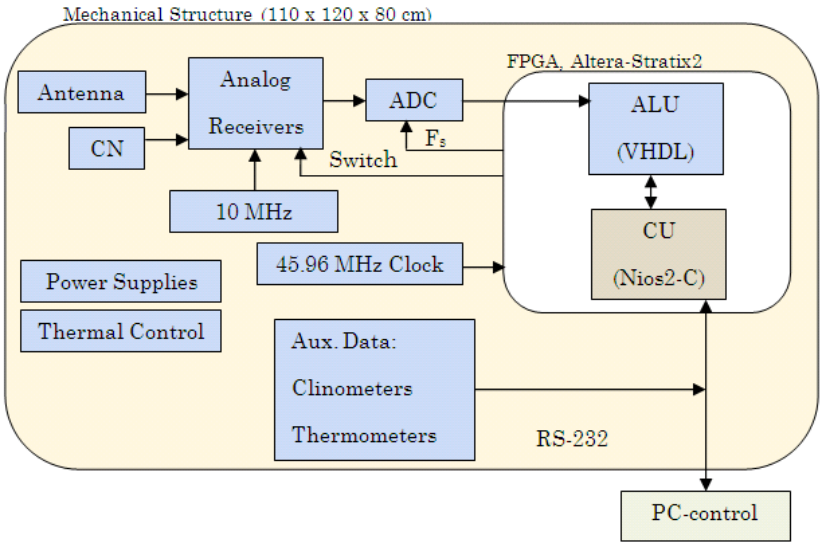

Figure 7.2. Sketch of the PAU-RAD subsystems and their interaction, in blue the hardware subsystems and in grey the software ones.

This chapter is organized following these two groups of subsystems: The hardware part of PAU-RAD, and the software part.

7.2 PAU-RAD Hardware Implementation

Hardware subsystems are analyzed in the following sections.

7.2.1 Antenna

The elementary antenna is a GPS-L1 band (1575.42 MHz) patch antenna with two feeders, one for each polarization, horizontal and vertical (Figure 7.3). It was designed following the expertise acquired during the LAURA radiometer antenna design [113].

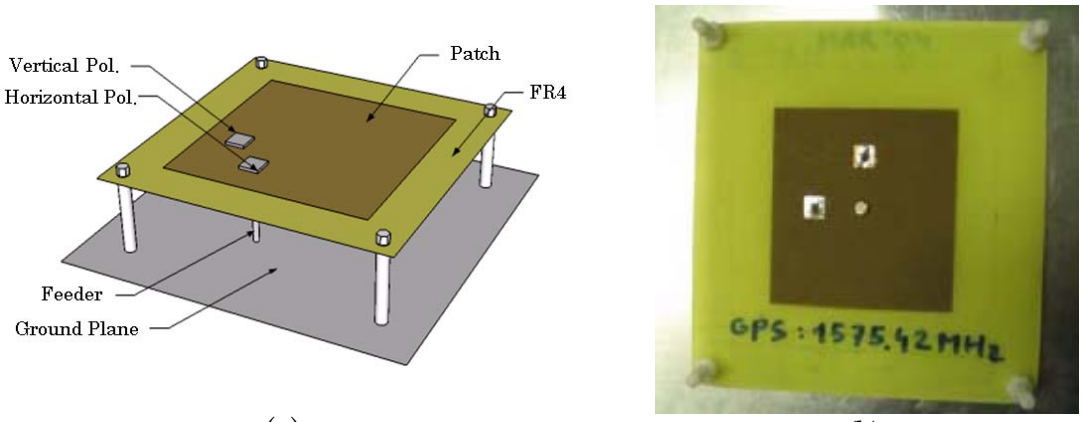

(a) (b)

Figure 7.3. Patch antenna, (a) sketch, and (b) first prototype picture.

The patch antenna is printed on a dielectric substrate with FR4 glass/epoxy specifications, and mounted on a ground plane using nylon screws. The separation between the antenna and the ground plane is air to ensure a high antenna Ohmic efficiency (low Ohmic losses, η_Ω=0.98).

Figure 7.4 shows the antenna pattern of a patch, measured in the UPC anechoic chamber [118]. Figure 7.4a shows the cut on the E plane, and Figure 7.4b shows the cut on the H plane. As it can be observed, around the maximum the antenna pattern can be reasonably well approximated by a cardioid. Both of them have a large agreement except for large off-boresight angles, where the antenna pattern is much attenuated in both cases, and the disagreement has no relevance. The patch has a beamwidth at -3 dB of 60º.

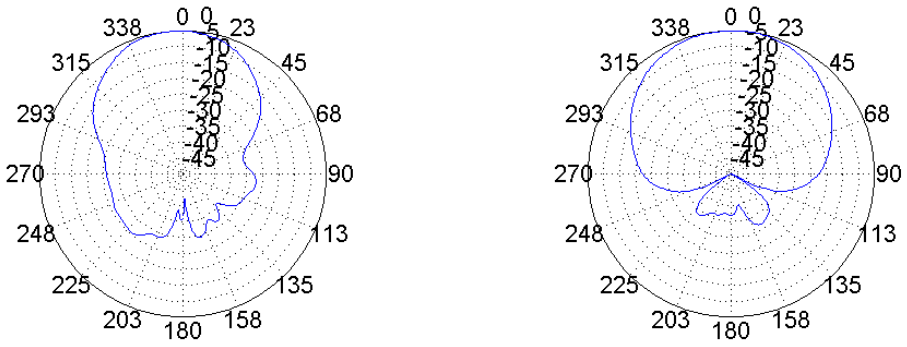

(a) (b)

Figure 7.4. Measured antenna pattern for a patch antenna: (a) E plane, and (b) H plane.

Furthermore, another important parameter to measure is the antenna matching (the antenna's parameter) to ensure that is well matched and tuned at the working frequency (1575.42 MHz).

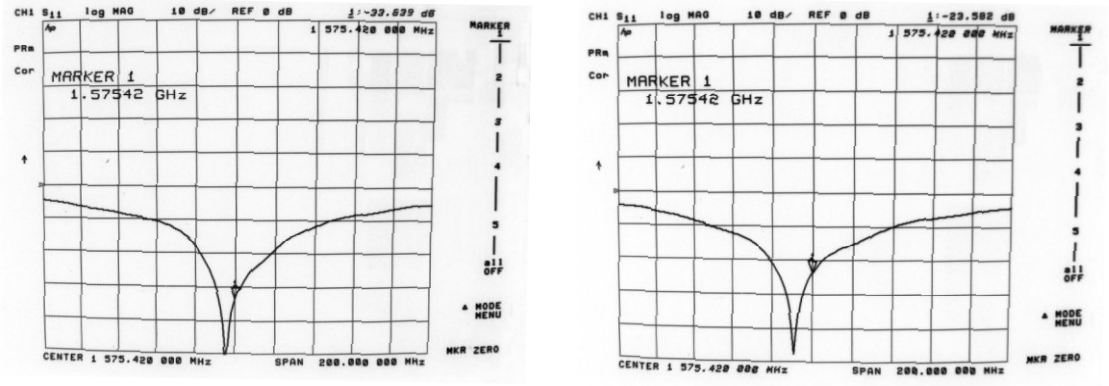

(a) (b)

Figure 7.5. Measured parameter of a patch antenna: (a) vertical polarization, and (b) horizontal polarization.

Figure 7.5 shows the measured parameter for a patch antenna. For both polarizations the resonance peak is at a lower frequency than the operation frequency. This is not a problem since the working frequency has a matching of -33 dB for the vertical, and -23 dB for the horizontal polarization.

Once the elementary antenna has been defined, prototyped and characterized, the next step is to build the antenna array using these patches (Figure 7.6).

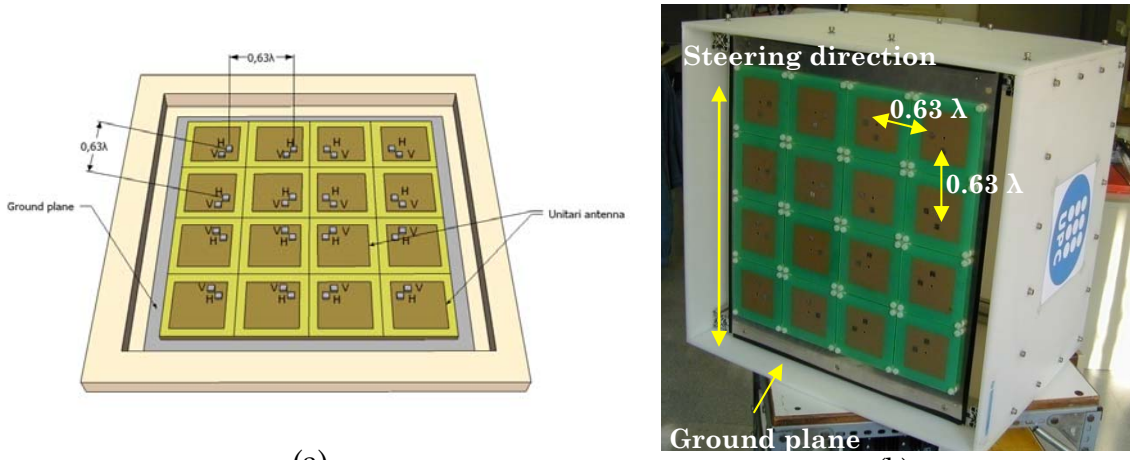

(a) (b)

Figure 7.6. Antenna array: (a) sketch, and (b) picture of the real array using the patch antennas.

As it can be seen in (Figure 7.6), the antenna array is a square of 4x4 elements with a separation between antennas of 0.63λ. The vertical direction is the one where the DBF is applied, so it is steerable, the horizontal direction is composed a RF using power combiners with the window 1:2:2:1. Moreover, the patches have been rotated sequentially to mitigate the cross-polar component. The rotated components have then to be phase shifted before being combined with the rest of the signals.

7.2.2 Analog Receiver

Analog receivers (Figure 7.7) are the most sensitive element of the analog part and they have been specially designed to avoid channel cross-talk, EMC problems and a frequency response with at least 40 dB between the band-pass and the rejected band.

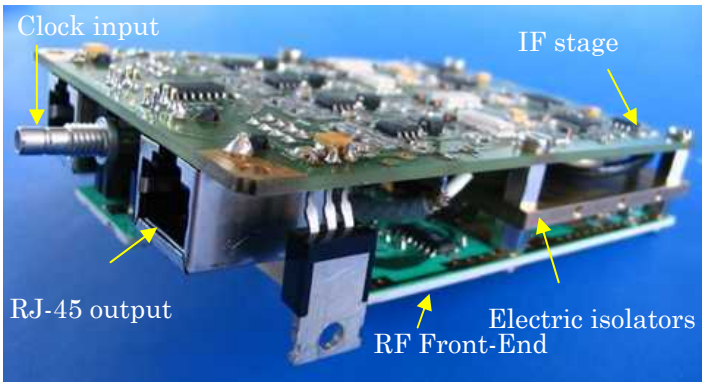

Figure 7.7. Ensembled PAU-RAD receiver out of its metallic and electrical isolation box [119].

The analog received has been designed in two separated boards (Figure 7.8 and Figure 7.9), one performing the RF stage in a microstrip board over a substrate Rogers 4003 (H=0.8 mm), with the input switches, the Wilkinson power splitters and the Low Noise Amplifiers (LNA) and the Band Pass Filters (BPF). The other board performs the IF stage and it has been implemented in FR4 dielectric substrate. The IF stage has a 3 step down-converter, going from 1574.2 MHz to 4.309 MHz (performed with the commercial chip Zarlink GP2015). Furthermore, it has a video amplifier, a matching network, and the output connector to the ADC (RJ-45 type).

7.2.2.1 The RF Front End

As discussed in Chapter 6, the DBF has strong channel equalization requirements (a maximum standard deviation of 0.1 dB in amplitude and 2º in phase in the whole array). The RF front-end (Figure 7.8 and Figure 7.9) was designed with these *a priori* specifications, including hardware elements to characterize and estimate the amplitude and phase disagreement between channels [119].

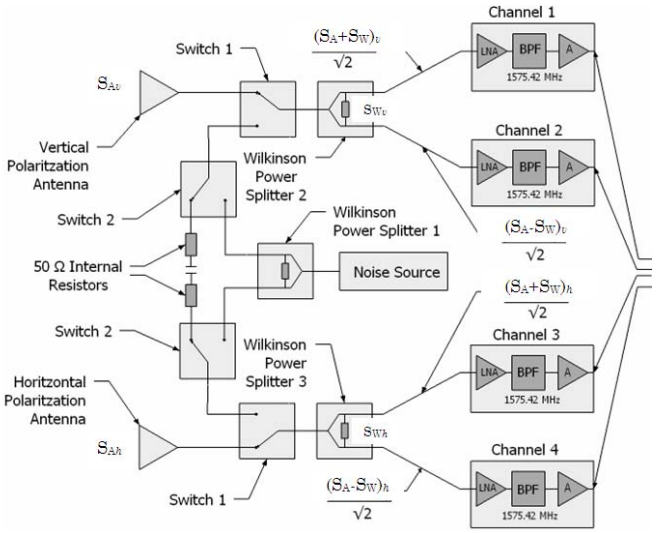

Figure 7.8. Analog receiver, RF front-end including antennas, switches, Wilkinson power splitters and four channels, 2 per polarization LNA, and BPF, the output of this stage is the input of the IF stage.

So that, two switches (switch1 and switch2 in Figure 7.8), allow the selection of the input from three different ports. The position of the input switches is controlled by the FPGA. Depending on the current state of the control unit, it switches the input port to get one of the following possible inputs:

- the antenna signal, for radiometric measurements,
- the correlated noise signal, for phase and amplitude estimation, and
- the uncorrelated noise signal, for offset calibration purposes.

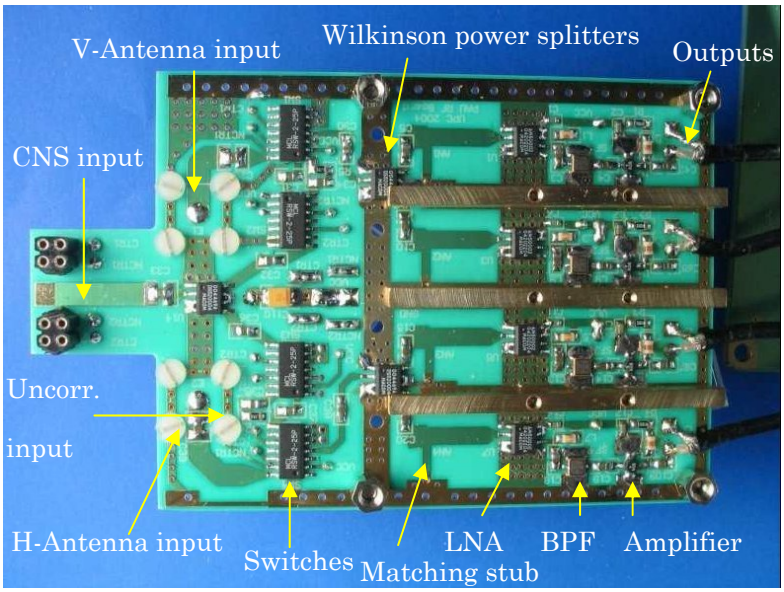

Figure 7.9. RF front-end picture, with the CNS, the antenna and the uncorrelated inputs and the output for each channel. Furthermore, the switches bank is identified and the low noise amplifier stage for each channel as well [119].

The antenna signal input is connected directly to the patch antenna through a SMA connector, while the uncorrelated noise port is connected to an internal matched load (50 Ω). The most relevant input port is the correlated noise one, which is connected to a CNS through a 1:4 power splitter. Then, it is possible to ensure, by properly switching the input port, to have identical signals at the inputs of each receiver. Correlating the output of the receivers having the same input it is possible to estimate the amplitude and phase difference among them. After the input switch, the Wilkinson power splitter splits the signal in two, one for each receiver chain. After the Wilkinson power splitter, signals follow different channels, which are symmetrical, but independent. So, the noise added from that point onwards can be considered uncorrelated among the upper and the lower branches. The first element after the Wilkinson power splitter is a LNA, despite a BPF should be the expected element before the LNA, following the communication theory. This order inversion is to minimize the whole Noise Figure (NF) of the receiver, dominated by the elements before the first LNA. After the LNA and BPF, it follows an amplifier to provide the required amplification for the best input resolution to the next element, the commercial down-converter.

All the amplification chains, after the Wilkinson power splitter are isolated among them using ground drills and a metallic structure to electrically isolate the channels and minimize the cross-talk, as it can be seen in Figure 7.9.

The main requirements of the RF front-end are summarized in Table 7.1. The gain has to be at least 20 dB, keeping a low NF. The matching of the input ports has to be better than -10 dB, for the antenna, the CNS and the matched load input. The most critical design parameters are the isolation between the CNS port and the antenna (required being lower than -80 dB) and the cross-talk (required to be better than -40 dB).

Table 7.1.Summary of the requirements of the RF stage, (a) picture of the upper channel in a generic RF stage, containing the port names, and (b) requirements accordingly the system specifications and the nomenclature established in (a).

(a)

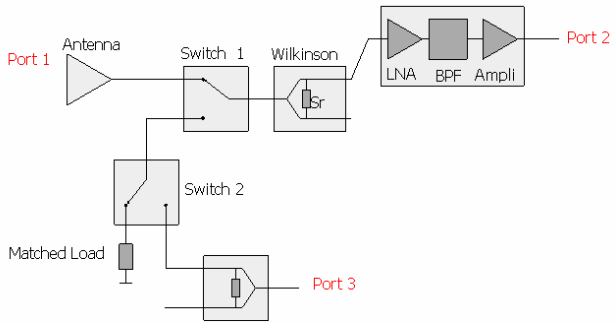

(b)

G_{RF}	> 20 dB
NF	↓↓
$\|S_{11}\|$ and $\|S_{33}\|$	<< -10 dB
$\|S_{31}\|$	< -80 dB
Cross-talk	< -40 dB

7.2.2.1.1 Noise Figure Calculation

Figure 7.10 shows the elements that have a relevant impact on the calculation of the NF. Following the Friis formula, the NF is mainly affected by the switch, the Wilkinson power splitter, and the LNA.

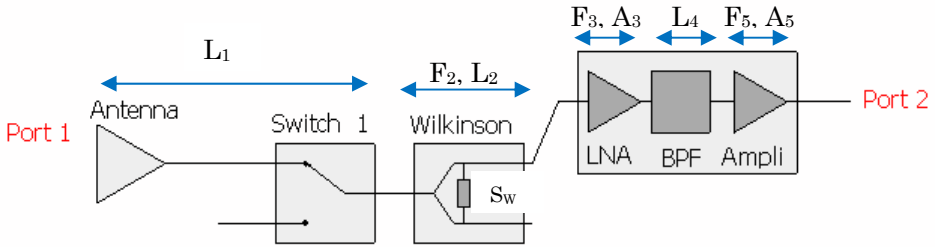

Figure 7.10. Block diagram for the RF stage to calculate the NF of the system.

In Figure 7.10, L_1 are the loses of the antenna connector and the switch input, L_2 are the loses of the Wilkinson power splitter, L_4 are the insertion loses of the RF filter, F_2 is the noise factor of the Wilkinson power splitter, F_3 is the noise factor of the LNA, F_4 is the noise factor of the RF filter and F_5 of the second stage amplifier. A_3 is the gain of the LNA and A_5 is the gain of the second stage amplifier.

From the sketch presented in Figure 7.10 the equivalent noise figure can be calculated by following the Friis formula:

$$F_{eq}=L_1 + L_1(F_2 - 1) + L_1L_2(F_3 - 1) + \frac{L_1L_2}{A_3}(F_4 - 1) + \frac{L_1L_2L_4}{A_3}(F_5 - 1). \quad (7.1)$$

Taking into account that the gain of the LNA is high (26 dB), then, it is possible to neglect the two last terms (the ones divided by the LNA gain), and Eqn. (7.1) becomes:

$$F_{eq}=L_1 + L_1(F_2 - 1) + L_1L_2(F_3 - 1). \quad (7.2)$$

The measured values to substitute the terms on the Eqn. (7.2) can be found in Table 7.2, which summarizes the detailed description and values of these NF contributors.

Table 7.2. Summary of the detailed description of the NF contributors.

Element	Detailed Description	Value (dB)
L_1	Antenna connector + switch +2 DC block	0.1+1.1+2·0.05=1.2
L_2	Insertion loses Wilkinson + DC block	0.4+0.05=0.45
F_2	Wilkinson splitter	3
F_3	Noise figure of the LNA	1
A_3	Gain of the LNA	26
L_4	BPF Insertion losses	2
A_5	Gain of the amplifier	12

And finally the NF is obtained by substituting values of Table 7.2 in Eqn. (7.2):

$$NF = 10\log(3.4) = 5.3 \text{ dB} \quad (7.3)$$

The resulting noise factor is quite high for radiometric applications, but it has to be taken into account that the $T_{Wilkinson}$, mentioned in Chapter 6, is already included into this figure. Approximately, the radiometer has a T_{sys} = 720 K which can be decomposed into $T_{Wilkinson}$=300 K and the equivalent temperature of the receiver T_R ~ 420 K.

7.2.2.1.2 RF Front-End Gain

To calculate the total gain of the RF front-end it is necessary to follow the same Figure 7.10 and perform the calculation including the gain and the insertion loses of each element as follows:

$$G = A_3(\text{dB}) + L_2(\text{dB}) + L_1(\text{dB}) + L_4(\text{dB}) + A_5(\text{dB}) = 33.35 \text{ dB}. \quad (7.4)$$

The result of Eqn. (7.4) fulfills the required gain (Table 7.1). After computing the gain of the RF section, the range of the input signal to the down-converter can be readily calculated in terms of Kelvin. The minimum input power corresponds to a T_{Cold} (T_{Cold} ~ 0 K) and the maximum corresponds to a T_{Hot} (T_{Hot} ~ 300 K) during the radiometric calibration. Then the down-converter input temperature range is:

$$T_{SYS} = T'_A + T_R = \begin{Bmatrix} 0 \text{ K} \\ 300 \text{ K} \end{Bmatrix} + 700 \text{ K} = \begin{Bmatrix} 720 \text{ K} \\ 1020 \text{ K} \end{Bmatrix}, \quad (7.5)$$

from where it is possible to calculate the input power range in dBm units

$$P_{\text{IN-GP2015}} = k \begin{Bmatrix} 720 \text{ K} \\ 1020 \text{ K} \end{Bmatrix} BG = \begin{Bmatrix} -73.25 \text{ dBm} \\ -71.74 \text{ dBm} \end{Bmatrix}, \quad (7.6)$$

where:

- k is the Boltzman constant, and
- B is the equivalent noise band.

The input power range obtained in Eqn. (7.6) is within the linear range of the GP2015 (down-converter) specifications. So, the gain achieved in the RF front end is suitable for the radiometric application.

7.2.2.1.3 Other Figures of Merit of the RF Front End

In addition to the NF, the gain and the down-converter input power range, other parameters have been measured to ensure that the receiver is suitable for radiometric applications.

Table 7.3. Comparison between specifications and measured values of crucial design parameters for a regular receiver

Parameter	Specifications	Measured	Description
$\|S_{11}\|_v$	<-10 dB	-13.9 dB	v-pol. port input
$\|S_{11}\|_h$	<-10 dB	-13.8 dB	h-pol. port input
$\|S_{22}\|_{ch1}$	<-10 dB	-13.7 dB	Channel1 output
$\|S_{22}\|_{ch2}$	<-10 dB	-13.3 dB	Channel2 output
$\|S_{33}\|$	<-10 dB	-13.6 dB	Corr. port input
Isolation	<-40 dB	-44.3 dB	Channels 1-2

Table 7.3 summarizes the most important measured parameters. For instance, each input, both polarizations and correlated noise, and output ports have a matching better than -13 dB, fulfilling the design specifications. Furthermore, the channels isolation is always better than -44 dB, fulfilling the design specifications again.

7.2.2.2 The IF Stage

The IF stage (Figure 7.11) down-converts the input signal from 1575.42 MHz to the output signals which are centered at an IF of 4.309 MHz with a bandwidth of 2.2 MHz.

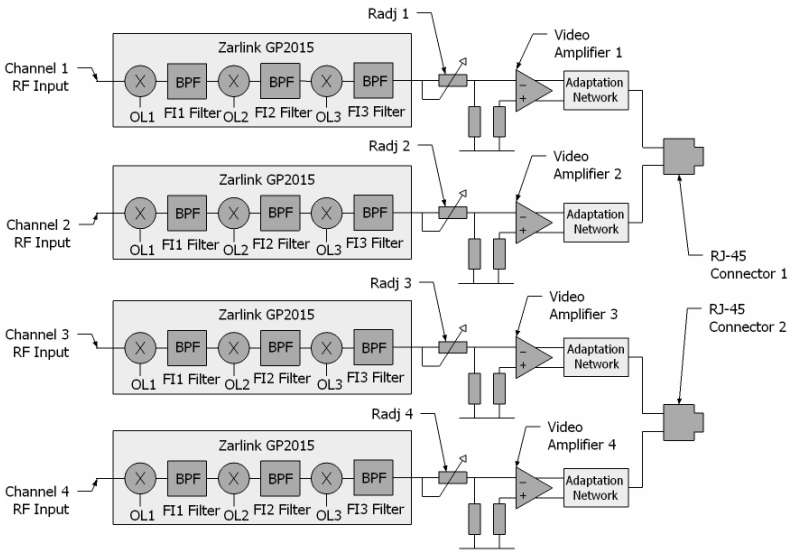

Figure 7.11. Analog receiver sketch, IF stage with 4 channel (2 per polarization) including the 3 steps down-converter (Zarlink GP2015), a video amplifier per channel, output matching network and the connector to the ADC (RJ-45 type).

Mainly, it consists of a 3 stages down-converter, video amplifiers and an impedance matching network. The video amplifiers allow a manual amplitude adjustment (by modifying R_{adj}) to ensure that all the system channels have the same output power with accuracy better than ±1 dB. Note that the fine amplitude adjustment is then

performed in the digital part, using advanced processing algorithms as described later on. After the IF stage, signals are sampled using 8 bits analog-digital converters and processed in the FPGA.

The most remarkable fact of the IF stage is that a commercial GPS receiver (Figure 7.12) is used for radiometric applications. Usually, a GPS receiver, even the GP2015, has an Automatic Gain Control (AGC) system which modulates the gain depending on the input signal to have a constant power level at its output. On the contrary, the aim of the radiometry is to measure the input power, but with this system enabled in the receiver it is no possible. Fortunately, the GP2015 has the AGC control accessible on the chip pins (23 and 24 in Figure 7.12), and it has been tuned for disabling the AGC by forcing a static voltage between the AGC pins. This AGC tuning gives approximately an extra 30 dB of constant gain to the down-converter.

Another remarkable feature of this chip is that not only it has the typical IF signal digitized two bits output (sign and magnitude), but it also has available the IF signal in the analog domain (pin 1), which after the last amplification stage and a matching network is 8 bit sampled and processed in the FPGA. As it has already discussed on Chapter 4, two bits are not enough to calculate the cross-correlation or the power of the signals without a significant linearity error.

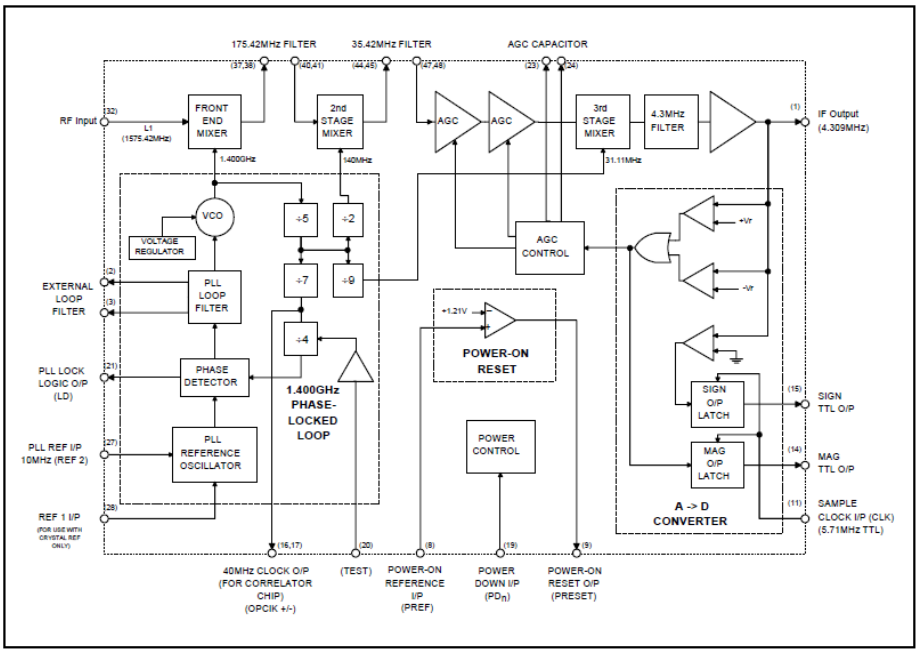

Figure 7.12. GP2015 block diagram, showing the clock sequence generation for each mixer stage, the Automatic Gain Control, the analog IF output and two bits (sign and magnitude) digitized output [107].

The GP2015 has a 48 pin Thin Quad Flat Pack (TQFP) package with dimensions 7 x 7 x 1.4 mm, its power supply range goes from 3 up to 5 volts, the power consumption when is supplied at 3 V is 200 mW, and the maximum power at the RF stage is +15 dBm.

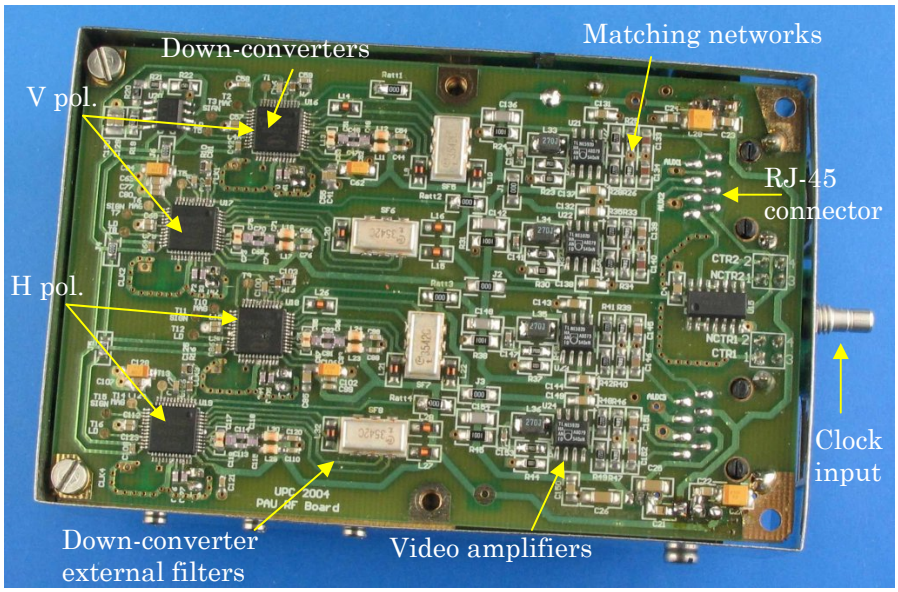

Figure 7.13. Analog receiver picture, IF stage with 4 channel (2 per polarization) including the down-converter (Zarlink GP2015 [107] and a video amplifier per channel [119].

Figure 7.13 shows a picture of the IF board of a PAU receiver. There are 4 down-converter (GP2015) channels (2 per polarization) with its external filters. Each channel has its own video amplifier and its own matching network.

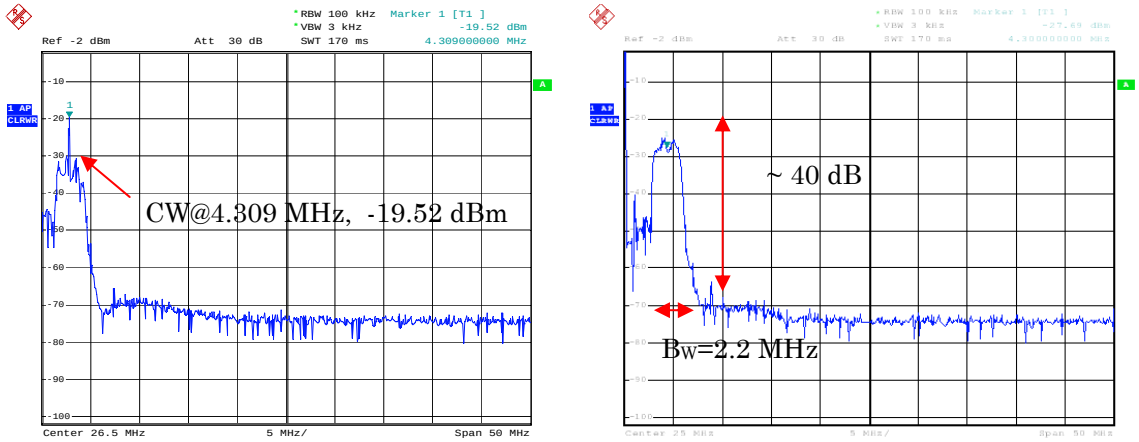

(a) (b)

Figure 7.14. Frequency response of the RF-IF receiver (a) Receiver #1 channel 1, test performed with a Carrier Wave (CW) centered at 1575.42 MHz with a power of -110 dBm at the RF-front end input, and (b) Receiver #2 channel 1, system response without input.

Figure 7.14 shows the frequency response of two whole RF-IF receiver. This test was performed entering a carrier signal centered at 1575.42 MHz with a power of -110 dBm at the antenna port. The output signal is centered exactly at 4.309 MHz, the down-conversion is properly working, and the output power is -19.52 dBm, the whole receiver gain, is about 91 dB (distributed along different down-conversion stages to avoid input output coupling). Furthermore, it shows that the frequency

response has a bandwidth of 2.2 MHz and a 40 dB of attenuation between the pass-band and the rejected band.

PAU-RAD requires 4 of these RF-IF analog receivers (2 polarizations per each) to perform the beamforming (one per antenna row) although they are not presented here for brevity. All receivers have similar features and performance.

7.2.3 Analog to Digital Converter

After the IF stage, signals are digitized and processed in the FPGA. This section focus on the Analog to Digital Converter (ADC). The number of required bits for a correlation radiometer is a topic that has been analyzed on Chapter 5. The number of bits used in PAU-RAD is 8 for two main reasons: to get an estimation of the correlation value close enough to the true correlation without any required linearity conversion, and to have a low standard deviation with short integration periods.

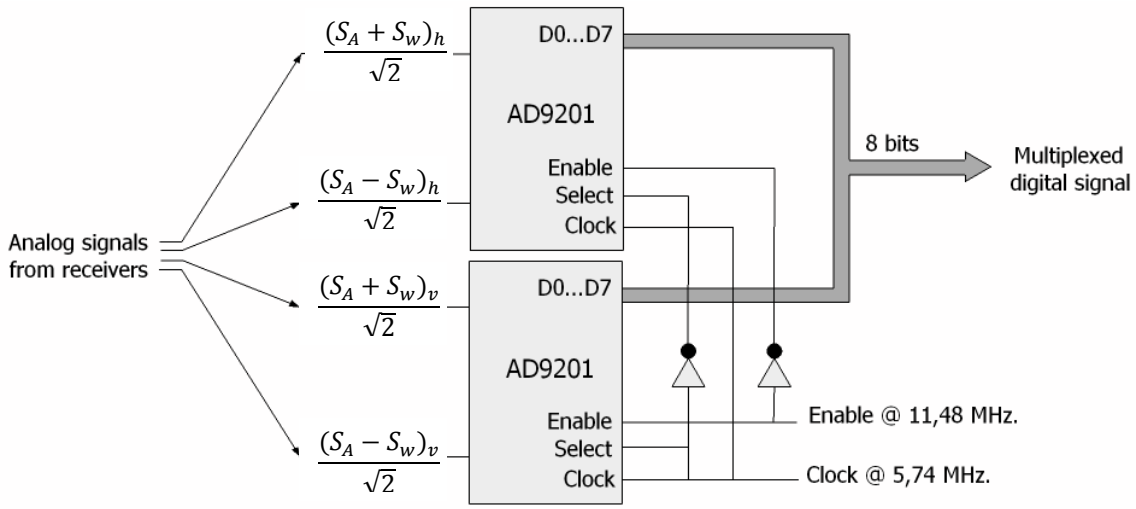

Figure 7.15. ADC sampling scheme, it digitizes 2 polarizations (4 channels), the output is time multiplexed over an 8 bit bus. Two control signals synchronize the sampling and time multiplexing.

Therefore, the analog signals are sampled using 8 bits at 5.745 MHz, a sampling rate higher than the IF, which allows a kind of "band-pass sampling" technique [122] to be applied producing the PAU-RAD input signals centered at 0.25 times the digital frequency. The digitization of the 4 receiver channels (one receiver or 2 complete polarizations) is performed with a 2 dual-channel 8-bit A/D converter (Analog Devices AD9201 [120]). The output bus is shared by both ADCs (Figure 7.15), which are synchronized and operate at a sampling frequency of 5.745 MHz (Clock). An internal multiplexer determines which digitalized channel is present at the chip's outputs, and it is controlled by a signal at 11.49 MHz (Enable), so in half-period of Clock each chip will be able to put both channels information in the output bus. The control signals are supplied by the FPGA to keep the synchronism through the internal digital process.

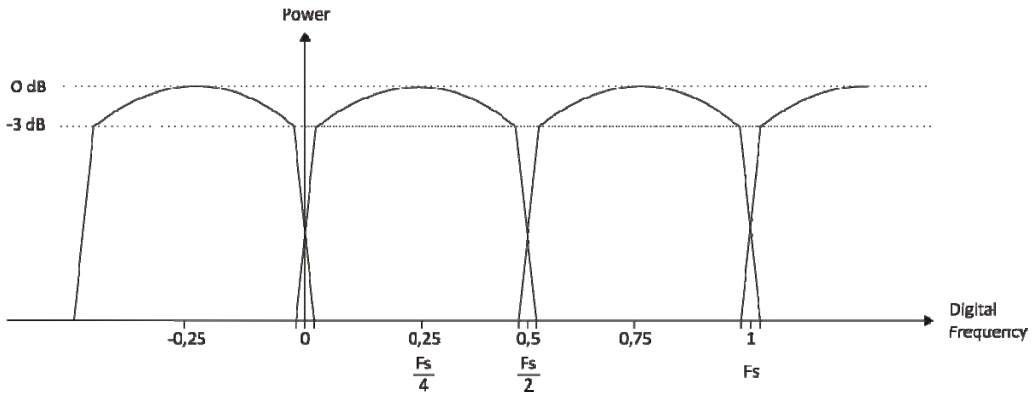

Figure 7.16. Sampled signal frequency plan.

Taking into account that the input signals are centered at 4.309 MHz, the outputs are then centered at 1.436 MHz. With a sampling rate of 5.745 MHz the spectrum is centered at a 0.25 times the digital frequency (Figure 7.16). As it has already been said, this is a kind of band pass sampling and the Nyquist sampling rate is fulfilled as the bandwidth of the signal is B_w = 2.2 MHz and, so that $F_s > 2B_w$. On the other hand, Figure 7.16 clearly shows that the spectrum of the input signal goes from 0 to 0.5 times the digital frequency, so the analog signal has to have a high attenuation (-40 dB) rejecting band to avoid alias overlapping.

The signals from each of the 2 polarizations enter into the FPGA multiplexed by 4, taking into account that there are 4 elements, the FPGA must be capable to process 91.92 Mbytes per second. In other way, to properly process this data flux the FPGA design must operate, at least, at 4 times the sampling frequency, *i.e.* 22.98 MHz Figure 7.17 shows a picture of one ADC used in PAU-RAD. Figure 7.17a shows the input pins of the control signals, the output 8 time multiplexed bus and the ground connectors to unify the FPGA, the analog receiver and the ADC grounds, and Figure 7.17b shows the buffer to sharp the digital outputs (increasing their slew-rate), the ADCs set, the input matching network and the RJ-45 connector from where the inputs signals enters from the analog receiver though an Ethernet cable (Z_{in} = 75 Ω).

In order to have less than 0.1 % samples out of range (clipping) the standard deviation of the signal must be σ_{signal} = 110 mV since the ADC dynamic range (V_{ADC}) is set to 1 V. The digital output values go from 0 that corresponds to -0.5 V, to 255 that corresponds to +0.5 V. A 128 offset value is present at the output data and it has to be removed in the first processing stages of the FPGA.

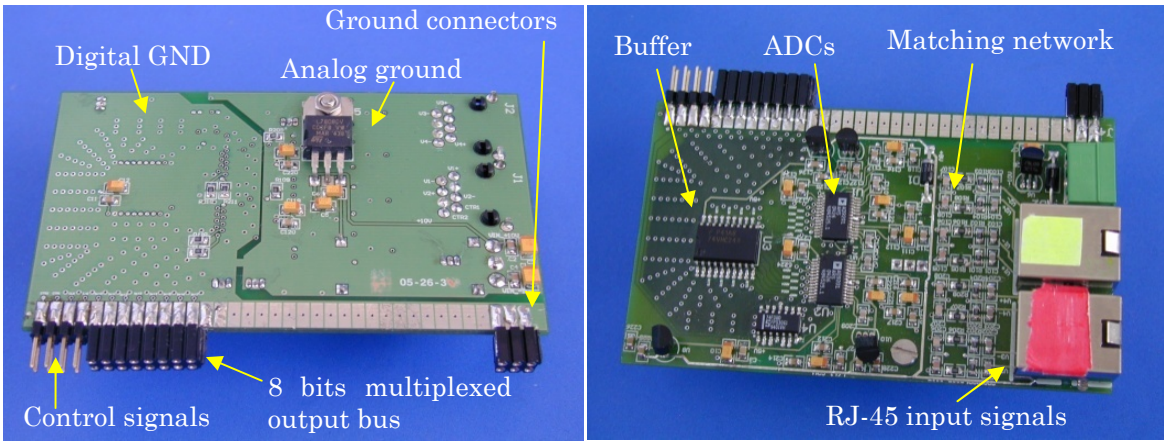

(a) (b)

Figure 7.17 Picture of one ADC, (a) back view, showing the input pins of the control signals, the output is x8 time multiplexed in the bus and the ground connectors, the analog receiver and the ADC grounds, and (b) front view, showing the buffer to sharp the digital outputs (increasing their slew-rate), the ADCs set, the input matching network and the RJ-45 connector.

Although here are not presented for brevity, PAU-RAD requires 4 of these ADC (one per analog receiver). All ADCs have similar features and performance.

7.2.4 Controlled Noise Source

The CNS (Figure 7.18) is a hardware subsystem that provides a different power and a common reference signal through the correlated noise port to the 4 receivers to estimate their relative amplitude and phase. It consists of a temperature controlled box with a very stable noise source [121] (NC346, ENR=17.5 dB at 1.5 GHz, $\Delta ENR/\Delta T$ = 0.009 dB/K and $\Delta ENR/\Delta V$= 0.002 dB/%V), a variable attenuator, and a mechanical switch connected to the variable attenuator and to a matched load.

With this hardware configuration (CNS + power splitter by 4 outputs) and properly choosing the attenuators, it is possible to have at the input of each receiver a common signal of 450, 370 or 300 K. Receivers' response are linear within these three values and they are separated enough to ensure a correct performance of the estimation of the amplitude and phase errors.

The CNS has two external bits (Figure 7.18) that are controlled by the FPGA. In fact they are controlled by the control unit, which has the finite state machine. Depending on the current state, it switches the control bits to get one of the three possible internal temperature references.

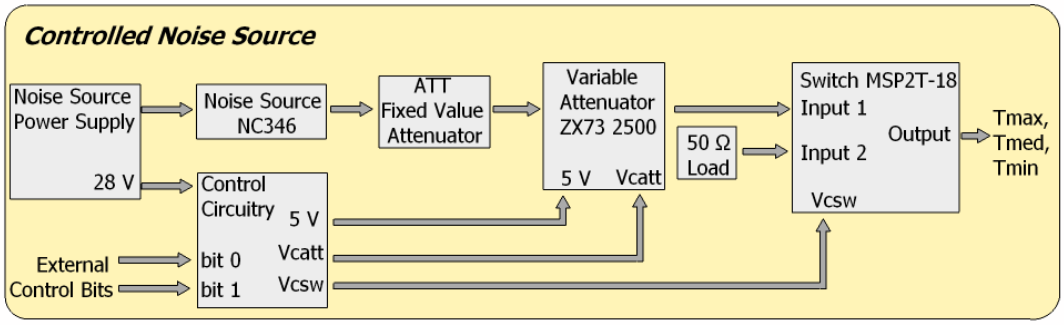

Figure 7.18 The Controlled Noise Source sketch, it shows the two bits control signal provided by the FPGA and the three possible output temperatures: T_{max}, T_{med}, and T_{min}.

Figure 7.18 shows a sketch of the CNS, which is contained in a thermal isolated box. The noise source (NC346) provides the stabilized noise, this is attenuated by a static attenuator. Thence, it is attenuated depending on the control bit configuration by the variable attenuator (ZX73) and a switch (MSP2T) provides the output to a 1:4 power splitter, which distributes the signal with four cables to the receivers. Even with exact length cables it is not possible to ensure that at the input of each receiver there is the same signal in phase and amplitude terms. This is due to the S parameter matrix of the power splitters, which have different amplitude and phase values for different outputs. As the difference of amplitude and phase of the distribution network is static it is possible to estimate the amplitude and phase errors among receivers by using a pre-calibration algorithm (Chapter 8).

The static and the variable attenuators have been calculated to ensure that at the input of each channel receiver, not at the output of the CNS, there is a correlated noise with a power of 450, 370 or 300 K. So that, in the Friis formula to calculate these values there is included the 1:4 splitter, the distribution cables, the RF receiver loses, and the Wilkinson power splitter.

7.2.5 Thermal Control System

Temperature stability becomes critically important for a radiometer because even a small change in the physical temperature of the receiver can lead to noticeable fluctuation in gain and change the reference load temperature, thus degrading the radiometric resolution. So that, a thermal control system has been developed for PAU-RAD in order to stabilize the system and avoid these output fluctuations.

The thermal control part consists of a commercial Proportional Integrative Derivative (PID) control using a 100 Platinum Resistance Thermometer (PT100) thermal sensor, offering an excellent accuracy over a wide temperature range. The control uses an H-bridge to drive enough current to eight 2 A Peltier cells, which are the active part of the control. Each Peltier cell is assembled with fans and heat

sinks to ensure an efficient thermal system. PAU-RAD is thermally insulated by using expanded polystyrene foam (EPS) boards (Figure 7.19), which has a high thermal resistivity [123] about 28 mK/W. Moreover, internal fans are used to obtain a good temperature homogenization. With this thermal control system, a previously tested demonstrator [40] has achieved an internal temperature peak to peak variation < 0.2ºC.

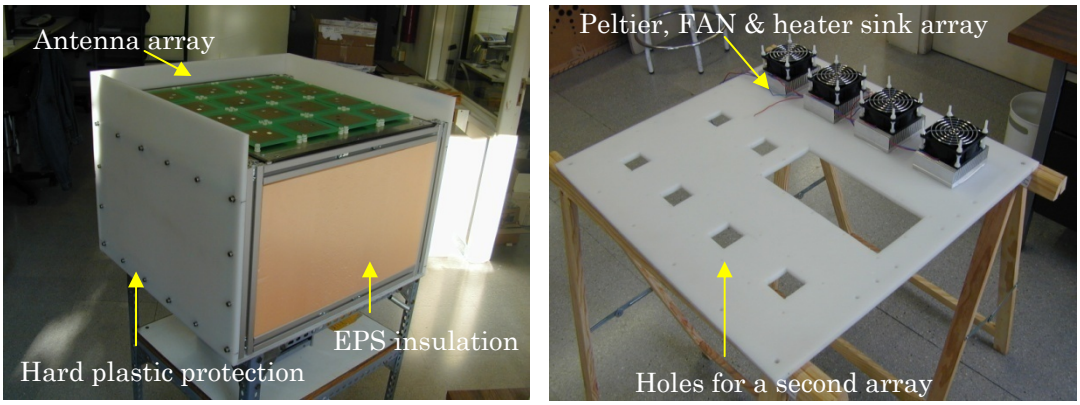

(a) (b)

Figure 7.19 PAU-RAD thermal insulation, (a) side view showing the EPS layer and the hard plastic protection, and (b) back view, opposite to the antenna array side, showing the fans and heat sinks being mounted (8 elements in total).

The thermal control is an autonomous system which does not depend on any other part of PAU-RAD. Even the thermal control power supply (1.5 kW) is a separated power supply, without relation with the rest of the power systems, to avoid current peaks which can interfere or damage the receivers or the FPGA. The commercial PID has a display with two key front-end which allows the configuration of the target temperature and some other parameters.

Even though the thermal control is independent from the rest of the systems, there is a set of digital thermometers (15 in total) to sense the current temperature inside the PAU-RAD system. There are two thermometers for each receiver (8 in total), two located on the heat sinks, two on the receivers' power supplies, one inside the CNS, one sensing the FPGA, and another one sensing the PAU-RAD's inside air temperature.

7.2.6 Mechanical Structure and System Integration

The PAU-RAD mechanical structure (Figure 7.20) consists of an aluminum cube of 110 x 120 x 80 cm size. The antenna ground plane is placed on the top of the structure (see Figure 7.20a), on the opposite side there is the hooker system to attach the system to other structure to be able to measure. Furthermore, in this side there are the plugs to power the system and the communication connectors, the thermal control display, and the two four-element Peltier, fan and heat sinks.

Due to the reduced dimensions of the system there is little space to attach the different subsystems that compose the PAU-RAD. So that, two laterals have a foldable 5 mm aluminum sheet to allow attaching on them, while providing the accessibility to the inside of the system. On these foldable sides there are attached the power supplies, the h-bridges for the thermal control, and the power distribution system.

(a) (b)

Figure 7.20 PAU-RAD mechanical aluminum structure with a size 110 x 120 x 80 cm, (a) the structure empty, and (b) the structure being mounted, with the empty FPGA's structure in the center.

Figure 7.20b shows the structure during the assembling process from the back side view, the antenna ground plane has been attached to the structure and the analog receivers have been placed over the ground plane. A new support has been attached in the center of the structure (Figure 7.21).

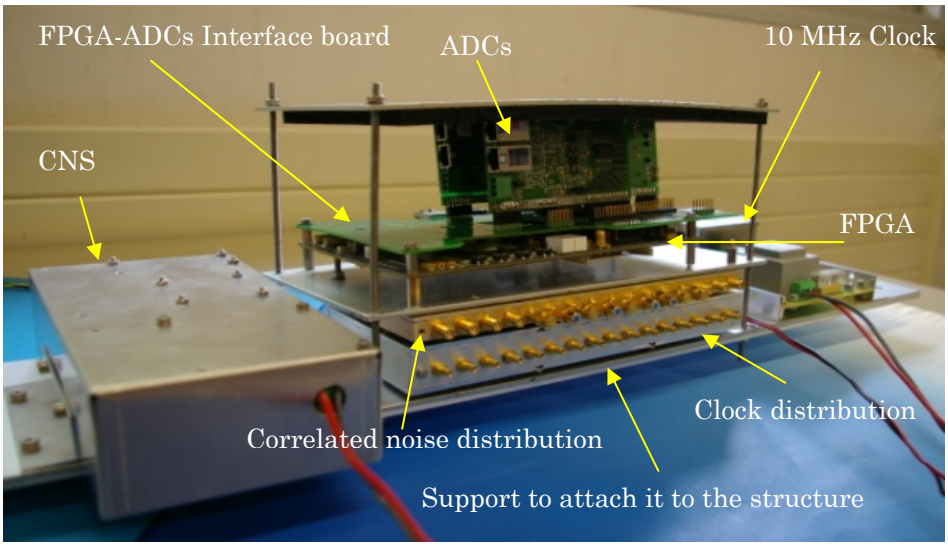

Figure 7.21. The middle structure with the FPGA and other crucial systems attached on it.

Figure 7.21 is the support for the FPGA, the 10 MHz clock, the distribution clock system to drive the analog receivers, the CNS, and the correlated noise distribution (power splitter). These subsystems have been placed in the middle of the structure

to have a symmetrical distribution, with similar lengths, of the receiver's common signals such as the clock, the CNS signal, and the receivers output.

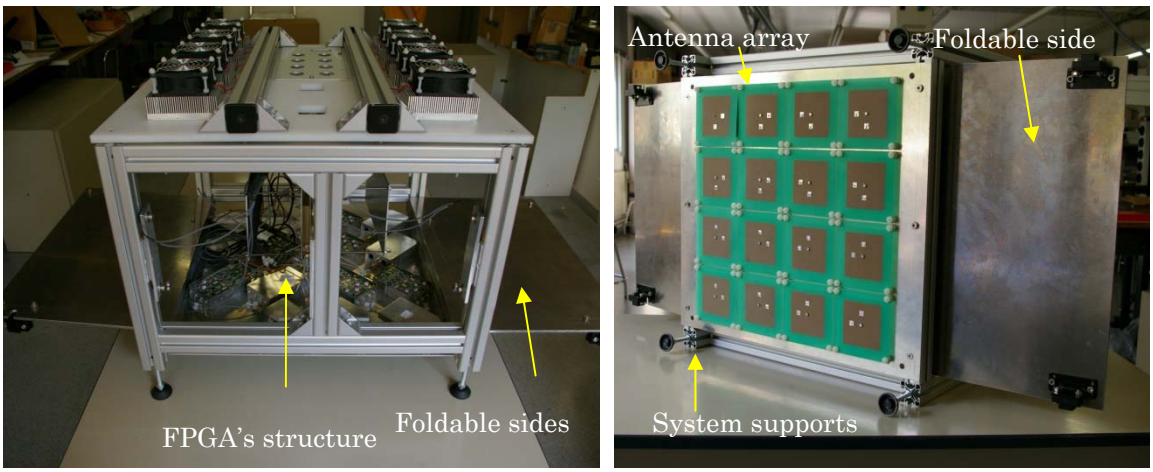

(a) (b)

Figure 7.22. PAU-RAD mechanical structure being integrated: (a) a lateral view of the structure open, and (b) an antenna array perspective.

Figure 7.22 shows two other perspectives of the PAU-RAD, Figure 7.22a shows the structure from the top, the two transversals aluminum bars at the top are the system hook, then there are the two thermal arrays at the edges of the structure. Furthermore, it is possible to see in the middle of the two bars, the holes for the power and communication plugs. Figure 7.22b shows an antenna array perspective, there are four supports at the borders of the ground plane, they are there only for assembling purposes to avoid damaging the antenna, after the assemble process they are removed, so as not to disturb the antenna pattern.

7.3 PAU-RAD Digital Radiometer

This section is related to the digital design of PAU-RAD. As it has been already said at the beginning of this chapter, there is not a single way to perform a digital beamformer. Here the PAU-RAD solution is described. It gives versatility to the system and allows to easily modifying any of its parts, being an ideal platform for developing, testing and measuring.

For simplicity, the digital part, implemented inside the FPGA, has been designed in two parts (Figure 7.23). One of these parts is an VHDL-93 [108] self-designed Arithmetic-Logic Unit (ALU), where the DBF and radiometric data process takes place, and a Control Unit (CU), which is a Nios2 from ALTERA [124] (a 32 bit VHDL-embedded microprocessor) and manages the system.

However, this design split has some advantages, but it appears a communication problem as the ALU and the CU have a high level of interaction and data

exchanging. This problem has been overcome with an efficient self-designed data-exchanging protocol.

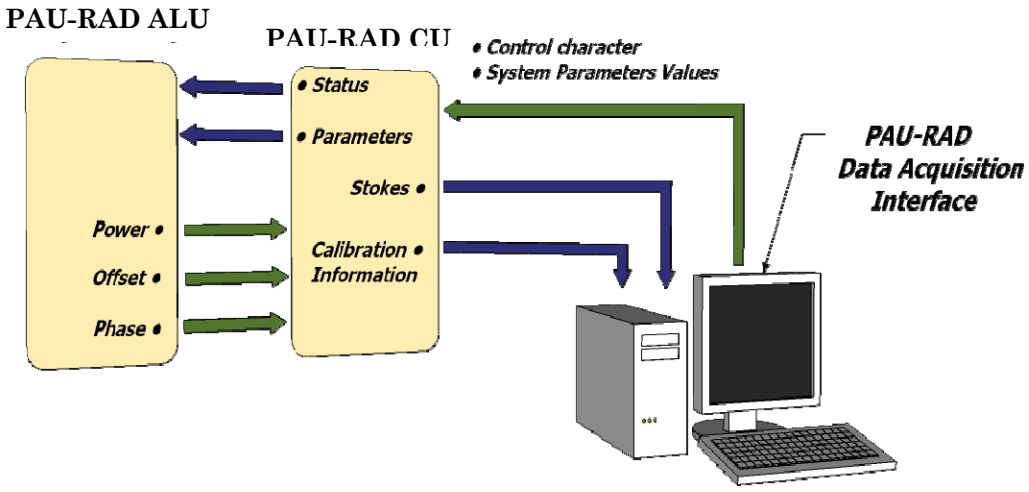

Figure 7.23. PAU-RAD digital part, ALU, CU, and PC data flux sketch.

Figure 7.23 shows the main interaction of the digital part of PAU-RAD, the ALU processes the input data from the ADC, and delivers the results to the CU (power, offset, and visibilities). The CU sends that data package to an external Personal Computer (PC) through a RS-232 connection. The PC displays in real-time the received data and storages it into a record file. The PC has a Graphical User Interface (GUI) to ease the interaction between the user and the PAU-RAD. Several configuration parameters can be modified through the GUI such as the integration time, the steering angle or the system status. Once the CU receives the new order, it reconfigures itself to follow the command. Furthermore, the CU is a finite state machine that periodically changes it status sending commands and data to the ALU. The most important data that sends the CU to the ALU are the values of the look-up tables of the Numerical Controlled Oscillators, used to equalize the channels and to down-convert the signals (from 0.25 times the digital frequency to 0).

7.3.1 The Altera's Development Board

PAU-RAD digital design has been embedded in an Altera Nios2 Development Board (Figure 7.24), which is an FPGA development board that can contain a Nios2 [124] microprocessor. The FPGA of this development board is the Stratix II EP2S60F672C5, it is programmed through a Joint Test Action Group protocol (JTAG) connector and the implemented digital hardware is described using the hardware description language VHDL-93.

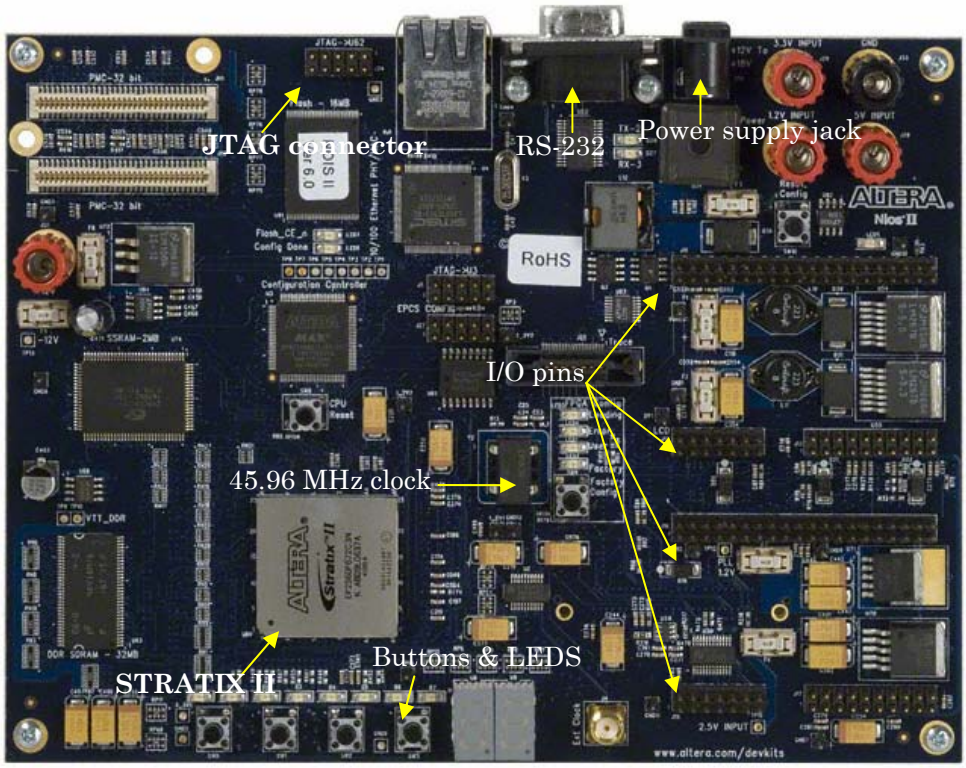

Figure 7.24 Altera Nios2 development board picture, with the Stratix II FPGA

The Nios2 development board, Stratix II Edition, provides a hardware platform for developing embedded systems based on Altera Stratix II devices. The development board provides the following features (illustrated in Figure 7.24):

- one Stratix II FPGA (EP2S60F672C5),
- 16 Mbytes of flash memory,
- 1 Mbyte of static RAM,
- 16 Mbytes of SDRAM,
- two 5 V-tolerant expansion/prototype headers each with access to 41 Stratix II user I/O pins,
- a RS-232 DB9 serial port,
- four push-button switches connected to Stratix II user I/O pins, and
- JTAG connectors to Altera devices.

In addition of the features of the board, the FPGA has its own resources and features that determine if the design fits in it or not. The most relevant parameters are summarized in Table 7.4. The significant ones are the number of Logic Elements (LE), the number of Random Access Memory (RAM) blocks, the number of Digital Signal Processing blocks and the number of multipliers.

Table 7.4. Summary of the detailed features and resources of the Stratix II EP2S60F672C5.

Element	Number of elements
Equivalent LEs	60440
M512 RAM blocks	329
M4K RAM blocks	255
M-RAM blocks	2
Total RAM bits	2544192
DSP blocks	36
18-bit x 18-bit multipliers	144
Enhanced PLLS	4
Fast PLLs	8

On the other hand, the software used to design the Nios2 Central Process Unit (CPU) and its peripherals is the System on a Programmable Chip Builder v7.1 (SOPC Builder), which is an Altera software that automates connecting VHDL-hardware components to create a complete computer system that runs embedded on an FPGA. Furthermore, it incorporates a library of pre-developed components (memory controllers, interfaces, and peripherals) and an interface for incorporating custom ones. A GUI is the only tool used to configure the VHDL-hardware components. Quartus2 v7.1, software of Altera, has been used for coding the VHDL. This Altera provided software allows synthesis and analysis of HDL designs. It performs timing analysis, examination of Resistor Transistor Logic (RTL) diagrams, simulation of a design's reaction to different stimuli, and configuration of the target device with the JTAG programmer.

7.3.2 Arithmetic-Logic Unit

The PAU-RAD ALU has been coded using the VHDL-93 digital description language. It has been compiled and synthesized using the standard tools provided by Altera, and taking advantage of the DSP resources (multipliers and accumulators) available in the development board. Since the input frequency is 5.75 MHz and the FPGA clock is 45.96 MHz (8 times faster), signal multiplexing and hardware reuse have been intensively used in order to save FPGA recourses and maximize their use.

Instead of using one dedicated digital design for each input signal, these techniques use a digital design for more than one input signal. This is done by taking advantage of the non-action periods of the FPGA (in this case 7 over 1) due to the much higher clock frequency. Obviously, this increases the synchronism complexity because it is necessary to relate the ADC output to a synchronous signal to know which signals being processed at every clock cycle. Furthermore, to improve the maximum operating frequency two techniques are used:

- Parallelization, that involves sequential circuits (changes a multiple cycle serial operation to a multiple stage parallel operation), and

- Pipelining, that involves combinational circuits (changes a high delay combinational circuit in to multiple low delay circuits with registers). In these conditions the PAU-RAD operating frequency must be the same as the sampling frequency, but data will be actually processed at a much higher frequency, approaching the FPGA maximum cycle.

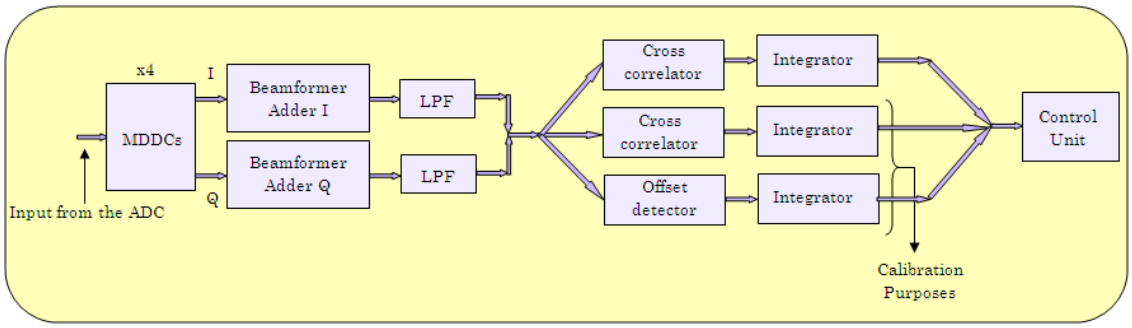

Figure 7.25. PAU-RAD digital radiometer data processing scheme.

From a functional point of view, the ALU processes the acquired data (8 bits per 2 polarizations and per 4 receivers), equalizes the channels, performs the DBF and computes the four Stokes parameters. The data path is schematically shown in Figure 7.25. First, each ADC output is acquired, independently down-converted and treated in a block so-called Multiplexed Digital Down-Converter (MDDC). Then, for each polarization signals, the in phase (I) and quadrature (Q) components are properly added creating the selected beam. From here, signals are low pass filtered (LPF). Thus, depending on the CU status, filtered signals are complex cross-correlated, and accumulated to obtain polarimetric antenna information or phase and amplitude differences between channels. Meanwhile, signals are integrated without any correlation to compute their offset. Offset information is used for calibration purposes. All the results are sent to the CU, which it can use this information to update the NCOs or only re-sending it to the PC.

7.3.2.1 Multiplexed Digital Down-Converter

The Multiplexed Digital Down-Converter (MDDC) (Figure 7.26) is a block which processes all the signals coming from a single ADC (2 signals per 2 polarizations). This is done taking advantage of the higher working frequency of the FPGA (45.96 MHz) and the time-multiplexed way in which signals enters into the FPGA. Furthermore, the MDDC block is also fully adaptive to create new beams or compensate the phase/amplitude error correction.

The raw input signal, as it comes from the ADC, is not suitable for data processing because it has an offset (128). This offset is related with the ADC output that gives a binary quantification of the analog signal between 0 and 255. So that, it is necessary to subtract this offset to have positive and negative values symmetrically and, at the same time, convert the signals into 2's complement.

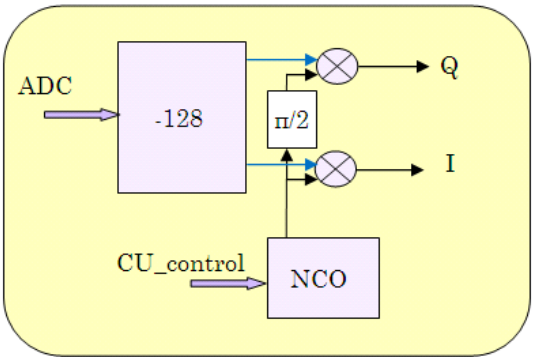

Figure 7.26. Multiplexed Digital Down-Converter sketch, the ADC's offset is subtracted to the input signal and then down-converted to in-phase and quadrature signals.

Before to perform the digital beamforming, all channels have to be down-converted from 0.25 times the digital frequency to 0, must have a zero relative phase and same amplitude, and a progressive complex weight has to be properly assigned to each receiver to steer the beam. As it has already been discussed, channels have to be previously equalized. Channels phase differences are related to the fact that the analog receivers do not have the same Local Oscillator (LO), but a 10 MHz reference clock is distributed and the phase at each PLL locks is a uniform random variable within 0 to 2π radians. Amplitude differences are introduced by gain variations (aging and drifts) from each receiver's chain, and are expected to be within ±1 dB.

It is possible to down-convert the signals to baseband, apply the beam steering phase and perform the phase and amplitude equalization the signals performing with a single multiplication between the signal and a two trigonometric functions (cosine and sinus). The cosine signal is created by the Numerically Controlled Oscillator, which consists of a simple look-up table accessed periodically and sequentially. On the other hand, a similar process is followed to create the sinus signal, but with an extra phase of π/2 with respect the cosine function (at 0.25 times the digital frequency it consist of a 1 sample delay). The CU updates the NCO's amplitude and phase according the requirements. In fact, the NCO shown in Figure 7.26 is a set of oscillators instead of only one. Each channel of each polarization has its own NCO (2 channels x 2 polarizations x 4 receivers, 16 NCOs in total). Furthermore, NCOs are time-multiplexed as the whole MDDC block. The content of each NCO look-up table is shown in Eqn. (7.7):

$$\mathrm{LUT}_i(n) = (A_{Beam}A_{Cal}A_{ph}) \cdot \cos\left(2\pi\Omega n + (\theta_{Beam} - \theta_{Cal} - \theta_{ph})\right) \qquad (7.7)$$

where:

- $\mathrm{LUT}_i(n)$ stands for Look-Up Table of the i^{th} receiver,
- Ω and n are the digital frequency and digital time, respectively,

- A_{beam} and θ_{Beam} are the modulus and phase of a complex weight assigned to each receiver to steer the beam in the desired direction,

- A_{Cal} and θ_{Cal} are the modulus and phase of a complex weight assigned to each receiver for hardware equalization, and

- A_{ph} and θ_{ph} are the modulus and phase of a complex weight to correct any antenna error such as center phase or different path lengths. These values were measured at the UPC anechoic camber [118], and set as system parameters.

Values of the LUT_i are calculated by the CU depending on the beam steering, estimated phase and amplitude equalization, and the physical correction determined on the anechoic chamber. The NCO is updated when a new beam is synthesized or the instrument is equalized.

Although this topic has been discussed on Chapter 6, another important parameter of this block is the amplitude and phase resolution of the NCO, which clearly depends on the number of bits and the maximum amplitude difference to be corrected. In this case, the NCO uses 18 bits (2 dedicated 9 bits multiplier for each I/Q down-conversion) to correct the amplitude within a ±10 dB range with a resolution of 4.10^{-5} and the phase within the range from 0 to 2π with a resolution of 0.003 rad (0.2º)

7.3.2.2 Beamformer, Low Pass Filter, and Cross-Correlator

After the MDDC, the digital beamformer signal is formed by adding the 4 signals that came from the MDDCs, this is done for the I and Q components of each channel (upper and lower ones) of each polarization (2 x 2 x 2 beams composed of 4 signals each one, in total 8 beams with the same steering but different signals). The beamforming is performed using a weighted adder (1:2:2:1) in order to have a triangular illumination on the steering direction. Once the signal of the beamformer has been created, the next step is to filter the 8 beams. To do this an IIR filter has been chosen instead of FIR one, due to the smaller order (fewer resources) than required to obtain the same attenuation as compared to a FIR. Even though, the main drawback of the IIR filters is that they have an infinite memory due to the output feedback loop. This makes the IIR filters potentially unstable when they saturate, to avoid this possibility the PAU-RAD filter has a control system that resets all the registers of the filter in case of an output overload is detected.

Usually, a digital filter is a combination of adders and coefficient multipliers, which usually requires a significant amount of hardware resources to be implemented, DSP blocks or LEs, as the signal is multiplied by single precision resolution coefficients. In this case, each coefficient of the filter selected for PAU-RAD (Eqn. (7.8)) is a power of two (in fact, all of them are 0.5), which implies to halve the

input signal, *i.e.* a right shift of the bit vector (exchanging multipliers by bit shifters), which saves a significant amount of resources and simplifies the filter's design.

$$H(z) = \frac{0.5 + z^{-1} + z^{-2} + 0.5z^{-3}}{1 + 0.5z^{-2}} \tag{7.8}$$

The diagram sketch of this filter, described in Eqn. (7.8), is shown in Figure 7.27, as it is implemented in the FPGA. The total hardware resources used are four adders, three right vector shifters, and five vector digital latches for having up to 3 delayed samples for the input signal and up to 2 delayed samples for the output signal.

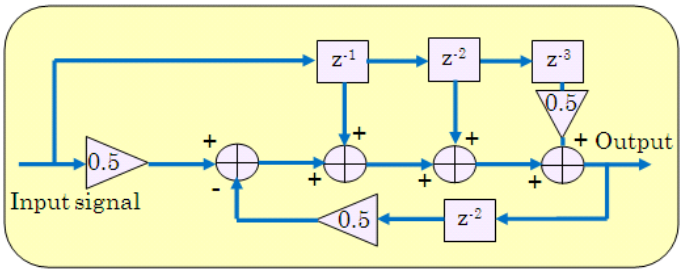

Figure 7.27. PAU-RAD post down-conversion IIR filter sketch, described in VHDL.

The frequency response of the PAU-RAD filter is presented on Figure 7.28:

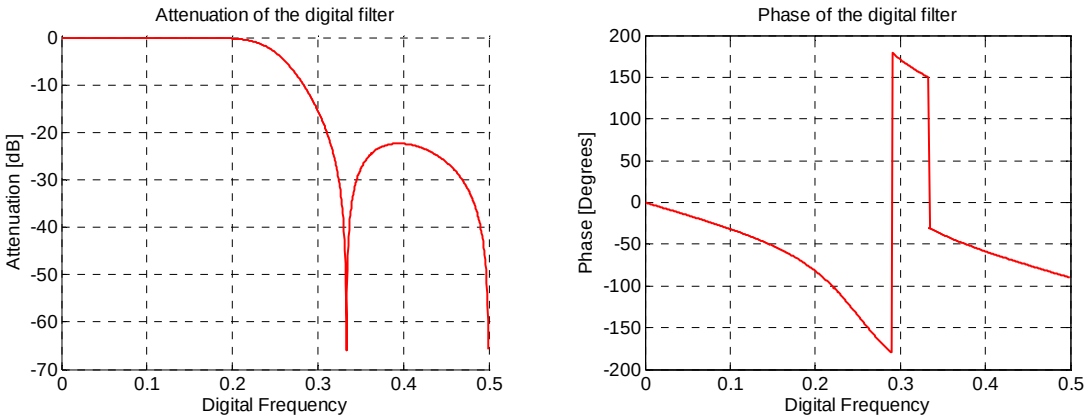

Figure 7.28. PAU-RAD filter frequency response, (a) attenuation, and (b) phase.

As it can be seen, the bandwidth at -3 dB is 0.25 times the digital frequency which exactly matches the bandwidth of the input signal, and the rejected band is -23 dB. The phase remains linear over almost the whole pass-band, from 0 up to 0.25 times the digital frequency. These features make this filter suitable for the PAU-RAD application.

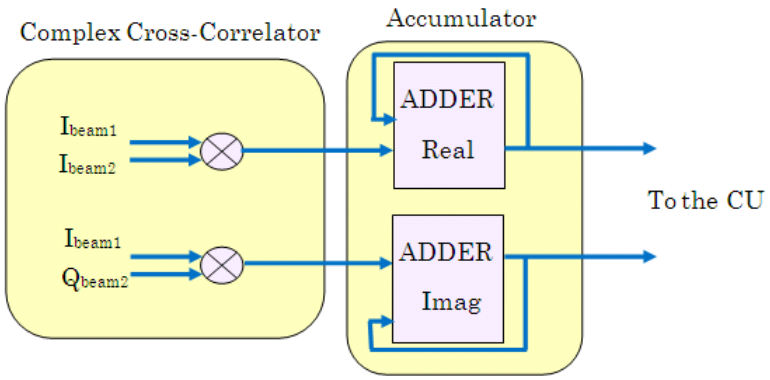

Figure 7.29. Complex cross-correlator and accumulator sketch, signals are multiplied and then accumulated. PAU-RAD has 3 of these correlator-accumulator blocks, two for the vertical and horizontal polarization, and another one for the vertical-horizontal correlation.

Once the beamformer signals are obtained and filtered, they are cross-correlated by properly multiplying their in-phase and quadrature components and accumulating the results in the accumulator block as shown in Figure 7.29. The correlation on the complex cross-correlator block is performed at 8 bits, enough to ensure linearity between the true and the digitized correlations (Chapter 4). After the cross-correlation, signals are accumulated using two adders with a feedback loop. The real adder accumulates the real part of the complex correlation, and the imaginary adder accumulates the imaginary part of the complex correlation. Signals are continuously accumulated waiting for the end of the integration period, which is triggered by a dedicated timer (a discounter adder initialized by the CU). When integration time is done, the accumulated complex correlations are latched in a special registers and, thence sent to the CU. Meanwhile, the accumulator has been reset and it keeps on accumulating without losing any sample.

PAU-RAD has 3 of these correlator-accumulator blocks, two for the vertical and horizontal polarizations (first and second Stokes parameters), and another one for the vertical-horizontal correlation (third and fourth Stokes parameters). The difference between them is their input signals. For instance, in the case of the vertical polarization, the inputs are the filtered signals $I_{beam1}= I_{beam\_V}+I_{beam\_WilkinsonV}$, $I_{beam2}= I_{beam\_V}-I_{beam\_WilkinsonV}$, and $Q_{beam2}= Q_{beam\_V}-Q_{beam\_WilkinsonV}$. So, if the relative phase of the beam composing signals is exactly zero, then the real accumulator result is proportional to the vertical antenna temperature minus the Wilkinson temperature ($T_{A_v} - T_{w_v}$), and the imaginary accumulator result is zero (Chapter 6). Otherwise, if the relative phase of the signals is not zero, due to a miss-equalization or residual errors, then the modulus of the result is the same, but it is rotated by the averaged residual phase ($\theta_{residual}$). Hence, the real accumulator result is proportional to $(T_{A_v} - T_{w_v})\cos\theta_{residual}$, and the imaginary accumulator result is proportional to $(T_{A_v} - T_{w_v})\sin\theta_{residual}$. The case of the horizontal polarization is equivalent in inputs and results.

On the other hand, when the signals to be correlated are the vertical and horizontal polarizations at the same time, the inputs are the filtered signals $I_{beam1}=$

$I_{beam\_V}+I_{beam\_WilkinsonV}$, $I_{beam2}= I_{beam\_H}-I_{beam\_WilkinsonH}$, and $Q_{beam2}= Q_{beam\_H}-Q_{beam\_WilkinsonH}$. So, if the relative phase of the beam composing signals is exactly zero, the real accumulator result is proportional to the half of the third Stokes parameter and the imaginary accumulator result is proportional to the half of the fourth Stokes parameter. Otherwise, the third and fourth Stokes parameters are rotated exactly in the same way the first and second Stokes parameters are rotated.

7.3.2.3 Amplitude and Phase Estimation

Additionally to the subsystems shown at the beginning of this Section (Figure 7.2), there is another essential sub-system, which is not directly related to the radiometer data processing. This sub-system accomplishes the function of estimating the amplitude and phase errors between receivers (Figure 7.30). When this hardware block is enabled, the CU switches the input analog receiver signal from the antenna signal to a correlated noise signal to estimate the phase and amplitude errors. The correlated noise is needed to ensure that at the input of each chain has the same power and phase, in this way it is possible to determine the relative errors between channels and equalize them.

The complex correlation between a reference receiver signal (I_{REF}) and the RUT signals (I_{RUT} and Q_{RUT}) gives information about the amplitude and phase differences among them (Chapter 9). Thereafter, this result is sent to the CU, where mathematical algorithms to derive the amplitude and the phase differences are implemented and Kalman filtered [96] reduce the estimation error. This information is used to update the correspondent RUT's NCO look-up table.

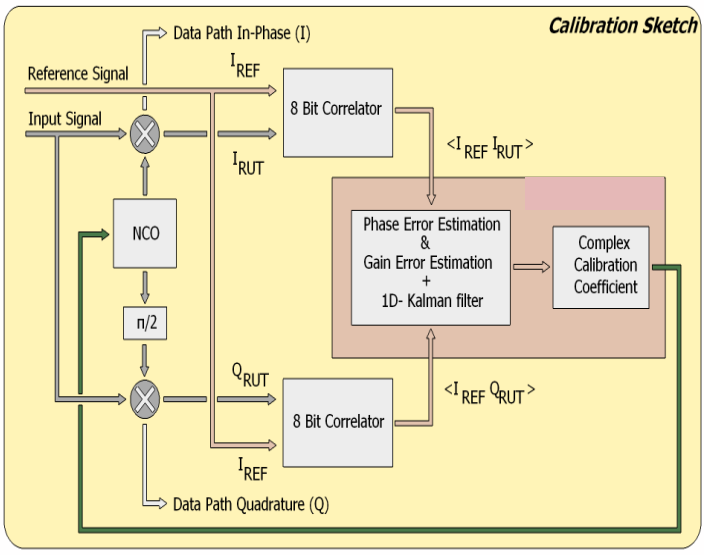

Figure 7.30. Error estimation and calibration sketch. The ALU performs the complex correlation to estimate the complex equalization, and the error correction (NCO). On the other hand, the CU performs the error retrieval and the 1D-Kalman filter.

Although the detailed method to estimate the phase and amplitude from the cross-correlation values is described on Chapter 8, here a glimpse is given for a better understanding of this section. Roughly, the system can be considered to be equalized when all the RUTs satisfy these two points:

- $<I_{REF}Q_{RUT}>=0$, then the system is phase equalized, and
- $<I_{REF}I_{RUT}>_{Tmax} - <I_{REF}I_{RUT}>_{Tmed} = <I_{REF}I_{REF}>_{Tmax} - <I_{REF}I_{REF}>_{Tmed}$, then the system is amplitude equalized. The previous relationship means that the increment of correlation for two different input temperatures should be the same in case of having a cross-correlation (REF, RUT), or the correlation of the reference signal (REF, REF).

This block is a complex correlator with an accumulator. It is equivalent to the block shown in the previous section, with 8 bit multipliers and accumulators. The main difference between them is that now the input signals are not the beam signals, but are reference signals coming from a reference receiver (arbitrarily chosen) and a signal coming from the Receiver Under Test (RUT). The RUT is the receiver which is currently being phase and amplitude estimated with respect the reference receiver. The RUT input signals are changed sequentially accordingly the dispositions of the CU through an input multiplexer in order to estimate the phase and amplitude errors of all receivers.

7.3.3 The Control Unit

The CU implements the PAU-RAD finite state machine, performs the communication protocol between the ALU and the CU, and between the CU and the PC. Furthermore, it calculates the equalization coefficients using the information of the cross-correlation and the appropriate algorithms (Chapter 8). The CU runs over a Nios2 microprocessor, embedded in the FPGA of the development board. The CU has been written in ANSI C language using the Eclipse Integrated Development Environment (IDE) v3.1.

7.3.3.1 Nios2 Processor and Its Peripherals

The Nios2 processor is a 32 bit Reduced Instruction Set Computer (RISC) with instruction cache, memory cache, branch prediction, hardware multiply and hardware divide. Operating at 91.92 MHz (twice the current FPGA working frequency, obtained through a PLL) it has a performance up to 59 MIPS (Millions of Instructions per Second). Additionally to the processor itself, the SOPC Builder software allows to the user to include and interconnect several peripherals to the Nios2 processor (Figure 7.31).

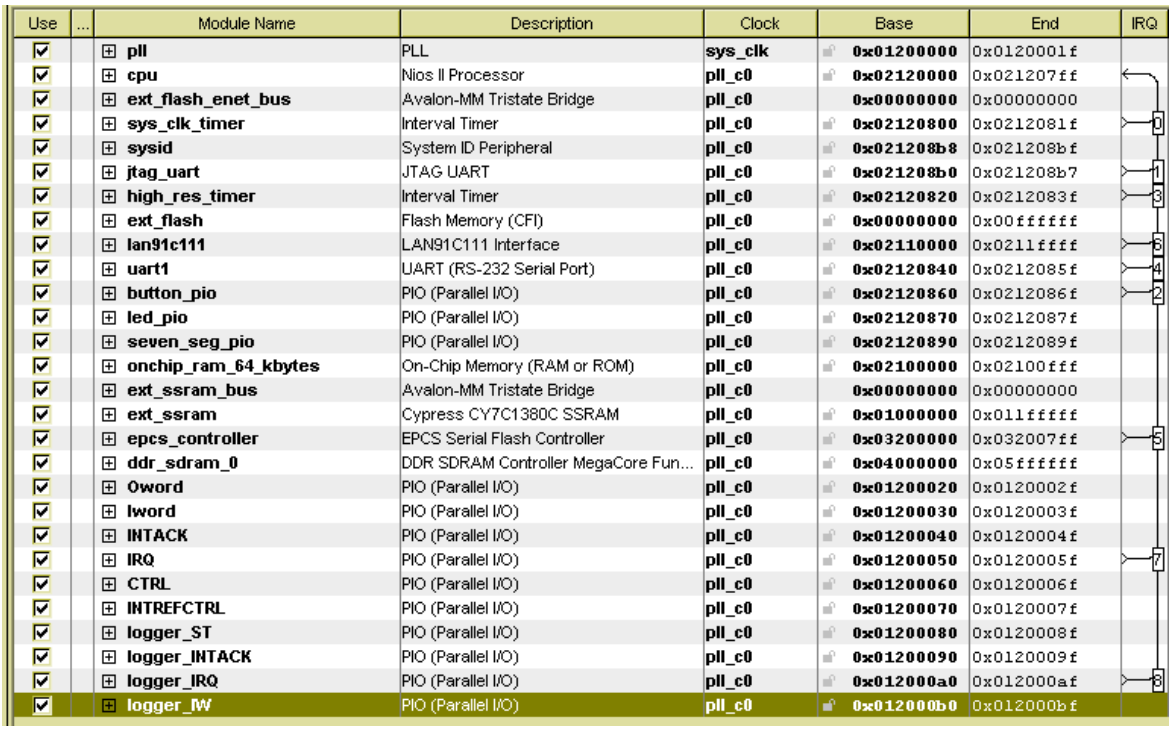

Use	...	Module Name	Description	Clock	Base	End	IRQ
☑		pll	PLL	sys_clk	0x01200000	0x0120001f	
☑		cpu	Nios II Processor	pll_c0	0x02120000	0x021207ff	
☑		ext_flash_enet_bus	Avalon-MM Tristate Bridge	pll_c0	0x00000000	0x00000000	
☑		sys_clk_timer	Interval Timer	pll_c0	0x02120800	0x0212081f	0
☑		sysid	System ID Peripheral	pll_c0	0x021208b8	0x021208bf	
☑		jtag_uart	JTAG UART	pll_c0	0x021208b0	0x021208b7	1
☑		high_res_timer	Interval Timer	pll_c0	0x02120820	0x0212083f	3
☑		ext_flash	Flash Memory (CFI)	pll_c0	0x00000000	0x00ffffff	
☑		lan91c111	LAN91C111 Interface	pll_c0	0x02110000	0x0211ffff	6
☑		uart1	UART (RS-232 Serial Port)	pll_c0	0x02120840	0x0212085f	4
☑		button_pio	PIO (Parallel I/O)	pll_c0	0x02120860	0x0212086f	2
☑		led_pio	PIO (Parallel I/O)	pll_c0	0x02120870	0x0212087f	
☑		seven_seg_pio	PIO (Parallel I/O)	pll_c0	0x02120890	0x0212089f	
☑		onchip_ram_64_kbytes	On-Chip Memory (RAM or ROM)	pll_c0	0x02100000	0x02100fff	
☑		ext_ssram_bus	Avalon-MM Tristate Bridge	pll_c0	0x00000000	0x00000000	
☑		ext_ssram	Cypress CY7C1380C SSRAM	pll_c0	0x01000000	0x011fffff	
☑		epcs_controller	EPCS Serial Flash Controller	pll_c0	0x03200000	0x032007ff	5
☑		ddr_sdram_0	DDR SDRAM Controller MegaCore Fun...	pll_c0	0x04000000	0x05ffffff	
☑		Oword	PIO (Parallel I/O)	pll_c0	0x01200020	0x0120002f	
☑		Iword	PIO (Parallel I/O)	pll_c0	0x01200030	0x0120003f	
☑		INTACK	PIO (Parallel I/O)	pll_c0	0x01200040	0x0120004f	
☑		IRQ	PIO (Parallel I/O)	pll_c0	0x01200050	0x0120005f	7
☑		CTRL	PIO (Parallel I/O)	pll_c0	0x01200060	0x0120006f	
☑		INTREFCTRL	PIO (Parallel I/O)	pll_c0	0x01200070	0x0120007f	
☑		logger_ST	PIO (Parallel I/O)	pll_c0	0x01200080	0x0120008f	
☑		logger_INTACK	PIO (Parallel I/O)	pll_c0	0x01200090	0x0120009f	
☑		logger_IRQ	PIO (Parallel I/O)	pll_c0	0x012000a0	0x012000af	8
☑		logger_IW	PIO (Parallel I/O)	pll_c0	0x012000b0	0x012000bf	

Figure 7.31. SOPC Builder v7.1 screenshot with the current Nios2 design. It shows how are related the Nios2 processor (cpu) and its peripherals.

Figure 7.31 shows the PAU-RAD CPU and its peripherals in five main columns. The first significant column is the Modulus Name, where components are listed by name. The Clock column relates the system clocks. All the peripherals work with the output of the PLL (pll_c0), except for the PLL itself which is using the system clock (sys_clk). The Base and End columns show the Nios2 memory mapping in hexadecimal format. Finally, the IRQ (Interrupt ReQuest) column indicates the IRQ priority of each peripheral. The most remarkable peripherals shown in Figure 7.31 are:

- PLL is a PLL used to multiply by two the nominal working frequency (from 45.96 to 91.92 MHz),
- CPU is the Nios2 core, which executes the C code,
- JTAG_UART is the JTAG interface to download executable software to the Nios2,
- UART1 is the Universal Asynchronous Receiver-Transmiter (UART) and it is used for communication purposes between the UC and the external PC,
- Iword (Input Word) is a 32 bit Parallel Input Output (PIO) mapped into the Nios2 memory, it is used for the communications from the UC to the ALU,
- Oword (Output Word) is a 32 bit PIO mapped into the Nios2 memory, it is used for the communications from the ALU to the UC,

- IRQ is a 1 bit PIO mapped into the Nios2 memory, it accomplishes the function of an IRQ signal, and it is generated by the ALU to indicate to the UC that there is a new ready to acquire data on the Oword PIO.

- INTACK is a 1 bit PIO mapped into the Nios2 memory, used as Interruption Acknowledged, and it is generated by the UC to indicate to the ALU that the Oword PIO has been already read.

- CTRL is a 2 bit PIO mapped into the Nios2 memory, they are the control of the RF hardware switch described in Section 7.2.1.1 , and

- INTREFCTRL is a 2 bit PIO mapped into the Nios2 memory, they are the control of the CNS switch described in Section 7.2.3.

In addition to the devices described before, the microprocessor has more devices such as a bus control system, a Local Access Network (LAN-Ethernet) interface, a high resolution timer, a button-push PIO, seven segment displayer, and different memory type controllers among others less important.

Once the system has been defined, it is VHDL generated by the SOPC-Builder and the result is imported by the Quartus2 to be linked to the general design. Once the Nios2 has been generated, some support C libraries are created for making easy the interaction with the peripheral, the memory access and the main system functions calls.

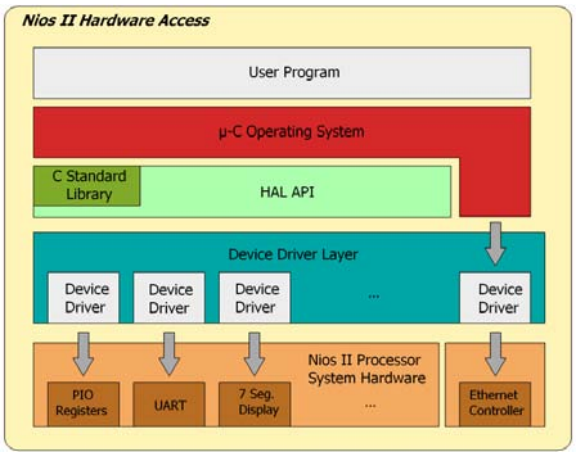

Figure 7.32. Nios 2 hardware access protocol and its abstraction layers

Figure 7.32 shows a sketch of the Nios 2 hardware access layers. Mainly, it has four hierarchical abstraction layers for accessing to a peripheral. The top layer is the final user program. The second layer, that is an optional layer, corresponds to the µ-C OS (Operating System). The next level corresponds to the Hardware Abstraction Layer (HAL), which is a mix of standard C libraries and the specific libraries created by the SOPC-Builder when the processor is synthesized. This layer allows the Nios 2 accessing to the development board peripherals. The fifth, and the last, level is the peripheral drivers, which are very low level functions.

Despite this well organized structure, there are some limitations that make impossible to use the OS for this application, such as it is impossible to control and make constant the timing for the execution of the different steps of the program due to OS internal process. Of course, using the OS it is possible to time-control a function with the internal timer, but it is still impossible to have the whole system timing well delimitated, which is crucial for the PAU-RAD equalization and acquisition procedures.

For that reason the UC has been programmed as a standalone application instead of an OS application. Furthermore, the UC has been developed between the HAL and the driver device layers, for having much control over the system and peripherals. However, there are drawbacks on not using the OS, one of them is the impossibility of use the Ethernet controller because its libraries are only available on the OS layer. This is why the output data are sent through the UART despite there is an Ethernet controller, faster than the UART.

7.3.3.2 The CU Algorithm Description

The CU is a finite state machine (Figure 7.33) that changes the system status according to internal variables and external requests through the PC program (*External Control*). The entire CU system and the data flow shown in Figure 7.33 have been written in ANSI C. For the state machine state data flow, the most important state variables are the integration time for each radiometric sample, and the inter-calibration time, between hardware calibrations.

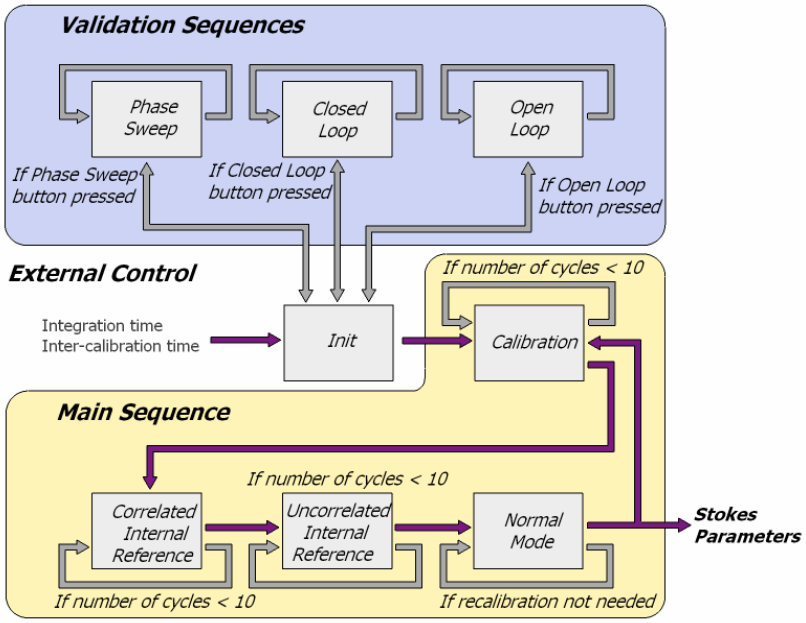

Figure 7.33. CU finite states machine diagram and interactions.

The states of the CU can be classified in two groups: the *Main Sequence* ones that perform the radiometric normal operation and flow, and the *Validation Sequences* used for testing and debugging purposes. The *Main Sequence* states are:

- *Init*: is the initialization mode and waits for the PC remote control connection.

- *Calibration*: the CU sets the ALU to measure the complex cross-correlations between the reference receiver and, sequentially, the other ones, when the CNS is connected to receivers' inputs (using the 2 bit CTRL signal). The temperature of the input signal is selected among the three possible values by the CU (using the 2 bit INTREFCTRL signal). The measured amplitude and phase at different time instants are then filtered using a Kalman filter to reduce the noise variance (Chapter 9). Finally, the CU updates the RUT's look-up table and modifies the NCO amplitude and phase values accordingly (using the IWord signal). At this time, the relative equalization has been performed and the DBF is ready to operate.

- *Correlated Internal Reference*: the CU sets the ALU to compute the Stokes parameters from the signals obtained after the DBF, when the CNS is connected to the receiver's inputs. This mode is used to perform the internal radiometric calibration, maximizing the period between external calibrations, and it is performed for each synthesized beam.

- *Uncorrelated Internal Reference*: the CU sets the ALU to compute the Stokes parameters from the signal obtained after the DBF, when the matched loads are connected to receivers' inputs. This mode is used to compute the offsets of the Stokes parameters and it is performed for each synthesized beam.

- *Normal mode*: the CU sets the ALU to compute the Stokes parameters (radiometric observables) from the signals obtained after the DBF, when the antennas are connected to the receiver's inputs. The system stays in this mode since the receiver phase and gain drifts degrade the beam. This loop is shown in Figure 7.33 labeled as *if calibration not needed*. This period is established empirically and depends on the required performance and the application. Moreover, it determines the tradeoff between calibration and measurement time.

The validation sequences states are:

- *Phase Sweep*: the CU sets the ALU to measure the complex cross-correlations between the reference receiver and a RUT. The goal of this sequence is to sweep the phase of each NCO from 0 to 2π. As described in [28] and [82], this test helps to determine amplitude unbalances between I and Q branches, quadrature and phase errors, and offset errors. In PAU-RAD, since signals are sampled at IF and I/Q demodulation and low-pass filtering is performed digitally, there are only offset errors, therefore only information related to the RUT's complex offset is obtained.

- *Open Loop*: same as before, but with all RUTs and keeping constant the NCO to evaluate RUTs' temporal drifts.
- *Closed Loop*: same as before, but updating the RUTs' NCO to track equalization errors.

7.3.4 ALU-CU Communication Protocol

In order to discharge the ALU of any communication procedure that can result in a signal process miss attending, there is still another VHDL block called NiosCom (Figure 7.34). The aim of the NiosCom block is to manage the communications between the ALU and the CU, and to receive, decode, and execute the instructions sent by the CU to the ALU. So that, NiosCom establishes is a fully bidirectional communication channel between the ALU and the UC. NiosCom has two different blocks for attending the two possible communication directions. The nioscom_r block performs the communication from ALU to CU, and the nioscom_w block performs the communications backwards.

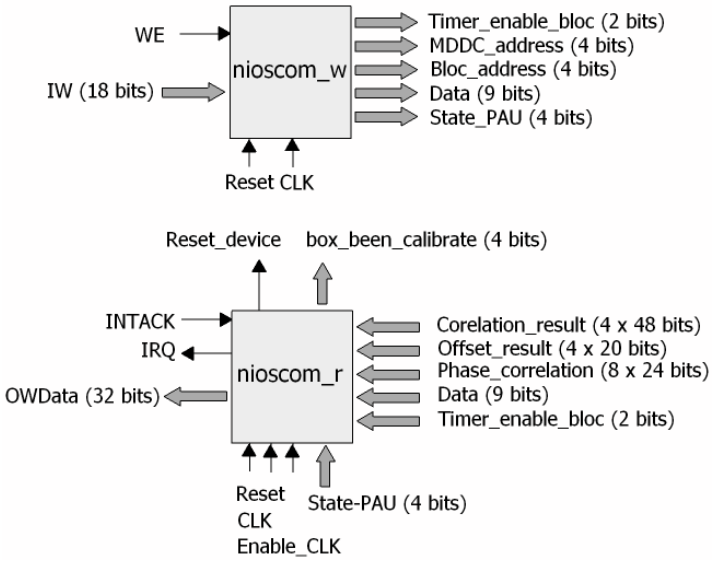

Figure 7.34. NiosCom sketch, the VHDL blocks which interface the UC and the ALU. It is split in two blocks: nioscom_w from CU to ALU communications direction, and nioscom_r from ALU to CU.

The nioscom_w block decodes the system status (State_PAU) from the messages sent by the CU (through the IWord input). Furthermore, it synchronizes all the NCOs look-up table writing from the CU (through the MDDC_address output), and sets the integration time timer (Timer_enable_bloc).

Table 7.5. IWord register structure for the communication protocol.

	Bit Number				
	19	18	17…14	13..9	8..0
Register fields	WE	f	A	B	Data

Table 7.5 shows the internal structure of the IWord register, mapped into the Nios2 memory. Despite the Nios2 word has 32 bits, for this protocol only 20 bits are used. It is divided into five different segments. The last segment, called Data, has 9 bits and it contains the information to be transmitted to the ALU such as part of the timer period or part of a position of an NCO's loop-up table. The B segment has 5 bits and contains the position in an NCO's look-up table, or the timer position, of the Data content. The A segment has 4 bits and contains the address of the NCO of the Data content and the system status depending on the flag f. Finally, WE is a flag to indicate to the ALU that there is a new available data in the IWord register.

On the other hand, the nioscom_r block sends the CU all the system results data using the signals INTACK, IRQ and the Oword register, which is mapped in the Nios2 memory. The CU has to read a memory position to read the new data from the ALU. As it has been explained the CU is executed in a microprocessor, so that is not possible to suppose that the CU will be always ready to read data from the ALU. So that, a communication flux control has been implemented by using the IRQ and INTACK signals.

Table 7.6. OWord register structure for the communication protocol.

	Bit Number	
	30..24	23…0
Register fields	Address	Data

Table 7.6 shows the internal structure of the OWord register, mapped into the Nios2 memory. Despite the Nios2 word has 32 bits, for this protocol only 31 bits are used. It is divided into two different segments. The last segment called Data has 24 bits and contains the ALU results (48 bits), which has been separated into most significant bits (first 24 bits) and less significant bits (last 24 bits). The Address segment has 7 bits and is the Data identifier for further reconstruction and identifying the sent word.

7.3.5 Digital Design Overview

Once the digital design has been completed it is time to summarize the digital design from the FPGA point of view. The most important resources used in the PAU-RAD digital radiometer are summarized in Table 7.7.

Table 7.7. FPGA resources used for the PAU-RAD digital radiometer

Element	LEs	DSP elements	Memory bits
Radiometer	4921	22	0
NiosCom	1119	0	0
CU	3969	8	89088
Total design	10098	30	89088

Table 7.7 shows that only the 24 % of the whole LE resources of the FPGA are used in this design. This is a good enough occupancy, because due to the architecture of the FPGA cells, when the FPGA starts to be full, it is not possible to find a good

routing for adjacent signals and then the maximum working frequency decreases dramatically. On the other hand, the DSP resources are only used at 10 %, and the memory bits at 4 %. Finally, the longest system path takes 13.64 ns to be propagated, which it means that the maximum working frequency is 73.29 MHz, (higher than the required 45.98 MHz).

7.4 PAU-RAD PC Interface

The PAU-RAD PC Graphical User Interface (GUI) is a user-friendly from where the instrument is operated and the acquired data is stored (Figure 7.35). It has been written in C# with the Windows Visual Studio 2008 Software Design Environment (SDE). The control interface has the total control of the instrument, and the communications between the control interface and the CU are bidirectional.

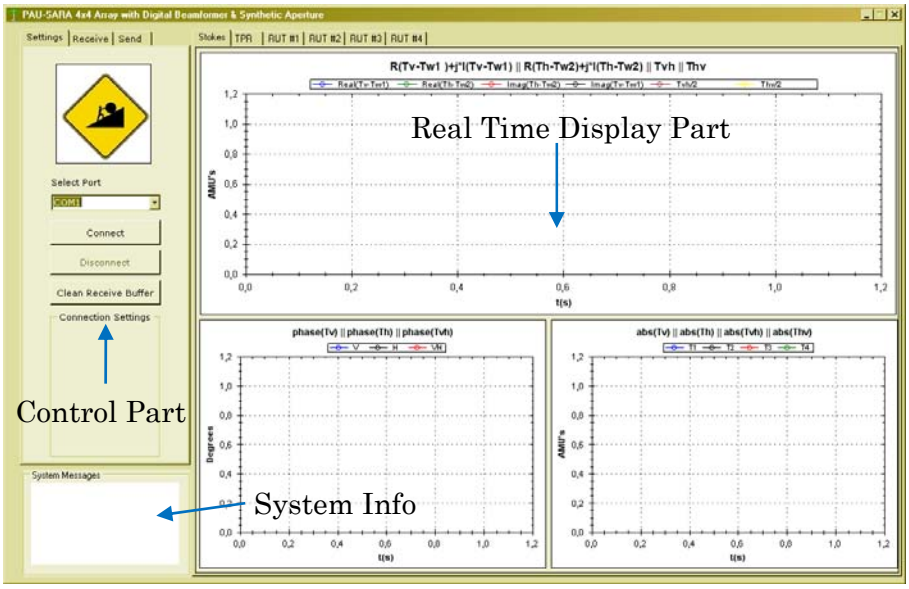

Figure 7.35. Frontal panel of the PAU-RAD PC interface.

The GUI has a real-time display to present the information sent by the CU (Figure 7.35). The most relevant information displayed regards to the system status, the current radiometric acquisitions, and RUTs calibration information. The graphical interface helps understanding the system's operation and detecting hardware or software errors. All the received data is collected, time stamped and stored for further processing. The control part has three labels allowing switching between the panel of the communications settings, the received data analysis panel, and the control panel, which has a pop-up menu with all the available instructions to the CU. On the other hand, the real time display part has six labels, two for display of the antenna measurements, and four to supervise the phase and modulus of each channel of all receives, to evaluate their equalization in real-time.

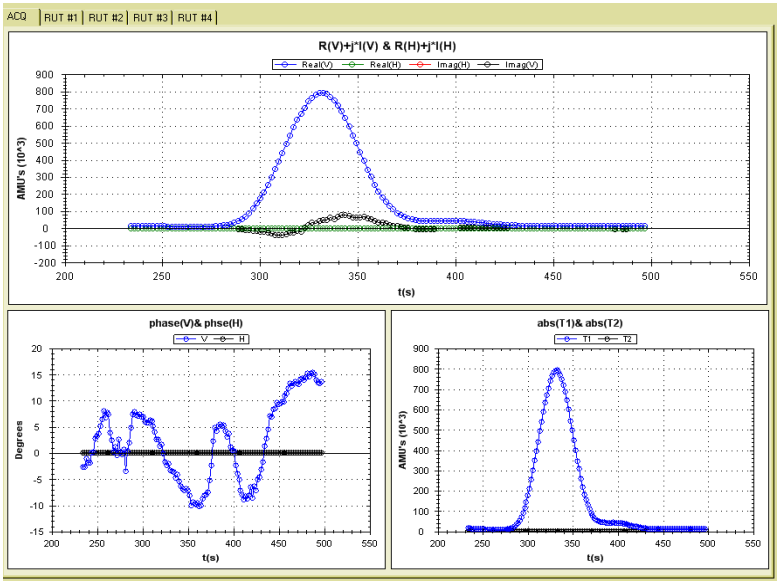

Figure 7.36. PAU-RAD GUI display part, real time displaying the antenna array measurement in the UPC anechoic chamber.

Figure 7.36 shows the real time display part of the GUI measuring the antenna array in the UPC anechoic chamber [118]. The upper window shows the raw data measurements (complex numbers), and the lower left windows shows the phase of these acquired data and at the lower right window shows the modulus of the data.

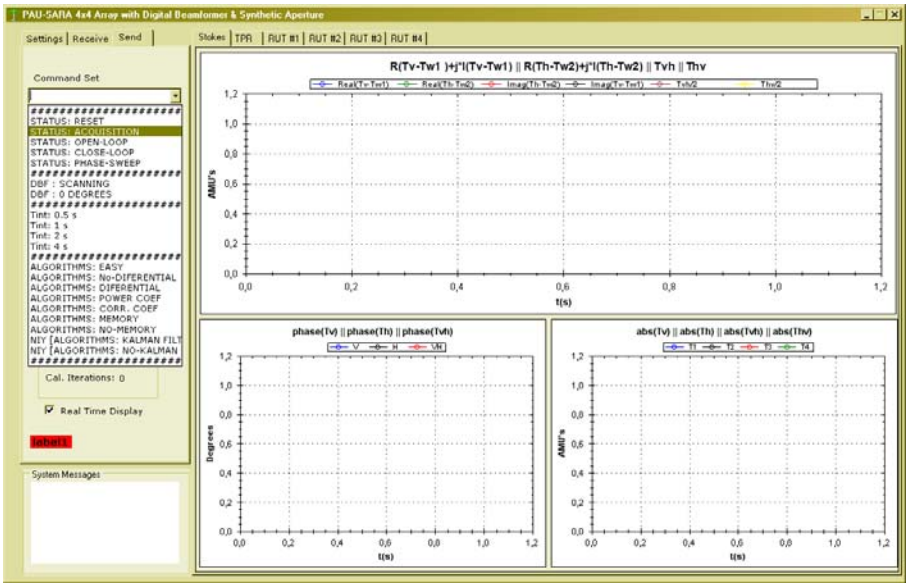

Figure 7.37. PAU-RAD GUI control part showing the UC changeable parameters

Figure 7.37 shows control part pop-up menu with the parameters that can be changed in real time by sending a message to the CU. They are grouped in four different sets:

- the current CU status choosing between reset, acquisition (main sequence in Section 7.3.3.2), or within validation sequences such as open loop, close loop or phase sweep,

- the steering system choosing between doing a continuous scan from -20º to 20º in 5º steps or pointing to the antenna array boresight,
- the integration time choosing within 0.5, 1, 2, or 4 seconds, and
- the equalization method choosing between different calibration algorithms, depending on the measurement type.

7.4.1 UC-PC communication protocol

The communications channel between the CU and the PC consists of a bidirectional serial communication protocol using a universal asynchronous receiver/transmitter (UART) with a throughput of 115 Kbits per second. Over this serial protocol, there is a self-designed application layer.

The CU sends a start sequence byte to allow the PC to be aware for the new reception, when the PC receives at least one start sequence byte it keeps waiting for the rest of the message. It starts with a datagram identifier (ID) and then the PC reads 87 bytes. The meaning and interpretation of the read sequence depends on the ID, as it is shown in Table 7.8:

Table 7.8. Communication Protocol from the CU to the PC

ID	Header	Datagram
Radiometric Measurements	BeamID Id2 InSelect	TData12 TData34 OffsetData,
Error Estimation Measurements	nRut nRef InSelect	IData Qdata PData

When the ID stands for radiometric measurements, the message has to be decoded as it follows: BeamID is the steering angle identifier, Id2 is a dummy parameter, InSelect is the RF switches position, TData12 are the complex data for the first and second Stokes parameters, TData34 are the complex data for the third and fourth Stokes parameters, and OffsetData is the offset for all the Stokes parameter. On the other hand, when the ID stands for error estimation measurements, the message has to be decoded as it follows: nRut is the RUT identifier, nRef is the reference receiver identifier, InSelect is the RF switches position, IData are the real parts of the cross-correlation between the RUT and the reference, Qdata are the imaginary parts, and PData are the RUT power measurements.

For the communication direction from the PC to the CU, a simple byte (a word of 8 bits) is sent for the PC to the CU with no other parameters. This byte is decoded in the CU using a switch C structure. The decoder has as many cases as possible instructions the CU can receive, *i.e.* for setting the integration time to 0.5 s or 1 s a different byte has to be sent, the integration time is implicit on the byte, so the integration time itself, is not sent. Using this simple technique the CU is able to understand up to 256 different instructions.

7.4.2 PAU-RAD Record File

As stated in the previous section, all the collected data with no distinction from which sensor has been generated is written into a raw ASCII text file. This file is opened automatically when the PC and CU connection is successfully established. The name of the file is automatically generated following the current time, to avoid overwriting files and have a clear time reference of when the file was created.

Table 7.9. Detailed information of the content of the raw data file

Element	Header	Datagram
PAU-RAD	h m s ms ID	Header Datagram

In order to simplify the file loading task for further off-line process, this file is organized in rows and columns as is shown in Table 7.9. Each new acquisition is written in a new row and each row has exactly the same number of columns.

In Table 7.9 the header is composed by h (hour), m (minute), s (second), ms (millisecond) and the ID, which has been sent by the CU. The datagram is composed by the header and the datagram sent by the CU, detailed in Table 7.8.

7.5 Conclusions

In this section the PAU-RAD implementation has been shown from the conceptual sketch up to the detailed design. Mainly, the conceptual sketch consist of an analog part that collects the input signals thought the antennas, and then it performs the RF-IF down-conversion from 1.57542 GHz to 4.039 MHz. Once signals are at IF, they are digitized using 8 bits and introduced into an FPGA. Inside the FPGA, each channel is equalized, in phase and amplitude, and down-converted to baseband using its own NCO. Then the DBF is performed and finally signals are properly correlated in order to obtain the Stokes parameters.

The detailed analysis has been conducted through the analog and the digital part of the PAU-RAD focusing on:

- a 4x4 antenna array with a beamwidth of 25º designed for having an MBE higher than 94 % and capable to steer the beam in the vertical direction,
- the RF part with the control switches to allow phase and amplitude equalization among all the channels of the receivers, the Wilkinson power splitters, and the LNA. The RF section has a gain of 33.35 dB a NF of 5.3 dB and an isolation between same polarization channels of -44.3 dB,
- the IF part which consist of the Zarlink GP2015 chip with the AGC disabled, a reject band of -40 dB, and a bandwidth of 2.2 MHz. Furthermore, this part has

an video amplifier and a matching network to match the cables which propagate the signal to the ADC,

- the 8 bit time multiplexed ADCs and its frequency plan that centers the digitized signal at 0.25 times the sampling frequency,

- the VHDL ALU design with the MDDC, which using its NCO down-converts the signals to base band, equalizes the channels and steers the beam, the beamformer adder, the LPF and the cross-correlation block. In addition, the ALU has another cross-correlation block to estimate the phase and amplitude differences among receivers,

- the ANSI C implementation of the CU, with the main sequence which manages the radiometer, and

- the GUI running on the external PC to control the whole system, and the record file for further emissivity and geo-physical retrieval.

Once the system has been successfully implemented, the error estimation algorithms, which run on the UC, and the PAU-RAD performance will be analyzed on the next chapters.

Chapter 8

8 EQUALIZATION ALGORITHM AND ITS PERFORMANCE

Chapter 6 concluded that each signal of PAU-RAD had to be equalized before the synthesis of the beams with the DBF. Moreover, Chapter 7 has presented the dedicated hardware for the amplitude and phase error estimation and equalization, such as the RF switch, the CNS, and the digital complex-cross correlator and the NCO. This chapter analyzes the phase and amplitude equalization procedure. This is done by presenting the voltage signals from the pair of receivers to be cross-correlated have been provided in order to analyze the impact of the different terms o the equation. Furthermore, the equations of the differential algorithm for phase and amplitude estimation have been provided, and analyzed. After the estimation of these parameters from the raw complex-cross correlation their measurement standard deviation is reduced by using a Kalman filter. Then, the equalization performance is analyzed in depth for one RUT and, finally the summary of the entire PAU-RAD instrument calibration performance is provided.

8.1 Equalization Algorithm Overview

As it has been discussed in Chapter 6, each signal of PAU-RAD has to be equalized before the synthesis of the beams with the DBF, which means that signals coming from each channel of the different receivers must all have the same amplitude and phase. The performance of the DBF requires only a relative calibration, which implies having all the amplitudes and phases equalized. It does not require an absolute calibration, *i.e.* set all the phases to 0^{o} and all the amplitudes to a predetermined value.

Chapter 7 presented the dedicated hardware block for the error estimation, and the other hardware requirements to be able to estimate the error including the RF special switches, which ensure a common signal at the input of each receiver chain, and the CNS, which can generate reference signals with three different input powers. Furthermore, Chapter 7 presented the NCO that down-converts the signals to base-band, and equalizes them taking into account the amplitude and phase errors estimated in the equalization algorithm.

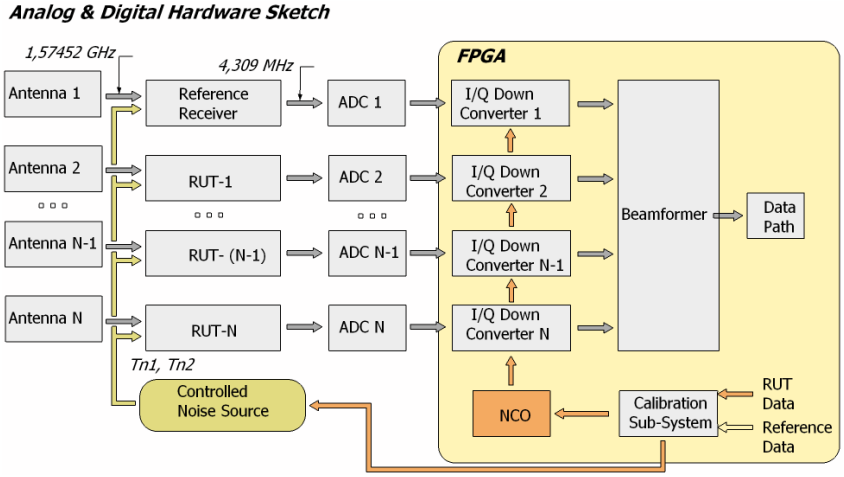

Figure 8.1 Equalization algorithm performed in two steps: estimating the phase and amplitude differences between the reference and the RUTs, and compensating these errors with the NCO.

This chapter is devoted to the analysis of the phase and amplitude equalization procedure. The signals' equalization is achieved in two steps (Figure 8.1). The first step is the estimation of the phase and amplitude differences among the signals. In order to estimate these differences, the switch of each RF chain has to be connected to the CNS input signal. Then, one of the signals has to be selected to be the reference one (arbitrarily chosen), and consequently all the computed phase and amplitude differences will be referenced to the phase and amplitude of that reference signal. Moreover, it is not required to assume that the reference signal has a constant phase and amplitude. If it is not, all the signals will follow the phase and amplitude drifts of the reference signals. The second step is to correct this phase and amplitude differences in order to equalize the signals. This is performed

by changing the phase and amplitude of the NCO of each signal accordingly to the estimated values in the previous step. The NCO is allocated at the digital part of the design.

Figure 8.2 shows a simplified phase and amplitude difference estimation sketch, including one polarization receiver with the RF part switch to the CNS input (S_{CNS}), two RF-IF down-converters and a complex correlator. As it can be seen, each RF-IF down-converter has its own S_{21} coefficient (labeled as g_i in Figure 8.2), which it is usually a complex value, and its phase depends both on the PLL lock conditions (totally random), and on its own receiver noise (labeled as n_i at Figure 8.2).

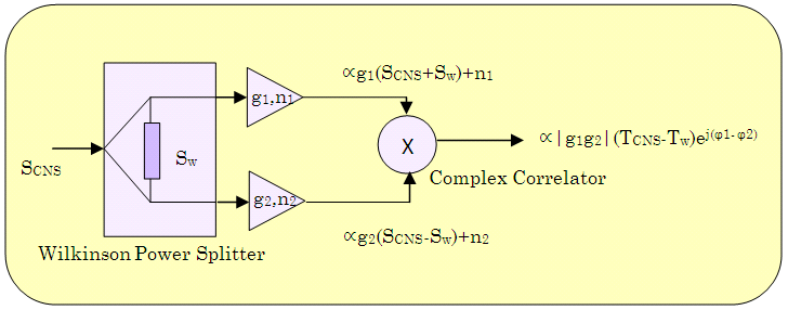

Figure 8.2 PAU-RAD receiver sketch with the input switched to the CNS

The output of the complex correlator is proportional to $|g_1 g_2|(T_{CNS} - T_w)e^{j(\varphi_1 - \varphi_2)}$, where T_{CNS} is the temperature of the signal coming from the CNS, T_w is the temperature of the Wilkinson's power splitter, and $\varphi_1 - \varphi_2$ and $|g_1 g_2|$ are the phase difference and gain coefficient due to the upper and the lower receivers' chains, respectively. Once the complex correlation is obtained, the $\varphi_1 - \varphi_2$ and the $|g_1 g_2|$ coefficients are estimated, and then compensated changing the NCO of the lower receiver's chain. Note that, it has been assumed that the reference signal is the upper chain. This procedure can be done iteratively in order to further reduce the equalization error. Roughly, the system can be considered to be equalized when the estimated phase and amplitude errors satisfy these two points:

- $\varphi_1 - \varphi_2 = 0$, then both receiver chains have the same phase (phase equalized), and
- $|g_1 g_2| = |g_1|^2$, then both receiver chains have the same amplitude (amplitude equalized).

Due to the nature of the complex correlator's output signal, which is the subtraction of the CNS and the Wilkinson temperatures, some considerations have to be done before estimating the amplitude and phase in order to precessily know the behaviour of the system. Figure 8.3 shows a CNS input temperature swept from 0 up to 1000 Kelvin, with a constant Wilkinson temperature (T_w = 300 K). As the result is a complex number, phase and modulus results are displayed sparately. The modulus figure (Figure 8.3a) shows that the output power is T_w when the T_{CNS} = 0 K, and from here it decreases as the input power increases up to the

minimum output temperature of 0 K, which occours when $T_{CNS} = T_w$. From this point, the output power increases as the input power increases. Although low input temperatures, even lower than the physical temperature (T_{ph}), can be achieved easily using active cold loads [125], they cannot reach very low values ($T_{CNS} = 0$ K). Its aim is to study the general behaviour of the modulus of the complex correlation output. The phase (Figure 8.3b) shows that the output phase is 180º shifted and constant when $T_w > T_{CNS}$, and it has the expected value (at this time 0º) when $T_{CNS} > T_w$.

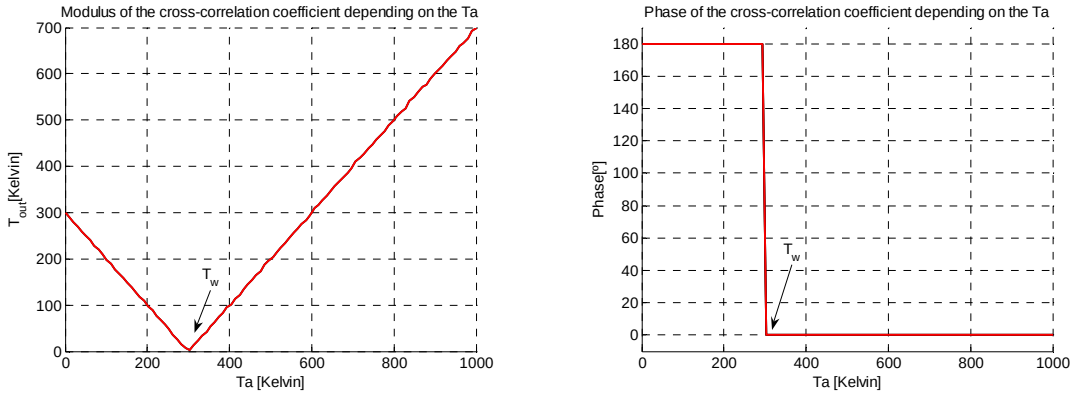

(a) (b)

Figure 8.3 Simulation of the PAU-RAD complex correlator output for an input temperature swept, (a) cross-correlation modulus, and (b) cross-correlation phase.

The main conclusion of that input swept anlysis, is that to estimate the phase and amplitude error the T_{CNS} has to ensure that it is always higher than T_w. This is important to avoid any uncertainly related with the different behaviour of the complex correlation output depending on the T_w.

This simplified case of amplitude and phase estimation, which only considers a polarization of the same receiver, has the particularity that both signals share the same RF Wilkinson power spliter. So that, the complex cross-correpation output has a correlation term called T_w, depending on the physical temperature of the spliter. In a general case, the RUT and the reference signals are not in the same receiver, and consequently they do not share the RF Wilkinson power spliter. Nevertheless, signals from different receivers not only share the common S_{CNS} signal generated by the CNS, but they always share a counter-phase signal coming from the Noise Distribution Net (NDN, 1:4, 2 cascaded Wilkinson power splitters), which drives the CNS signal to every receiver input port. Clearly, in this case the equivalent noise temperature depends not only on the physical temperature, but on the Friis formula, and that must be taken into account in the general PAU-RAD equalization algorithm.

8.2 Amplitude and Phase Error Estimation

Despite the hardware block that performs the complex cross-correlation was presented in Chapter 7, a brief presentation is repeated here for clarity. The complex correlation between a reference receiver signal and a RUT signals is performed at base-band. Therefore, signals are analytic and they have a real (in-phase, I) and an imaginary (quadrature, Q) part. The in-phase reference signal (I_{REF}) and the RUT signals (I_{RUT} and Q_{RUT}) give information about the amplitude and phase differences among them. Thereafter, this result is sent to the CU, where mathematical algorithms to derive the amplitude and the phase differences are implemented and Kalman filtering is applied to reduce the estimation error (Figure 8.4). This information is used to update the correspondent RUT's NCO look-up table.

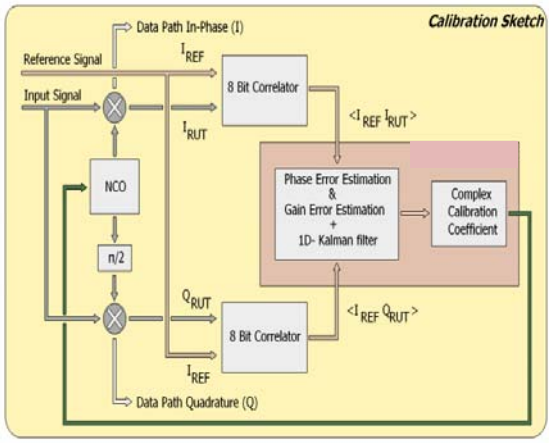

Figure 8.4 Phase and amplitude differences estimation and calibration sketch. The ALU performs the complex correlation to estimate the complex equalization, and the error correction (NCO). On the other hand, the CU performs the error retrieval and the 1D- Kalman filter.

This block performs the cross-correlation between the reference signal coming from a reference receiver (arbitrarily chosen) and a signal coming from the Receiver Under Test (RUT). The RUT input signals are changed sequentially accordingly the dispositions of the CU through an input multiplexor in order to estimate the phase and amplitude errors of all receivers.

8.2.1 Estimation Algorithm

As it has been explained before, to estimate the errors, all receivers have to be driven by the same input signal, which is injected through a correlated noise input port. The CNS, which is capable to drive three different noise power levels using two control bits, is used to inject this common signal to all receivers. As this phase and amplitude information is derived from the result of a complex correlation and it is relative to the reference signal, this process is performed by pairs. Voltage

signals from the pair of receivers that have been considered for the error estimation are shown in Eqns. (8.1) and (8.2):

$$S_{\mathrm{REF}} = A_{\mathrm{REF}} e^{j\,\varphi_{\mathrm{REF}}} \left(\frac{(S_{\mathrm{CNS}} + S_{\mathrm{NDN-REF}})}{\sqrt{2}} + S_{pre\mathrm{LNA-REF}} \right) + S_{post\mathrm{LNA-REF}}, \tag{8.1}$$

$$S_{\mathrm{RUT}} = A_{\mathrm{RUT}} e^{j\,\varphi_{\mathrm{RUT}}} \left(\frac{(S_{\mathrm{CNS}} + S_{\mathrm{NDN-RUT}})}{\sqrt{2}} + S_{pre\mathrm{LNA-RUT}} \right) + S_{post\mathrm{LNA-RUT}}, \tag{8.2}$$

where:

- S_{REF} is the output complex signal of the reference receiver, S_{RUT} is the output complex signal of the RUT,
- S_{CNS} is the common signal coming from the CNS, which is uncorrelated to the other noise terms,
- $S_{pre\mathrm{LNA-REF}}$ and $S_{pre\mathrm{LNA-RUT}}$ are the reference and RUT receiver's noises before the first LNA. That noise is affected by the amplitude and phase of all the receiving chain (Section 7.2.2.1). They are uncorrelated among them, and with the other terms,
- $S_{post\mathrm{LNA-REF}}$ and $S_{post\mathrm{LNA-RUT}}$ are the reference and RUT receiver's noises after the first LNA, including it. That noise is not affected by the amplitude and phase of all the receiving chain (Section 7.2.2.1). They are uncorrelated among them, and with the other terms,
- $S_{\mathrm{NDN_{REF}}}$ and $S_{\mathrm{NDN_{RUT}}}$ are the noise signals introduced by the Noise Distribution Network (NDN) on the reference and the RUT signals, respectively. The equivalent noise temperature of these signals depends not only on the physical temperature, but on the Friis formula as well. Hence, these signals are composed by various signals, each power splitter step, up to the RF-IF down-converter input, has its own contribution. These two signals are uncorrelated among the other terms, but the correlation level among these two signals depends on the pair of receivers which are being cross-correlated. The higher cross-correlation level occurs when the reference and the RUT signals are in the same polarization of the same receiver (sharing the same RF-Wilkinson). On the other hand, the lower level occurs when the reference and the RUT signals are not in the same receiver and the CNS input port of each receiver is driven by signals with the largest distance on the NDN,
- A_{REF} and A_{RUT} are the reference and RUT amplitudes, respectively, and
- φ_{REF} and φ_{RUT} are the reference and RUT phases, respectively.

The correlation of the reference and RUT signals, and their cross-correlation can be obtained from Eqns. (8.1) and (8.2), results are presented in Eqns. (8.3) to (8.5):

$$\langle S_{\mathrm{REF}} S_{\mathrm{REF}}^{*} \rangle = 2\{\langle \mathrm{I_{REF}} \mathrm{I_{REF}} \rangle - j\langle \mathrm{I_{REF}} \mathrm{Q_{REF}} \rangle\} = \\ = \frac{A_{\mathrm{REF}}^{2}}{2}\left(\mathrm{T_{CNS}} + \mathrm{T_{NDN-REF}} + \mathrm{T}_{pre\mathrm{LNA-REF}}\right) + \mathrm{T}_{post\mathrm{LNA-REF}}, \tag{8.3}$$

$$\langle S_{\mathrm{RUT}} S_{\mathrm{RUT}}^{*} \rangle = 2\{\langle \mathrm{I_{RUT}} \mathrm{I_{RUT}} \rangle - j\langle \mathrm{I_{RUT}} \mathrm{Q_{RUT}} \rangle\} = \\ = \frac{A_{\mathrm{RUT}}^{2}}{2}\left(\mathrm{T_{CNS}} + \mathrm{T_{NDN-REF}} + \mathrm{T}_{pre\mathrm{LNA-RUT}}\right) + \mathrm{T}_{post\mathrm{LNA-RUT}}, \tag{8.4}$$

$$\langle S_{\mathrm{REF}} S_{\mathrm{RUT}}^{*} \rangle = 2\{\langle \mathrm{I_{REF}} \mathrm{I}_{RUT} \rangle - j\langle \mathrm{I_{REF}} \mathrm{Q}_{RUT} \rangle\} = \\ = \frac{A_{\mathrm{REF}} A_{\mathrm{RUT}}}{2} e^{j(\varphi_{\mathrm{REF}} - \varphi_{\mathrm{RUT}})}(\mathrm{T_{CNS}} + \mathrm{T_{cNDN}}), \tag{8.5}$$

where:

- $\langle \cdot \rangle$ is the expectation operator (in this case, due to the ergodic properties of the thermal noise: $\langle \mathrm{AB}^{*} \rangle = \frac{1}{T} \lim_{T \to \infty} \int_{0}^{T} \mathrm{AB}^{*} dt$),
- j is the imaginary constant ($j = \sqrt{-1}$),
- $\langle S_{\mathrm{REF}} S_{\mathrm{REF}}^{*} \rangle$ and $\langle S_{\mathrm{REF}} S_{\mathrm{REF}}^{*} \rangle$ are real values, ($\langle \mathrm{I_{REF}} \mathrm{Q_{REF}} \rangle = 0$ and $\langle \mathrm{I_{RUT}} \mathrm{Q_{RUT}} \rangle = 0$), except for quadrature errors, which are negligible as the down-conversion to baseband is performed digitally,
- $\mathrm{T_{CNS}}$ is the noise equivalent temperature of the CNS signal injected at receivers' input,
- $\mathrm{T_{NDN-REF}}$ and $\mathrm{T_{NDN-RUT}}$ are the NDN's equivalent noise temperatures of the reference receiver and RUT, respectively,
- $\mathrm{T}_{pre\mathrm{LNA-REF}}$ and $\mathrm{T}_{pre\mathrm{LNA-RUT}}$ are the receiver's noise temperatures before the first LNA of the reference and the RUT receivers, respectively. Notice that the first difference between channels, in amplitude and phase terms, is inferred by the LNA (Section 7.2.2). Before it, channels are physically identical and there is no active component to change the phase or the amplitude. Even though, the most significant phase difference is due to the PLL of the RF-IF down-converter and the amplitude differences are distributed, related with the several amplification steps along the receiver chain, such as the LNA, the amplifier, the RF-IF down-converter, and the video amplifier,
- $\mathrm{T}_{post\mathrm{LNA-REF}}$ and $\mathrm{T}_{post\mathrm{LNA-RUT}}$ are the receiver's noise temperatures after the first LNA, including it, of the reference and the RUT receivers, respectively,

- I_{REF} is the real part of the analytic S_{REF} signal ($S_{REF}= I_{REF}+jQ_{REF}$),

- I_{RUT} and Q_{RUT} are the real and imaginary parts of the analytic S_{RUT} signal ($S_{RUT}= I_{RUT}+jQ_{RUT}$),

- T_{cNDN} is the equivalent noise temperature of the NDN common terms shared by the reference and the RUT signals at the same time. Each single contribution is added or subtract at the final value (T_{cNDN}) and it depends on the relative phase of the cross-correlated signals *i.e.* on the the pair of receivers which are being cross-correlated. For instance, when the reference and the RUT signals are in the same polarization of the same receiver (sharing the same Wilkinson power splitters) then $T_{cNDN}e^{j\varphi_{cNDN}} = T'_{cNDN} - T_W$, where T'_{cNDN} is the contribution of the NDN and T_W is the contribution of the Wilkinson power splitters, and

- atan(·) is the inverse tangent function.

Although the phase difference between the reference and the RUT signals can be readably obtained from the cross-correlation (Eqn. (8.5)), it is necessary to make an assumption to retrieve the amplitude difference. To obtain the relative amplitude from the signals auto-correlations (Eqns. (8.3)-(8.4)), it has to be ensured that the terms affected by the amplitude coefficient are much higher than the term that is not (Eqn. (8.6)). This requirement is fulfilled by the PAU-RAD hardware as it can be shown in Section 7.2.2.1.1 (for T_{CNS} = 500 K and T_{ph} = 300 K, T_{preLNA} ~ 850 K and $T_{postLNA}$ ~ 80 K).

$$\frac{A^2}{2}\left(T_{CNS} + T_{NDN} + T_{preLNA}\right) \gg T_{postLNA}, \tag{8.6}$$

From Eqns. (8.3)-(8.5), the relative phase and amplitude between the RUT and reference receiver can be obtained straightforwardly as shown in Eqns. (8.7)-(8.8):

$$A_{Cal-RUT} = \sqrt{\frac{|\langle S_{REF} S^*_{REF}\rangle|}{|\langle S_{RUT} S^*_{RUT}\rangle|}}, \text{and} \tag{8.7}$$

$$\varphi_{Cal-RUT} = \text{atan}\frac{-\langle I_{REF} Q_{RUT}\rangle}{\langle I_{REF} I_{RUT}\rangle}, \tag{8.8}$$

where:

- $A_{Cal-RUT}$ is the estimated amplitude equalization coefficient (Note that the amplitude equalization coefficient has no units as it is a square root of a power ratio), and

- $\varphi_{\mathrm{Cal-RUT}}$ is the estimated relative phase equalization coefficient between the reference receiver and the RUT, and it has units of degrees.

Both estimated coefficients are to be used in the computation of the trigonometric functions stored in the $\mathrm{LUT_{RUT}}$ of each NCO, for equalizing the input signal (Section 7.3.2.1).

However, the implementation of Eqns. (8.7)-(8.8) is prone to offset errors induced by two main implicit assumptions that are not necessarily fulfilled for the hardware system:

- for computing the amplitude difference properly, the algorithm assumes that $\mathrm{T_{NDN-REF}} = \mathrm{T_{NDN-RUT}}$, $\mathrm{T}_{pre\mathrm{LNA-REF}} = \mathrm{T}_{pre\mathrm{LNA-RUT}}$, and the condition stated in Eqn. (8.6) has to be fulfilled for all the RUTs, and

- for achieving the correlation results reported in Eqns. (8.3)-(8.5), it is assumed that input signals are composed only by the terms described in Eqns. (8.1)-(8.2). However, these equations can have extra correlated terms, due to miss-matches in the noise distribution net between the CNS and the receivers' input. These extra correlated terms can introduce offsets in Eqns. (8.3)-(8.5).

When the first assumption is not fulfilled, it creates an uncertainly on the amplitude estimation. Figure 8.5 shows an example of the cross-correlation correlation between a reference and a RUT signals, when both of them are in the same polarization of the same receiver (sharing the same RF-Wilkinson), with two different Wilkinson's equivalent temperature noise. Considering different values of $\mathrm{T}_{pre\mathrm{LNA}}$ has similar effects on the power computation that the ones reported in Figure 8.5 for the cross-correlation. Recall that the power computation is also affected when considering different values of $\mathrm{T_{NDN}}$.

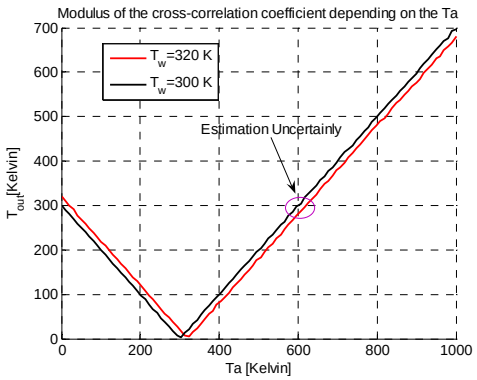

Figure 8.5 Simulation of the PAU-RAD modulus complex correlator output for an input temperature swept and two different $\mathrm{T_w}$, 300 K and 320 K.

To overcome this offset uncertainly a differential version of the previous technique has been developed. The correlations are now computed for two different power inputs ($\mathrm{T_{CNS\text{-}max}}$ and $\mathrm{T_{CNS\text{-}min}}$) driven by the CNS, as reported in Section 7.2.4.

Results of the correlation are previously subtracted among them before estimating the amplitude and phase difference. The procedure results are shown in the following Equations (8.7)-(8.8):

$$\langle S_{\mathrm{REF}} S_{\mathrm{REF}}^{*} \rangle_{\mathrm{T_{CNS-min}}}^{\mathrm{T_{CNS-max}}} = A_{\mathrm{REF}}^{2} \mathrm{T_{CNS}}_{\mathrm{T_{CNS-min}}}^{\mathrm{T_{CNS-max}}} + \mathrm{T_{offset-RUT}}, \tag{8.9}$$

$$\langle S_{\mathrm{REF}} S_{\mathrm{RUT}}^{*} \rangle_{\mathrm{T_{CNS-min}}}^{\mathrm{T_{CNS-max}}} = A_{\mathrm{REF}} A_{\mathrm{RUT}} \mathrm{T_{CNS}}_{\mathrm{T_{CNS-min}}}^{\mathrm{T_{CNS-max}}} + \mathrm{T_{offset-CM}}, \tag{8.10}$$

$$\mathrm{A_{Cal-RUT}} = \sqrt{\frac{\left| \langle S_{\mathrm{REF}} S_{\mathrm{REF}}^{*} \rangle_{\mathrm{T_{CNS-max}}} - \langle S_{\mathrm{REF}} S_{\mathrm{REF}}^{*} \rangle_{\mathrm{T_{CNS-min}}} \right|}{\left| \langle S_{\mathrm{REF}} S_{\mathrm{RUT}}^{*} \rangle_{\mathrm{T_{CNS-max}}} - \langle S_{\mathrm{REF}} S_{\mathrm{RUT}}^{*} \rangle_{\mathrm{T_{CNS-min}}} \right|}}, \text{and} \tag{8.11}$$

$$\varphi_{\mathrm{Cal-RUT}} = \mathrm{atan} \frac{-\left(\langle \mathrm{I_{REF}} \mathrm{Q_{RUT}} \rangle_{\mathrm{T_{CNS-max}}} - \langle \mathrm{I_{REF}} \mathrm{Q_{RUT}} \rangle_{\mathrm{T_{CNS-min}}} \right)}{\left(\langle \mathrm{I_{REF}} \mathrm{I_{RUT}} \rangle_{\mathrm{T_{CNS-max}}} - \langle \mathrm{I_{REF}} \mathrm{I_{RUT}} \rangle_{\mathrm{T_{CNS-min}}} \right)}, \tag{8.12}$$

where $\mathrm{T_{offset-RUT}}$ and $\mathrm{T_{offset-CM}}$ include all the terms in Eqns. (8.3) and (8.5), respectively, different than $\mathrm{T_{CNS}}$ and any other possible offset due to unbalances or correlated noise.

In order to properly select the values of $\mathrm{T_{CNS-max}}$ and $\mathrm{T_{CNS-min}}$, three practical considerations must be taken into account:

- the minimum equivalent noise temperature generated by the CNS has to be higher than the maximum equivalent noise temperature of the NDN common terms shared by the reference and the RUT signals at the same time ($\mathrm{T_{CNS-min}} > \mathrm{T_{cNDNmax}}$). This is required to ensure that both input powers ($\mathrm{T_{CNS-max}}$ and $\mathrm{T_{CNS-min}}$) are above of the minimum peak of output power (Figure 8.5). Otherwise, the increment of P_{out}/P_{in} does not reflect the slope (gain) of the receiver and the phase can have a 180º shift,

- the values of $\mathrm{T_{CNS-max}}$ and $\mathrm{T_{CNS-min}}$ have to be close to the expected antenna measured temperatures (but not much higher than it), in order to ensure that there are within the linear region of the RF-IF receivers, and

- the values of $\mathrm{T_{CNS-max}}$ and $\mathrm{T_{CNS-min}}$ have to be separated enough. If they are too close, the estimated amplitude and phase are very sensitive to measurement errors (finite radiometric resolution). In the limit, when $\mathrm{T_{CNS-max}} = \mathrm{T_{CNS-min}}$, the result is not determined.

The current values used in the algorithm are $\mathrm{T_{CNS-max}}$= 450 and $\mathrm{T_{CNS-min}}$ = 370 K.

8.2.2 Estimation Error Kalman Filtering

A Kalman filter is an efficient recursive filter that estimates the state of a linear dynamic system from a series of noisy measurements. It is a well-known and used technique in control engineering, indeed it is used in remote sensing applications especially on radar and lidar. Assuming that the amplitude and phase errors are linearly drift, and knowing that the estimated errors are noisy, a one-dimensional Kalman filter can be applied to the measured cross-correlation [126]. The aim of using this recursive estimator lies in the minimization of the noise impact to fulfill the residual calibration errors requirements. Each channel of every RUT has its own NCO, so it has its own Kalman filter (16 simultaneous Kalman filters have been used in total), which are coded in C and they run in the CU as it has been reported in Chapter 7.

The implementation of the Kalman filter and the experimental results have been reported in [40]. It is important to realize that, this really good performance is not for the whole array, it is only for one receiver. More effects must be considered when the whole array performance is taken into account, the main ones are: the whole array has 4 receivers, the performance of the RF power combining net, and the estimation of the difference between the CNS and the antenna signal path, which is the highest error source. The equation which defines the Kalman filter is described below:

$$\mathrm{A}[n] = \mathrm{A}[n-1] + K[n-1](\mathrm{B}[n] - \mathrm{A}[n-1]), \tag{8.13}$$

where :

- n is the iteration sample,
- $\mathrm{A}[n]$ is the filter output for the n^{th} iteration,
- $\mathrm{B}[n]$ is the filter input for the n^{th} iteration, and
- K is the Kalman's coefficient which is time depending, it is updated at each new sample, and it is defined as:

$$K[n] = \frac{\sigma_{\mathrm{A}}^2[n]}{\sigma_{\mathrm{A}}^2[n] + \sigma_{\varepsilon}^2}, \tag{8.14}$$

- σ_{ε}^2 is the variance of the error of the measurement, and
- $\sigma^2{}_A[n]$ is the variance of the filtered value and it is calculated as in Eqn. (8.15):

$$\sigma_{\mathrm{A}}^2[n] = (1 - K[n-1])(\sigma_{\mathrm{A}}^2[n-1] + \mathrm{K}[\mathrm{n}-1](\mathrm{B}[\mathrm{n}-1] - \mathrm{A}[\mathrm{n}-1])^2). \tag{8.15}$$

For convenience, in this work no constant has been taken into account when processing in the digital domain, so that the measurements of power have units of arbitrary power unit (*apu*), but not directly Watts. Therefore, units of the input and output signals of the Kalman filter (A and B) are *apus*. Thus, the units of σ_A^2 and σ_ε^2 are squared *apus* (*apu*^{2}), and that of the Kalman coefficient is unit less.

A Kalman filter has to initialize two parameters, which can be identified following Eqns. (8.14) and (8.15). The first one is an initial guess estimation of the variance of the filtered signal ($\sigma_A^2[0]$) and the second is the variance of the error associated to the estimation of the cross-correlation, *i.e.* the variance of the measurement error (σ_ε^2). It is possible to set an arbitrary value for $\sigma_{\phi_f}^2[0]$, because it is a recursive algorithm and it will converge to the real value of σ_A^2 . The closest the guessed value of $\sigma_A^2[0]$ to the real one, the fastest the filter convergence. On the other hand, the value of σ_ε^2 can be easily measured from the cross-correlation measurements variance. From an implementation point of view, the parameter σ_ε^2 determines the tradeoff between the convergence velocity and the accuracy of the best performance. Although σ_ε^2 can be measured, usually it is tuned to have better performance in terms of convergence speed despite having a worse accuracy.

Despite of a Kalman filter can estimate the state of a linear dynamic system, and of the assumption that the amplitude and phase errors drift linearly is fulfilled, its relative position on the equalization algorithm has to be carefully chosen in order to ensure the stability of the filter. The phase and amplitude estimation procedure has two non-linear operations (computing the modulus and the phase of the complex result) that the Kalman filter cannot be placed after them. A stable performance was obtained when filtering the real and the imaginary parts separately, instead of filtering the amplitude and the phase (Figure 8.6). Therefore, two Kalman filters are required to reduce the estimation error of the phase and amplitude. Moreover, as the algorithm is differential and there are two values for the real part, and two values for the imaginary part, one for $T_{CNS-max}$ and another for $T_{CNS-min}$, there are four Kalman filters for each single NCO.

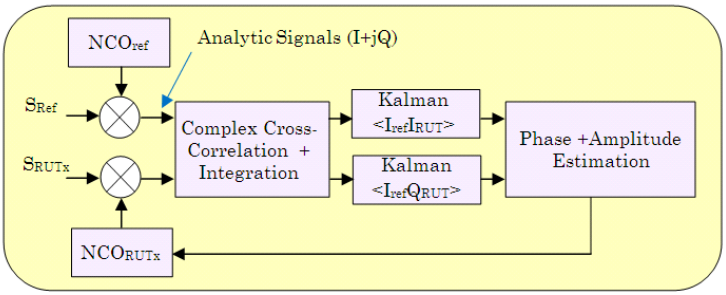

Figure 8.6 Cross-Correlation Kalman filtering for reducing the phase and amplitude differences estimation.

Figure 8.7 shows the results of applying a Kalman filter to the phase and amplitude equalization coefficients. The simulation parameters were realistic accordingly with the PAU-RAD instrument, and with 18º of a phase difference of and amplitude coefficient of 0.8 between the reference and the RUT signal. The

Kalman filter clearly reduces the measurement error in the phase and in the amplitude estimation.

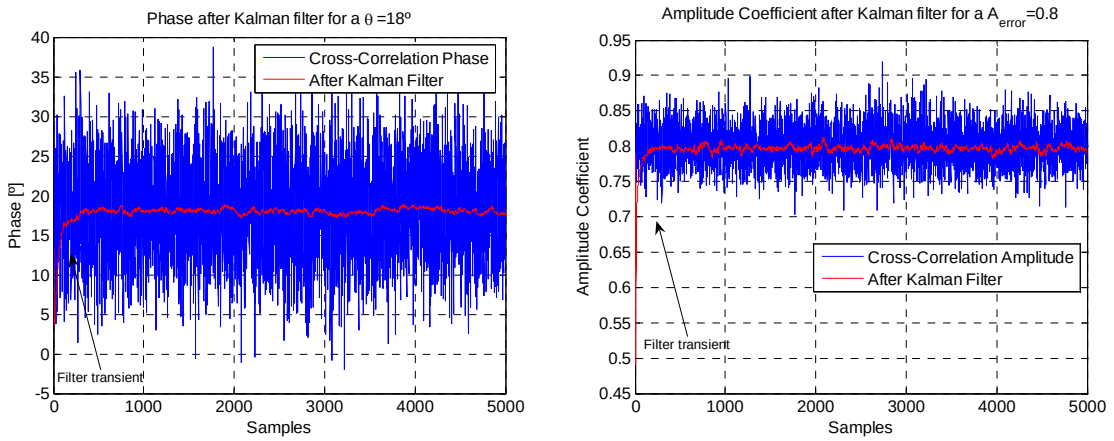

(a) (b)

Figure 8.7 Simulation of the phase and amplitude estimation, and $\sigma_\varepsilon^2 = 5 \cdot 10^4$ *apu*² (a) directly from the cross-correlation , and (b) after the Kalman filter.

However, the filter has a transient which is shown in Figure 8.7, the time that it needs to start tracking the mean value, which causes miss-estimations and, consequently, a wrong operation of the filter. In the real case, to avoid this transient the filter starts estimating phase and amplitude without using its results for the close the loop which feeds the NCO, instead of the Kalman filter output, the instantaneous values are used. Once the output of the filter is stabilized, the estimation source is switched from the instant value to the filter output.

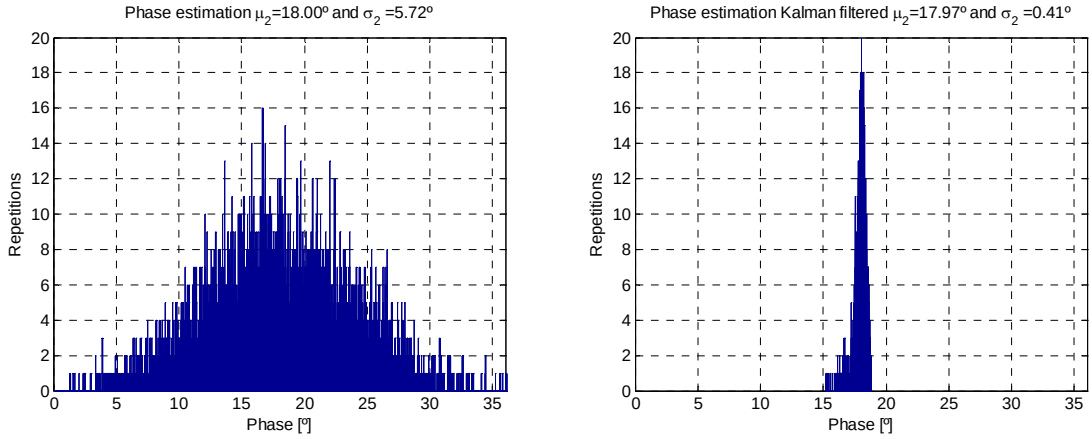

(a) (b)

Figure 8.8 Simulation of the phase estimation, and $\sigma_\varepsilon^2 = 5 \cdot 10^4$ *apu*²: (a) histogram of the estimation directly from the cross-correlation, and (b) histogram of the estimation after the Kalman filter.

To properly analyze the performance and impact of the Kalman filter on the estimated phase and amplitude Figure 8.8 and Figure 8.9 show the histogram of both parameters, estimated directly from the cross-correlation and estimated from the Kalman filter outputs.

Figure 8.8 shows the phase, there is not much difference regarding with the mean of both estimations, it is 18.00º for the cross-correlation and 17.97º for the Kalman estimation. On the standard deviation of the estimator is where the filter has more impact, and it is shown as a valuable technique. The standard deviation is 5.72º for the cross-correlation directly estimation and 0.41º for the Kalman estimation.

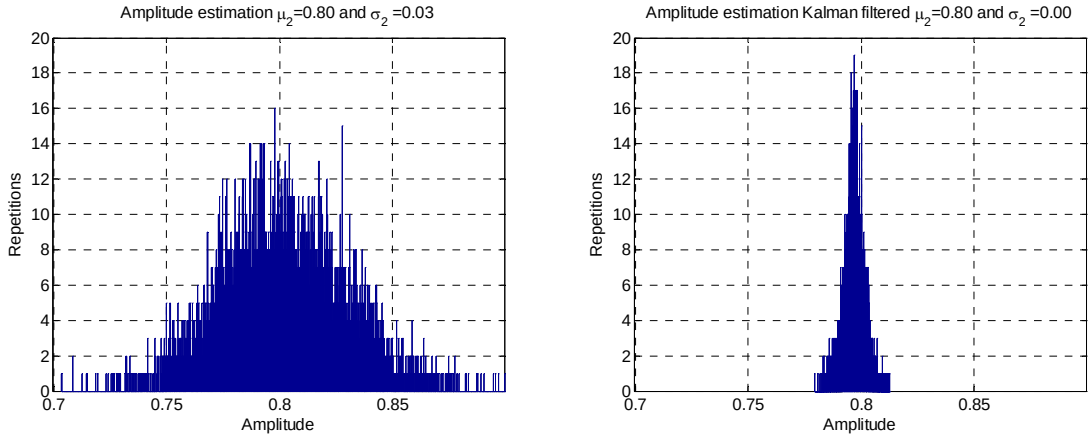

(a) (b)

Figure 8.9 Simulation of the amplitude estimation, and $\sigma_\varepsilon^2 = 5 \cdot 10^4$ apu^2: (a) histogram of the estimation directly from the cross-correlation, and (b) histogram of the estimation after the Kalman filter.

Figure 8.9 shows the amplitude, there is no difference regarding the mean of both estimations, it is 0.8 for the cross-correlation and for the Kalman estimation. The standard deviation is 0.03 for the cross-correlation directly estimation and 0.001 for the Kalman estimation.

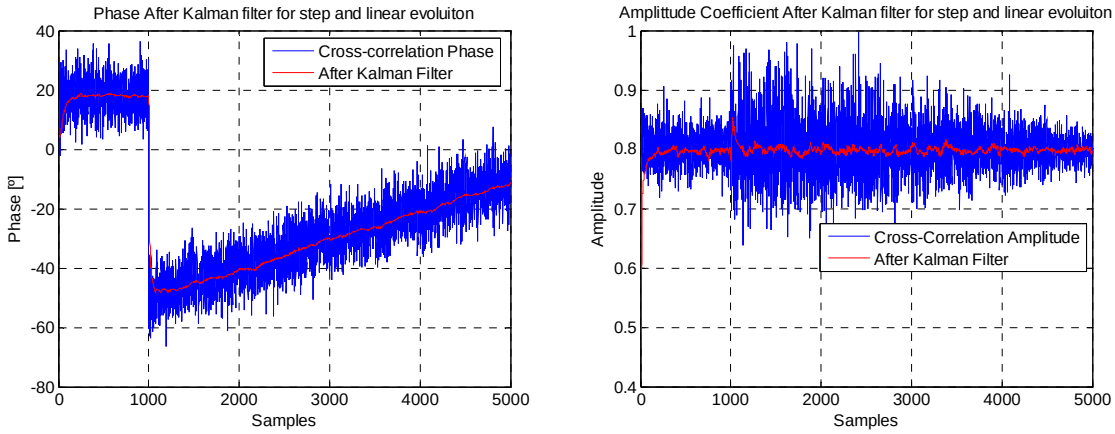

(a) (b)

Figure 8.10 Simulation of the phase and amplitude estimation having a phase step and drift, and $\sigma_\varepsilon^2 = 5 \cdot 10^4$ apu^2: (a) estimation directly from the cross-correlation, and (b) estimation after the Kalman filter.

Another feature that is expected from a Kalman filter is that it must track a linear drift and it has to follow an offset step. As it has been said, the possibility to perform these features can be achieved by tuning the parameter σ_ε^2 which gives flexibility to non-linear changes by having less accuracy in a stationary situation.

Figure 8.10 shows a time stationary phase until the 1000th sample, and then it is followed by a phase step and drift, which is drifting at 0.1 º/sample. The σ_ε^2 was specifically and empirically tuned to the filter be able to follow it.

8.2.3 Drawbacks of the Kalman Filter

Despite of the good performance of the Kalman filter, it has a drawback. It comes from the parameter σ_ε^2, which determines the tradeoff between the convergence velocity and the accuracy of the best performance. When selecting a σ_ε^2 value to achieve good accuracy [40], it provides a too much slow response for high speed drifts (higher than the expected ones) for instance when the system has not reach yet the thermal stability provided by the thermal control system or, even for a phase or amplitude step, for instance when an unlock and a posteriori lock of the PLL. On the other hand, when selecting a σ_ε^2 value to achieve good performance on the parameter tracking [40] it provides a noise output, and the Kalman filter cannot reduce the variance of the measurement error, as expected. Figure 8.11 and Figure 8.12 illustrates the importance of a good determination of the coefficient σ_ε^2 . Figure 8.11 shows what happens when a too restrictive coefficient σ_ε^2 value is chosen ($\sigma_\varepsilon^2 = 5 \cdot 10^6$, the optimum has been found to be $\sigma_\varepsilon^2 = 5 \cdot 10^4$). Although the Kalman filter output has not had enough time to reach the mean value (the K coefficients constantly decreases from 0 until the 3000th sample), it has a really low variance. When the system starts to drift, the Kalman's output cannot track it and appears a significant offset that invalidates the phase equalization coefficient.

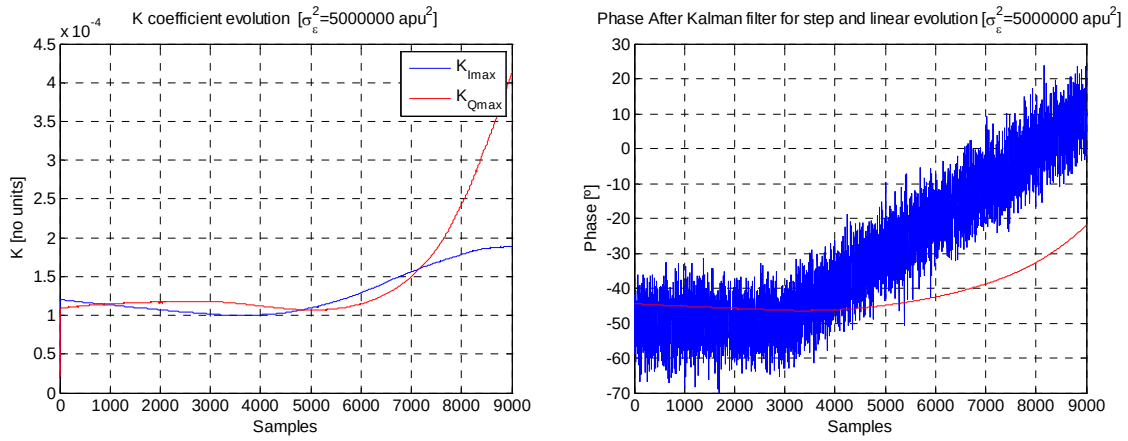

(a) (b)

Figure 8.11 Simulation of the phase estimation having a phase drift, and a high σ_ε^2 value: (a) Kalman coefficient evolution of the I_{max} and Q_{max}, and (b) estimation directly from the cross-correlation value and from the Kalman filter output.

On the other hand, Figure 8.12 shows what happens when a too restrictive coefficient σ_ε^2 is chosen ($\sigma_\varepsilon^2 = 5 \cdot 10^3$, the optimum has been found to be $\sigma_\varepsilon^2 = 5 \cdot 10^4$). The Kalman filter output has converged to the mean value very quickly, since the firsts samples, but it has a high variance and it is not decreasing with the number of samples.

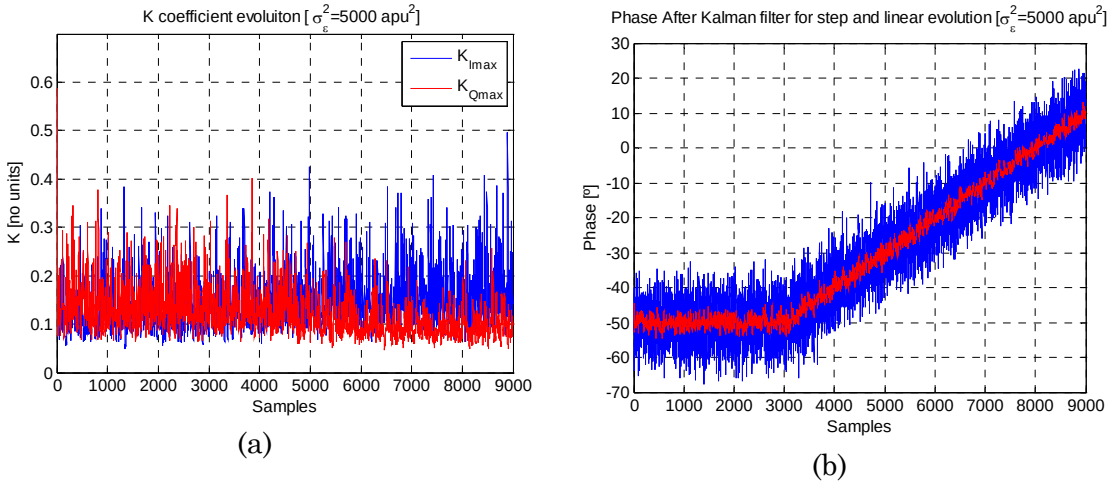

Figure 8.12 Simulation of the phase estimation having a phase drift, and a low σ_ε^2 value: (a) Kalman coefficient evolution of the I_{max} and Q_{max}, and (b) estimation directly from the cross-correlation value and from the Kalman filter output.

Figure 8.12a shows the evolution of the K coefficients, which is noise and higher than the ones shown in Figure 8.11a. Although the output of the Kalman filter is always very noisy, when the system starts to drift, the Kalman's output tracks the drift without any offset.

In conclusion, σ_ε^2 is a very sensitive parameter which determines the behavior of Kalman filter. It has to be properly tuned to ensure that it will follow the expected thermal drifts with the lowest variance at the output. In the PAU-RAD system this value has been empirically tuned to ensure a good performance.

8.3 Equalization Performance

In this section the equalization procedure performance is presented and analyzed. The equalization procedure includes the phase and amplitude estimation, the error variance reduction due to the Kalman filter, the differential estimation algorithm, and the signal equalization using each NCO. For the sake of clarity, the performance is analyzed for only one RUT, which includes four chain (two per polarization), during a measurement period of two days and with an integration time of 1 s. ($\tau_i = 1$ s). As it has been stated before, for convenience in this work no constant has been taken into account when processing in the digital domain, so that the measurements of power have units of arbitrary power unit (*apu*), but not directly Watts. There is a proportional relationship between the measured *apus* and Watts, which constant is the product of all the missed constants along the processing path.

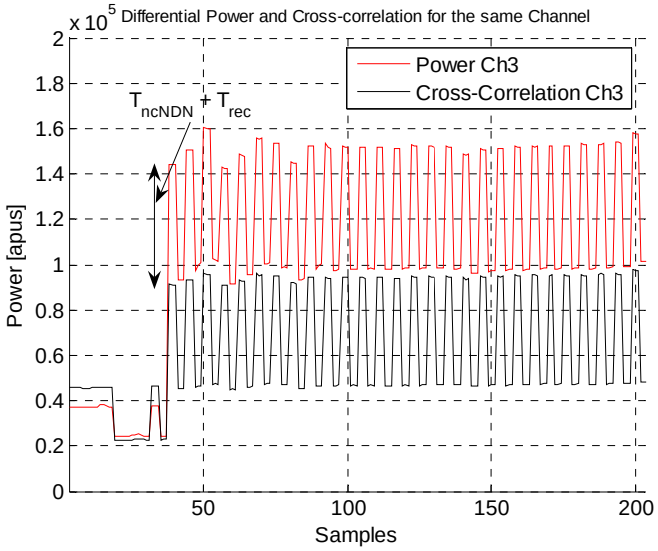

Figure 8.13 Measured auto-correlation of the chain 3 (Ch3), and modulus of the cross-correlation between the reference and the chain 3, for 200 samples.

Figure 8.13 presents the measured auto-correlation (power) of chain 3 (Ch3), and the modulus of the cross-correlation between the reference and chain 3 signals. Obviously, these two signals are related to the amplitude estimation. By analyzing Figure 8.13, it can be observed that the power and the cross-correlation have approximately the shape of a squared signal. The high levels correspond with the output for the $T_{CNS-max}$ input, and the lower levels correspond with the output for the $T_{CNS-min}$ input. Another important point is that, as expected, the cross-correlation signal has less noisy than the power signal. The offset difference between the cross-correlation and the power (which is higher) signals are the terms stated in Eqns. (8.3) and (8.5), which are mainly $T_{ncNDN} + T_{rec-ch3,}$ where $T_{rec-ch3} = A_{Ch3}^2/2\, T_{preLNA-Ch3} + T_{postLNA-Ch3}$.

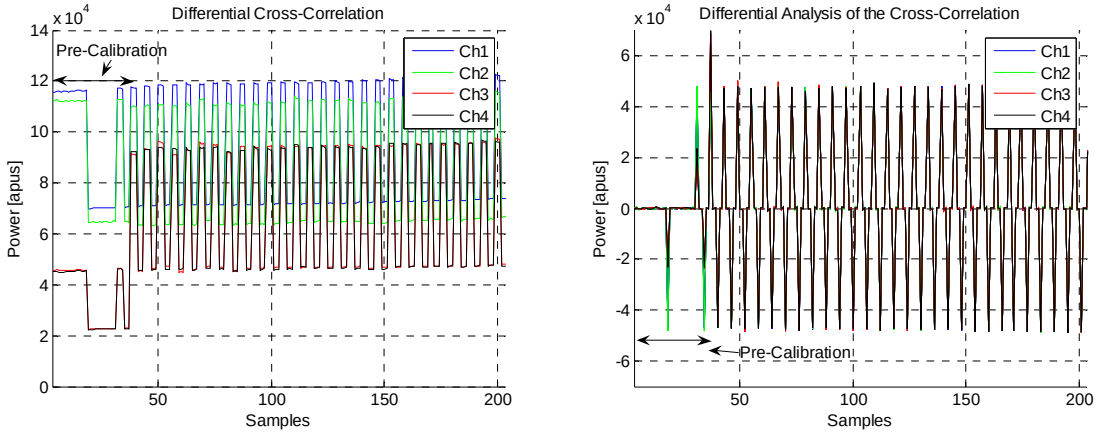

(a) (b)

Figure 8.14 Measured modulus of the cross-correlation for one RUT (four receiving chains, where ch1 is the reference signal): (a) corresponds to the output of the $T_{CNS-max}$ and $T_{CNS-min}$ squared input signal, and (b) differential analysis of the modulus of the cross-correlation.

Figure 8.14 presents the measured cross-correlation for one RUT, four receiving chains, including the reference signal. Figure 8.14a presents the output of the $T_{CNS-max}$ and $T_{CNS-min}$ squared input signal. At the beginning of the sequence there is a pre-calibration guard time in where the Kalman filter and the entire equalization algorithm is initialized and stabilized by using more calibration samples than usual. After this period, the chains are equalized in amplitude and in phase. However, Figure 8.14 only presents the amplitude equalization.

It is difficult to analyze the performance of the equalization from Figure 8.14a, because signals have different levels of cross-correlation between them due to the different T_{cNDN} terms, stated in Eqn. (8.5). Figure 8.14b shows the amplitude equalization algorithm from a differential point of view, so that there is positive values ($T_{CNS-max} - T_{CNS-min}$) and negative values ($T_{CNS-min} - T_{CNS-max}$). In any case, the positive and negative values are taken into account by using the modulus of the difference. From Figure 8.14b it is easier to analyze the equalization algorithm, it can be observed that in the pre-calibration the amplitude differences between the $T_{CNS-max}$ and $T_{CNS-min}$ for the different cross-correlations are different (for instance the Ch2 and Ch4 with the reference signal cross-correlation). After the pre-calibration period the differences become similar, and it can be considered that this RUT has been equalized in amplitude.

The amplitude and phase coefficients of this section are the ones calculated directly from the cross-correlation, not from the output of the Kalman filter, which are used to track the amplitude with the NCO.

Figure 8.15 presents the histograms of the amplitude coefficient of three chains of the RUT (Eqn. (8.11)). The reference signal is not displayed on Figure 8.15 because it has no relevance as its amplitude equalization coefficient is described always by $\mu_1=1$ and $\sigma_1=0$, thence is deterministic instead of being a random process. The number of samples that composes each histogram corresponds with two consecutive days of acquisitions, not only 200 samples as it has been presented in Figure 8.13 and Figure 8.14. Figure 8.15 shows the amplitude residual error is a random process which follows a Gaussian probability distribution function. Furthermore, it can be observed that the mean value of the amplitude equalization coefficient is 1 for the three histograms, the minimum standard deviation is 1% and the maximum is 2 %. Thus, there are two possible lectures of the data contained in Figure 8.15:

- the first one is that the amplitude equalization algorithm works properly, which can be deduced from the mean value ($\mu_i=1$ for i=2, 3, and 4), and the low standard deviation of the amplitude equalization coefficient. Nevertheless, if the algorithm does not work properly the mean value should not be 1 (indicating that the chains have different amplitudes), and consequently the standard deviation should be higher, and

- the second possible lecture is that the thermal control is working properly. This can be inferred from the fact that the amplitude equalization coefficient are

very stable (μ_i=1 and σ_i<<1, for i=2, 3, and 4). On the contrary, if the thermal control did not work properly, the reference signal (first chain) and all the rest of the signals would start drifting. Thus, the standard deviation would increase significantly. Even though, in this case if the drift speed is within the specifications, the mean would be 1 as well, because the tracking algorithm will follow any fluctuation of the reference signal. Otherwise, the mean should not be 1.

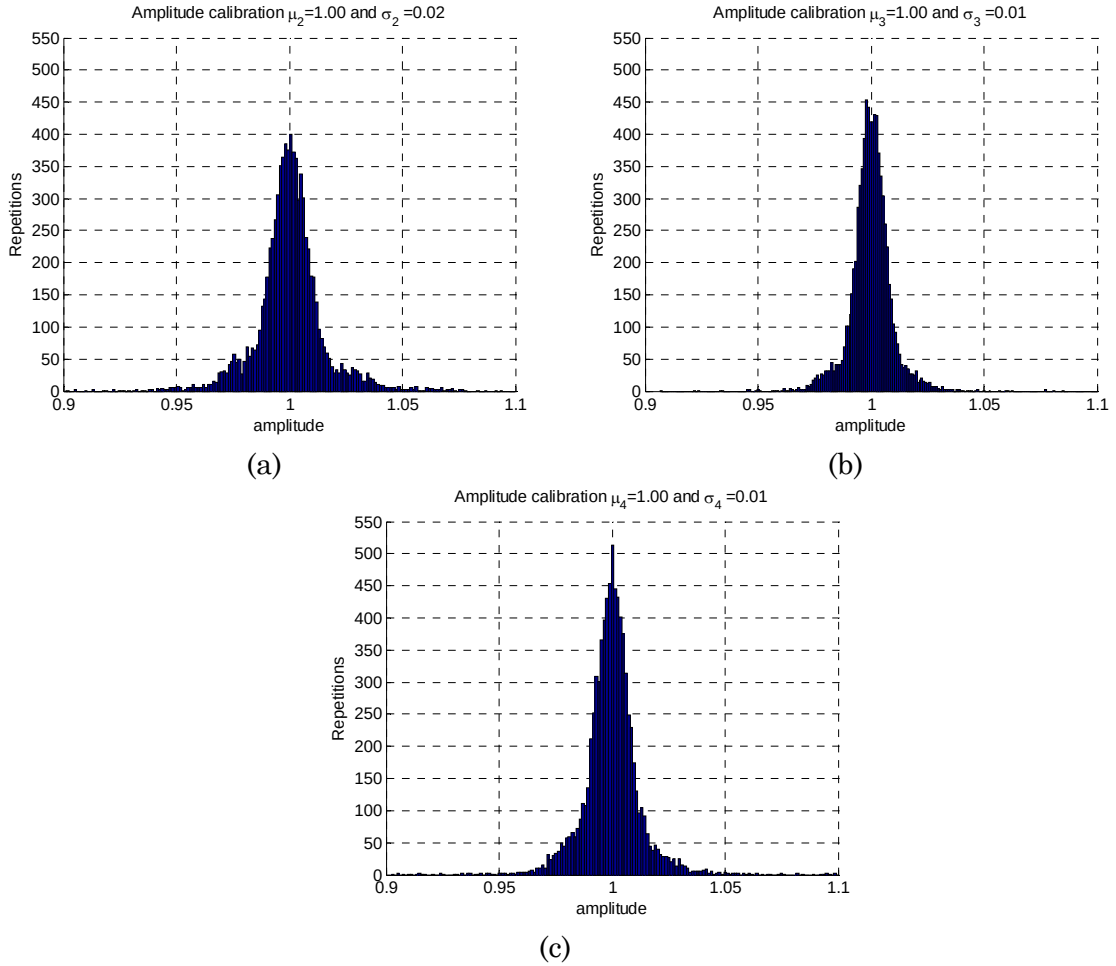

Figure 8.15 Measured amplitude coefficient (Eqn. (8.11)), histogram and statistics of the residual error for one RUT (four receiving chains, where ch1 is the reference signal): (a) Chain 2, (b) Chain 3, and (c) Chain 4.

Furthermore, Figure 8.15 shows that the histograms are not perfectly Gaussian, and a triangular distribution overlaps the Gaussian distribution in the three cases. So that, histograms have a non-expected high repetitions for amplitude values that should have very low number of repetitions. This amplitude noise behavior is similar to the phase noise pattern of a PLL, so that, this effect should be related with the feedback loop.

Figure 8.16 presents the measured phase of the complex cross-correlation for one RUT, four receiving chains, including the reference signal. Figure 8.16a presents the phase when the input are the $T_{CNS-max}$ and $T_{CNS-min}$ squared signal. At the beginning of the sequence there is a pre-calibration guard time in where the

Kalman filter and the entire equalization algorithm is initialized and stabilized by using more calibration samples than it is usual. After this period, the chains are equalized in amplitude and in phase. The amplitude has already presented in Figure 8.14, now Figure 8.16 presents the phase equalization performance.

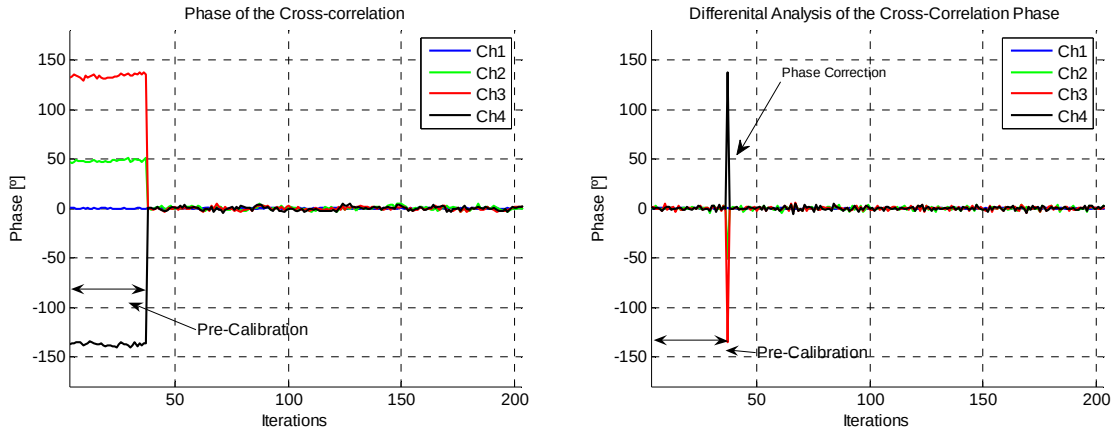

(a) (b)

Figure 8.16 Measured phase of the cross-correlation for one RUT (four receiving chains, where ch1 is the reference signal): (a) corresponds to phase of the complex correlation when the input are the $T_{CNS-max}$ and $T_{CNS-min}$ squared signal, and (b) differential analysis of the phase of the cross-correlation (1 iteration corresponds to 1 s).

As expected, the phase of the complex cross-correlation has not any dependence with the input signal. Then, its value does not change depending on the $T_{CNS-max}$ or $T_{CNS-min}$. However, as it has been explained before, the phase has an input dependence when $T_{CNS} < T_{cNDN}$ (Figure 8.5), but the values of the CNS have been chosen to avoid this problem. It can be observed that after the calibration, all the phase values of the cross-correlation between the chains and the reference signal are 0º. Thence, all the phases are equal and the RUT has been equalized.

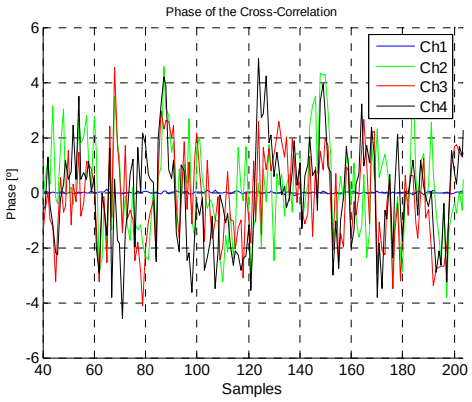

Figure 8.17 Measured phase of the cross-correlation for one RUT (four receiving chains, where ch1 is the reference signal, zoom of the Figure 8.16a (1 sample corresponds to 1 s).

Figure 8.17 provides a zoom of the calibrated interval. It can be seen that the reference signal has always a phase equal to 0º. It does not mean that its absolute phase does not drift with the time, it means that the relative phase between the relative signal and the relative signal is always zero, as expected. The phases of the other chains fluctuate between the maximum values of ±4º. It can be observed a high correlation between the phases of the chains, this is due to the fact that all of them are referred to the absolute phase of the reference signal. Part of these fluctuations are due to this relationship, hence their fluctuation patterns are similar.

Figure 8.18 presents the histograms of the phase coefficient of the four receiving chains of the RUT (Eqn. (8.12)). Although the histogram of the phase of the reference signal is displayed on Figure 8.18a, it is not truly a relative phase. In fact, it is the angle of a complex auto-correlation, which it is expected to be real. If it is not, then it is the quadrature error due to NCO problems.

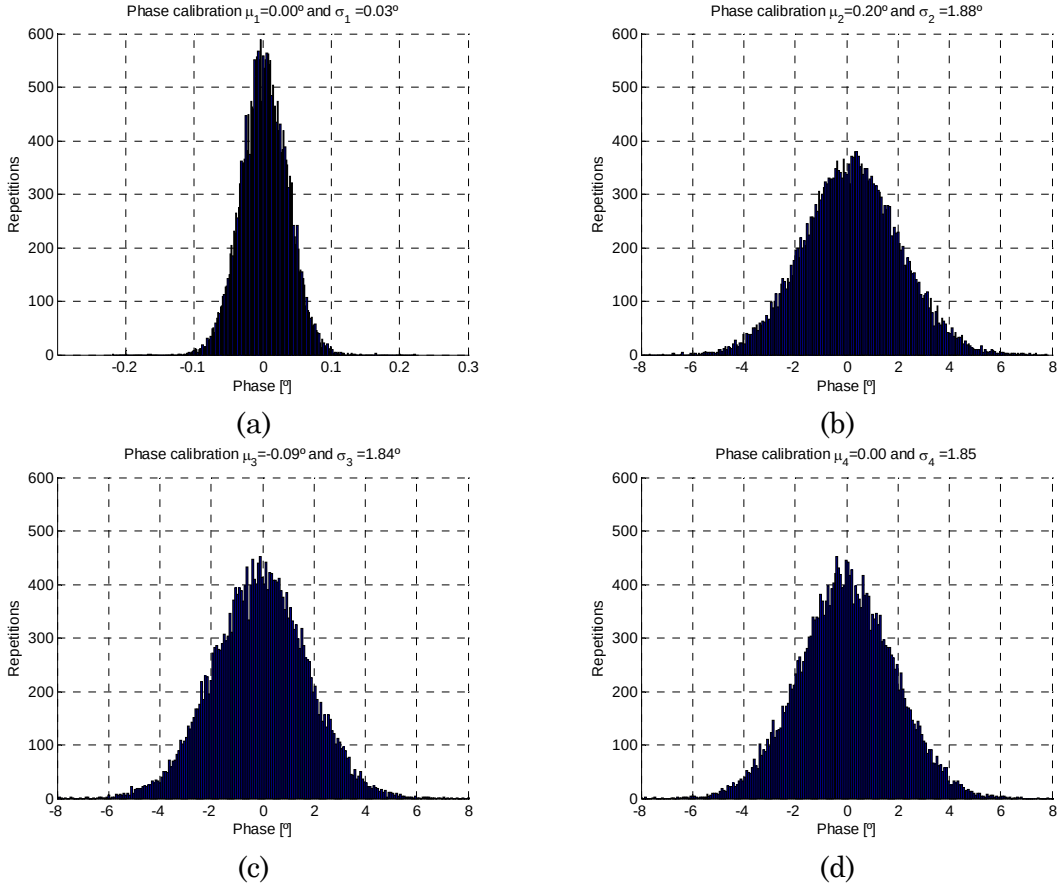

Figure 8.18 Measured phase coefficient (Eqn. (8.12)), histogram and statistics of the residual error for one RUT (four receiving chains, where ch1 is the reference signal): (a) Chain 1, (b) Chain 2, (c) Chain 3, and (d) Chain 4.

As it can be seen in Figure 8.18a, this error is very small ($\mu_1 = 0^o$ and $\sigma_1 = 0.03^o$) and, thus negligible. The relative phase of the reference signal is deterministic, thence it is defined by $\mu_1 = 0^o$ and $\sigma_1 = 0^o$. The number of samples that composes each histogram corresponds to two consecutive days of acquisitions. From Figure

8.18, it is shown that the phase residual error is a random process which follows a Gaussian probability distribution function.

In Figure 8.18 it can be observed that the mean value of the phase equalization coefficient is almost 0º for the three histograms (Figure 8.18b, Figure 8.18c, and Figure 8.18d), the standard deviation is around 1.80º, which is lower than the maximum standard deviation specified in Chapter 6 ($\sigma_{max} = 2^o$).

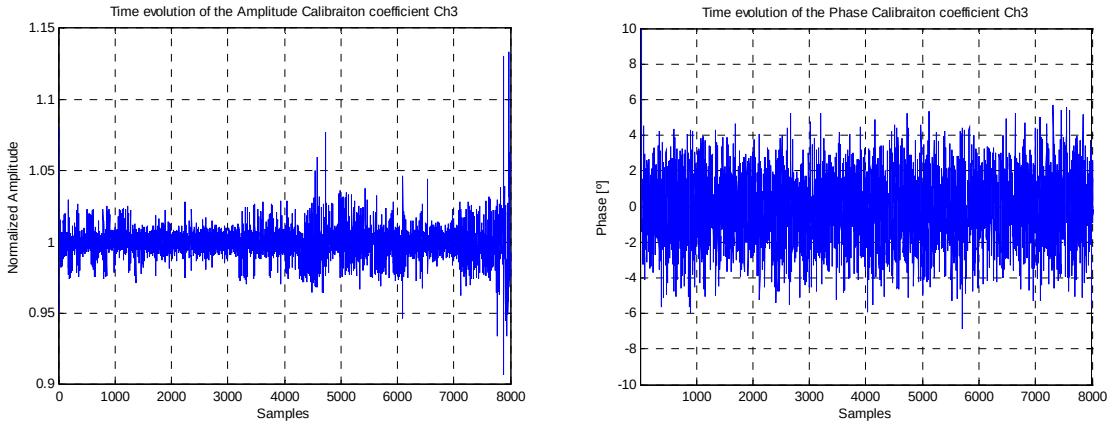

(a) (b)

Figure 8.19 Time evolution of the complex equalization coefficient for the chain 3: (a) amplitude, and (b) phase (1 sample corresponds to 1 s).

Finally, Figure 8.19 shows the time evolution of the complex equalization coefficient for the chain 3. It can be observed that the amplitude (Figure 8.19a) mean value is 1, but it has some fluctuations which are calibrated in the next iterations. For the phase (Figure 8.19b) the mean value is 0º having an acceptable level of noise ($\sigma_3 = 1.84^o < \sigma_{max}$).

8.3.1 Summary of the PAU-RAD Equalization

The calibration performance for one RUT has been presented in the previous section. In this section the amplitude and phase performance for the entire PAU-RAD system (for the 16 receivers' chains) is summarized in Table 8.1.

Table 8.1. Summary of the residual error in the phase and amplitude equalization of the whole PAU-RAD system for a continuous two days measurement.

RUT	Chain	Amp. mean	Amp. std.	Phase mean	Phase std.
RUT1	*v*-pol.+	1.00	0.00	0.0º	0.03º
	v-pol.-	1.00	0.01	0.20º	1.88º
	h-pol.+	1.00	0.01	-0.09º	1.84º
	h-pol.-	1.00	0.01	0.0º	1.85º
RUT2	*v*-pol.+	1.00	0.01	0.2º	1.97º
	v-pol.-	1.01	0.05	-0.17º	1.73º
	h-pol.+	1.00	0.01	0.02º	2.08º
	h-pol.-	1.00	0.02	-1.36º	2.50º
RUT3	*v*-pol.+	1.00	0.01	-0.78º	2.01º

	v-pol.-	1.01	0.01	-1.00º	2.18º
	h-pol.+	1.00	0.01	-0.05º	1.78º
	h-pol.-	1.00	0.03	-0.31º	1.65º
RUT4	*v*-pol.+	1.00	0.01	0.97º	2.37º
	v-pol.-	1.01	0.02	0.45º	2.12º
	h-pol.+	1.00	0.01	-0.47º	1.92º
	h-pol.-	1.00	0.02	-0.34º	2.14º

This analysis has been performed using the same data set used by the previous one RUT analysis, using two consecutive days of acquisitions.

As it can be seen in Table 8.1, the mean of the amplitude coefficients is very close to 1 and its residual error (standard deviation) is within the interval 0.01 and 0.05. On the other hand, the mean of the phase coefficient is around 0º, with the worst value of -1.37º. Its residual error around is 2º. The higher standard deviation is 2.5º and the lower 1.73º.

It can be concluded that following the equalization algorithm and procedures described in this chapter, the whole PAU-RAD fulfills the equalization requirements stated in Chapter 6. Hence it is suitable for performing a DBF to fulfill the radiometric requirements.

8.4 Conclusions

This chapter has analyzed the phase and amplitude equalization procedure. Focusing on the hardware needed to do it, such as the RF switch, the CNS, and the digital complex-cross correlator and NCO, and on the algorithm to estimate the phase coefficients, which contains a Kalman filter to reduce the estimation error. Then, the equalization performance has been analyzed in deep for one RUT and, finally the summary of the entire PAU-RAD instrument calibration performance has been provided.

The equalization procedure can be described in two steps: error estimation and error equalization. The error estimation step estimates the phase and amplitude differences of signals. In order to estimate these differences, the switch of each RF chain has to be connected to the CNS input signal. Then, signals are cross-correlated and from this complex value the phase and amplitude equalization coefficients are determined. The error equalization step corrects this phase and amplitude differences in order to equalize the signals. This is done by changing the phase and amplitude of the NCO of each signal accordingly to the estimated values in the previous step.

Due to the nature of the complex correlator's output signal, which is the subtraction of the CNS and the NDN temperatures, to estimate the phase and amplitude error the T_{CNS} has to ensure that it is always higher than $T_{NDN.}$ This is

important to avoid any uncertainly related with the different behaviour of the complex correlation output depending on the T_{NDN}.

The voltage signals from the pair of receivers to be cross-correlated have been provided in order to analyze the impact of the different terms o the equation. Furthermore, the equations of the differential algorithm for phase and amplitude estimation have been provided, and analyzed. After estimate these parameters from the row complex-cross correlation their measurement standard deviation is reduced by using a Kalman filter. If the Kalman filter is correctly tuned using the parameter σ_ε^2 is able to reduce the standard deviation of the measurement and to track thermal drifts of the coefficients.

Finally, the entire PAU-RAD instrument calibration performance has been provided seen in Table 8.1 the mean of the amplitude coefficient is 1 and its residual error (standard deviation) is within the interval 0.01 and 0.05. On the other hand, the mean of the phase coefficient is around 0º, with the worst value of -1.37º. Its residual error around is 2º. The higher standard deviation is 2.5º and the lower 1.73º.

It can be concluded that following the equalization algorithm and procedures described in this chapter, the whole PAU-RAD fulfills the equalization requirements stated in Chapter 6. Hence it is suitable for performing a DBF to fulfill the radiometric requirements.

Chapter 9

9 PAU-RAD PERFORMANCE AND TEST

The PAU-RAD hardware has been described in Chapter 7, and the equalization process and its performance has been analyzed in Chapter 8. This chapter is devoted to the analysis of the PAU-RAD performance from three different aspects: the beamforming performance, the real and synthetic aperture relationship (stated in Chapter 4), and finally, the reliability of the system performing radiometric field measurements. Concluding this analysis and comparing the results with the design requirements, it can be summarized that the PAU-RAD system fulfills the design requirements and it is able to measure radiometric data depending on the measurement set up. So, it can be considered ready for operation as a radiometer in regular measurement campaigns.

9.1 Performance and Tests Overview

The performance and tests of PAU-RAD has been devised to have three different steps:

- the first one is to analyze the DBF performance for each synthesizable beam, and the evaluation criteria for this analysis must be the suitability of these beams for radiometric applications. With this purpose, the PAU-RAD instrument was mounted in the rotor of the *Universitat Politècnica de Catalunya* (UPC) anechoic chamber [118] where the beams were accurately measured. Furthermore, the radiometric resolution and Allan's variance [127] were also measured in this RFI clean environment,

- taking advantage that the system was in the anechoic chamber, the system has been operated as a synthetic aperture radiometer as well to assess the hypothesis of Chapter 4: that a radiometer with DBF can be completely described and implemented in the synthetic aperture radiometry framework, and

- last, but not least, testing point consisted of measuring the radiometric capabilities of the PAU-RAD system in a field campaign, obtaining the emissivity from each of the synthesizable incidence angles from different surfaces such as bare soil, wet soil and soil with vegetation canopies and comparing them with the theoretical emissivity curves.

After this set of tests to assess the system performance, the system can be considered to be ready for operating in regular measurement campaigns.

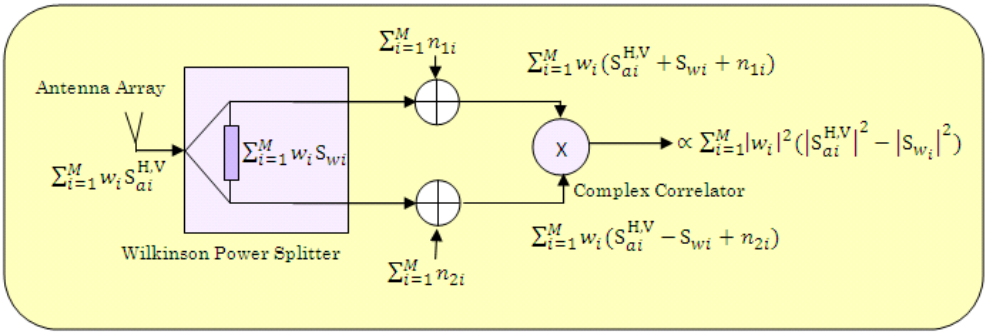

Figure 9.1 PAU-RAD equivalent sketch, where the current signals have been substituted by the array signals.

Figure 9.1 shows an equivalent sketch of the PAU-RAD where the current signals have been substituted by the array signals (the complex weight addition of the equalized signals). The antenna signal (S_a) is split in two, and the Wilkinson noise ($\pm S_w$) is added in phase (upper chain) and in 180º-phase (lower chain). Then, the noise receiver is added for each chain. The output is the complex-cross correlation of the upper and lower beams, as already explained in Chapter 6. As it has been

explained in Chapter 8, for convenience, in this work no constants have been taken into account when processing in the digital domain, so that, the measurements of cross-correlation have units of arbitrary power unit (*apu*), which are proportional, but not directly Watts.

9.2 DBF Performance

In order to test the PAU-RAD performance, the instrument was mounted in an azimuth and elevation antenna rotors (Figure 9.2) at UPC anechoic chamber. After thermal stabilization, the antenna array was illuminated with a noise signal at GPS-L1 frequency transmitted from a corrugated horn. The tests conducted to measure the DBF performed has been grouped in two categories:

- evaluation of the hardware calibration goodness measuring its impact on the DBF and correction of the array phase center [128] (the point from which the electromagnetic radiation spreads spherically outward, with the phase of the signal being equal at any point on the sphere), and
- DBF stability and quality of the beams.

Figure 9.2 shows the preparation of the measurement set up in the anechoic chamber, showing the process of attaching the PAU-RAD system in the rotors involving a gantry crane and several high qualified anechoic chamber personnel. Furthermore, the system has to be aligned with the rotors from which the illumination signal is transmitted. This was done by attaching properly the instrument in the rotor and using the alignment screws for fine tuning.

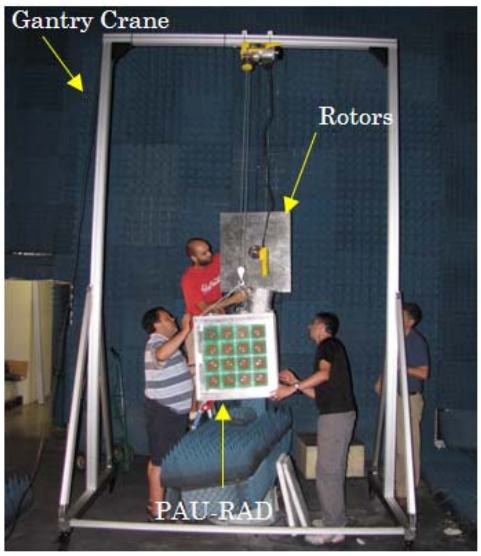

(a)

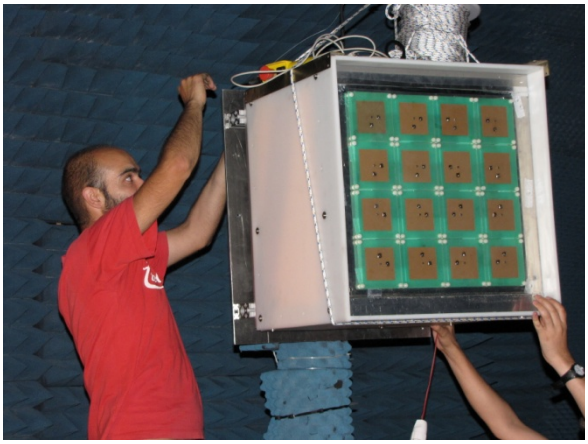

(b)

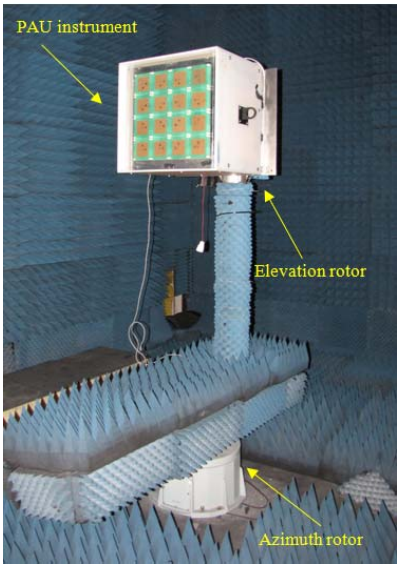

(c)

Figure 9.2 UPC anechoic chamber set up for measuring the PAU-RAD instrument, (a) PAU-RAD carried with a gantry crane to attach it in the rotor, (b) attaching and the instrument to the rotors and aligning it with the transmitter rotors, and (c) the instrument attached and ready to be measured in the UPC anechoic chamber.

Figure 9.2c shows the PAU-RAD instrument finally attached in the rotors, ready to measure its performance.

9.2.1 Thermal Control Performance

As it has been said in the previous section, PAU-RAD has to be thermally stabilized before start measuring its beams. Otherwise, temperature fluctuations make the phase and gain of the analog receivers' drift, having a big impact on the performance of the beam. However, the equalization algorithm is able to track the phase and amplitude of the receivers, so that, it is capable to restore the beams performance by equalizing again the system. The equalization period or time between two consecutive equalization procedures, depends on the velocity of the phase and amplitude drifts, so, mainly and to a large extent on the goodness of the thermal control. If the system has significant temperature drifts, then receivers will change their phase and amplitude faster and PAU-RAD performance will degrade faster. The better the thermal control performance, the longer the equalization period. A long equalization period is desirable as the system can dedicate more time to measure the antenna temperature, instead of equalizing itself.

The results of the thermal control during the anechoic chamber measurements are presented in Figure 9.3. Using the thermal monitor sub-system (Section 7.2.5), thermal records from the 15 different digital thermometers were acquired each 2 seconds. Figure 9.3a shows the record of 8 of the 15 digital thermometers. The system has a transient and, after approximately 1 hour and 40 minutes, it

stabilizes. Although the PID was set to be 44º C, each thermometer stabilizes at different temperatures. These differences are related with the big dimensions of the system (110 x 120 x 80 cm) which leads into several temperature gradients inside it. This is a well-know problem in temperature control, so it was tried to minimize it by installing two fans to homogenize the temperatures by moving the air as much as possible.

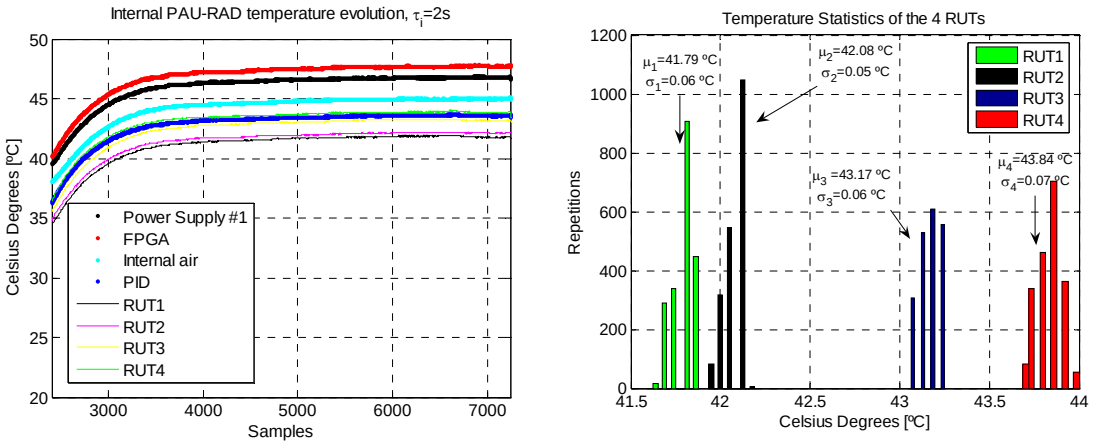

(a) (b)

Figure 9.3 Thermal control of the PAU-RAD in the anechoic chamber, (a) time evolution of 8 of the digital thermometers, and (b) histograms of the RUTs thermometers (1 sample corresponds to 2 s).

Despite that effort, differences about 6º C can be found inside the PAU-RAD. However, differences between RUTs are roughly 2º C. The higher temperatures are for the FPGA and the power supplies, which stabilizes around 47º C. Figure 9.3b shows the histograms of the temperature of the RUTs when stabilized (not taking into account the transient).

Table 9.1. Temperature statistics for the RUT when stabilized

	Mean (μ)	Std. (σ)
RUT1	41.79º C	0.06º C
RUT3	42.08º C	0.05º C
RUT3	43.17º C	0.06º C
RUT4	43.84º C	0.07º C

Table 9.1 summarizes the temperature statistics of the RUT when stabilized. There is a difference of 2.05º C between the means and the standard deviation is always lower than 0.1º C. However, these were the statistics for the anechoic chamber measuring conditions, and higher standard deviations are expected outdoors with higher thermal variations.

9.2.2 Evaluation of the Equalization Goodness

As it has been shown in Chapter 7 (Section 7.2.2.1), receivers have different paths for the signals coming from the CNS and from the antenna. Moreover, this

difference changes among receivers, and it has to be empirically measured and further compensated on the calibration algorithms. Furthermore, the correction of the array phase center (due to elemental antenna miss-alignments), is still another effect that has to be measured and further compensated with the equalization algorithms. This was the aim of the first test performed in the anechoic chamber. To do it, first of all the phases and amplitudes of the analog receivers was equalized using the internal reference CNS. Then, the system was set to measure the antenna signal complex cross-correlations. These cross-correlations were performed between the reference receiver and the rest of them, with the aim of estimating the phase and amplitude difference among them when pointing to the antenna. These phases and amplitudes obtained are the differences between the CNS and the antenna signal path, and they are set as system parameters to be used in the equalization algorithm (Eqn. (7.7), this equation has been presented in detail in Section 7.3.2.1, and it is repeated here for clarity Eqn. (9.1)). Slight corrections among receivers (< 4º and < 0.2 dB) were required, and it was straightforwardly solved by adding these measured divergences to the weighting equalization coefficients A_{ph} and ϕ_{ph} in Eqn. (9.1). A missestimation of these parameters can introduce an offset on the direction of the steered beams and, a loss of performance as well.

$$\mathrm{LUT_i}(n) = (A_{Beam}A_{Cal}A_{ph}) \cdot \cos\left(2\pi\Omega n + (\theta_{Beam} - \theta_{Cal} - \theta_{ph})\right) \qquad (9.1)$$

where:

- $\mathrm{LUT_i}(n)$ stands for Look-Up Table of the NCO of the i^{th} receiver,
- Ω and n are the digital frequency (Ω = 0.25 times the sampling frequency) and digital time, respectively,
- A_{beam} and θ_{Beam} are the modulus and phase of a complex weight assigned to each receiver to steer the beam in the desired direction,
- A_{Cal} and θ_{Cal} are the amplitude and phase of a complex weight assigned to each receiver for hardware equalization, and
- A_{ph} and θ_{ph} are the modulus and phase of a complex weight to correct any antenna error such as center phase or different path lengths. These values were measured once at the UPC anechoic camber and set as a system parameter.

Once the feasibility of the calibration approach and the DBF performance are checked, the DBF stability itself is analyzed. For this purpose, the synthesized beam was steered to 0º and radiometric data was acquired during 100 min. with an integration time of 1 s. Figure 9.4 shows the results for the v-pol. of this test, the modulus and the phase of the complex correlation in a time line. There are no relevant fluctuations, the system remains quite constant, for the whole 100

minutes. Then, it is possible to conclude that, with the thermal control described in the previous section, the phase and amplitude of the receivers remains constant for at least 100 minutes.

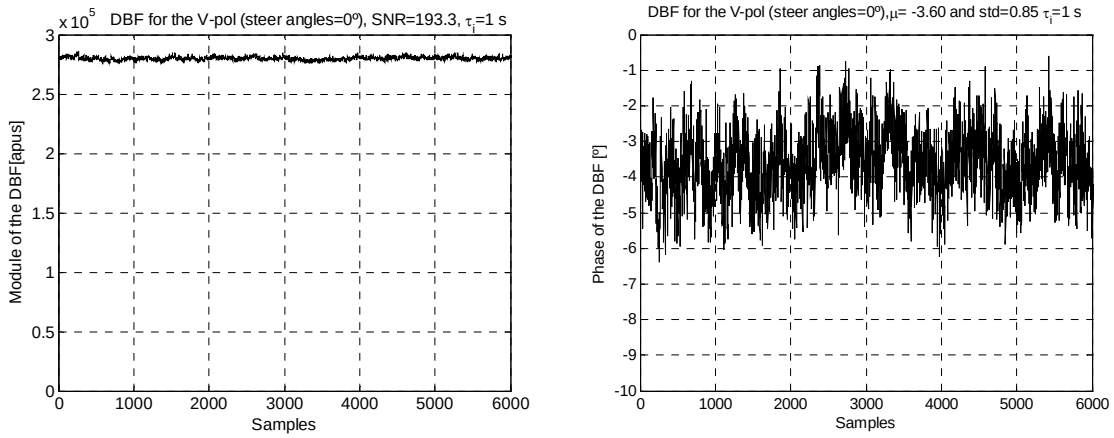

Figure 9.4 PAU-RAD long term DBF results for the *v*-pol. 0º beam: (a) Modulus of the complex cross-correlation collected by the beam and (b) Phase of the complex cross-correlation

On the other hand, Figure 9.5 shows the histograms and statistics of the Figure 9.4a shows the histogram of the modulus with a clear Gaussian distribution having a mean of 279923 *apus* and a standard deviation of 1448 *apus* (which it implies an SNR=193.3).

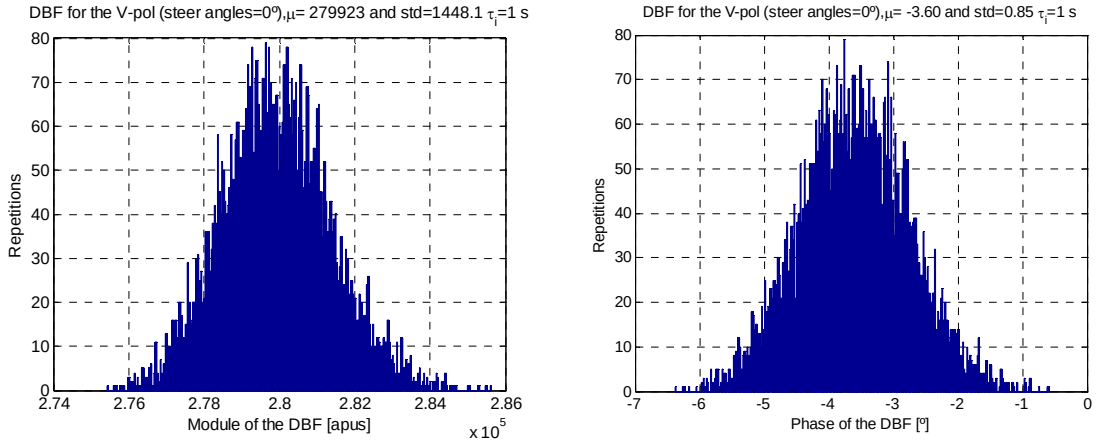

Figure 9.5 Complex of the cross-correlation of the PAU-RAD long term DBF, for 100 minutes with a τ_i=1 s: (a) histogram of the modulus, and (b) histogram of the phase.

Figure 9.5b shows the histogram of the phase of the complex correlation with a clear Gaussian distribution having a mean of -3.6º and a standard deviation of 0.85º. Although the standard deviation is well below of the calibration requirement, there is a phase offset (-3.39º) that can be associated with a residual error of the CNS-antenna path or to the phase center calibration.

The last part of this analysis takes into account the time evolution of the first and second order statistic moments of the DBF *v*-pol. output, the mean and the Allan's variance [127], respectively. The Allan's variance is intended to estimate stability due to noise processes and not that of systematic errors or imperfections such as phase and amplitude drifts diminishing the performance of the DBF and of its antenna brightness temperature. In addition, the Allan's variance is usually provided in radiometry as a common figure of merit of radiometer's stability.

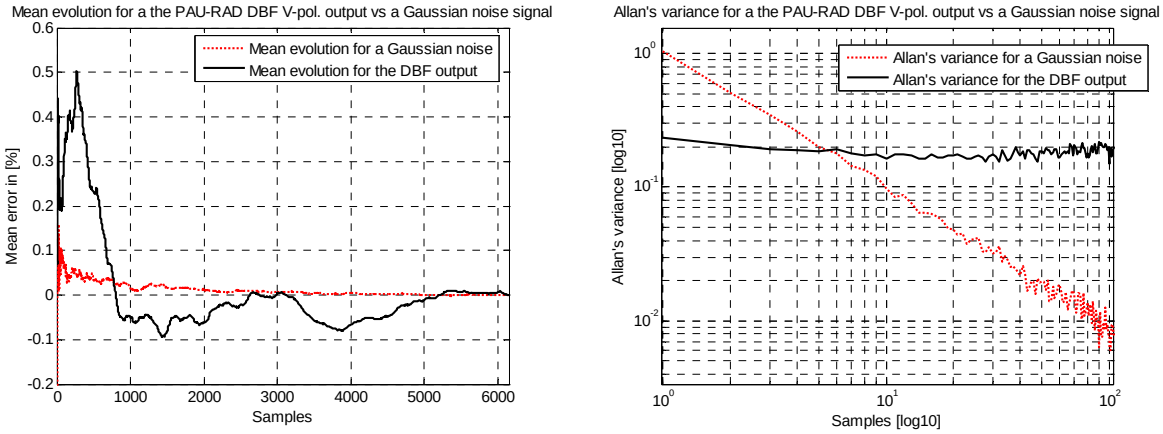

(a) (b)

Figure 9.6. Comparison of statistic's time evolution for the v-pol. output and a white noise signals: (a) mean for 100 minutes with a τ_i=1, and (b) the Allan's variance for 100 seconds with τ_i=1 (both axes have logarithmic units) (1 sample corresponds to 1 s).

Furthermore, these statistical moments for the DBF output are compared with the ones of a Gaussian white noise signal. Figure 9.6a shows the error in % of the time evolution of the mean, it can be observed that the Gaussian noise signal mean decreases more rapidly than the DBF output, which has a random decreasing trend. Although this time evolution of the DBF output, the maximum error is 0.5 % which can be neglected (*i.e.*: T_A = 300 K the mean error peak corresponds to 1.5 K). On the other hand, Figure 9.6b shows that the Allan's variance of the Gaussian noise signal decreases one decade per one decade, as expected for white noise. It is clear that the output of the DBF is not Gaussian because it does not follow the noise trend. The output of the DBF signal has time fluctuations, which can be observed in both Figure 9.6 plots. These time fluctuations imply that considering only in a short period of time the output is not Gaussian. Otherwise, when considering a large time interval the output is Gaussian (histogram shown in Figure 9.5a). This time Gaussianity (Section 3.3.1) can be explained with Central limit theorem, which states conditions under which the mean of a sufficiently large number of independent random variables, each with a finite mean and variance, can be approximately normally distributed [129].

9.2.3 Beamformer Performance and Steering Tests

The aim of this test was to study the performance of the beamformer, since the system is fully polarimetric, the DBF has to be characterized for the four Stokes's parameters. As the antennas of the system have only two polarizations, vertical and horizontal, the third and fourth parameters are measured by cross-correlating these inputs. The beams of the third and fourth parameters are identical among them because they are the real and imaginary parts, respectively, of the cross-correlation of the horizontal and vertical beams. Then, the analysis is focused in the horizontal (*h*) and vertical (*v*) polarizations, and the cross-correlation (*hv*).

As it has been already explained in Chapter 6, there are a number of figures of merit to measure the quality of an array. In this case, the MBE has been selected because it unifies different parameters (main beamwidth, side lobe levels (SLL), backlobe, *etc*) in a single one. In general, the MBE is defined as the ratio between the collected power by the main beam of the array and the total collected power. Theoretically, the main beam ends in the nulls between the main beam and the first side lobes, but in practice, these nulls are difficult to determine due to noise phase errors and the finite angular resolution of the measurement system. In practice, to compute the edge of the main beam, it is considered that the main beam ends when it reaches the maximum side lobe amplitude level. In any case, this approximation gives a slightly lower MBE value than the real one.

To compute the MBE and the beamwidth of the synthesized beams in different directions, the whole antenna pattern was measured by scanning across the azimuth angle (φ) range and the elevation angle (θ) range. The synthesized beam was steered from -20º to +20º in 5º steps, in total: 9 different beams.

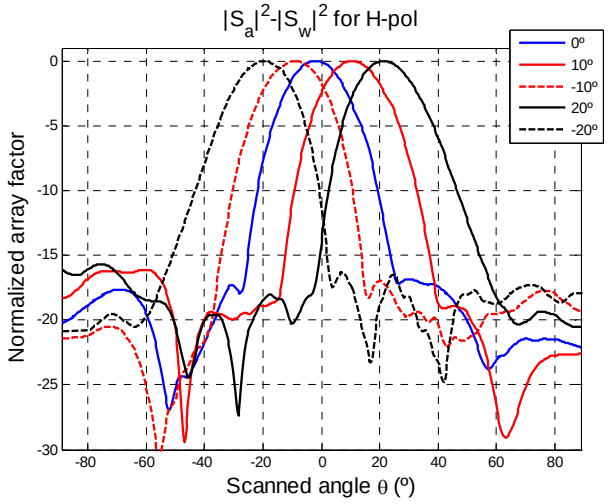

Figure 9.7. PAU-RAD measured DBF results. Measured normalized array factors in dB for multiple beams (*h*-pol. and scanning the θ domain range).

For the sake of clarity only 5 of these normalized DBF results are presented in Figure 9.7 these beams correspond to the horizontal polarization scanning across the θ angle. Synthesized beams in have a SLL of -17 dB in the best case, the 0º

steering beam and a -16 dB in the worse case, for the ±20º angle. Furthermore, in some beams there is a misalignment of ±2º due to the residual calibration errors, which do not impact the instrument's performance. Figure 9.8 presents the measurement of the array pattern, from which the MBE is calculated, in the cosines director domain ($(\xi,\eta) = (\sin\theta\cos\varphi, \sin\theta\sin\varphi)$ with respect the x and y axes) for four different cases. The first one is the beam for the *h*-pol. and 0º steering angle. The second one (Figure 9.8b) consists of the beam for the *h*-pol. but for 20º steering angle.

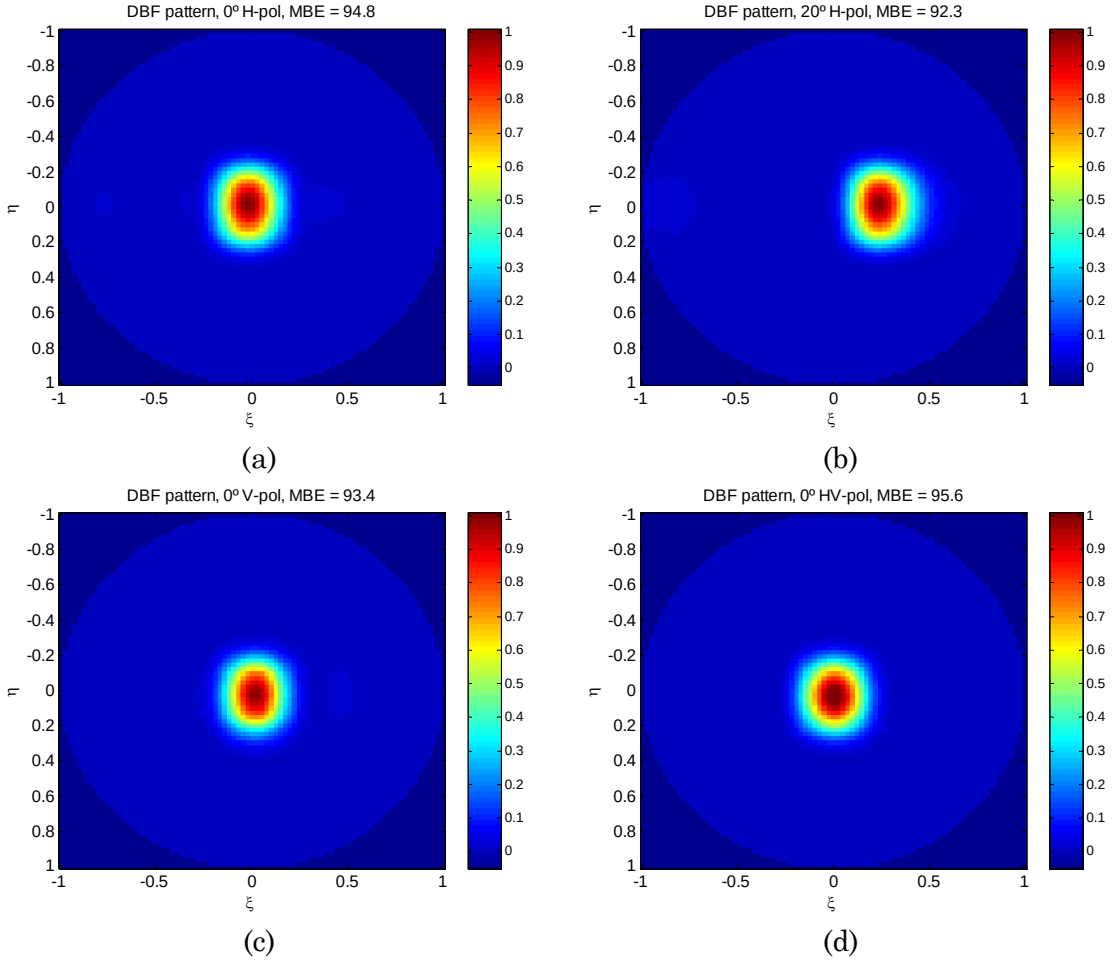

Figure 9.8. PAU-RAD measured array patterns in the cosines director domain ($(\xi,\eta) = (\sin\theta\cos\varphi, \sin\theta\sin\varphi)$ with respect the x and y axes) for different array configurations, (a) *h*-pol., and 0º steering angle, (b) *h*-pol., and 20º steering angle, (c)*v*-pol., and 0º steering angle, and (d) *hv*-pol., and 0º steering angle.

From the measured array patterns the MBE can be calculated as previously explained. Another important design parameter is the array beamwidth, which can also be calculated from the array pattern. Table 9.2 and Table 9.3 summarize the results in terms of MBE and beamwidth for the *h*-pol., *v*-pol. and *hv*-pol. beams. For all the possible steering angles the MBE is better than 91 % and the best result is for 0º where the MBE reaches a value of 95.6 % for *hv*, 94.8 % for *h*, and 93.4 % for the *v* polarization. On the other hand, the worst results are achieved, as expected, when the angle of steering is high (±20º). Note that the design

specification was to have a MBE higher than 94 %, which has been achieved for the 0º steering beam and it is almost fulfilled for all other beams.

The other design parameter was the beamwidth, in this case the best performance is again for the 0º steering angle when the $\Delta\theta_{-3dB}$ = 22.8º for the *h*-pol., $\Delta\theta_{-3dB}$=22.4º for *v*-pol., and $\Delta\theta_{-3dB}$= 23.33º for *hv*-pol. Again, the worst results are for the largest steering angles, then the beamwidth values reaches the maximum of $\Delta\theta_{-3dB}$ = 25.5º. So that, the beamwidth requirements have been fulfilled in almost all cases.

Table 9.2. MBE for the synthesized beams

Polarization	*h*	*v*	*hv*
-20º	92.5 %	91.8 %	94.2 %
-15º	93.2 %	92.6 %	95.0 %
-10º	93.2 %	92.7 %	95.1 %
-5º	93.3 %	92.9 %	95.2 %
0º	**94.8 %**	**93.4 %**	**95.6 %**
5º	92.9 %	92.5 %	95.0 %
10º	92.8 %	91.9 %	95.0 %
15º	92.7 %	91.7 %	94.2 %
20º	92.3 %	91.2 %	93.8 %

In addition, Table 9.2 shows that the *hv* beams have the best performance in terms of MBE, but the largest beamwidth (Table 9.3). This is due to the way this beam is created from the cross-correlation of the *h* and *v* beams.

Table 9.3 $\Delta\theta_{-3dB}$ for the synthesized beams

Polarization	*h*	*v*	*hv*
-20º	24.6 º	24.2 º	24.8 º
-15º	25.0 º	24.8 º	25.5 º
-10º	24.1 º	24.0 º	24.6 º
-5º	23.7 º	23.1 º	24.2 º
0º	**22.8 º**	**22.4 º**	**23.3 º**
5º	23.7 º	23.3 º	24.2 º
10º	24.6 º	24.2 º	24.8 º
15º	23.8 º	23.5 º	24.2 º
20º	24.2 º	24.1 º	24.6 º

Once the steering capabilities and excellent performance of the instrument have been demonstrated, Figures 8-10 analyze the polarimetric nature of the beams. For brevity purposes only the 0º steering angle is shown.

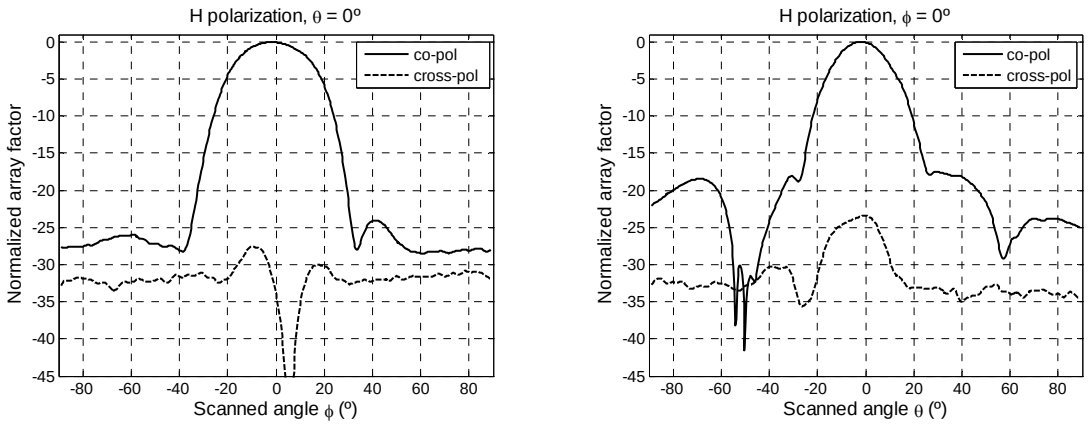

(a) (b)

Figure 9.9. PAU-RAD DBF results in dB for the 0º steered beam and *h* polarization, (a) polar and cross-polar beams scanning on the φ domain (non-steerable), (b) polar and cross-polar beams scanning on the θ domain (steerable).

Figure 9.9 shows the DBF results in dB for the 0º steered beam and *h*-polarization for the polar and cross-polar beams scanning on the non-steerable domain (φ). In this case the SLL is -25 dB and the cross-polar level is -30 dB, which fulfills another design requirement (< -25 dB). Figure 9.9b shows the steerable beam which is slightly worse than the previous one, but it still has a good performance. The SLL is -17.5 dB and the cross-polar level is -25 dB.

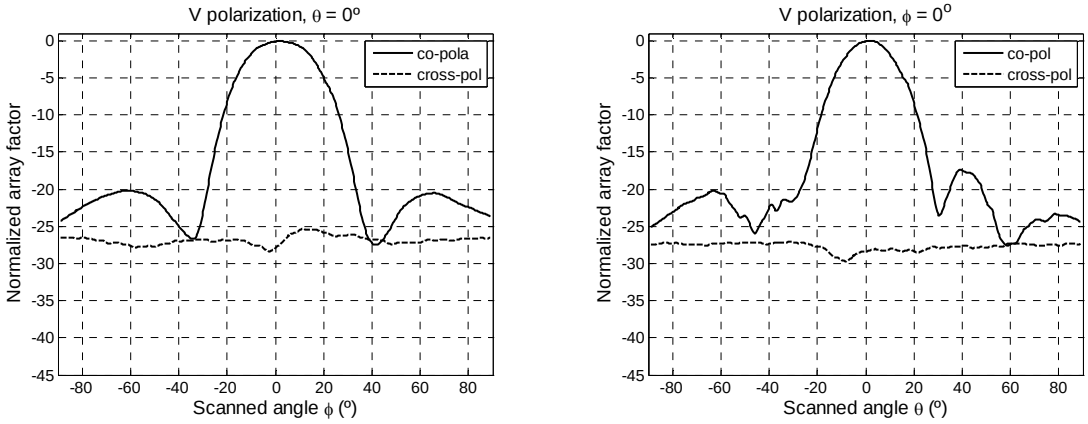

(a) (b)

Figure 9.10. PAU-RAD DBF results in dB for the 0º steered beam and V polarization, (a) polar and cross-polar beams scanning on the φ domain (non-steerable), (b) polar and cross-polar beams scanning on the θ domain (steerable).

Figure 9.10 shows the DBF results in dB for the 0º steered beam and *v*-polarization for the polar and cross-polar beams. In this case the SLL is -20 dB and the cross-polar level is -27 dB. Figure 9.10b shows the steerable beam which is again slightly worse than the previous one, but it still has a good performance. The SLL is -17.5 dB and the cross-polar level is -27 dB.

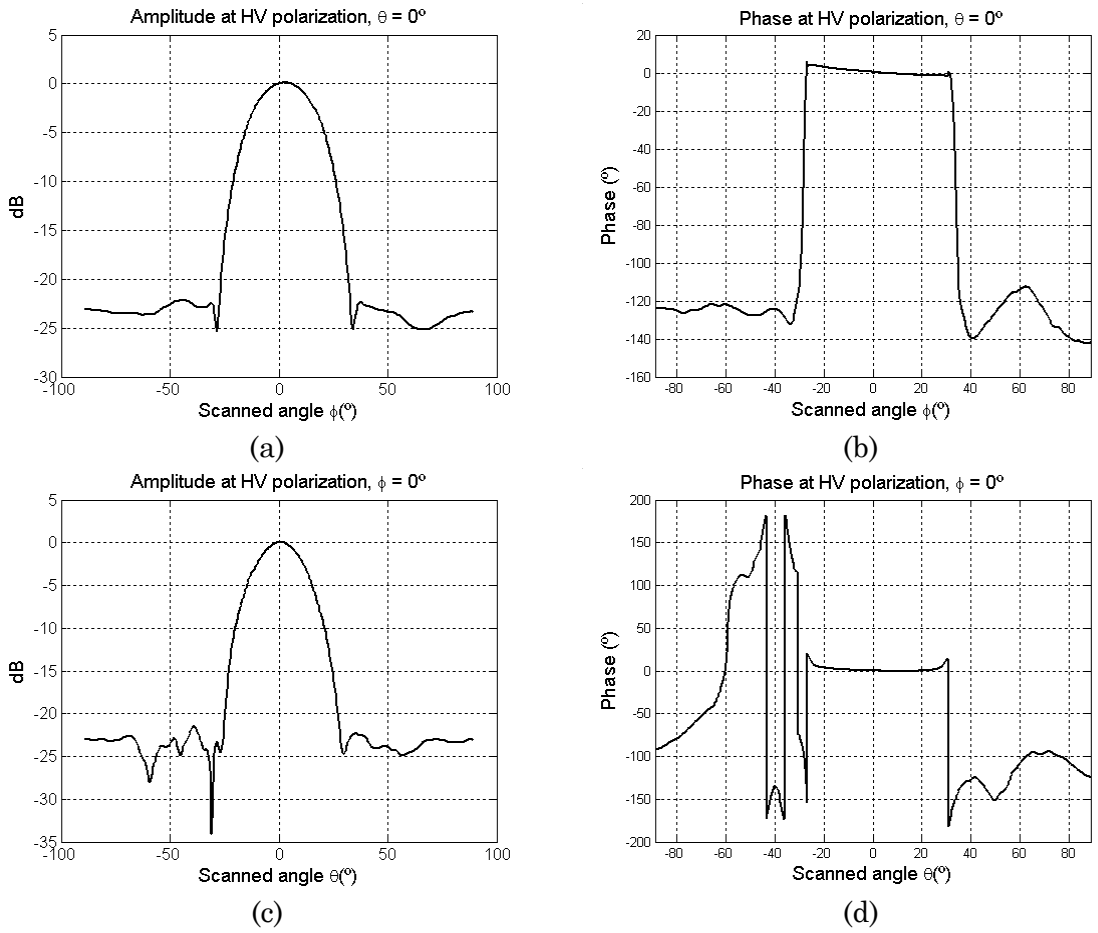

Figure 9.11. PAU-RAD DBF results in dB for the 0º steered beam and HV polarization, (a) modulus of the beam scanning on the φ domain (non-steerable), (b) phase of the beam on the φ domain, (c) modulus of the beam scanning on the θ domain (steerable), (d) phase of the beam scanning on the θ domain (steerable).

Figure 9.11 shows the θ = 0º and φ = 0º cuts of the *hv*-polarization. This case is different from the previous two ones, because the third Stokes parameter is computed from the real part of the product of antenna patterns, and the fourth one from the imaginary part. So that, amplitude and phase of the cross-correlation beam have to be presented to show the instrument performance on this full polarimetric mode. Figure 9.11a and Figure 9.11c show the modulus in [dB] of the DBF results for the 0º steered beam and *hv*-polarization scanning over the φ and θ, respectively. In both cases, the SLL is better than -22.5 dB. Figure 9.11b and Figure 9.11d show the phase of the DBF results for the 0º steered beam and *hv*-polarization, at the main beam there is a phase error of 1.5º, which induces an error of about -17 dB in the fourth and third Stokes parameters.

9.3 Measured Radiometric Resolution

The radiometric resolution was measured after measuring the beams performance of the PAU-RAD. This test was also performed in the anechoic chamber using a microwave absorber (emissivity close to 1, as for the black body) at a physical temperature of 289 K. The PAU-RAD instrument was covered with the microwave absorber, and then all the beams were periodically steered and integrated with an integration time of 1 s. Figure 9.12 summarizes the radiometric resolution for each beam and polarization. The mean value is 3 K, but there are some beams, especially in the *v*-pol., with poorer radiometric resolution, around 5 K.

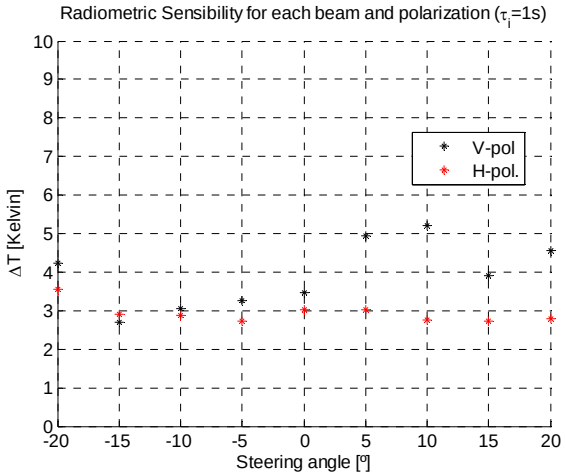

Figure 9.12. PAU-RAD measured radiometric resolution for each beam and for both polarizations.

Notice that these values are given an optimistic resolution performance of the system. They are optimistic because they have been calculated using a microwave absorber (T_{abs} ~ 300 K) and the PAU-RAD topology is equivalent to a Dicke radiometer and T_w ~ 300 K. In this case the temperature measured by PAU-RAD is close to zero, (T_{PAURAD} ~ 0 K when T_{abs} ~ 300 K). The worst case, the highest temperature measured, occurs when calibrating with a cold load (T_{PAURAD} ~ 294 K when T_{SKY} ~ 6 K).

After this test, the measurements in the anechoic chamber continued looking for the relationship between the real and synthetic aperture radiometers.

9.4 PAU-RAD Real and Synthetic Aperture Working Modes

Another test performed in the anechoic chamber was oriented to assess the Chapter 4 hypothesis, that one in which a radiometer with DBF can be described in

the synthetic aperture radiometry framework. In order to prove the real aperture digital beamforming and the synthetic aperture relationships the PAU-RAD instrument is used. As explained in Chapter 7, PAU-RAD has both imaging capabilities implemented: digital beamforming and interferometric synthetic aperture capabilities. From the digital beamforming point of view, the beam can be steered from -20º up to 20º over the vertical axis without a significant degradation of the MBE factor (> 93 %) [113]. Once the signals are inside the FPGA, they are phase and amplitude equalized, the beam is steered in real-time towards the desired direction following the Eqn. (9.2) (Section 4.2), and finally, the polarimetric measurements are obtained:

$$S^{p}_{\mathrm{DBF}}(t,\xi_0,\eta_0) = \sum_{\mathrm{m}=1}^{M} w_m(\xi_0,\eta_0)\, S^{p}_{m}(t), \tag{9.2}$$

where:

- $S^{p}_{\mathrm{DBF}}(t,\xi_0,\eta_0)$ is the resulting signal at the beamformer's output at time t, polarization p, and steered in the (ξ_0,η_0) direction, and
- $S^{p}_{m}(t)$ is the signal collected by the m^{th} antenna at time t and p polarization.

The beam creation process is simultaneously performed with the phase and amplitude calibration, obtaining only one general complex weight for each receiver. From the synthetic aperture point of view, there are 7 non-redundant visibility samples aligned on the vertical axis, all the possible combinations of 4 elements. Once the signals are inside the FPGA, each signal is correlated at 8 bits with the other signals and the non-redundant visibility samples set are obtained. These results are then sent to a personal computer where the RSC algorithm [88] for amplitude and phase calibration is applied and then the image reconstruction takes place following Eqn. (9.3):

$$\widetilde{\mathrm{T}}^{pq}_{\mathrm{a}}(\xi,\eta) = \mathrm{IDFT}\{\overline{\mathrm{V}}^{pq}(\mathrm{u},\mathrm{v})\}, \tag{9.3}$$

where, according to Section 4.1:

- $\widetilde{\mathrm{T}}^{pq}_{\mathrm{a}}(\xi,\eta)$ is the modified brightness temperature,
- IDFT stands for the inverse discrete Fourier transform, and
- $\overline{\mathrm{V}}^{pq}(\mathrm{u},\mathrm{v})$ is the visibility vector.

First, the system was configured to work as a DBF and several zenith scans within the range [-π/2, π/2] were performed and different steered beams were acquired (Figure 9.13a). Then, a second measurement set was conducted, the system was configured to work as a synthetic aperture. The instrument was performing 7 point images (non-redundant visibilities samples set for 3 different baselines, Section

4.3). The instrument was pointed to specific zenith angles and then 7-point images were acquired. Results were calibrated and the image reconstructed using a triangular window (Figure 9.13b).

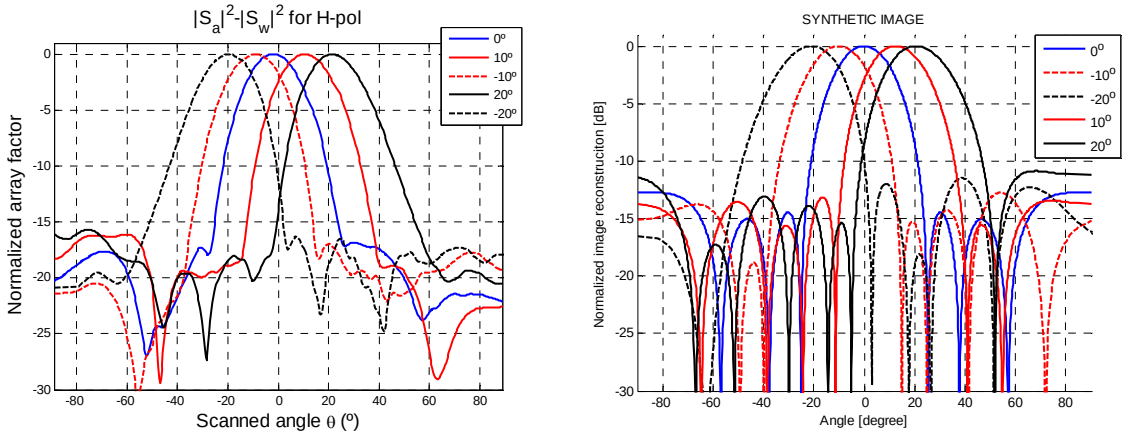

(a) (b)

Figure 9.13. Sample of PAU-RAD measurements at the UPC anechoic chamber. (a) PAU-RAD DBF measured results, normalized array factor for multiple measured beams in the H polarization scanning the zenith range, (b) reconstructed synthetic images for different point sources at different zenith angles.

From Eqns. (9.2) and (9.3) it is possible to infer that, by scanning the zenith angle in the DBF working mode the whole system array factor is obtained. On the other hand, when pointing to a specific angle and the image reconstruction is applied and using a triangular windowing for image reconstruction, the whole array factor is obtained again as the transmitter in the anechoic chamber acts as a point source. Therefore, both measurements have to agree to prove the relationship.

Figure 9.13a and Figure 9.13b show an excellent agreement at any pointing angle, all the DBF – synthetic aperture pairs have a beamwidth of 22º and an Side Lobes Level (SLL) below -15 dB. Note that in this case the residual phase noise masks the notches of the antenna pattern. Obviously, Figure 9.13b has a worse performance because it has been reconstructed using only 7 points (non-redundant visibilities samples set) and then optimally interpolated using zero-padding and a 256 points Fast Fourier Transform (FFT). Meanwhile, Figure 9.13a has 180 measured points (scanning angular resolution 1º).

9.5 Field Experiments

After testing the PAU-RAD in a controlled environment such as an anechoic chamber and measuring its performance, a field experiment was carried in a real environment. The main goal of this field campaign was to measure the impact of the GPS signal on the radiometric measurements and to measure the emissivity from different surfaces of various incidence angles using the DBF. These tests took

place on October 5th of 2010, in Palau d'Anglesola (Lleida, Catalonia), within an intensive agricultural environment. The coordinates of the experiment site were latitude 41º 39' 57" North, and longitude 0º 52' 43" East (Figure 9.14).

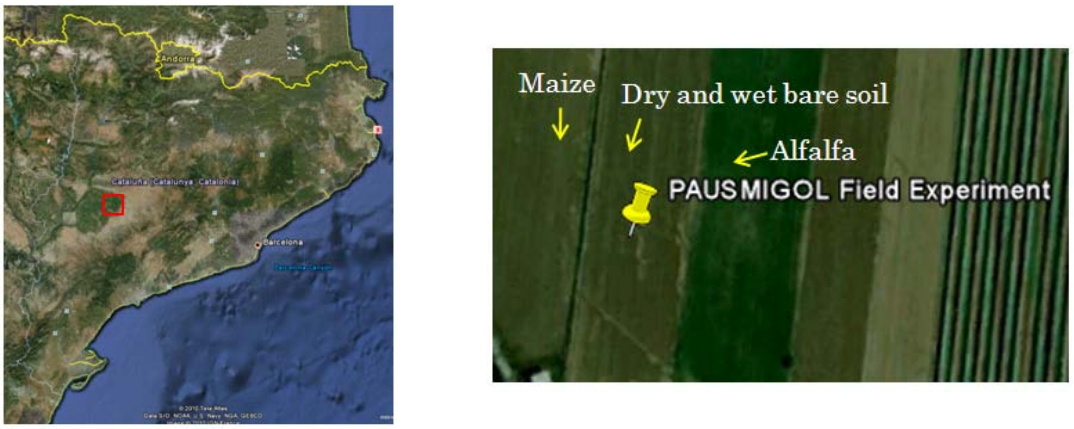

(a) (b)

Figure 9.14. Palau d'Anglesola experiment site. (a) The test site in Catalonia context (b) the three agricultural fields used in the experiment with maize, alfalfa and bare soil.

The instruments deployed (Figure 9.15) were the PAU-RAD, an infrared radiometer (IR) [130] and the Soil Moisture Interference-pattern GNNS Observations at L band (SMIGOL) reflectometer [56]. The three instruments were mounted to measure simultaneously the same nadir point (Figure 9.15b).

(a) (b)

Figure 9.15. Deployed instruments for the field campaign. (a) PAU-RAD being carried by a lifter on a tractor (b) the three deployed instruments ready to measure.

PAU-RAD is a heavy instrument (~ 80 kg), in order to operate it has to be carried by a mobile and mechanical lifter, to conduct measurements in different soils types and elevate the PAU-RAD up to 3 meters. It was found that the best lifter platform to operate in agriculture fields it was a tractor with a lifter (Figure 9.15a). PAU-RAD was attached to the platform using a mechanical interface. Furthermore, this platform is able to change the incidence angle of the instrument using two security screws.

To successfully develop the instrument in the field experiment, the campaign logistics and scheduling was planned in detail. It was determined that the experiment should be conducted focusing in two main points:

- Measurement of the GPS impact on the radiometric data, and
- Measurement of the emissivity curves from an incidence angle of 20º up to 60º, and for different types of surfaces.

The first point was required to assess the hypothesis that in some measurements configuration it is possible to perform radiometric measurements in the GPS-L1 band (Section 6.9), and determine the conditions when these measurements are not valid due to the presence of the GPS signals, or in this case, GPS interference. The second part of the experiment was focused on the radiometric performance itself. In order to have different contrast during the experiment, three different fields were used, one with a huge vegetation layer (maize), another with no vegetation (bare soil) and the last one with a thin layer of vegetation (alfalfa). Furthermore, to increase the variability of the measurements a water tank was provided to irrigate the bare soil and change the soil moisture (SM) value.

9.5.1 Impact of GPS on the Radiometer Measurements

As it has been said, the first part of this campaign was focused to measure the impact of the GPS signals, determining in which measurement configuration it is negligible, so that it is able to perform radiometric measurements in this band. For this purpose the SMIGOL instrument was set up pointing to the same direction as PAU-RAD. Here, the mission of the SMIGOL instrument was to have an instrument capable to measure GPS presence for further comparison with the PAU-RAD power (antenna temperature) fluctuations, to ensure that these fluctuations are coming from the GPS signal, and not from any other RFI source or are internally generated. SMIGOL is the instrument implementing the Interference Pattern Technique (IPT) ([55], [56], and [57]). It is mainly composed of one patch antenna pointing to the horizon and one GPS receiver connected to this antenna. The GPS receiver processes and sends to a PC some observables of the received signal. SMIGOL measures the interference pattern between the GPS direct and reflected signals (the interference power), after they impinge over the land surface, which can be bare soil or vegetation-covered soil (Figure 9.16a). The measured interference signal provides information on the soil moisture content of the surface and also, on the vegetation height, as it has been previously demonstrated in [56]. This interference pattern depends on the incidence angle of the reflected signal. Obviously, as the GPS satellites are moving the incidence angle is changing, so that as the time goes on an angular incidence swept is automatically performed (Figure 9.17).

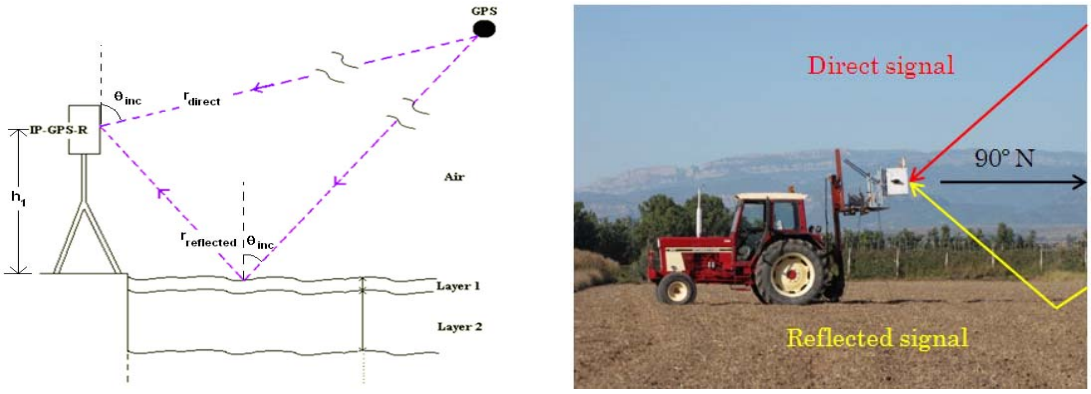

(a) (b)

Figure 9.16. Measuring GPS impact on the radiometric measurement depending on the measurement set up. (a) PAU-RAD pointing to the horizon and being interfered by the GPS direct and reflected signal [55], and (b) SMIGOL reflectometer measurement sketch.

The experiment consisted of pointing the PAU-RAD to the horizon to have equivalent measurements as in the SMIGOL instrument (Figure 9.16b). The main difference it is that the SMIGOL instrument correlates the interfered input signal with a clear local replica [115], but PAU-RAD computes the power of this interference minus the weighted average of the Wilkinson temperatures (Figure 9.1). Both instruments were pointing to the same direction (exactly the East), so they were essentially measuring the same interference signal.

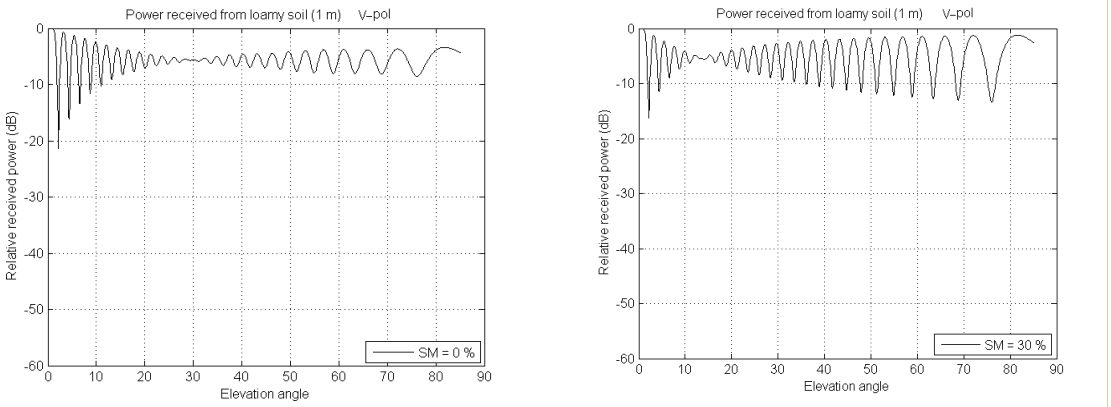

(a) (b)

Figure 9.17. Theoretical interference pattern curves obtained with the SMIGOL instrument [56]. (a) for a dry soil (SM = 0 %), and (b) for a wet soil (SM = 30 %).

Figure 9.18 shows the antenna temperature for 3 hours of acquisitions when pointing to the horizon in the East direction. The PAU-RAD system was in scanning mode, which it means that it measured from 70º up to 110º, and then started again, this is the reason of the pattern of the curves going up and down. Using the information provided by the SMIGOL instrument, it is possible to identify different regions on the Figure 9.18.

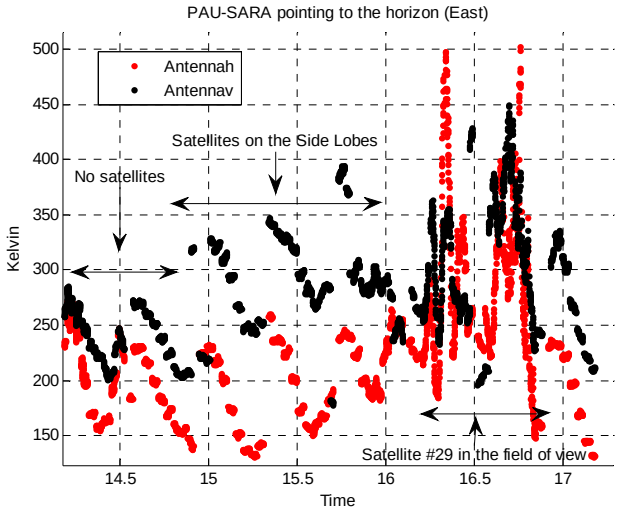

Figure 9.18. Antenna temperature of PAU-RAD when measuring pointing to the East horizon during 3 hours, from 14h to 17h.

The first region, corresponds to a period of time when there were not satellites in view on the East, then a satellite (PRN #29) started to appear in the side lobes of the beam. As the time went on, the satellite entered in the field of view (main beam) of the PAU-RAD and finally it got out from it passing by the side lobes. The impact when entering from the side lobes starts with ~ 50 K, and as it is approaching the main lobe this increases up to 100 K. When entering from the main beam it is around 200 K, which is actually higher than the value predicted in Section 6.9.

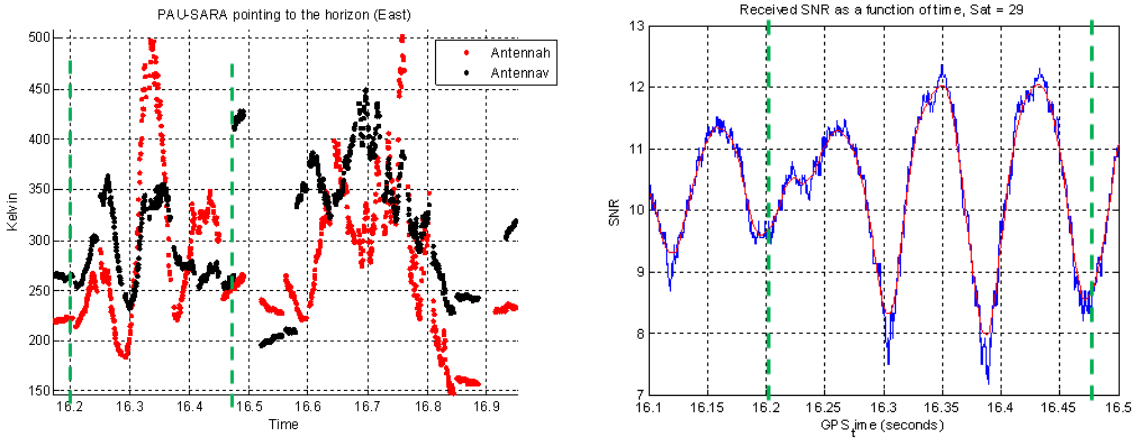

Figure 9.19. PAU-RAD and SMIGOL measurements direct comparison, (a) PAU-RAD antenna temperature, and (b) SMIGOL measured SNR.

The next point is to make sure that these fluctuations correspond to a GPS signal and they are not internally generated or come from another RFI source. To do that, PAU-RAD and SMIGOL measurements are directly compared to the region where the satellite #29 is inside the main beam of the PAU-RAD. Figure 9.19 shows this comparison, the exactly times are surrounded by two green dashed lines in both figures. Except for the shape that can infer the different directivities

(D_{SMIGOL} ~ 6 dB and $D_{PAU-RAD}$ ~ 20 dB) and beamwidth ($\Delta\theta_{SMIGOL}$ ~ 60º and $\Delta\theta_{PAURAD}$ ~ 23º) of each instrument, both measurements have exactly the same trend. Therefore it can be concluded that the origin of the radiometer output fluctuation is the GPS signal from satellite #29.

The conclusion of this section is that when the GPS signals are not entering neither from the main lobe not from the largest side lobes, the impact of the GPS signal on the radiometric signal can be neglected (first region in Figure 9.18). This can be easily achieved by measuring pointing to the North (lesser density of satellites) and pointing to 45º instead of pointing to the horizon. To make sure that the signal is not interfered by any GPS signal a GPS receiver can be mounted pointing to the same direction of the PAU-RAD, and flag these radiometric measurements in which the GPS receiver detects some satellite, despite the measurement set up.

9.5.2 Emissivity Measurements

The second part of the field experiment consisted of measuring the soil emissivity. Some calculus and estimations were performed first to properly conduct the experiment. First of all, for practical reasons it was decided to measure from 3 meters of height, with a 45º incidence angle (Figure 9.20).

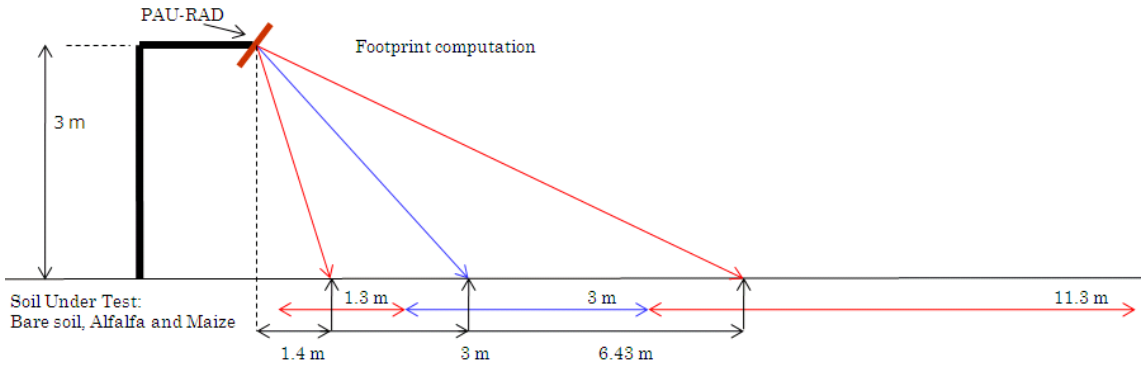

Figure 9.20. PAU-RAD structure and sketch for the radiometric measurement in the Palau d'Anglesola test site.

In these conditions the far field conditions are fulfilled and the central footprint (beam steered 0º or pointing with an incidence angle of 45º) of 3 meters centered at 3 meters from the nadir point. The footprints characteristics for the edge fore-looking beams are:

- θ_i = 25º (steering angle -20º) has footprint of 1.3 meters centered at 1.4 meters of the nadir point, and
- θ_i = 65º (steering angle +20º) has a footprint of 11.3 meters and it is centered at 6.4 meters from the nadir point.

Another important issue is that the structure that supports the PAU-RAD must not interfere in the radiometric measurements, so that the radiometer should be hold from a certain distance from the main structure as shown in Figure 9.20.

Not only the footprints have to be taken into account, a security margin to ensure the homogeneity of the measured soil has to be considered (Figure 9.21). Usually this security margin includes another footprint around the central one being measured.

Figure 9.21. PAU-RAD footprints: (a) theoretical sketch (not to scale), and (b) real footprints projected in the bare soil field.

These requirements are fulfilled and sketched in Figure 9.21a, where the footprints and the security margin are being considered. The total dimensions of the soil under test are a square of 5.5 per 17.6 m. Figure 9.21b and Figure 9.22a show the real area where the radiometric measurements for bare soil were acquired. In order to be able to compare the measured emissivity curve with the theoretical ones, ground truth measurements had to be acquired. Several instruments were used, such as a network of Decagon soil moisture probes (5 ECH2O probes) [131] buried with an inclination of 45º at 5 cm (Figure 9.22b). Figure 9.22c shows the measurement of one of these probes in dry bare soil, a multimeter and batteries were required for this measurement.

After preparing the PAU-RAD antenna and radiometer, and deploying the ground truth instruments, the campaign to measure the emissivity was ready to start. Figure 9.22a shows the measurement of the area under test. Meanwhile, the radiometric hot-load calibration was performed using a microwave absorber as a black body and a thermometer to measure its temperature. After the hot-load calibration ($T_{absorver}$ = 291 K), the cold-load was performed pointing to the North trying to minimize the effect of the GPS signals. However, lots of samples set were contaminated by the GPS signals, after several acquisitions it was possible to measure the cold-load using the sky ($T_{sky\ at\ L\text{-}band}$ = 6 K). As shown in Figure 9.22a, the measurements started with the bare soil. First, a measurement was carried out with the dry soil (SM = 22.4 %). Due to seasonal raining the soil it was wetter that it was expected when preparing the campaign.

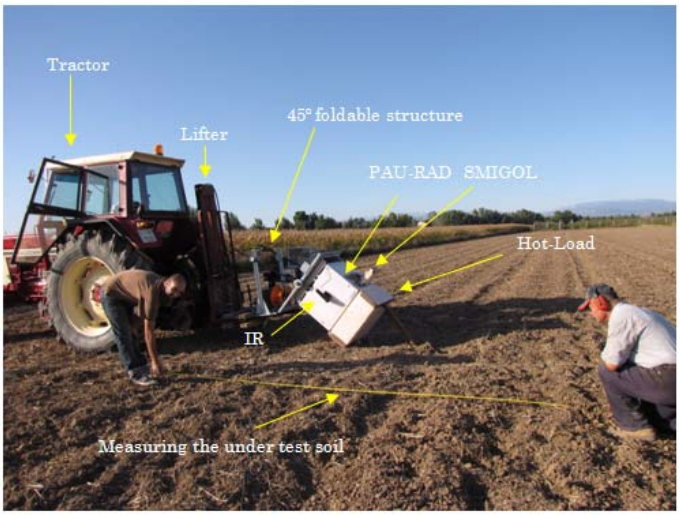

(a)

(b)

(c)

Figure 9.22 Measuring the emissivity of the bare soil. (a) measuring and determining the soil under test, simultaneously the hot-load calibration was performed, (b) deploying the Decagon ECH20 SM [131] probes to get the ground truth, and (c) testing the SM probes.

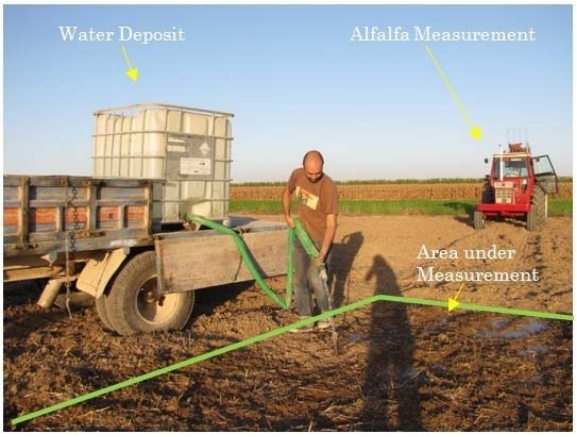

(a)

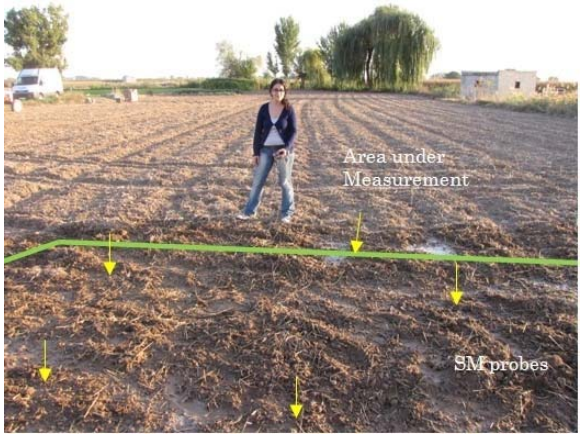

(b)

Figure 9.23 Irrigating and measuring the soil under measurement for further radiometric measurements: (a) irrigating it using a water deposit, and (b) measuring the ground truth using the deployed network of SM probes.

After the measurement of the dry soil, the same soil was irrigated using a water deposit specially prepared for this purpose (Figure 9.23a), and then, a second measurement took place. After that, the ground truth soil moisture was measured again (SM=30 %) using the SM network deployed previously (Figure 9.23b).

The first step is to convert the measured *apus* into emissivity was to ensure that the data sets do not have reflected GPS signals entering from the main lobe. Then, the apus were converted into antenna brightness temperature using the T_{hot}-T_{cold} radiometric calibration, and from here to the emissivity using the temperature of the soil, recorded using the IR, and cross-checked with an in-situ thermometer. The measured emissivity curves for the polarizations *v* and *h*, for the range of the incidence angles from 25º up to 65º (obtained with the DBF scan without mechanical movement) in the dry and wet soils are presented in Figure 9.22.

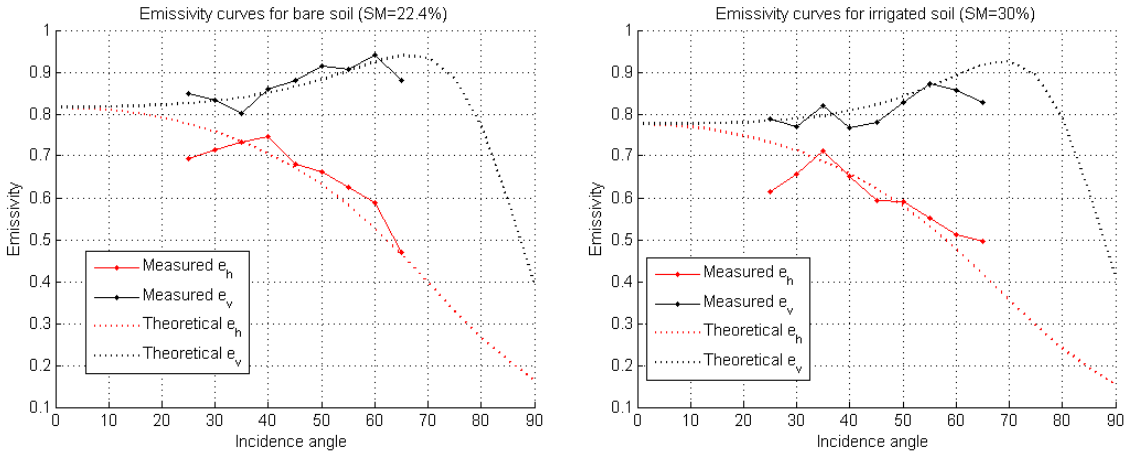

Figure 9.24 Comparison between the measured and theoretical emissivities. (a) for a bare soil with a SM = 22.4 % and (b) for an irrigated bare soil with SM = 30 %.

Figure 9.24a shows the mean, after averaging 2 minutes of row radiometric data, of the measured emissivity for the dry soil (SM = 22.4 %). In this case there the standard deviation of the measurements is not displayed because after the 2 minute samples averaging is really low and does not add significant information to the plot. The trends of both polarizations follow the theoretical curves (obtained by simulating a rough soil with the identical composition, moisture and physical temperature conditions than the measured one. It is plotted with dotted lines). Although the two polarizations, *h*- and *v*-pol., show a good agreement with the theoretical curves, they have fluctuations over the mean theoretical value. The higher incidence angle emissivity underestimation for the *v*-pol. with respect the theoretical values can be due to the fact that for these synthesized beams there is a side lobe pointing to the sky. On the contrary, the lower incidence angle underestimation for the *h*-pol. can be related with a back lobe pointing to the sky as well. Figure 9.24b shows the measured emissivity for wet soil (SM = 30 %). Again, the trends for both polarizations follow the theoretical curves (obtained by simulating for the measurement conditions plotted with dotted lines assuming a roughness surface).

After the bare soil measurements, the PAU-RAD was set to measure the soil covered with two different vegetation canopies. The first one was an alfalfa field (Figure 9.25a), with SM = 25 %, the height of the alfalfa was 15 cm ($h_{alfalfa}$ = 15 cm) and the physical temperature was T_{soil} = 287.1 K.

(a)

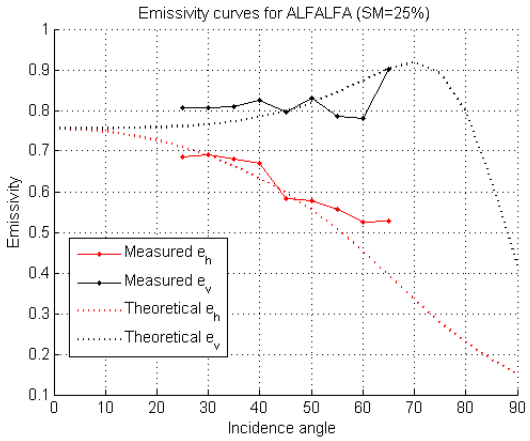

(b)

Figure 9.25 Alfalfa field measurement: (a) measuring the alfalfa field with the PAU-RAD, IR, and SMIGOL instrument, and (b) measured and theoretical emissivity comparison.

The second one was a dry-maize field (Figure 9.26a), with the SM = 28 %, the height of the maize was 2.85 m (h_{maize} = 2.85 m) and the temperature was T_{soil} = 285.3 K.

(a)

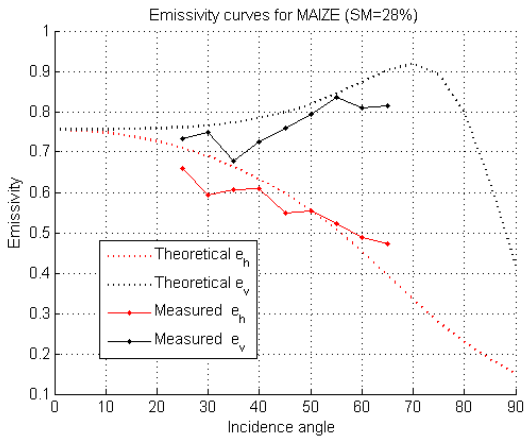

(b)

Figure 9.26 Maize field measurement, (a) measuring the alfalfa field with the PAU-RAD, IR, and SMIGOL instrument, and (b) measured and theoretical emissivity comparison.

Both measurements, over alfalfa and maize, show a good agreement with the theoretical curves simulated using realistic conditions. It can be observed that the soils with vegetation canopy are quite similar to the bare soil emissivity measurements. This is due to the low value of the Vegetation Water Content (VWC) of the maize at this time of the year (VWC_{maize} = 0.9 kg/m^2), one week before to be harvested, and the alfalfa layer was very short ($h_{alfalfa}$ = 15 cm).

Probably, the *v*-pol. disagreement is due to the fact that the figures are comparing soil brightness temperature with antenna temperature, and it seems that *v*-pol. has an important side lobe pointing to the sky when steering large incidence angles. Thus, the T_{sky} interference is the responsible of having an antenna temperature lower than the expected.

9.6 Conclusions

This chapter has been devoted to measure the entire PAU-RAD performance from different aspects which have been separated in three different steps:

- Analysis of the DBF performance for each synthesizable beam. The evaluation criteria for this analysis are the suitability of these beams for radiometric applications. For this purpose, the PAU-RAD instrument was mounted in the UPC anechoic chamber and its beams were accurately measured. Tests and their results are summarized here:

  - The first test was to measure the performance of the thermal control, which has shown differences about 6º C inside the PAU-RAD. Therefore, differences between the mean temperatures of the RUTs are 2.1º C and the standard deviation is always lower than 0.1º C. However, these were the statistics for the anechoic chamber measuring conditions, and larger standard deviations are expected when measuring outdoors with larger thermal variations,

  - receivers have different paths for the signals coming from the CNS and from the antenna. This difference and the phase center error have been empirically measured and further compensated on the equalization algorithms. After this correction, the beam has been steered to 0º and the cross-correlation has been measured for a period of 100 minutes. The main conclusion of that experiment is that, with the previously thermal control described, the phase and amplitude of the receivers remains constant for at least 100 minutes. Furthermore, modulus and phase histograms of these experiments have been presented. The most remarkable fact is that the phase is showing a clear Gaussian distribution with a mean value of -3.39º and a standard deviation of 0.85º. Although the standard deviation is well below of the calibration requirement, there is a phase offset (-3.39º) that can only be attributed to a residual error of the CNS-antenna path or to the phase center calibration. Moreover, the MBE and the beamwidth have been measured for all the steerable *h*-pol., *v*-pol. and *hv* beams,

  - results have shown that, for all the possible steering angles the MBE is better than 91% and the best result is for 0º where the MBE reaches a value of 95.6% for *hv*, 94.8 % for *h* and 93.4 % for the *v*-polarization. On the other

hand, the worse results are achieved, as expected, for the largest steering angles (±20º). Recall that the design specification was to have a MBE higher than 94%, which has been achieved for the 0º steering beam and it is almost fulfilled for all steerable beams,

- regarding the beamwidth, the best performance is again for the 0º steering angle when the $\Delta\theta_{-3dB}$ = 22.8º for the *h*-pol., $\Delta\theta_{-3dB}$ = 22.4º for *v*-pol. and $\Delta\theta_{-3dB}$ = 23.33º for *hv*. Again, the worst results are for the largest steering angles, then the beamwidth values reach the maximum of $\Delta\theta_{-3dB}$ = 25.5º. So that, the beamwidth requirements has been fulfilled in almost all the cases. In addition, Table 1 shows that the *hv* beams have the best performance in terms of MBE, but the largest beamwidths. Which is due to the way this beam is created from the cross-correlation of the *h*-pol. and v-pol. beams, and

- finally, the radiometric resolution has been found to be 3 K for the most of the beams, except for some high incidence angles in the *v*-pol. having a radiometric resolution around 5 K,

- the system has also been operated as a synthetic aperture radiometer to assess the Chapter 4 assessment, that a radiometer with DBF can be described in the synthetic aperture radiometry framework. Results from both working modes have been presented showing an excellent agreement at any pointing angle, all the DBF – synthetic aperture pairs have a beamwidth of 22º and an SLL below -15 dB. Obviously, as a synthetic aperture radiometer it has a poorer radiometric performance (noisier) because it has been reconstructed using only 7 points (non-redundant visibilities samples set), and then optimally interpolated using zero-padding and a 256 points FFT. Meanwhile, the real aperture has 180 measured points (scanning angular resolution 1º).

- Finally, a field campaign was conducted with two main goals: to measure the impact of the GPS signal on the radiometric measurement, and to measure the emissivity from different soil surfaces at different incidence angles using the DBF radiometer. These tests took place the October 5th of 2010 in Palau d'Anglesola (Lleida, Catalonia). Tests and their results are summarized here:

  - first of all, the PAU-RAD was deployed to measure the impact of the GPS signal on the radiometric data. The conclusion is that the GPS impact over the radiometric data depends on from where it is entering in the pattern array. When the GPS signals are not entering from the main lobe neither from the highest side lobes, the impact of the GPS signal on the radiometric signal can be neglected. This can be easily achieved by measuring pointing to the North (less present satellites) and pointing to an incidence angle of 45º instead of pointing to the horizon. On the other hand, when the GPS signal is entering from the main lobe the interference level can be about 200 – 300 K. When it is entering from high values of the side lobes, the interference is lower but is still important for soil moisture applications (30 – 50 K), and

- antenna temperatures from different surfaces were measured. The test started measuring bare dry soil (SM = 22.4 %) and wet soil (SM = 30 %). The trends of the measured emissivities from both polarizations follow the theoretical curves. Although *h*-pol. shows a better agreement with the theoretical curves, *v*-pol. has a negative offset that gives an underestimation with respect the expected values for the whole curve. Two more types of soils, with alfalfa and maize, were measured as well, with similar results and conclusions.

PAU-RAD performance has been measured and tested, and it has been raised out that it is possible to perform radiometric measurements at the GPS-L1 band taking into account the geometrical disposition of the satellites and the beam of the antenna.

Chapter 10

10 CONCLUSIONS AND FUTURE RESEARCH LINES

In this chapter the main conclusions of this PhD dissertation are reached. After discussing them, the future research lines are envisaged.

10.1 Conclusions

The present PhD. dissertation is a contribution to the development of a new generation of passive sensors that combine microwave radiometers and reflectometers using GNSS signals of opportunity and perform, for the first time – to author's knowledge – real time digital beamforming synthesis and polarization synthesis. This report started emphasizing the importance of the polarimetric and multi-angular L-band radiometric measurements in the oceanographic and climatologic studies.

This work consists of a theoretical study performed on digital correlation radiometers with beamforming from the point of view of the synthetic aperture radiometers and an extended analysis of the impact of the digitization scheme. Moreover, the requirements to build a correlation radiometer with real-time digital beamforming and polarization synthesis have been stated. This instrument has been built, internally equalized for the amplitude and phase of each receiver, tested and characterized in the UPC anechoic chamber, and in a field campaign obtaining soil emissivity values for a range of incidence angles.

The first contribution of this work has been the discovery, formulation and analysis of the relationship between synthetic aperture and real aperture radiometers. Actually, a real aperture radiometer can be analyzed as a highly redundant synthetic aperture one. This property has been demonstrated theoretically (Chapter 4) and experimentally (Chapter 9). These results have allowed extrapolating some advanced analysis developed for synthetic aperture radiometers to beamforming radiometers. Furthermore, a performance analysis of the radiometric resolution and the scanning angular resolution has been performed. For imaging radiometers, it has been found that the use of orthonormal vectors such as those implicitly generated by an IFFT, provide uncorrelated measurements in the space. However, it is also possible to increase the sampling resolution using non-orthogonal vectors, but then the correlation between adjacent beams rapidly increases as the square root of the array pattern. Furthermore, a new implementation of a digital beamforming using the concept of visibility samples from synthetic aperture radiometers has been envisaged and an implemented in a hardware to validate this relationship with real measurements (Chapter 9) [132]. This concept has been extrapolated to other receivers used for remote sensing such as SARs and GNSS- Reflectometers.

The second contribution of this work has been the general and comprehensive study of the impact of a general digitization scheme in the cross-correlation of two signals (Chapter 5) ([133]-[134]). First of all the quantization has been expressed and analyzed as a non-linear transformation. Despite the quantization scheme can significantly distort the value of the ideal cross-correlation (ρ_{xy}), if the signals' statistics are *a priori* known, it is possible to recover this ideal correlation (ρ_{xy}) from the measured one (R_{xy}) using an inverse function $\rho_{xy} = q^{-1}[R_{xy}]$, that can

always be numerically computed. It has been found that for each quantization scheme there is an optimum value of the ratio of the analog-to-digital converter (V_{ADC}) digitations window to the standard deviation of the input signals ($\sigma_{x,y}$) ($V_{ADC}/\sigma_{x,y}$) for which the linearity with respect the ideal correlation is minimized. Furthermore, quantization distorts and spreads the spectrum of the cross-correlation, decreasing the resolution. Sampling also affects the cross-spectrum function, and depending on the sampling rate, replicas of the cross-spectrum can overlap the main one. This can be due to a sampling rate below the Nyquist rate or, even above the nominal Nyquist rate, due to the non-linear quantization process which spreads the spectrum. In both cases, there is an impact on the SNR, and therefore on the radiometric resolution. Other sampling effects have been analyzed, such as the clock inaccuracies (skew and jitter) and, the impact of both effects, quantization and sampling, on the variance of the measurements, which has been found to be strongly dependent on the relationship between the bandwidth of the cross-spectrum and the sampling rate. As the sampling rate increases, consecutive samples are more correlated, so less new information is added to the measured cross-correlation and the variance decreases slowly.

After these two theoretical Chapters the PAU-RAD instrument has been defined and the design constraints have been stated as the previous step to build the system (Chapter 6). This process started with a general overview of the instrument defining its basic requirements. PAU-RAD antenna is a 4x4 rectangular antenna array with an antenna spacing of 0.63 λ (d = 0.63 λ) and triangular illumination in both directions to achieve a MBE ≥ 0.94 at boresight. It is capable to steer the beam up to ±20º from the array boresight in 5º steps. Each antenna of the antenna array is combined by rows using analog techniques. Each combiner has its own dual-polarization receiver (actually, 4 receiving chains, 2 per polarization) that down-converts the RF signal to an IF signal. Once the signals are at IF, they are digitalized and sent to a FPGA. In the FPGA signals are amplitude and phase equalized and then processed in order to calculate the four Stokes parameters. The main analyzed points of this chapter are discussed below:

- PAU-RAD differs from other radiometers in the fact that has been conceived to share the front-end with a GPS reflectometer. In order to understand the basic interactions of the system, a full noise wave analysis for one receiver has been performed. Theoretical Stokes parameters have been obtained from a DBF point of view (proportional to $T_A - T_w$), and the radiometric sensibility has been computed for the first and the second Stokes's parameters $\Delta T = \frac{1}{2}(T_A + T_R + 2T_{REC})/\sqrt{B\tau}$ and for the third and fourth parameter $\Delta T = \sqrt{(T_{Av} + T_R + 2T_{REC})(T_{Ah} + T_R + 2T_{REC})}/\sqrt{B\tau}$,

- the impact of the receiver frequency response over the Stokes parameters has been analyzed using the well-know concept of the fringe-washing function. In the error budget, the most restricting residual equalizing error is the residual phase error, which rapidly degrades the MBE. To fulfill the radiometric

requirements (MBE ≥ 0.94) a residual standard deviation error of ≤ 2º for the phase and ≤ 0.1 dB for the amplitude must be achieved,

- the trigonometric signal that has to equalize these errors has to be quantized with 18 bits to overcome the problem of the phase-amplitude dependence (AM-PM conversion). It has been found that the phase resolution only depends on the number of bits, but not on the maximum range of amplitude to equalize, and

- the GPS-L1 signal impact on the radiometric measurement can be separated in two different situations:

  - the worst situation occurs when the specular reflection point is at the antenna's boresight. In this case the antenna temperature increase due to the GPS interference is T_{GPS} ~ 65 K, and

  - the best situation occurs when the reflection point comes ~ 90º out of boresight the radiometric measurement contribution is then T_{GPS} ~ 0.35 K. This scenario allows performing radiometric measurements with enough radiometric resolution, for example for soil moisture observations.

After stating the design requirements, the PAU-RAD instrument has been built (Chapter 7). Mainly, the conceptual sketch consists of an analog part that collects the input signals thought the antennas, and then it performs the RF-IF down-conversion from 1.57542 GHz to 4.039 MHz. Once the signals are at IF, they are digitized using 8 bits and sent to an FPGA. Inside the FPGA, each channel is down-converted to baseband using its own Numerical Controlled Oscillator (NCO), which also equalizes in phase and amplitude. Then, the DBF is performed and finally, signals are properly correlated in order to obtain the Stokes parameters. The detailed report has been conducted through the analog and the digital parts of the PAU-RAD focusing on:

- a 4x4 antenna array with a beamwidth of 25º designed for having an MBE higher than 0.94 and capable to steer the beam in the vertical direction,

- the RF part with the control switches to allow phase and amplitude equalization among all the receiving channels, the Wilkinson power splitters, and the LNA,

- the IF part, which consists of the Zarlink GP2015 chip with the AGC disabled, and attenuation in the a rejected band of -40 dB, and a bandwidth of 2.2 MHz,

- the 8 bit time-multiplexed ADCs and its frequency plan that centers the digitized signal at 0.25 times the sampling frequency to perform band-pass sampling and easy the demodulation process, and

- the VHDL ALU design with the Multiplexed Digital Down-Converter (MDDC), which using its NCO down-converts the signals to base-band, equalizes the

channels and steers the beams in the desired direction, the beamformer adder, the LPF and the cross-correlation block.

Once the system has been successfully built, the equalization algorithms, and the PAU-RAD performance has been analyzed in Chapter 8. This analysis has been performed by focusing on the hardware, and on the algorithm to estimate the phase coefficients. The equalization procedure can be described in two steps: error estimation and error equalization. The error estimation step estimates the phase and amplitude differences of signals. To calculate these differences, the switch of each RF chain has to be connected to the Controlled Noise Source (CNS) input signal. Then, signals are cross-correlated and from these complex values, the phase and amplitude equalization coefficients are determined for each channel. The error equalization step is to correct this phase and amplitude differences in order to equalize the signals, by changing the phase and amplitude of each NCO according to the estimated values in the previous step. Due to the nature of the complex correlator's output signal, which is the subtraction of the CNS and the Noise Distribution Network (NDN) temperatures, to estimate the phase and amplitude error the T_{CNS} has to ensure that it is always higher than T_{NDN}. This is important to avoid any uncertainly related with the different behaviour of the complex correlation output depending on the T_{NDN}. Furthermore, the equations of the differential algorithm for phase and amplitude estimation have been provided, and analyzed. After estimating these parameters from the row complex-cross correlation, their measurement standard deviation is reduced by using a Kalman filter, which is tuned using the σ_ε^2 parameter, it is able to reduce the standard deviation of the measurements, and to tracks the thermal drifts of the coefficients [40].

Finally, the entire PAU-RAD instrument calibration performance has been performed, the mean of the amplitude coefficient is 1 and its residual error (standard deviation) is within the interval 0.01 and 0.05. On the other hand, the mean of the phase coefficient is ~ 0º, with the worst value of -1.37º. The residual standard deviation error is ~ 2º, and the higher standard deviation is 2.5º.

After this analysis, it can be concluded that after the equalization algorithm, PAU-RAD fulfills the equalization requirements stated in Chapter 6. Hence it is suitable for performing a DBF to fulfill the radiometric requirements. Finally, in Chapter 9 the whole system performance has been measured from different aspects which have been separated in three different steps:

- Analysis of the DBF performance for each synthesizable beam. The evaluation criterion for this analysis is the suitability of these beams for radiometric applications. For this purpose, the PAU-RAD instrument was mounted in the UPC anechoic chamber, and its beams were accurately measured. The main results are reported below [80]:

  - The first test was to measure the performance of the thermal control. The second part of this test consists on measuring the difference of the receiver's

paths for the signals coming from the CNS and from the antenna, this difference and the phase center error have been empirically measured and further compensated on the calibration algorithms,

- after this correction, the beam has been steered to 0º and the cross-correlation has been measured for a period of 100 minutes. The main conclusion of that experiment is that, with the actual thermal control, the phase and amplitude of the receivers remains constant for at least 100 minutes. Furthermore, modulus and phase histograms of these experiments have been presented. The most remarkable fact is that the phase is showing a clear Gaussian distribution with a mean value of -3.39º and a standard deviation of 0.85º. Although the standard deviation is well below of the calibration requirement, there is a phase offset (-3.39º) that can only be attributed to a residual error of the CNS-antenna path or to the antenna path phase calibration,

- the MBE and the beamwidth have been measured for all the steerable *h*-pol., *v*-pol., and *hv* beams. Results have shown that, for all the possible steering angles the MBE is always better than 0.91 and the best result is for 0º where the MBE reaches a value of 0.956 for *hv*, 0.948 for *h* and 0.934 for the *v* polarization. On the other hand, the worse results are achieved, as expected, when the angle of steering is high (±20º). Recall that the design specification was to have a MBE higher than 0.94 which has been achieved for the 0º steering beams and it is almost fulfilled for all steerable beams. Regarding the beamwidth, the best performance is again for the 0º steering angle when the $\Delta\theta_{\text{-3dB}} = 22.8^{\circ}$ for the *h*-pol., $\Delta\theta_{\text{-3dB}} = 22.4^{\circ}$ for *v*-pol. and $\Delta\theta_{\text{-3dB}} = 23.33^{\circ}$ for *hv*. Again, the worst results are for the largest steering angles, then the beamwidth values reaches the maximum of $\Delta\theta_{\text{-3dB}} = 25.5^{\circ}$. So that, the beamwidth requirements has been fulfilled in almost all the cases, and

- Table 9.1 shows that the *hv* beams have the best performance in terms of MBE, but the largest beamwidth. This is due to the way this beam is created from the cross-correlation of the *h* and *v* beams. Finally, the radiometric resolution has been found to be 3 K for most of the beams, except for some high incidence angles in the *v*-pol. having a radiometric resolution around 5 K.

- The system has also been operated as a synthetic aperture radiometer to assess the theory shown in Chapter 4, that a radiometer with DBF can be completely described in the synthetic aperture radiometry framework. Results from both operation modes have been presented showing an excellent agreement at any pointing angle, all the DBF – synthetic aperture pairs have a beamwidth of 22º and an SLL below -15 dB. Obviously, as a synthetic aperture radiometer it has a poorer performance because it has been reconstructed using only 7 points (non-redundant visibilities samples set), and then optimally interpolated using

zero-padding and a 256 points FFT. Meanwhile, the real aperture has 180 measured points (scanning angular resolution 1º) [132], and

- a field campaign was conducted with two main goals: to measure the impact of the GPS signal on the radiometric measurement, and to measure the emissivity from different soil surfaces from different incidence angles using the DBF radiometer. These tests took place the October 5th of 2010 in Palau d'Anglesola (Lleida, Catalonia). Main results are reported here:

  - first of all, the PAU-RAD was deployed to measure the impact of the GPS signal on the radiometric data and to measure the emissivity over different surfaces. The conclusion is that the GPS impact over the radiometric data depends on the direction from where it is entering in the pattern array. When the GPS signals are not entering from the main lobe neither from the highest side lobes, the impact of the GPS signal on the radiometric signal can be neglected. This can be easily achieved by measuring pointing to the North (less presence of satellites) and pointing to an incidence angle of 45º instead of pointing to the horizon. On the other hand, when the GPS signal is entering in the main lobe the interference level is about 200 – 300 K. When it is entering from the highest side lobes, the interference is lower, but is still important for soil moisture applications (30 – 50 K), and

  - antenna temperatures from different surfaces were measured. The test started measuring dry bare soil (SM = 22.4 %) and wet bare soil (SM = 30 %). The trends of the measured emissivity from both polarizations follow well the theoretical curves. Although the *h*-pol. shows a better agreement with the theoretical curves, the *v*-pol. has a negative offset that gives an underestimation with respect the expected values for the whole curves. Two more types of soils, with alfalfa and maize, were measured with similar results and conclusions.

The main conclusion of this performance and test analysis chapter is that the PAU-RAD has been successfully tested. It has been raised out that it is possible to perform radiometric measurements at the GPS-L1 band taking into account the geometrical disposition of the satellites and the beam of the antenna.

10.2 Future Research Lines

The future research lines opened by the work presented on this PhD dissertation are:

- develop a real-time radio frequency detector and canceller able to cancel the PRN codes transmitted by the GPS-L1 and allow any configuration and time radiometric measurement,

- increase the number of receivers to be able to steer the beam in both directions, horizontally and vertically,
- enlarge the FPGA hardware in order to be able to create more beams simultaneously,
- retrieve soil moisture from the multi-angular an polarimetric measured emissivities and analyze the performance of having a DBF,
- perform multi-angular and polarimetric measurements and studies over the soil, the soil with vegetation canopies and the sea, an
- study other array topologies with non-redundant baselines.

LIST OF PUBLICATIONS

In this section the publications that the PhD candidate has co-authorized during his PhD thesis are listed. Publications are sorted following the author criteria, and they are grouped in four groups: journal papers, conference papers, supervised master thesis, and patents.

JOURNAL PAPERS

- **X. Bosch-Lluis**, N. Rodriguez-Alvarez, A. Camps, I. Ramos-Perez, E. Valencia, H. Park, "Soil Moisture Retrieval with a GPS-L1 Digital Beamforming Radiometer," *Radio Science,* (**Submitted**).

- **X. Bosch-Lluis**, I. Ramos-Perez, A. Camps, N. Rodriguez-Alvarez, E. Valencia, H. Park, "A General Analysis of the Digitization Impact in Microwave Correlation Radiometers," *Sensors Journal,* (**Submitted**).

- **X. Bosch-Lluis**, I. Ramos-Perez, A. Camps, N. Rodriguez-Alvarez, E. Valencia, J.F. Marchan-Hernandez, "Common Mathematical Framework for Real and Synthetic Aperture Radiometers," *IEEE Transactions on Geoscience and Remote Sensing*, **(Submitted).**

- **X. Bosch-Lluis**, I. Ramos-Perez, A. Camps, N. Rodriguez-Alvarez, E. Valencia, J.F. Marchan-Hernandez, "Description and Performance of an L-Band Radiometer with Digital Beamforming," *Remote Sensing,* Vol. 3, pp. 14-40, 2011.

- **X. Bosch-Lluis**, A. Camps, I. Ramos-Perez, J.F. Marchan-Hernandez, N. Rodriguez-Alvarez, E. Valencia, "PAU/RAD: Design and Preliminary Calibration Results of a New L-Band Pseudo-Correlation Radiometer Concept," *Special issue Remote Sensing of Natural Resources and the Environment, Sensors Journal,* Vol. 8, n.7, pp. 4392 – 4412, 2008.

- A. Camps, **X. Bosch-Lluis**, I. Ramos-Perez, J.F. Marchan-Hernandez, N. Rodriguez-Alvarez, E. Valencia, J.M Tarongí, A. Aguasca and R. Acevo "New Passive Instruments Developed for Ocean Monitoring at the Remote Sensing Lab-Universitat Politècnica de Catalunya," *Sensors Journal*, Vol. 9, pp. 10171-10189, 2009.

- N. Rodriguez-Alvarez, **X. Bosch-Lluis**, A. Camps, M. Vall-llossera, E. Valnecia, J.F. Marchan-Hernandez, I. Ramos-Perez, "Soil Moisture Retrieval Using GNSS-R Techniques: Experimental Results Over a Bare Soil Field,"

IEEE Transactions on Geoscience and Remote Sensing, Vol. 47, pp. 3616-3624, 2009.

- I. Ramos-Perez, **X. Bosch-Lluis**, A. Camps, N. Rodriguez-Alvarez, J.F. Marchan-Hernandez, E. Valencia, C. Vernich, S. de la Rosa, S. Pantoja, "Calibration of Correlation Radiometers Using Pseudo-Random Noise Signals," *Sensors Journal*, Vol. 9, pp. 6131-6149, 2009.

- A. Camps, **X. Bosch-Lluis**, I. Ramos-Perez, J. F. Marchan-Hernandez, B. Izquierdo and N. Rodriguez, "New Instrument Concepts for Ocean Sensing: Analysis of the PAU-Radiometer," *IEEE Transactions on Geoscience and Remote Sensing*, Vol. 45, n. 10, pp. 3180 – 3192, 2007.

- R. Acevo-Herrera, A. Aguasca, **X. Bosch-Lluis**, A. Camps, J. Martinez-Fernandez, N. Sanchez-Martin, C. Perez-Gutierrez, "Design and First Results of an UAV-Borne L-Band Radiometer for Multiple Monitoring Purposes," *Sensors Journal*, Vol. 2, pp. 1662-1679, 2010.

- N. Rodriguez-Alvarez, A. Camps, M. Vall-llossera, **X. Bosch-Lluis**, A. Monerris, I. Ramos-Perez, E. Valencia, J. F. Marchan-Hernandez, J. Martinez-Fernandez, G. Baroncini-Turricchia, C. Perez-Gutierrez, and N. Sanchez, "Land Geophysical Parameters Retrieval Using the Interference Pattern GNSS-R Technique," *IEEE Transactions on Geoscience and Remote Sensing*, Vol. 49, n.1, pp. 71-84, 2011.

- E. Valencia, A. Camps, J.F. Marchan-Hernandez, **X. Bosch-Lluis**, N. Rodriguez-Alvarez, I. Ramos-Perez, "Advanced architectures for real-time Delay-Doppler Map GNSS-reflectomerters: The GPS reflectometer instrument for PAU griPAU)," *Advances In Space Research*, Vol. 46, pp. 196-207, 2010.

- J.F. Marchan-Hernandez, A. Camps, N. Rodriguez-Alvarez, **X. Bosch-Lluis**, I. Ramos-Perez and E. Valencia, "PAU/GNSS-R: Implementation, Performance and First Results of a Real-Time Delay-Doppler Map Reflectometer Using Global Navigation Satellite System Signals," *Special issue Remote Sensing of Natural Resources and the Environment, Sensors Journal*, pp. 3005-3019, 2008.

- J.F. Marchan-Hernandez, A. Camps, N. Rodriguez-Alvarez, E. Valencia, **X. Bosch-Lluis**, I. Ramos-Perez, "An Efficient Algorithm to the Simulation of Delay–Doppler Maps of Reflected Global Navigation Satellite System Signals," *IEEE Transactions on Geoscience and Remote Sensing*, Vol. 47, pp. 2733-2740, 2009.

- J.F. Marchan-Hernandez, N. Rodriguez-Alvarez, , A. Camps, , **X. Bosch-Lluis**, I. Ramos-Perez, E. Valencia, "Correction of the Sea State Impact in the L-Band Brightness Temperature by Means of Delay-Doppler Maps of Global Navigation Satellite Signals Reflected Over the Sea Surface," *IEEE*

Transactions on Geoscience and Remote Sensing, Vol. 46, n.10, pp. 2914 – 2923, 2008.

- E. Valencia, A. Camps, J.F. Marchan-Hernandez, N. Rodriguez-Alvarez, I. Ramos-Perez, **X. Bosch-Lluis**, "Experimental Determination of the Sea Correlation Time Using GNSS-R Coherent Data," *IEEE Geoscience and Remote Sensing Letters*, Vol. 7, pp. 675-679, 2010.

CONFERENCE PAPERS

- **X. Bosch-Lluis**, H. Park, A. Camps, S.C. Reising, S. Sahoo, S. Padmanabhan, N. Rodriguez-Alvarez, I. Ramos-Perez, E. Valencia, "A radiometer concept to retrieve 3-D radiometric emission from atmospheric temperature and water vapor density," (Abstract submitted for IGARS11).

- A. Camps, **X. Bosch-Lluis**, H. Park, "Impact of receiver's frequency response in GNSS reflectometers," *IEEE International Geoscience and Remote Sensing Symposium*, pp.3817-3820, Honolulu, USA, 2010.

- I. Ramos-Perez, **X. Bosch-Lluis**, A. Camps, E. Valencia, N. Rodriguez-Alvarez, M. Vall-llossera, "On-ground tests and measurements of the Passive Advanced Unit Synthetic Aperture (PAU-SA)" *Proceedings of the International Geoscience and Remote Sensing Symposium*, pp. 3114 - 3117, Honolulu, USA, 2010.

- N. Rodriguez-Alvarez, **X. Bosch-Lluis**, R. Acevo, A. Aguasca, A. Camps, M. Vall-llossera, I. Ramos-Perez, E. Valencia, "Study of maize plants effects in the retrieval of soil moisture using the interference pattern GNSS-R technique," *Proceedings of the IEEE International Geoscience and Remote Sensing Symposium*, pp. 3813-3816, Honolulu, Hawaii, USA, 2010.

- N. Rodriguez-Alvarez, R. Acevo-Herrera, A. Aguasca, E. Valencia, A. Camps, M. Vall-llossera, **X. Bosch-Lluis**, I. Ramos-Perez, "Altimetry study performed using an airborne GNSS-Reflectometer," *IEEE International Geoscience and Remote Sensing Symposium,* pp. 3833-3836, Honolulu, USA, 2010.

- R. Acevo-Herrera, A. Aguasca, **X. Bosch-Lluis**, A. Camps, "On the Use of Compact L-Band Dicke Radiometer (ARIEL) and UAV for Soil Moisture and Salinity Map Retrieval: 2008/2009 Field Experiments," *In Proceedings of the IEEE International Geoscience and Remote Sensing Symposium*, Vol. 4, pp. 729 – 732, Cape Town, South Africa, 2009.

- P. Ferre-Lillo, N. Rodriguez-Alvarez, **X. Bosch-Lluis**, E. Valencia, J.F. Marchan-Hernandez, A. Camps, "Delay-Doppler Maps study over ocean, land and ice from space," *Proceedings of the International Geoscience and Remote Sensing Symposium*, Vol. 2, pp. 722 - 725, Cape Town, South Africa, 2009.

- N. Rodriguez-Alvarez, J.F. Marchan-Hernandez, A. Camps, **X. Bosch-Lluis**, E. Valencia, I. Ramos-Perez, M. Vall-llossera, A. Monerris, J. Martinez-

Fernandez, C. Perez-Gutierrez, G. Baroncini-Turricchia, N. Sanchez-Martin, "Topographic profile retrieval using the Interference Pattern GNSS-R technique," *Proceedings of the International Geoscience and Remote Sensing Symposium*, Vol. 3, pp. 420 - 423, Cape Town, South Africa, 2009.

- I. Ramos-Perez, **X. Bosch-Lluis**, A. Camps, E. Valencia, J.F. Marchan-Hernandez, N. Rodriguez-Alvarez, "Preliminary results of the Passive Advanced Unit Synthetic Aperture (PAU-SA)," *Proceedings of the International Geoscience and Remote Sensing Symposium*, Vol. 4, pp. 121 - 124, Cape Town, South Africa, 2009.

- **X. Bosch-Lluis,** I. Ramos-Perez, A. Camps, N. Rodriguez-Alvarez, J.F. Marchan-Hernandez, "Digital beamforming analysis and performance for a digital L-band Pseudo-correlation radiometer," *Proceedings of the International Geoscience and Remote Sensing Symposium*, Vol. 5, pp. 184 - 187, Cape Town, South Africa, 2009.

- M. Talone, A. Camps, J.F. Marchan-Hernandez, J.M. Tarongi, M. Piles, **X. Bosch-Lluis**, I. Ramos-Perez, E. Valencia, N. Rodriguez-Alvarez, M. Vall-llossera, "Preliminary results of the advanced L-band transmission and reflection observation of the sea surface (ALBATROSS) campaign: Preparing the SMOS calibration and validation activities," *Proceedings of the International Geoscience and Remote Sensing Symposium*, Vol. 4, pp. 725 - 728, Cape Town, South Africa, 2009.

- N. Rodriguez-Alvarez, A. Monerris, **X. Bosch-Lluis**, A. Camps, M. Vall-llossera, J.F. Marchan-Hernandez, I. Ramos-Perez, E. Valencia, J. Martinez-Fernandez, N. Sanchez-Martin, G. Baroncini-Turricchia, C. Perez-Gutierrez, "Soil moisture and vegetation height retrieval using GNSS-R techniques," *Proceedings of the International Geoscience and Remote Sensing Symposium*, Vol. 3, pp. 869 - 872, Cape Town, South Africa, 2009.

- N. Rodriguez-Alvarez, J.F. Marchan, A. Camps, E. Valencia, **X. Bosch-Lluis**, I. Ramos-Perez, J.M. Nieto, "Soil Moisture Retrieval Using GNSS-R Techniques: Measurement Campaign in a Wheat Field," *Proceedings of the International Geoscience and Remote Sensing Symposium 2008*,Vol. 2, pp.245 – 248, Boston, USA, 2008.

- **X. Bosch-Lluis**, I. Ramos-Perez, A. Camps, J.F. Marchan-Hernandez, N. Rodriguez-Alvarez, E. Valencia, and M. A. Guerrero, "Initial Results of a Digital Radiometer with digital beamforming," *Proceedings of the International Geoscience and Remote Sensing Symposium 2008*, Vol. 2, pp. 485 - 488, Boston, USA, 2008.

- E. Valencia, R. Acevo, **X. Bosch-Lluis**, A. Camps, A. Aguasca, N. Rodriguez-Alvarez, I. Ramos-Perez, J.F. Marchan-Hernandez, M. Glenat and F. Boo, "PAU One-Receiver Airborne Instrument: Initial Results," *Proceedings of the*

International Geoscience and Remote Sensing Symposium 2008, Vol. 2, pp. 1176 – 1179, Boston, USA, 2008.

- J.F. Marchan-Hernandez, M. Vall-llossera, A. Camps, N. Rodriguez-Alvarez, I. Ramos-Perez, E. Valencia, **X. Bosch-Lluis**, M. Talone, J.M. Tarongi, M. Piles, "Ground-Based GNSS-R Measurements with the PAU Instrument and their Application to the Sea Surface Salinity Retrieval: First Results," *Proceedings of the International Geoscience and Remote Sensing Symposium 2008*, Vol. 4, pp. 530 – 533, Boston, USA, 2008.

- I. Ramos-Perez, E. Valencia, A. Camps, **X. Bosch-Lluis**, J.F Marchan-Hernandez, N. Rodriguez-Alvarez, F. Canales-Contador, M. Donadio, "Initials Results of the Passive Advanced Unit - Synthetic Aperture (PAU-SA)," *Proceedings of the International Geoscience and Remote Sensing Symposium 2008*, Vol. 2, pp- 1148-1151, Boston, USA, 2008.

- **X. Bosch-Lluis,** I. Ramos-Perez, A. Camps, E. Valencia, J.F. Marchan-Hernandez, N. Rodriguez-Alvarez, A. Guerrero and M.Vericat, *"*The Impact of the Number of Bits in Digital Beamforming Real Aperture and Synthetic Aperture Radiometers*," Microrad 2008*, Florence, Italy, 2008.

- A. Camps, N. Rodriguez-Alvarez, **X. Bosch-Lluis**, J.F. Marchan, I. Ramos-Perez, M. Segarra, Ll. Sagues, D. Tarrago, O. Cunado, R. Vilaseca, A. Tomas, J. Mas, J. Guillamon, *"*PAU in SeoSAT: A Proposed Hybrid L-band Microwave Radiometer/GPS Reflectometer to Improve Sea Surface Salinity Estimates from Space*," Microrad 2008*, Florence, Italy, 2008.

- A. Camps, J. F. Marchan-Hernandez, N. Rodriguez-Alvarez, **X. Bosch-Lluis**, and I. Ramos-Perez, "On the Use of GNSS-Reflectometry to Improve Sea Surface Salinity Measurements by Means of Microwave Radiometry," *1st Colloquium on Scientific and Fundamental Aspects of the Galileo Programme,* Toulouse, France, 2007.

- N. Rodriguez-Alvarez, A. Camps, **X. Bosch-Lluis**, I. Ramos-Perez and J.F. Marchan-Hernandez, "PAU-IR: Sea surface temperature retrieval using IR-radiometry and atmospheric modeling: Simulation and experimental results*,*" *Proceedings of the International Geoscience and Remote Sensing Symposium 2007*, pp. 933-936, Barcelona, 2007.

- **X. Bosch-Lluis**, M. Moussaif, A. Camps, J. F. Marchan-Hernandez, I. Ramos-Perez, N. Rodriguez-Alvarez, "PAU-RAD Instrument Web-based*," Proceedings of the International Geoscience and Remote Sensing Symposium 2007*, pp. 2905-2908, Barcelona, 2007.

- **X. Bosch-Lluis**, A. Camps, J.F. Marchan-Hernandez, I. Ramos-Perez, N. Rodriguez-Alvarez, X. Banque and M. A. Guerrero, "Calibration and Performance Analysis of the PAU-RAD instrument", *Proceedings of the*

International Geoscience and Remote Sensing Symposium, pp. 2419-2422 Barcelona, 2007.

- I. Ramos-Perez, A. Camps, **X. Bosch-Lluis**, J. F. Marchan-Hernandez and N. Rodriguez-Alvarez , "Synthetic Aperture PAU, a new instrument to test potential improvement for future SMOSops," *Proceedings of the International Geoscience and Remote Sensing Symposium*, pp. 247-250, Barcelona, 2007.

- A. Camps, A. Aguasca, **X. Bosch-Lluis**, J. F. Marchan-Hernandez, I. Ramos-Perez, N. Rodriguez-Alvarez, F. Bou, C. Ibáñez, X. Banque and R. Prehn, "Measurements and First Results of the One-Receiver PAU Instruments," *Proceedings of the International Geoscience and Remote Sensing Symposium*, pp. 2901-2904, Barcelona, 2007.

- **X. Bosch-Lluis**, A. Camps, J.F. Marchan-Hernandez, I. Ramos-Perez, R. Prehn, B. Izquierdo, X. Banque, and J. Yeste, "FPGA-based Implementation of a Polarimetric Radiometer with Digital Beamforming," *Proceedings of the International Geoscience and Remote Sensing Symposium*, pp. 1176-1179, Denver, USA, 2006.

- I. Ramos-Perez, **X. Bosch-Lluis,** A. Camps, J. F. Marchan-Hernandez and R. Prehn, "Design of a compact dual-polarization receiver for pseudo-correlation radiometers at L-band," *Proceedings of the International Geoscience and Remote Sensing Symposium*, pp. 1172-1175, Denver, USA, 2006.

- J.F. Marchan-Hernandez, I. Ramos-Perez, **X. Bosch-Lluis**, A. Camps, and R. Prehn, "FPGA-based implementation of a DDM-generator for GPS-reflectometry", *Proceedings of the International Geoscience and Remote Sensing Symposium*, pp. 1180 – 1183, Denver, USA, 2006.

- A. Camps, J.F. Marchan-Hernandez, I. Ramos-Perez, **X. Bosch-Lluis**, R. Prehn, "New Radiometer Concepts for Ocean Remote Sensing: Description of the Passive Advanced Unit (PAU) for Ocean Monitoring," *Proceedings of the International Geoscience and Remote Sensing Symposium*, pp. 3988-3991, Denver, USA, 2006.

MASTER THESIS SUPERVISED DURING THIS PhD

- M.A. Guerrero, "Equalization algorithms for digital radiometers," advisors: A. Camps and X. Bosch, 2009.

- M. Vericat, "Specifications and performance of digital radiometers," advisors: A. Camps and X. Bosch, 2009.

- A. Duperrier, "Soil moisture retrieval using an airborne L-band radiometer," advisors: A. Camps and X. Bosch, 2009.

- M. Glenat, "Georeferencing in Google Earth radiometric data from UAV: Simulation and experimental data processing," advisors: A. Camps and X. Bosch, 2008. (1st award of the IEEE GRSS Spanish Section to the best Master Thesis on Remote Sensing in 2008).

- M. Moussaif, "Design and implementation of a web-GUI for a digital beamforming radiometer," advisors: A. Camps and X. Bosch, 2007.

- F. Bou, "Design and implementation of a light radiometer/reflectometer for a remote control aircraft," advisors: A. Aguasca and X. Bosch, 2007.

- X. Banque, "Design and implementation of a CU, equalization and communication for a digital beamforming radiometer," advisors: A. Camps and X. Bosch, 2006.

- J. Yeste, "Design and implementation of a GUI for PAU-RAD and a PAU-RAD PAU-GNSS communication module," advisors: A. Camps and X. Bosch, 2006.

PATENTS

- A. Camps, **X. Bosch**, J. F. Marchan, and I. Ramos, "*Sistema híbrido receptor de señales Gnss-Reflejadas/Radiómetro diferencial de Pseudo-Correlación para la observación pasiva del océano*," Spanish patent P-200602778, October 2006.

  [A pseudo-correlation radiometer/reflectometer hybrid system for passive observation of the ocean.]

- "*Sistema Aerotransportado para la medida de la humedad del terreno y el contenido de agua de la vegetación*," **(Patent pending)**.

  [An airborne system for soil moisture and vegetation water content measurement.]

- "*Sistema para la recuperación de parámetros geofísicos usando señales de satélites de navegación*," **(Patent pending)**.

  [A system for geophysical parameters retrieval using navigation satellites' signals.]

BIBLIOGRAPHY

[1] H.M.J. Barre, B. Duesmann, Y.H. Kerr, “SMOS: The mission and the system,” *IEEE Transactions on Geoscience and Remote Sensing*, vol. 46, n.3, pp. 587 – 593, 2008.

[2] D. M. Le Vine, G. S. E. Lagerloef, F. R. Colomb, S.H. Yueh, and A. Pellerano, “Aquarius: An Instrument to Monitor Sea Surface Salinity From Space,” *IEEE Transactions on Geoscience and Remote Sensing*, vol. 45, n. 7, pp. 2040-2049, 2007.

[3] R.H. Dicke, "The measurement of thermal radiation at microwave frequencies," *Revision on Science Instrumentation*, vol. 17, pp. 268-275, 1946.

[4] E. R. Westwater, "The accuracy of water vapor and cloud liquid determination by dual frequency ground-based microwave radiometry," *Radio Science*, vol. 32, pp. 677-685, 1978.

[5] B. Aja, E. Artal, L. de la Fuente, J.P. Pascual, A. Mediavilla, N. Roddis, D. Kettle, W.F. Winder, L.Pi. Cara, P. de Paco, “Very low-noise differential radiometer at 30 GHz for the PLANCK LFI,” *IEEE Transactions on Microwave Theory and Techniques*, vol.53, n.6, pp. 2050-2062, 2005.

[6] R.M. Lerner, J.P. Hollinger. “Analysis of 1.4 GHz radiometric measurements from Skylab,” *Remote Sensing of Environment*, Vol. 6, pp. 251-269, 1977.

[7] D.M. LeVine, J.C. Good, “Aperture synthesis for microwave radiometers in space,” *NASA memorandum*, NASA-TM-8503, 1983.

[8] P.J. Napier, A.R. Thompson, R.D. Ekers, "The very large array: Design and performance of a modern synthesis radio telescope," *Proceedings of the IEEE*, vol.71, n.11, pp. 1295 – 1320, 1983.

[9] C.S. Ruf, C.T Swift, A.B Tanner, D.M. LeVine, “Interferometric Synthetic Aperture Microwave Radiometry for the Remote Sensing of the Earth,” *IEEE Transactions on Geoscience and remote sensing*, Vol. 26, n. 5, pp 597-611, 1988.

[10] K. Rautiainen, J. Kainulainen, T. Auer, S. Tauriainen, M. Hallikainen, "Helsinki University of Technology Synthetic Aperture Radiometer -HUT-2D," *Proceedings of Geoscience and Remote Sensing Symposium, 2007,* pp. 3635-3638, Barcelona, 2007.

[11] A.B. Tanner, W.J. Wilson, B.H. Lambrigsten, S.J. Dinardo, S.T. Brown, P.P. Kangaslahti, T.C. Gaier, C.S. Ruf, S.M. Gross, B.H. Lim, S. Musko, S. Rogacki, and J.R. Piepmeier, "Initial Results of the Geostationary Synthetic Thinned Array Radiometer (GeoSTAR) Demonstrator Instrument," *IEEE Transactions on Geoscience and Remote Sensing*, vol. 45, pp. 1947-1957, 2007.

[12] C. Swift and R.E. McIntosh, "Considerations for microwave remote sensing of ocean surface salinity," *IEEE Transactions on Geoscience and Remote Sensing*, Vol. 21, n. 4, pp. 480-491, 1983.

[13] D. Marquardt, "An algorithm for least-squares estimation of non-linear parameters," *Journal of the Society for Industrial and Applied Mathematics*, Vol. 11, pp. 431-441, 1963.

[14] M. Talone, A. Camps, C. Gabarro, R. Sabia, J. Gourrion, M. Vall-llossera, B. Mourre, J. Font, "Contributions to the improvement of the SMOS Level 2 retrieval algorithm: Optimization of the cost function," *IEEE Proceedings of International Geoscience and Remote Sensing Symposium*, vol. 4, pp. 943 – 937, Boston, USA, 2008.

[15] C. Gabarro, J. Font, J. Miller, A. Camps, D. Burrage, J. Wesson, "Use of empirical sea surface emissivity models for a rough estimation of sea surface salinity from an airborne microwave radiometer," *Scientia Marina*, vol. 72, pp. 329-336, 2008.

[16] A. Camps, J. Font, M. Vall-llossera, I. Corbella, N. Duffo, F. Torres, S. Blanch, A. Aguasca, R. Villarino, C. Gabarro, L. Enrique, J. Miranda, R. Sabia, M. Talone, "Determination of the sea surface emissivity at L-band and its applications to SMOS salinity retrieval algorithms: Review of the contributions of the UPC – ICM," *Radio Science*, vol. 43, RS3008, 2008.

[17] A. Camps, M. Vall-llossera, I. Corbella, N. Duffo, F. Torres, "Improved Image Reconstruction Algorithms for Aperture Synthesis Radiometers," *IEEE Transactions on Geoscience and Remote Sensing*, Vol. 46, n. 1, pp. 146 – 158, 2008.

[18]I. Ramos-Perez, X. Bosch-Lluis, A. Camps, E. Valencia, J.F. Marchan-Hernandez, N. Rodriguez-Alvarez, F. Canales-Contador, "Preliminary results of the passive advanced unit synthetic aperture (PAU-SA)," *IEEE Proceedings of International Geoscience and Remote Sensing Symposium*, Vol. 4, pp. 121 – 124, Cape Town, South Africa, 2009.

[19] J.P. Hollinger, J.L. Peirce, G.A. Poe, "SSM/I instrument evaluation," IEEE Transactions on Geoscience and Remote Sensing, vol. 28, n .5, pp. 781 – 790, 1990.

[20]M.A. Goodberlet, C.T. Swift, J.L. Miller, "A compact imaging L-band radiometer for remote sensing of salinity in the coastal zone," *IEEE Transactions on Geoscience and Remote Sensing*, Vol. 6, pp. 2543 – 2545, 2000.

[21] SMOS: ESA's Water Mission. *ESA SMOS Brochure*, BR-224, 14. 2004.

[22]UNEP. United Nation Environmental Program - Climate. Retrieved 2008.

[Online, Dec. 31st 2010] at http://www.grida.no/climate/vital/32.html

[23]W. Emery, and R. Wert, "Temperature-Salinity Curves in the Pacific and their Application to Dynamic Height Computation," *Journal of Physical Oceanography* Vol. 6, pp. 613-617, 1976.

[24]S. Michel, B. Chapron, J. Tournadre, N. Reul,"Global Analysis of Sea Surface Salinity variability from Satellite Data," *Oceans - Europe*, pp. 11-16, 2005.

[25] S. Levitus, T. Boyer, M. Conkright, T. O'Brien, J. Antonov, C. Stephens, et al. "World Ocean Database," *National Oceanographic Data Center, NOAA/NESIDS 18* . Silver Spring. 1998.

[26] A. Monerris, "Experimental estimation of soil emissivity and its application to soil moisture retrieval in the SMOS Mission," *Ph.D. dissertation*. Universitat Politècnica de Catalunya, 2009.

[Online, Dec. 31st 2010] at http://www.tdx.cat/TDX-1228109-101841/

[27] C. Koblinsky, P. Hildebrand, D. LeVine, F. Pellerano, "Sea Surface Salinity from Space: Science Goals and Measurement Approach". *Radio Science*, Vol. 38, n.4, 2003.

[28]A. Camps, "Application of Interferometric Radiometry to Earth Observation," *Ph.D. dissertation*. Universitat Politècnica de Catalunya, 1996.

[Online, Dec. 31st 2010] at http://www.tdx.cat/TDX-1020104-091741/

[29]R. Sabia, "Sea Surface Salinity Retrieval Error Budget within the ESA Soil Moisture and Ocean Salinity Mission," *PhD dissertation*. Universitat Politècnica de Catalunya, 2008.

[Online, Dec. 31st 2010] at http://www.grss-ieee.org/files/Sabia_PhD_Thesis_October_08.pdf

[30]P. Silvestrin, M. Berger, Y. Kerr, J. Font, ESA's Second Earth Explorer Opportunity Mission: The Soil Moisture and Ocean Salinity Mission - SMOS. *IEEE Geoscience and Remote Sensing Newsletter, 118*, pp. 11-14. 2001

[31]A. Camps, "Passive Advanced Unit (PAU): A hybrid L-band radiometer,GNSS-Reflectometer and IR-Radiometer for Passive Remote Sensing of the Ocean," *Project descriptions of the EURYI award winners 2004 Telecommunications Engineering*.

[Online, Dec. 31st, 2010] at http://www.esf.org/activities/euryi/awards-results/2004.html

[32] A. Camps, X. Bosch-Lluis, I. Ramos-Perez, J. F. Marchan, B. Izquierdo and N. Rodriguez, "New Instrument Concepts for Ocean Sensing: Analysis of the PAU-Radiometer", *IEEE Transactions on Geoscience and Remote Sensing,* vol. 45, n.10, pp: 3180 – 3192, 2007.

[33] M. Martin-Neira, "A Passive Reflectometry and Interferometry System (PARIS): Application to Ocean Altimetry," *ESA Journal,* Vol. 17, pp. 331-355. 1993.

[34] A. Camps; X. Bosch; I. Ramos; J. F. Marchan; N. Rodriguez; E. Valencia; J. M. Tarongí; A. Aguasca; R. Acevo, " New Passive Instruments Developed for Ocean Monitoring at the Remote Sensing Lab - Universitat Politècnica de Catalunya" *Sensors Journal*, Vol. 9, pp. 1013-1018, 2009.

[35] V.U, Zavorotny and A.G. Voronovich, "Scattering of GPS Signals from the Ocean with Wind Remote Sensing Application," *IEEE Transactions on Geoscience and Remote Sensing*, vol. 38 n. 2, pp. 951-964, 2000.

[36] E. Valencia, J.F. Marchan-Hernandez, A. Camps, N. Rodriguez-Alvarez, J.M. Tarongi, J.M.; M. Piles, I. Ramos-Perez, X. Bosch-Lluis, M. Vall-llossera, P. Ferre, "Experimental relationship between the sea brightness temperature and the GNSS-R Delay-Doppler Maps: Preliminary results of the ALBATROSS field experiments," *Proceedings of the IEEE International Geoscience & Remote Sensing Symposium,* Cape Town, South Africa,Vol. 3, pp. 741-744, 2009.

[37] J.F. Marchan; N. Rodriguez, A. Camps, X. Bosch, I. Ramos, E. Valencia, "Correction of the Sea State Impact in the L-Band Brightness Temperature by Means of Delay-Doppler Maps of Global Navigation Satellite Signals Reflected Over the Sea Surface," *IEEE Transactions on Geoscience and Remote Sensing*, Vol. 46 n.10, pp. 2914-2923, 2008.

[38] J.F. Marchan-Hernandez, E. Valencia, N. Rodriguez-Alvarez, I. Ramos-Perez, X. Bosch-Lluis, A. Camps, F. Eugenio, J. Marcello, "Sea-State Determination Using GNSS-R Data," *IEEE Geoscience and Remote Sensing Letters*, Vol.7, n.4, pp.621-625, 2010.

[39] F. T. Ulaby, R.K. Moore, A.K. Fung, "Microwave Remote Sensing. Active and Passive, Vol. I - Fundamentals and Radiometry," *Artech House*, 1981.

[40] X. Bosch-Lluis, A. Camps, I. Ramos-Perez, J.F. Marchan-Hernandez, N. Rodriguez-Alvarez, E. Valencia, "*PAU/RAD*: Design and Preliminary Calibration Results of a New L-Band Pseudo-Correlation Radiometer Concept," *Sensors Journal*, Vol. 8, pp. 4392-4412, 2008

[41] X. Bosch-Lluis, I. Ramos-Perez, A. Camps, J.F. Marchan-Hernandez, N. Rodriguez-Alvarez, E. Valencia, "Initial Results Of A Digital Radiometer With Digital Beamforming," *Proceedings of the IEEE International Geoscience & Remote Sensing Symposium*, Boston, MA, USA, Vol. 2, pp. 485-488, 2008.

[42] X. Bosch-Lluis, I. Ramos-Perez, A. Camps, N. Rodriguez-Alvarez, J.F. Marchan-Hernandez, E. Valencia, "Digital Beamforming Analysis and Performance of a Digital L-Band Pseudo-Correlation Radiometer," *IEEE Proceedings of International Geoscience and Remote Sensing Symposium 2009,* Cape Town, South Africa, vol. 5, pp. 184 – 187, 2009.

[43] I. Ramos-Perez, A. Camps, X. Bosch-Lluis, J.F. Marchan-Hernandez N, Rodriguez-Alvarez, "Synthetic Aperture *PAU*: a new instrument to test potential improvements for future SMOSops," In *Proceedings of the IEEE International Geoscience & Remote Sensing Symposium*, Barcelona, Vol. 1, pp. 247-250, 2007.

[44] M. Martin-Neira, S. Ribo, A.J. Martin-Polegre, "Polarimetric mode of MIRAS," IEEE Transactions on Geoscience and Remote Sensing, vol. 40, n. 8, pp. 1755 – 1768, 2002.

[45] I. Ramos-Perez, X. Bosch-Lluis, A. Camps, E. Valencia, N. Rodriguez-Alvarez, M. Vall-llossera, "On-ground tests and measurements of the Passive Advanced Unit Synthetic Aperture (PAU-SA)" *Proceedings of the International Geoscience and Remote Sensing Symposium 2010*, pp. 3114 - 3117, Honolulu, USA, 2010.

[46] I. Ramos-Perez, X. Bosch-Lluis, A. Camps, N. Rodriguez-Alvarez, J.F. Marchan-Hernandez, E. Valencia, S. de la Rosa, C. Vernich, S. Pantoja, "Calibration of Microwave Radiometers Using Pseudo-Random Noise Signals," *Sensors Journals*, Vol. 9, pp. 6131-6149, 2009.

[47] J.F. Marchan-Hernandez, A. Camps, N. Rodriguez-Alvarez, X. Bosch-Lluis, I. Ramos-Perez, E. Valencia, "PAU/GNSS-R: Implementation, Performance and First Results of a Real-Time Delay-Doppler Map Reflectometer Using Global Navigation Satellite System Signals," *Sensors Journal*, Vol. 8, pp. 3005-3019, 2008.

[48] E. Valencia, A. Camps, J.F. Marchan-Hernandez, X. Bosch-Lluis, N. Rodriguez-Alvarez, I. Ramos-Perez, "GPS Reflectometer Instrument for PAU (griPAU): Advanced Performance Real Time Delay Doppler Map Receiver," *2nd Workshop on Advanced RF Sensors and Remote Sensing Instruments*, ESTEC, Noordwijk, The Netherlands, 17-18 November 2009.

[49] A. Camps, A. Aguasca, X. Bosch-Lluis, J.F. Marchan-Hernandez, I. Ramos-Perez, N. Rodriguez-Alvarez, F. Bou, C. Ibanez, X. Banque, "PAU One-Receiver Ground-based and Airborne Instruments," *In Proceedings of the IEEE International Geoscience and Remote Sensing Symposium*, Barcelona, Vol. 1, pp. 2901-2904, 2007.

[50] R. Acevo-Herrera, A. Aguasca, X. Bosch-Lluis, A. Camps, J. Martinez Fernandez, N. Sanchez-Martin, C. Perez-Gutierrez, "Design and First Results of an UAV-Borne L-Band Radiometer for Multiple Monitoring Purposes," *Remote Sensing*, Vol. 2, pp. 1662-1679, 2010.

[51] N. Rodriguez-Alvarez, R. Acevo-Herrera, A. Aguasca, E. Valencia, A. Camps, M. Vall-llossera, X. Bosch-Lluis, I. Ramos-Perez, "Altimetry study performed using an airborne GNSS-Reflectometer," *IEEE International Geoscience and Remote Sensing Symposium,* pp. 3833-3836, Honolulu, USA, 2010.

[52] E. Valencia, R. Acevo, X. Bosch-Lluis, A. Aguasca, N. Rodriguez-Alvarez, I. Ramos-Perez, J.F. Marchan-Hernandez, M. Glenat, F. Bou, A. Camps, "Initial Results of an Airborne Light-Weight L-Band Radiometer," *In Proceedings of the IEEE International Geoscience and Remote Sensing Symposium*, Vol. 2, pp. 1176-1179, Boston, USA, 2008.

[53] R. Acevo-Herrera, A. Aguasca, X. Bosch-Lluis, A. Camps, "On the Use of Compact L-Band Dicke Radiometer (ARIEL) and UAV for Soil Moisture and Salinity Map Retrieval: 2008/2009 Field Experiments," *In Proceedings of the IEEE International Geoscience and Remote Sensing Symposium*, Cape Town, South Africa, Vol. 4, pp. 729 – 732, 2009.

[54] J.M. Tarongi, A. Camps, "Multifrequency experimental radiometer with interference tracking for experiments over land and littoral: Meritxell," *IEEE International Geoscience and Remote Sensing Symposium*, Vol. 4, pp. 653 -656, 2009.

[55] N. Rodriguez-Alvarez, X. Bosch-Lluis, A. Camps, M. Vall-llossera, E. Valencia, J.F. Marchan-Hernandez, I. Ramos-Perez, "Soil moisture retrieval using GNSS-R techniques: experimental results over a bare soil field," *IEEE Transactions on Geoscience and Remote Sensing*, Vol. 47 n.11, pp. 245-248, 2009.

[56]N. Rodriguez-Alvarez, A. Camps, M. Vall-Llossera, X. Bosch-Lluis, A. Monerrris, I. Ramos-Perez, E. Valencia, J.F. Marchan-Hernandez, J. Martinez-Fernandez, G. Baroncini-Turricchia, C. Perez Gutierrez N. Sanchez, "Land Geophysical Parameters Retrieval Using The Interference Pattern GNSS-R Technique" *IEEE Transactions on Geoscience and Remote Sensing*, Vol. 49 n.1, pp. 71-84, 2011.

[57]N. Rodriguez-Alvarez, X. Bosch-Lluis, R. Acevo, A. Aguasca, A. Camps, M. Vall-llossera, I. Ramos-Perez, E. Valencia, " Study of maize plants effects in the retrieval of soil moisture using the interference pattern GNSS-R technique" *Proceedings of the IEEE International Geoscience and Remote Sensing Symposium 2010*, pp. 3813-3816, Honolulu, Hawaii, USA, 2010.

[58]A. Monerris, N. Rodriguez-Alvarez, M. Vall-llossera, A. Camps, M. Piles, J. Martinez Fernandez, N. Sanchez Martin, C. Perez Gutierrez, G. Baroncini-Turricchia, R. Acevo, and A. Aguasca, "The GPS and RAdiometric Joint Observations Experiment At The REMEDHUS Site (Zamora-Salamanca Region, Spain)." Proceedings of the International Geoscience and Remote Sensing Symposium 2009, Vol. 3, pp. 286 - 289 Cape Town, South Africa, 2009.

[59]S. Gleason, "Remote Sensing of Ocean, Ice and Land Surfaces Using Bistatically Scattered GNSS Signals From Low Earth Orbit," *Ph.D. Thesis, University of Surrey*, 2006.

[60]A. Camps, N. Rodriguez-Alvarez, X. Bosch-Lluis, J.F. Marchan, I. Ramos-Perez, M. Segarra, Ll. Sagues, D. Tarrago, O. Cunado, R. Vilaseca, A. Tomas, J. Mas, and J. Guillamon, "PAU in SeoSAT: A Proposed Hybrid L-band Microwave Radiometer/GPS Reflectometer to Improve Sea Surface Salinity Estimates from Space," *In Proceedings of Microwave Radiometry and Remote Sensing of the Environment*, 2008.

[61]J. Font, G. Lagerloef, D. LeVine, A. Camps, O.Z. Zanife, "The Determination of Surface Salinity with the European SMOS Space Mission," *IEEE Transactions on Geoscience and Remote Sensing*, Vol. 42, n. 10, pp. 2196-2205, 2004.

[62] J.R. Piepmeier, D.G. Long, E.G. Njoku, "Stokes Antenna Temperatures," *IEEE Transactions on Geoscience and Remote Sensing*, Vol. 46, no. 2, pp. 516-527, 2008.

[63] J.R. Piepmeier, N.K. Simon, "A polarimetric extension of the van Cittert-Zernike Theorem for use with microwave Interferometers," *IEEE Geoscience and Remote Sensing Letters,* Vol.1, n.4, pp. 300- 303, 2004.

[64] R. W. Schmieder, "Stokes-Algebra Formalism," Journal Optical Society American, Vol. 59, pp. 297-302, 1969.

[65] S. H Yueh, D. Kwok, F. K. Li, S. V. Nghiem, W. J. Wilson, and J. A. Kong, "Polarimetric passive remote sensing of ocean wind vectors", *Radio Sci.*, Vol. 29 n.4, pp. 799–814, 1994.

[66]A. Camps, I. Corbella, J.M. Rius, "Extension of Kirchoff method under Stationary Phase approximation to determination for polarimetric thermal emission of the Sea," *Electronic Letters*, Vol. 34, pp. 1501-1503, 1998.

[67] J. Randa, J, Lahtinen, A. Camps, A.J. Gasiewski, M. Hallikainen, D.M. Le Vine, M. Martin-Neira, J. Piepmeier, P.W. Rosenkranz, C.S. Ruf, J. Shiue, N. Skou. "Recommended Terminology for Microwave Radiometry," *NIST Technical Note TN1551*; National Institute of Standards and Technology, Gaithersburg, MD, USA, 2008.

[68] N. Skou, "Microwave Radiometer Systems: Design & Analysis," *Artech House*, 1989.

[69] D.M. LeVine, C. Utku, "Comment on Modified Stokes Parameters," *IEEE Transactions on Geoscience and Remote Sensing,* vol. 47, n. 8, pp. 2707 – 2713, 2009.

[70] C.A. Balanis, "Antenna Theory: Analysis and Design," John Wiley & Sons, 3rd Edition, 2005.

[71] A.R. Thompson, J.M. Moran, G.W. Swenson, "Interferometry and synthesis in radio astronomy," John Wiley, New York, 2nd Edition, 2001.

[72] J.W. Goodman, "Introduction to Fourier Optics," Roberts and company Publishers, 3rd Edition, 2005.

[73] I. Corbella, N. Duffo, M. Vall-llosera, A. Camps, F. Torres, "The Visibility Function in Interferometric Aperture Synthesis Radiometry," IEEE Transactions on Geoscience and remote sensing, vol. 42, n. 8, pp. 1677 – 1682, 2004.

[74] A.B. Tanner and C.T. Swift, "Calibration of a synthetic aperture radiometer," IEEE Transactions on Geoscience and remote sensing, vol. 31, pp. 257 – 267, 1993

[75] A. Camps, C.T. Swift, "New Techniques in Microwave Radiometry for Earth Remote Sensing: Principles and Applications," Radio Science, vol. 32, pp. 499-517, 2002.

[76] H.A. Malliot, "A cross-beam interferometer radiometer for high resolution microwave sensing," *IEEE Aerospace Applications Conference,* pp.77 – 86, 1993.

[77] A.B Tanner, C.T Swift, "Calibration of a synthetic aperture radiometer," *IEEE Transactions on Geoscience and Remote Sensing*, Vol.31, no.1, pp.257-267, 1993.

[78] A. Camps, J. Bara, I. Corbella, F. Torres, "The Processing of Hexagonally Sampled Signals with Standard Rectangular Techniques: Application to 2D Large Aperture Synthesis Interferometric Radiometers," *IEEE Transactions on Geoscience and Remote Sensing*, vol. 35, pp. 183 – 190, 1997.

[79]J. Butler and R. Lowe, "Beam forming matrix simplifies design of electronically scanned antennas," *Electronic Design*, 1961.

[80] X. Bosch-Lluis, I. Ramos-Perez, A. Camps, N. Rodriguez-Alvarez, E. Valencia, J.F. Marchan-Hernandez, "Description and Performance of an L-Band Radiometer with Digital Beamforming," *Remote Sensing,* Vol. 3, pp. 14-40, 2011.

[81] A. Camps, F. Torres, I. Corbella, J. Bara, P. de Paco, "Mutual Coupling Effects on Antenna Radiation Pattern: An Experimental Study Applied to Interferometric Radiometers," *Radio Science*, vol. 33, pp. 1543 – 1552, 1998.

[82] A. Camps, F. Torres, I. Corbella, J. Bara, X. Soler, "Calibration and Experimental Results of a Two-Dimensional Interferometric Radiometer Laboratory Prototype," *Radio Science*, vol. 32, pp. 1821 – 1832, 1997.

[83] A. Camps, C.T. Swift, "A two-dimensional Doppler-radiometer for earth observation," *IEEE Transactions on Geoscience and Remote Sensing*, vol. 39, n. 4, pp. 1566 – 1572, 2001.

[84] J.W. Goodman, "Statistical Optics," *Wiley-Interscience*, Section 2.8, 1985.

[85] M.E. Tiuri, "Radio astronomy receivers," *IEEE Transactions on Antennas Propagation*, vol.12, pp. 930 – 938, 1964.

[86] R. Butora and A. Camps, "Noise maps in aperture synthesis radiometric images due to cross-correlation of visibility noise," *Radio Science*, vol. 38, n. 4, pp. 1067 –1074, 2003.

[87] J.D. Kraus, "Radio Astronomy," McGraw-Hill, 1966.

[88] A. Camps, F. Torres, P. Lopez-Dekker, S.J. Fraiser, "Redundant space calibration of hexagonal and Y-shaped beamforming radars and interferometric radiometers", *International journal of remote sensing*, vol. 24, n. 24, pp. 5183 – 5196, 2003.

[89] J.B. Hagen, D.T. Farley, "Digital-correlation techniques in radio science," *Radio Science*, vol. 8, pp. 775 – 784, 1973.

[90] M. Martin-Neira, M. Caparrini, J. Font-Rossello, S. Lannelongue, C. Vallmitjana, "The PARIS concept: an experimental demonstration of sea surface altimetry using GPS reflected signals," *IEEE Transactions on Geoscience and Remote Sensing*, vol.39, n.1, pp. 142 – 150, 2001.

[91] J.F. Marchan-Hernandez, "Sea state determination using GNSS-R techniques: Contributions to the PAU instrument," *PhD dissertation, Universitat Politècnica de Catalunya*, 2009.

[Online, Dec. 31st 2010] at http://www.tesisenxarxa.net/TDX-0529109-095953/

[92] S. Weinreb, "Digital radiometer," *Proceedings of the IEEE*, Vol. 49, p. 1099, 1961.

[93] B. F. Cooper, "Correlators with two-bit quantization," *Aust. J. Phys.*, vol. 23, pp. 521–527, 1970.

[94] J.H. Van Vleck and D. Middleton, "The spectrum of clipped noise," *Proceedings of the IEEE*, Vol. 54, n. 1, pp. 2–19, 1966.

[95] R. Price, "A useful theorem for nonlinear devices having Gaussian inputs," *IRE Transactions on Information Theory*, Vol. 4, n. 2, pp. 69–72, 1958.

[96] R.E. Kalman, "A new approach to linear filtering and prediction problems," *Transactions of the ASME-Journal of basic engineering*, vol. 82, pp. 35 – 40, 1960.

[97] J.R. Piepmeier, A.J. Gasiewski, J.E. Almodovar, "Advances in microwave digital radiometry," *Proceedings of IEEE International Geosci. and Remote Sensing Symposium*, vol. 7, pp. 2830-2833, 2000.

[98] M.A. Fischman and A. W. England, "Sensitivity of a 1.4 GHz direct sampling digital radiometer," *IEEE Transactions on Geoscience and Remote Sensing*, Vol. 37, pp. 2172-2180, 1999.

[99] C.S. Ruf, "Digital correlators for synthetic aperture interferometric radiometry," *IEEE Transactions on Geoscience and Remote Sensing*, Vol. 33, no. 5, pp. 1222-1229, 1995.

[100] M.A. Fischman, A. W. England, C.S. Ruf, "How digital correlation affects the fringe washing function in L-band aperture synthesis radiometry," *IEEE Transactions on Geoscience and Remote Sensing*, Vol. 40, no. 3, pp. 671-679, 2002.

[101] I. Corbella, F. Torres, A. Camps, J. Bara, N. Duffo, M. Vall-llosera, "L-band aperture synthesis radiometry: Hardware requirements and system performance," *Proceedings of IEEE International Geosci. and Remote Sensing Symposium*, vol. 7, pp. 2975-2977, 2000.

[102] A. Papoulis, "Probability, random variables, and stochastic processes," *McGraw-Hill*, pp. 427–442, 1991.

[103] R. Butora, M. Martin-Neira, and A. L. Rivada-Antich, "Fringe-washing function calibration in aperture synthesis microwave radiometry," *Radio Science*, vol. 38, no. 2, pp. 1-5, 2003.

[104] A. Camps, F. Torres, I. Corbella, J. Bara, J. A. Lluch, "Threshold and Timing Errors of 1 bit/2 level Digital Correlators in Earth Observation Synthetic Aperture Radiometry", *Electronics Letters*, Vol. 33, no 9, pp. 812-813, 1997.

[105] A. Demir, A. Mehrotra, J. Roychowdhury, "Phase noise in oscillators: A unifying theory and numerical methods for characterization," *IEEE Transactions on Circuits and Systems-I: Fundamental Theory and Applications*. Vol. 47, no. 5, pp. 655-674, 2000.

[106] H. Kobayashi, M. Morimura, K. Kobayashi, Y. Onaya, "Aperture jitter effects in wideband ADC systems," SICE Annual, 1999. Proceedings of the 38th Annual Conference, pp.1089-1094, 1999.

[107] Zarlink, GP2015 datasheet, 2007.

[Online, Dec. 31st, 2010] at http://www.zarlink.com/zarlink/gp2015-datasheet-sept2007.pdf

[108] "Standard VHDL synthesis packages", *IEEE Standard* 1076.3, 1997.

[109] S.W. Wedge and D.B. Rutledge, "Wave techniques for noise modeling and measurement," IEEE *Transactions on Microwave Theory and Techniques*, Vol. 40, no.11, pp. 2004 – 2012, 1992.

[110]J. Randa, "Noise characterization of multiport amplifiers," *IEEE Transactions on Microwave Theory and Techniques*, Vol. 49, n.10, pp. 1757 – 1763, 2001.

[111] I. Corbella, A. Camps, F. Torres, J. Bara, "Analysis of noise-injection networks for interferometric radiometer calibration," *IEEE Transactions on microwave theory and techniques*, 2000, Vol. 48, n. 4, pp. 545-552, 2000.

[112] A. Camps, X. Bosch-Lluis, H. Park, "Impact of receiver's frequency response in GNSS reflectometers," *IEEE International Geoscience and Remote Sensing Symposium*, pp.3817-3820, Honolulu, USA, 2010.

[113] R.M. Villarino, "Empirical Determination of the Sea Surface Emissivity at L-band: A contribution to ESA's SMOS Earth Explorer Mission," Ph.*D. thesis dissertation*, Barcelona, 2004.

[Online, Dec. 31st, 2010] at http://www.tdx.cesca.es/TDX-1019104-170028/

[114] A. Camps, J. Font, M. Vall-llossera, C. Gabarro, I. Corbella, N. Duffo, F. Torres, S. Blanch, A. Aguasca, R. Villarino, L. Enrique, J.J. Miranda, R. Arenas, A. Julia, J. Etcheto, V. Caselles, A. Weill, J. Boutin, S. Contardo, R. Niclos, R. Rivas, S.C. Reising, P. Wursteisen, M. Berger, M. Martin-Neira, "The WISE 2000 and 2001 field experiments in support of the SMOS mission: sea surface L-band brightness temperature observations and their application to sea surface salinity retrieval," *IEEE Transactions on Geoscience and Remote Sensing*, vol.42, no.4, pp. 804-823, 2004.

[115] B. Parkinson, J. Spilker, "Global Positioning System: Theory and Applications I/II/III," *Progress in Astronautics and Aeronautics*, 163, 1996.

[116] N. Smith, M. Lefebvre, "The global ocean data assimilation experiment (GODAE)", *Proceedings of International Symposium Monitoring Oceans in the 2000s: An Integrated Approach*, France, 1997.

[117] O. Nogues, "PITPOC Proposal," 2009.

[118] TSC-UPC anechoic chamber

[Online, Dec. 31st 2010] www.tsc.upc.es/researcheef/antennas/antennalab_website/r_grups_amp.html

[119] I. Ramos-Perez, X. Bosch-Lluis, A. Camps, J.F. Marchan-Hernandez, R. Prehn, B. Izquierdo, "Design of a Compact Dual-Polarization Receiver for Pseudo-Correlation Radiometers at L-band," IEEE International Conference on Geoscience and Remote Sensing Symposium, pp.1172-1175, 2006.

[120] Analog Devices AD9201 Datasheet

[Online, Dec. 31st 2010] http://www.analog.com/static/imported-files/data_sheets/AD9201.pdf

[121] NoiseCom NC346 Datasheet

[Online, Dec. 31st 2010] http://www.noisecom.com/~/media/Noisecom/Datasheets/NC346Datasheet_WEB.ashx

[122] A. Paula, and R.J. Pieper "A more complete analysis for subnyquist band-pass sampling", Proceedings System Theory SSST/CSA, pp. 20 – 24, 1992.

[123] Thermal evaluation of solid electrical insulating materials, "Standard for the preparation of test procedures for the thermal evaluation of solid electrical insulating materials", IEEE Standard 98-2002, 2002.

[124] ALTERA, "NIOS II processor reference handbook", 2009

[Online, Dec. 31st 2010] www.altera.com/literature/hb/nios2/n2sw_nii5v2.pdf

[125] R. H. Frater and D. R. Williams "Active cold noise source," *IEEE Transactions on Microwave Theory Technology*, vol. 29, n.4, pp. 344–347, 1981.

[126] X. Bosch-Lluis, A. Camps, I. Ramos-Perez, J.F. Marchan-Hernandez, N. Rodriguez-Alvarez, E. Valencia, "PAU/RAD: Design and Preliminary Calibration Results of a New L-Band Pseudo-Correlation Radiometer Concept," *Sensors Journal*, vol. 8, n.7, pp. 4392 – 4412, 2008.

[127] D. W. Allan, H. Hellwig, and D. J. Glaze, "An accuracy algorithm for an atomic time scale," *Metrologia*, vol. 1 , pp. 133-138, 1975.

[128] E. Nagelberg, "Fresnel region phase centers of circular aperture antennas," *IEEE Transactions on Antennas and Propagation*, Vol.13 (3), pp. 479-480. 1965.

[129] J. Rice, "Mathematical Statistics and Data Analysis (Second ed.)," *Duxbury Press*, 1995.

[130] N. Rodriguez-Alvarez, A. Camps, X. Bosch-Lluis, I. Ramos-Perez and J.F. Marchan-Hernandez, "PAU-IR: Sea surface temperature retrieval using IR-radiometry and atmospheric modeling: Simulation and experimental results," *Proceedings of the International Geoscience and Remote Sensing Symposium 2007*, pp. 933-936, Barcelona, 2007.

[131] ECH2O Soil Moisture Sensor.

[Online, Dec. 31st, 2010] http://www.decagon.com/ag_research /soil/ec5.php

[132] X. Bosch-Lluis, I. Ramos-Perez, A. Camps, N. Rodriguez-Alvarez, E. Valencia, "Common Mathematical Framework for Real and Synthetic Aperture Radiometers," *IEEE Transactions on Geoscience and Remote Sensing,* (Submitted).

[133] X. Bosch-Lluis, I. Ramos-Perez, A. Camps, N. Rodriguez-Alvarez, E. Valencia, H. Park, "A General Analysis of the Digitization Impact in Microwave Correlation Radiometers," *Sensors Journal,* (Submitted).

[134] X. Bosch-Lluis, I. Ramos-Perez, A. Camps J.F. Marchan-Hernandez, N. Rodriguez-Alvarez, E. Valencia, "The impact of the number of bits in digital beamforming real aperture and synthetic aperture radiometers," *Microwave Radiometry and Remote Sensing of the Environment, 2008. MICRORAD 2008*, pp.1-4, 2008.